

AD-A128 588

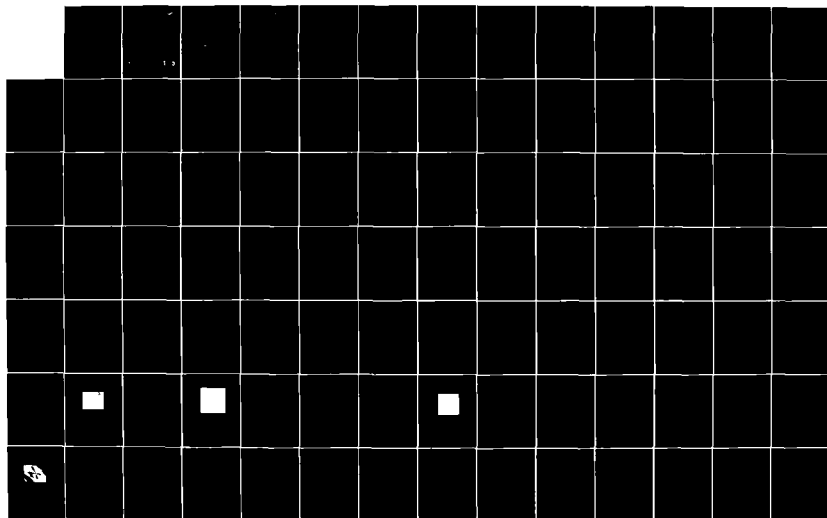
DEVELOPMENT OF HIGH EFFICIENCY STACKED MULTIPLE BANDGAP
SOLAR CELLS. (U) RESEARCH TRIANGLE INST RESEARCH
TRIANGLE PARK NC 5 M BEDAIR ET AL. SEP 82

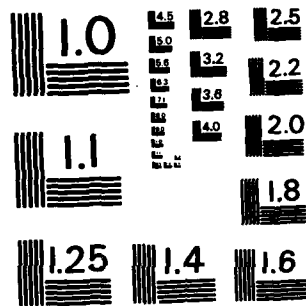
1/3

UNCLASSIFIED

RTI/1878/00-F-VOL-2 AFAPL-TR-79-2118-VOL-2 F/G 10/2

NL





MICROCOPY RESOLUTION TEST CHART
NATIONAL BUREAU OF STANDARDS-1963-A

2

AFAPL-TR-79-2116

Volume II

DEVELOPMENT OF HIGH EFFICIENCY, STACKED MULTIPLE BANDGAP SOLAR CELLS

Research Triangle Institute
P. O. Box 12194
Research Triangle Park, NC 27709

September 1982

FINAL REPORT FOR PERIOD OCTOBER 1979 - MARCH 1982

APPROVED FOR PUBLIC RELEASE; DISTRIBUTION UNLIMITED

AERO PROPULSION LABORATORY
AIR FORCE WRIGHT AERONAUTICAL LABORATORIES
AIR FORCE SYSTEMS COMMAND
WRIGHT-PATTERSON AIR FORCE BASE, OHIO 45433

DTIC
ELECTE
S APR 11 1983 D
D

83 04 08 055

ADA 126588

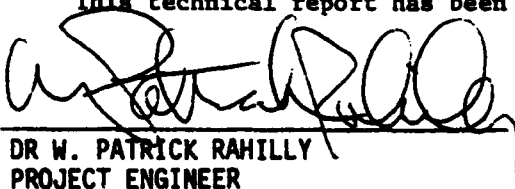
DTIC FILE COPY


NOTICE

When Government drawings, specifications, or other data are used for any purpose other than in connection with a definitely related Government procurement operation, the United States Government thereby incurs no responsibility nor any obligation whatsoever; and the fact that the government may have formulated, furnished, or in any way supplied the said drawings, specifications, or other data, is not to be regarded by implication or otherwise as in any manner licensing the holder or any other person or corporation, or conveying any rights or permission to manufacture use, or sell any patented invention that may in any way be related thereto.


This report has been reviewed by the Office of Public Affairs (ASD/PA) and is releasable to the National Technical Information Service (NTIS). At NTIS, it will be available to the general public, including foreign nations.

This technical report has been reviewed and is approved for publication.


DR W. PATRICK RAHILLY
PROJECT ENGINEER


PAUL R. BERTHEAUD
Acting Chief, Energy Conversion Branch
Aerospace Power Division
Aero Propulsion Laboratory

FOR THE COMMANDER


D. DAVID RANDOLPH, Major, USAF
Acting Chief
Aerospace Power Division
Aero Propulsion Laboratory

"If your address has changed, if you wish to be removed from our mailing list, or if the addressee is no longer employed by your organization please notify AFMAL/POOC-2, W-PAFB, OH 45433 to help us maintain a current mailing list."

Copies of this report should not be returned unless return is required by security considerations, contractual obligations, or notice on a specific document.

Unclassified

SECURITY CLASSIFICATION OF THIS PAGE (When Data Entered)

REPORT DOCUMENTATION PAGE		READ INSTRUCTIONS BEFORE COMPLETING FORM
1. REPORT NUMBER AGAPL-TR-79-2116 Volume II	2. GOVT ACCESSION A126 588	RECIPIENT'S CATALOG NUMBER
4. TITLE (and Subtitle) DEVELOPMENT OF HIGH EFFICIENCY, STACKED MULTIPLE BANDGAP SOLAR CELLS	5. TYPE OF REPORT & PERIOD COVERED Final 10-1-79 to 3-31-82	
7. AUTHOR(s) S. M. Bedair, R. J. Markunas, J. P. C. Chiang, and J. A. Hutchby	6. PERFORMING ORG. REPORT NUMBER RTI/1678/00-F	
9. PERFORMING ORGANIZATION NAME AND ADDRESS Research Triangle Institute P. O. Box 12194 Research Triangle Park, NC 27709	8. CONTRACT OR GRANT NUMBER(s) F33615-78-C-2077	
11. CONTROLLING OFFICE NAME AND ADDRESS (AFWAL/POOC-2) Aero Propulsion Laboratory Air Force Wright Aeronautical Lab (AFSC) Wright-Patterson AFB, Ohio 45433	10. PROGRAM ELEMENT, PROJECT, TASK AREA & WORK UNIT NUMBERS PE 3145 Proj. 314519 W. U. 31451969	
14. MONITORING AGENCY NAME & ADDRESS (if different from Controlling Office)	12. REPORT DATE September, 1982	
	13. NUMBER OF PAGES 248	
	15. SECURITY CLASS. (of this report) Unclassified	
	15a. DECLASSIFICATION/DOWNGRADING SCHEDULE	
16. DISTRIBUTION STATEMENT (of this Report) Approved for public release; distribution unlimited.		
17. DISTRIBUTION STATEMENT (of the abstract entered in Block 20, if different from Report)		
18. SUPPLEMENTARY NOTES		
19. KEY WORDS (Continue on reverse side if necessary and identify by block number) Cascade Solar Cells, Multijunction Solar Cells, III-V Compound Semiconductors, Gallium Arsenide, Aluminum Gallium Arsenide		
20. ABSTRACT (Continue on reverse side if necessary and identify by block number) * This report presents the results of a program conducted at RTI to develop a high efficiency, two junction cascade solar cell suitable for space applications. The bulk of the report focuses on the AlGaAs/GaAs material system. This work involved both theoretical and experimental studies. The technology developed for the LPE growth of the planar cascade structure is presented. This includes doping studies, and the development of optimum growth procedures for obtaining high quality LPE layers. Ohmic contact and AR coating		

DD FORM 1473 EDITION OF 1 NOV 65 IS OBSOLETE

Unclassified
SECURITY CLASSIFICATION OF THIS PAGE (When Data Entered)

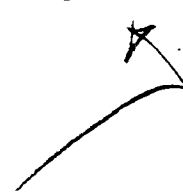
Unclassified

SECURITY CLASSIFICATION OF THIS PAGE(When Data Entered)

20. ABSTRACT (continued)

technologies are discussed and are related to experimental device performance. Experimental results are presented for individual top cells, bottom cells, and connecting junctions as well as for monolithic cascade structures. The experimental results are correlated with modeling results to determine the factors limiting the performance of these cells.

The maximum experimental efficiency achieved during the program was 15.1% under AMO, 1 sun conditions with no AR coating. Material constraints due to the degenerately doped tunnel junction were found to limit cascade cell performance and device yield. In response to the findings on the planar cascade structure, a novel cascade design, the Patterned Tunnel Junction cell, was developed.



Unclassified

SECURITY CLASSIFICATION OF THIS PAGE(When Data Entered)

PREFACE

The work described in this report was conducted in the Semiconductor Research Department of the Research Triangle Institute, Research Triangle Park, N. C. during the period from October 1, 1979 to March 31, 1982. The program was sponsored by the Air Force Wright Aeronautical Laboratory, Wright-Patterson Air Force Base, Ohio. W. P. Rahilly (AFWAL/POOC-2) was the Air Force Project Engineer.

The principal authors of this report are S. M. Bedair, R. J. Markunas, J. P. C. Chiang, and J. A. Hutchby. Significant contributions to the experimental effort were also made by G. Kelner, R. A. Connor, T. S. Colpitts, A. D. Brooks, M. Dubey, E. A. Andrews, M. L. Timmons, and F. S. Stevens. Others contributing to the program were M. F. Lamorte (modeling), J. R. Hauser, M. Simons, J. J. Wortman, and R. D. Alberts.

Accession For	
NTIS GRA&I	<input checked="checked" type="checkbox"/>
DTIC TAB	<input type="checkbox"/>
Unannounced	<input type="checkbox"/>
Justification	
By	
Distribution/	
Availability Codes	
Dist	Avail and/or Special
A	



TABLE OF CONTENTS

	<u>Page</u>
1.0 INTRODUCTION	1
2.0 AlGaAs-GaAs PLANAR CASCADE SOLAR CELL	3
2.1 Introduction	3
2.2 Modeling and Projected Performance	3
2.2.1 Introduction	3
2.2.2 Material Parameters	4
2.2.2.1 Bandgap	4
2.2.2.2 Effective Masses, Dielectric Constant and Electron Affinity	5
2.2.2.3 Mobility and Lifetime	8
2.2.2.4 Interface Recombination	11
2.2.3 Computer-Modeling Analysis	12
2.3 Experimental Planar Cascade Development	22
2.3.1 Evolution of the Cascade Structure	22
2.3.2 Material Growth by Liquid Phase Epitaxy	26
2.3.2.1 Overview of Materials Issue	27
2.3.2.2 Bottom Cell and Bottom Cell Window Layer	28
2.3.2.3 Tunnel Junction	50
2.3.2.4 Top Cell	68
2.3.2.5 Top Cell Window Layer	69
2.3.2.6 GaAs Contact Layer	69
2.3.3 Cell Fabrication	70
2.3.3.1 Electrical Contacts	70
2.3.3.2 Antireflection Coating	71

TABLE OF CONTENTS (continued)

	<u>Page</u>
3.0 EXPERIMENTAL CELL PERFORMANCE	77
3.1 Experimental Techniques	77
3.1.1 Current-Voltage Characteristics	77
3.1.2 Spectral Response	80
3.1.3 Diffusion Length	83
3.1.4 Resistance	84
3.1.4.1 Series Resistance	84
3.1.4.2 Contact Resistance	87
3.1.4.3 Shunt Resistance	88
3.2 Experimental Results	90
3.2.1 Introduction	90
3.2.2 Dark Current-Voltage Characteristics	93
3.2.2.1 Diode Factor	93
3.2.2.2 Reverse Saturation Current	103
3.2.3 Current-Voltage Characteristics Under Illumination	108
3.2.3.1 Introduction	108
3.2.3.2 Open Circuit Voltage	120
3.2.3.3 Short Circuit Current	120
3.2.3.4 Fill Factor	131
3.2.3.5 Efficiency	150
3.2.4 Spectral Response	152
3.2.5 Mobility and Diffusion Length	155
3.2.5.1 Mobility	155
3.2.5.2 Diffusion Length	163
3.2.6 Resistance	163
3.2.6.1 Series Resistance	163

TABLE OF CONTENTS (concluded)

	<u>Page</u>
3.2.6.2 Shunt Resistance	177
3.2.6.3 Contact Resistance	191
3.2.7 Summary of Best Results	191
4.0 AlGaAs-GaAs PATTERNED TUNNEL JUNCTION CELL	195
4.1 Introduction	195
4.2 Device Structure	200
4.3 Cell Development	202
4.3.1 Material Growth	202
4.3.1.1 Tunnel Junction and Bottom Cell	202
4.3.1.2 Tunnel Junction Etching	207
4.3.1.3 Tunnel Junction Stability	208
4.3.1.4 Initial Results on the Patterned Tunnel Junction Cell	208
5.0 SUMMARY AND CONCLUSIONS	217
APPENDIX I	221
REFERENCES	243

LIST OF ILLUSTRATIONS

		<u>Page</u>
Figure 2.1	Bandgap of $\text{Al}_x\text{Ga}_{1-x}\text{As}$ as a Function of Composition.	6
Figure 2.2	Band Structure Used in the Study and Parameters Obtained for Optimized Design by Maximizing Conversion Efficiency.	23
Figure 2.3	AlGaAs Cascade Solar Cell Configuration. (a) Original Structure Using Ge- and Sn-Doped Grown p-n Junction, and (b) Current Structure Using p-n Junction Formed by Be Diffused into Unintentionally Doped n-Layers.	24
Figure 2.4	The Dependence of Hole Concentration and Resistivity at Room Temperature on Al Composition in Be-doped $\text{Al}_x\text{Ga}_{1-x}\text{As}$. X_{Be}^{L} is approximately between 1 and 8×10^{-3} at.% in all the samples.	36
Figure 2.5	The Variation of Hole Concentration at Room Temperature with Be Concentration in the Ga Solution.	36
Figure 2.6	The Variation of the Distribution Coefficient of Be, K_{Be} , at 800°C in $\text{Al}_x\text{Ga}_{1-x}\text{As}$ as a Function of Al Composition. $K_{\text{Be}} = C_{\text{Be}}^{\text{S}}/C_{\text{Be}}^{\text{L}}$, where C_{Be}^{S} and C_{Be}^{L} are the concentration of Be in the Solid and Liquid Phases, Respectively. The solid circles show the results when C_{Be}^{S} for the acceptor impurity is taken to be equal to the hole concentration at room temperature because of degeneracy of these samples, whereas the open circles are the results when $C_{\text{Be}}^{\text{S}} = N_{\text{A}}$.	40
Figure 2.7	The Temperature Dependence of Hole Concentration in $\text{Al}_x\text{Ga}_{1-x}\text{As}$ Epilayers with Various Al Compositions. The doping level S_{Be}^{L} in the epilayers is about 4×10^{-2} at.% with the exception of $x = 0.45$, where $X_{\text{Be}}^{\text{L}} \approx 1.5 \times 10^{-3}$ at.%. The solid lines are the results calculated by least-square curve fitting.	41
Figure 2.8	The Temperature Dependence of Hole Concentration in $\text{Al}_{0.8}\text{Ga}_{0.2}\text{As}$ Epilayers Grown at Various X_{Be}^{L} . The solid lines are the results calculated by least-square curve fitting. X_{Be}^{L} in each sample is as follows; $\bullet, \blacksquare, \blacktriangle$: 4×10^{-2} at.%; \square : 8×10^{-2} at.%; ∇ : 8×10^{-2} at.%; Δ : 1.6×10^{-2} at.%. See Table 2.3.	42

LIST OF ILLUSTRATIONS (continued)

	<u>Page</u>
Figure 2.9 The Relationship of ΔE_A vs. N_A for Be-doped $Al_xGa_{1-x}As$ with $x = 0.8$ and 0.45 . The solid lines are calculated by least-square curve fitting.	45
Figure 2.10 The Temperature Dependence of Hole Hall Mobility in $Al_{0.8}Ga_{0.2}As$ with Various N_A Values. The symbols identifying the samples are the same as those in Figure 2.8.	45
Figure 2.11 The Variation of Hole Hall Mobility with N_A or p in $Al_{0.8}Ga_{0.2}As$ doped with Be. The open and solid triangles indicate the results for $x = 0.85$.	46
Figure 2.12 The Variation of Hole Hall Mobility with x Value in $Al_xGa_{1-x}As$ with the Acceptor Concentration $3.0 \times 10^{18} < N_A < 3.8 \times 10^{18} \text{ cm}^{-3}$. The solid line shows the result from calculations using an expression for alloy scattering rate in Ref. [2.61].	46
Figure 2.13 Voltage Current Characteristics of $AlGaAs$ Tunnel Diode; the Diode Area is $3 \times 10^{-2} \text{ cm}^2$. Scale: 0.1 V/div and 10 mA/div .	53
Figure 2.14 Forward Current-Voltage Characteristics at $78^\circ K$ of $Al_{0.17}Ga_{0.83}As$ Tunnel Diode. The diode area is $5 \times 10^{-2} \text{ cm}^2$.	55
Figure 2.15 Forward Current-Voltage Characteristic at $78^\circ K$ of $Al_{0.26}Ga_{0.74}As$ Tunnel Diode. The diode area is $1.5 \times 10^{-2} \text{ cm}^2$.	57
Figure 2.16 Current-Voltage Characteristics at Room Temperature of $Al_{0.35}Ga_{0.65}As$ Backward Diode. The diode area is $1.1 \times 10^{-2} \text{ cm}^2$.	59
Figure 2.17 Conical Hills Representative of those Observed for Heavy Te- or Se-Doping of $AlGaAs$. (Te = 0.4 atomic percent) Magnification 82.5. Sample L-274-B.	66
Figure 2.18 Current-Voltage Characteristic for an Illuminated $AlGaAs$ - $GaAs$ Cascade Solar Cell Before and After AR Coating.	72
Figure 2.19 Spectral Response for an Illuminated $AlGaAs$ - $GaAs$ Cascade Solar Cell Before and After AR Coating.	73
Figure 3.1 Schematic Representation of the Set-up for Dark I-V Measurements.	78
Figure 3.2 Block Diagram of the Set-up for I-V Measurements under AMO Illumination.	79

LIST OF ILLUSTRATIONS (continued)

	<u>Page</u>
Figure 3.3 Schematic Representation of the Set-up for Spectral Response Measurements.	81
Figure 3.4 Comparison of the Calibrated System and the Standard System for Spectral Response Measurements.	82
Figure 3.5 Schematic Representation of the Set-up for Diffusion Length Measurements.	85
Figure 3.6 Schematic Illustration for the Calculation of the Series Resistance of a Solar Cell.	86
Figure 3.7 Contact Pattern for Contact Resistance Measurements.	89
Figure 3.8 Resistance Versus Contact Spacing.	89
Figure 3.9 Scanning Electron Micrographs of an AlGaAs-GaAs Cascade Solar Cell Cross-Section. (a) Combined secondary-emission and electron-beam-induced-current modes, and (b) secondary emission mode only.	91
Figure 3.10 Composition Profile and Structure of a Cascade Cell for the Computer Simulation.	92
Figure 3.11a Dark I-V Measurements of Top and Bottom Cells.	94
Figure 3.11b Dark I-V Measurements of a Cascade Cell.	95
Figure 3.12 Model of Minority Carrier Flow Around the Junction at the Edge.	96
Figure 3.13a Contact Pattern for the Separation of the Edge Current from the Total Current.	96
Figure 3.13b Schematic Representation of the Set-up for the Separation of Currents through the Center and the Circumference.	96
Figure 3.14 I-V Measurements of Inner and Outer Diodes.	97
Figure 3.15a Short Circuit Current versus Open Circuit Voltage for Bottom Cells.	99
Figure 3.15b Short Circuit Current versus Open Circuit Voltage for Top and Cascade Cells.	100
Figure 3.16 Log ($I + I_{sc}$) versus Voltage Plots for a Bottom Cell under Various AMO Illumination Levels.	101

LIST OF ILLUSTRATIONS (continued)

		<u>Page</u>
Figure 3.17	Comparison of I-V Measurements using Various Approaches.	104
Figure 3.18a	Dark I-V Characteristics of the Top Cell as a Function of the Minority Carrier Lifetimes.	105
Figure 3.18b	Comparison Between the Calculated and Measured Reverse Saturation Currents of the Bottom Cell.	106
Figure 3.18c	Comparison Between the Calculated and Measured Reverse Saturation Currents of the Cascade Cell.	107
Figure 3.19a	I-V Measurements of a Top Cell under AMO Illumination.	109
Figure 3.19b	I-V Measurements of a Bottom Cell under AMO Illumination.	109
Figure 3.19c	I-V Measurements of a Cascade Cell under AMO Illumination.	110
Figure 3.20a	I-V Characteristics of the Top Cell under AMO Illumination.	111
Figure 3.20b	Dependence of Efficiency on the Terminal Voltage for the Top Cell.	112
Figure 3.20c	I-V Characteristics of the Bottom Cell under AMO Illumination.	113
Figure 3.20d	Dependence of Efficiency on the Terminal Voltage for the Bottom Cell.	114
Figure 3.20e	I-V Characteristics of the Bottom Cell with a Top Cell under AMO Illumination.	115
Figure 3.20f	Dependence of Efficiency on the Terminal Voltage for the Bottom Cell with a Top Cell.	116
Figure 3.20g	I-V Characteristics of the Cascade Cell under AMO Illumination.	117
Figure 3.20h	Dependence of Efficiency on the Terminal Voltage for the Cascade Cell.	118
Figure 3.21	Dependence of Efficiency on the Bandgap of the Top Cell in a Cascade Structure.	119
Figure 3.22	Dependence of Short Circuit Current on the Bandgap of the Top Cell in a Cascade Structure.	122

LIST OF ILLUSTRATIONS (continued)

	<u>Page</u>
Figure 3.23 I-V Characteristics of a Cascade Cell Showing the Current Mismatch between the Top Cell and the Bottom Cell.	123
Figure 3.24 I-V Characteristics of a Cascade Cell with an Improved Current Matching between the Top Cell and the Bottom Cell.	124
Figure 3.25a Carrier Generation Rate Profile of the Top Cell.	125
Figure 3.25b Carrier Generation Rate Profile of the Bottom Cell.	126
Figure 3.25c Carrier Generation Rate Profile of the Bottom Cell with a Top Cell.	127
Figure 3.25d Carrier Generation Rate Profile of the Cascade Cell.	128
Figure 3.26 Dependence of Spectral Currents within Various Regions of a Cascade Cell on the Thickness of the Window Layer.	129
Figure 3.27 Dependence of Short Circuit Current on p-n Junction Depth.	130
Figure 3.28a Effect of Window Layer Thickness on I-V Characteristics of the Cascade Cell.	132
Figure 3.28b Effect of Window Layer Thickness on the Efficiency of the Cascade Cell.	133
Figure 3.29 Dependence of Short Circuit Current on Hole Diffusion Length for a Top Cell with a Bandgap of 1.90 eV.	134
Figure 3.30 Dependence of Parameters on Diffusion Lengths for a Top Cell with a Bandgap of 1.97 eV.	135
Figure 3.31 I-V Characteristics of a Cascade Cell with a Poor Dark I-V Curve.	139
Figure 3.32 I-V Characteristics of the AlGaAs Tunnel Junction at Temperature 77°K.	140
Figure 3.33 I-V Characteristics of a Bottom Cell under Various AMO Illuminations.	142
Figure 3.34a Dependence of Open Circuit Voltage on Light Intensity.	143

LIST OF ILLUSTRATIONS (continued)

	<u>Page</u>
Figure 3.34b Dependence of Fill Factor on Light Intensity.	144
Figure 3.34c Dependence of Efficiency on Light Intensity.	145
Figure 3.35a Comparison of I-V Characteristics of a Cascade Cell under 1-sun and Multi-sun Illuminations.	146
Figure 3.35b Effect of Tunnel Junction on the Performance of a Cascade Cell Operated at High Solar Intensity.	147
Figure 3.36 Negative Resistance Region on I-V Characteristics of a Cascade Cell under Multi-sun Illumination.	148
Figure 3.37 I-V Characteristics of AlGaAs Tunnel Diode.	149
Figure 3.38 Improvement of Fill Factors under Multi-sun Condition for Cascade Cells with Poor Fill Factors at One Sun Illumination.	151
Figure 3.39 Reflection of Light on the Surface of AlGaAs Cascade Solar Cell.	153
Figure 3.40a Comparison of Calculated Spectral Responses and Experimental Measurements for Top Cells.	154
Figure 3.40b Comparison of Calculated Spectral Responses and Experimental Measurements for a Bottom Cell with a Tunnel Junction.	156
Figure 3.41a Comparison of Calculated Quantum Efficiencies and Experimental Measurements for Top Cells.	157
Figure 3.41b Comparison of Calculated Quantum Efficiencies and Experimental Measurements for Cascade Cells.	158
Figure 3.42a Relationship between Hole Mobility and Doping Density in AlGaAs.	159
Figure 3.42b Relationship between Hole Mobility and AlAs Composition in AlGaAs.	160
Figure 3.43a Relationship between Hole Mobility and Doping Density in $\text{Al}_{0.8}\text{Ga}_{0.2}\text{As}$.	161
Figure 3.43b Relationship between Hole Mobility and AlAs Composition in AlGaAs with a Doping Density $3.4 \times 10^{18}/\text{cm}^3$.	162
Figure 3.44 Dependence of Diffusion Lengths on AlAs Composition in AlGaAs.	164

LIST OF ILLUSTRATIONS (continued)

	<u>Page</u>
Figure 3.45a Effect of High Series Resistance on I-V Characteristics of a Cascade Cell.	165
Figure 3.45b Effects of High Series Resistance on I-V Characteristics of Cascade Cells.	166
Figure 3.46 Series Resistance Measurement for a Cascade Cell.	167
Figure 3.47a Series Resistance Effect on I-V Characteristics of the Top Cell under AMO Illumination.	169
Figure 3.47b Series Resistance Effect on I-V Characteristics of the Bottom Cell under AMO Illumination.	170
Figure 3.47c Series Resistance Effect on I-V Characteristics of the Cascade Cell under AMO Illumination.	171
Figure 3.48 Series Resistance Effect on Fill Factors of Solar Cells.	172
Figure 3.49a Series Resistance Effect on Efficiency of the Top Cell under AMO Illumination.	173
Figure 3.49b Series Resistance Effect on Efficiency of the Bottom Cell under AMO Illumination.	174
Figure 3.49c Series Resistance Effect on Efficiency of the Cascade Cell under AMO Illumination.	175
Figure 3.50 Series Resistance Effect on Efficiencies of Solar Cells.	176
Figure 3.51a Series Resistance Effect on Dark I-V Characteristics of the Top Cell.	178
Figure 3.51b Series Resistance Effect on Dark I-V Characteristics of the Bottom Cell.	179
Figure 3.51c Series Resistance Effect on Dark I-V Characteristics of the Cascade Cell.	180
Figure 3.52a Shunt Resistance Effect on I-V Characteristics of the Top Cell under AMO Illumination.	181
Figure 3.52b Shunt Resistance Effect on I-V Characteristics of the Bottom Cell under AMO Illumination.	182
Figure 3.52c Shunt Resistance Effect on I-V Characteristics of the Cascade Cell under AMO Illumination.	183

LIST OF ILLUSTRATIONS (continued)

	<u>Page</u>
Figure 3.53a Shunt Resistance Effect on Efficiency of the Top Cell under AMO Illumination.	184
Figure 3.53b Shunt Resistance Effect on Efficiency of the Bottom Cell under AMO Illumination.	185
Figure 3.53c Shunt Resistance Effect on Efficiency of the Cascade Cell under AMO Illumination.	186
Figure 3.54 Shunt Resistance Effect on Efficiencies of Solar Cells.	187
Figure 3.55a Shunt Resistance Effect on Dark I-V Characteristics of the Top Cell.	188
Figure 3.55b Shunt Resistance Effect on Dark I-V Characteristics of the Bottom Cell.	189
Figure 3.55c Shunt Resistance Effect on Dark I-V Characteristics of the Cascade Cell.	190
Figure 3.56a Comparison of the Calculated Dark I-V Characteristics and Experimental Measurements of a Bottom Cell.	192
Figure 3.56b Comparison of Calculated Dark I-V Characteristics and Experimental Measurements for a Top Cell.	193
Figure 4.1 AlGaAs-GaAs Cascade Cell with Patterned Tunnel Junction. Homotunnel Junction Cell.	196
Figure 4.2 AlGaAs-GaAs Cascade Cell with Patterned Tunnel Junction. Heterotunnel Junction Cell.	201
Figure 4.3 Homojunction Sequence.	205
Figure 4.4 Heterojunction Sequence.	206
Figure 4.5 Current-Voltage Characteristics of an AlGaAs Top Cell (Eg. = 1.85 eV) Grown on a Patterned GaAs Homotunnel Junction: (a) 6 suns, FF 0.77, V_{oc} 1.26 V; (b) 1 sun, FF 0.82, V_{oc} 1.10 V.	210
Figure 4.6 Sample G409--GaAs Tunnel Junction Grown at 800°C (TYPE 3) after a 10 min etch in AB etchant at 25°C. Magnification = 145X.	214
Figure A.0 Bandgap and Lattice Constant Values for the III-V Semiconductors.	222
Figure A.1 AlGaAs/AlGaAs/InGaAs Material System.	224

LIST OF ILLUSTRATIONS (concluded)

		<u>Page</u>
Figure A.2	AlAsSb/InGaP/InGaAs Material System.	229
Figure A.3	AlGaAsSb/AlGaAsSb/InGaAs Material System.	231
Figure A.4	Inverted GaInAs/AlGaAs Cell Structure.	233
Figure A.5	Hole Concentration vs Atomic Fraction of Mn in Melt.	236
Figure A.6	Temperature Dependence of Mn Distribution Coefficient: Open and Closed Circuits Represent our Data Points.	236
Figure A.7	Dependence of Hall Mobility on Hole Concentration.	237
Figure A.8	Hall Mobility vs. Temperature for Mn-Doped $p\text{-Ga}_{0.79}\text{In}_{0.21}\text{As}$.	238
Figure A.9	Hole Concentration vs. Inverse Temperature for Mn-doped $p\text{-Ga}_{0.79}\text{In}_{0.21}\text{As}$.	240

LIST OF TABLES

		<u>Page</u>
Table 2.1	Definition of Symbols	14
Table 2.2	Summary of Optimum (BOL - Beginning of Life) Design Parameters and Operating Conditions	21
Table 2.3	Summary of Results	39
Table 2.4a	Rationalized Tetrahedral Radii According to Phillips [2.79]	63
Table 2.4b	Tetrahedral Covalent Radii According to Pauling [2.80]	63
Table 2.5	Theoretical Analysis for Two-Layer AR Coating	75
Table 3.1	Dependence of Fill Factor on Carrier Lifetimes for a Top Cell with a Bandgap of 1.97 eV	137
Table 3.2	Ratios of Experimental Data and Theoretical	150
Table 3.3	Projected Cascade Efficiency Based on Best Measured Parameters	194
Table 4.1	Thermodynamic Data	198
Table 4.2	Layer Specifications for the Patterned Tunnel-Junction Cascade Structure - Homotunnel Junction	203
Table 4.3	Layer Specifications for the Patterned Tunnel-Junction Cascade Structure - Heterotunnel Junction	204
Table 4.4	Control Wafer EPD at 360 μm	211
Table 4.5	EPD (Etch Pit Density) Results Comparing $\text{n}^+(\text{Te})\text{GaAs}/\text{p}^+(\text{Ge})\text{GaAs}$ Tunnel Junctions with $\text{n}^+(\text{Te})\text{Al}_{.35}\text{Ga}_{.65}\text{As}/\text{p}^+(\text{Ge})\text{Al}_{.35}\text{Ga}_{.65}\text{As}$ Tunnel Junctions	212

1.0 INTRODUCTION

The goal of this program has been the development of the technology required to fabricate two-junction, monolithic cascade solar cells with greater than 25% conversion efficiency at 25°C in an AMO, 1 sun environment.

A number of ternary and quaternary material systems with potential application to the cascade solar cell were studied in the initial stages of this work. These other material systems are reviewed in the Appendix. The remainder of this report focuses on the AlGaAs/GaAs material system. This system was chosen primarily because the AlGaAs ternary is nearly lattice-matched to the GaAs binary over the entire alloy range. In addition, a number of essential growth and device fabrication technologies had been developed for this system through work on other devices, especially lasers.

Section 2 discusses the modeling and growth of the planar cascade solar cell with emphasis on the material constraints that influence cell performance. Section 3 compares the experimental performance of these cascade structures with the performance predicted by computer modeling, and focuses on the key technical issues limiting the performance of these cells. Section 4 presents a novel structure that RTI has developed in response to the findings presented in Sections 2 and 3. Section 4 also presents the results of the initial development of this structure, the Patterned Tunnel Junction cell.

Section 5 presents a program summary and conclusions pertinent to the continued development of the cascade solar cell.

2.0 AlGaAs-GaAs PLANAR CASCADE SOLAR CELL

2.1 Introduction

The AlGaAs-GaAs two-junction cascade cell is particularly attractive since it employs a well-proven materials technology with a ternary compound that is almost completely lattice-matched over its entire compositional range and can therefore be readily grown on GaAs substrate material. The energy bandgap range of the AlGaAs ternary system does not allow a bottom cell bandgap value of 0.95 eV that would be ideal for peak efficiency of a two-junction cascade cell in the space environment. However, the larger bottom cell bandgap (1.44 eV) used in the AlGaAs-GaAs system can be compensated for by increasing the top cell bandgap. Given a bottom cell bandgap of 1.44 eV, the optimized bandgap of the top cell is 1.94 eV. Thus the optimized AlGaAs/GaAs combination is 1.94/1.44 (eV) vs. 1.6/0.95 (eV) for the ideal unconstrained system. Computer-based modeling and optimization studies carried out at RTI show that the 1.94/1.44 (eV) AlGaAs/GaAs cascade structure can achieve an active area efficiency of 27.5 percent at 1 sun AMO, 28°C. At 100°C the efficiency is calculated to be 21 percent.

This section reviews the optimization procedure used to develop the high-efficiency AlGaAs-GaAs cell design and presents performance data for this structure.

2.2 Modeling and Projected Performance

2.2.1 Introduction

A better understanding of the operation of semiconductor devices can only be obtained through a complete device model which usually involves a numerical calculation. It is believed that through a

detailed comparison between theoretical and experimental studies, problems limiting the efficiency of these cells can be revealed.

The material parameters discussed in the following sections are analyzed by providing the material properties of AlAs and GaAs, along with the desired AlAs composition. Equations of both a theoretical and an empirical nature have been used to obtain the alloy material parameters from the corresponding binary material parameters. All parameters used in this study are calculated or measured at room temperature, although the effects of temperature, radiation and solar intensity are included in the computer program for future study. In the following sections, to simplify the notation, any parameter with the subscript 1 refers to AlAs while the subscript 2 refers to GaAs.

2.2.2 Material Parameters

2.2.2.1 Bandgap

The values used for the direct and indirect bandgaps of the two binary semiconductors are:

AlAs: direct bandgap : 2.95 eV , [2.1]

indirect bandgap : 2.16 eV [2.2]

and GaAs: direct bandgap : 1.439 eV , [2.3]

indirect bandgap : 1.87 eV . [2.3]

It has been shown experimentally that the direct energy bandgap in many mixed III-V alloy systems has an approximately quadratic dependence on the mole fraction of one compound. The direct bandgap for $\text{Al}_x\text{Ga}_{1-x}\text{As}$ was calculated as a function of composition by [2.3]

$$E_{gd}(x) = 0.468 x^2 + 1.042 x + 1.439 \quad (2.1)$$

where x = mole fraction of AlAs.

The indirect bandgap was taken as approximately linear with composition as

$$E_{g1}(x) = 1.87 + 0.29 x. \quad (2.2)$$

Fig. 2.1 shows the dependence of the bandgap of $Al_xGa_{1-x}As$ on the AlAs composition.

2.2.2.2 Effective Masses, Dielectric Constant and Electron Affinity

The effective masses for $Al_xGa_{1-x}As$ in terms of electron rest mass m_0 are [2.4]

$$\text{holes: } m_{p1}^* = 0.85 m_0,$$

$$m_{p2}^* = 0.68 m_0,$$

$$\frac{1}{m_p^*} = \frac{x}{m_{p1}^*} + \frac{1-x}{m_{p2}^*} \quad (2.3)$$

$$\text{electrons: direct valley: } m_{cd1}^* = 0.128 m_0,$$

$$m_{cd2}^* = 0.0636 m_0,$$

$$\frac{1}{m_{cd}^*} = \frac{x}{m_{cd1}^*} + \frac{1-x}{m_{cd2}^*} \quad (2.4)$$

$$\text{indirect valley: } m_{ci1}^* = (0.37)(3)^{2/3} m_0,$$

$$m_{ci2}^* = (0.39)(3)^{2/3} m_0,$$

$$\frac{1}{m_{ci}^*} = \frac{x}{m_{ci1}^*} + \frac{1-x}{m_{ci2}^*}, \quad (2.5)$$

$$n^* = [m_{cd}^*]^{3/2} \exp\left(\frac{E - E_{gd}}{kT}\right) + [m_{ci}^*]^{3/2} \exp\left(\frac{E - E_{gi}}{kT}\right) \quad (2.6)$$

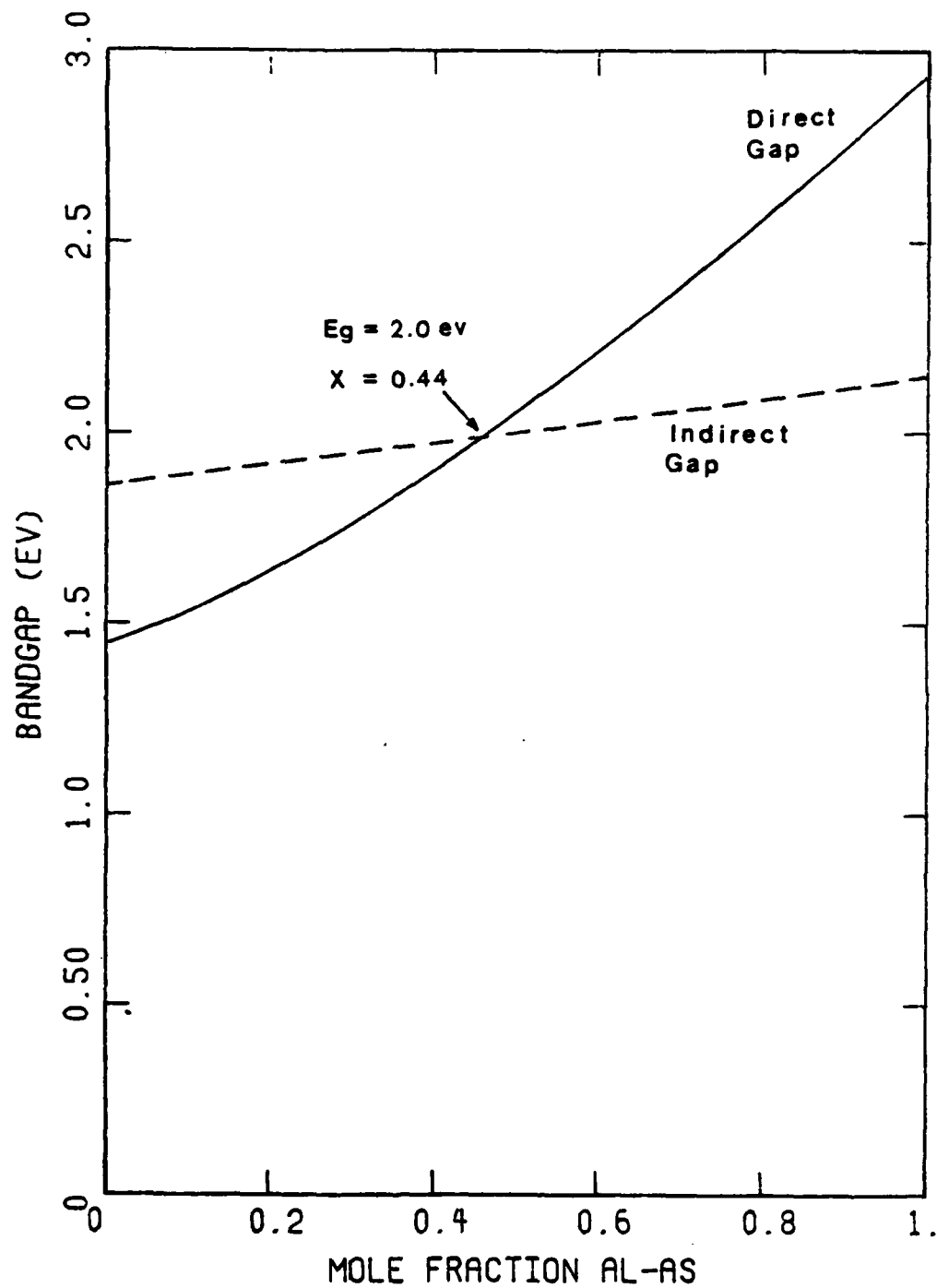


Figure 2.1. Bandgap of $\text{Al}_x\text{Ga}_{1-x}\text{As}$ as a Function of Composition.

The two sets of relative dielectric constants used are [2.5]:

$$\begin{aligned} \text{low frequency: } \epsilon_{l1} &= 10.9, \\ \epsilon_{l2} &= 13.2 \end{aligned}$$

$$\begin{aligned} \text{and high frequency: } \epsilon_{h1} &= 8.5, \\ \epsilon_{h2} &= 10.9. \end{aligned}$$

The dielectric constant for the alloy is estimated by the interpolation scheme [2.6]:

$$\epsilon = \frac{1+2[x(\frac{\epsilon_1-1}{\epsilon_1+2}) + (1-x)(\frac{\epsilon_2-1}{\epsilon_2+2})]}{1-x(\frac{\epsilon_1-1}{\epsilon_1+2}) - (1-x)(\frac{\epsilon_2-1}{\epsilon_2+2})} \quad (2.6)$$

The high frequency dielectric constant ϵ_h and the low frequency dielectric constant ϵ_l calculated in this way will be used in Sec. 2.2.2.3 for mobility calculations.

Following the experimental data for a direct bandgap ternary alloy by Tsu et al. [2.7] the electron affinity for $\text{Al}_x\text{Ga}_{1-x}\text{As}$ in the direct bandgap region ($x < 0.44$) can be approximated as

$$\chi_c = \chi_{c2} - K_a(E_{gd} - E_{g2}) \quad (2.7)$$

where K_a is a proportionality constant associated with the alloy being considered. Since electron affinity is defined as the energy difference between the conduction band edge and the vacuum level. The relationship between absolute bandgap and electron affinity in the indirect gap region ($x < 0.44$) was approximated by

$$\chi_c = \chi_{c2} - K_a (E_{gd} - E_{g2}) + E_{gd} - E_g, \quad (2.8)$$

where E_g is the absolute bandgap of the alloy. The values used are [2.8]:

$$K_a = 0.85,$$

$$\text{AlAs: } \chi_{c1} = 3.57 \text{ eV},$$

$$\text{and GaAs: } \chi_{c2} = 4.07 \text{ eV}.$$

2.2.2.3 Mobility and Lifetime

The hole mobility of GaAs expressed as a function of doping N is [2.6]

$$\mu_{p2}(N) = \frac{380 \text{ cm}^2/\text{V}\cdot\text{sec}}{[1 + (3.17 \times 10^{-17} \text{ cm}^3)\text{N}]^{0.266}}. \quad (2.9)$$

For the ternary compound

$$\mu_p = \frac{q \langle \tau \rangle_p}{m_p^*} = \mu_{p2} \frac{m_{p2}^*}{\langle \tau_{p2} \rangle} \frac{\langle \tau \rangle_p}{m_p^*}, \quad (2.10)$$

where $\langle \tau \rangle_p$ and $\langle \tau_{p2} \rangle$ are the mean times between scattering for holes in the alloy and in GaAs respectively. In the III-V semiconductors when polar optical scattering is assumed to be the major scattering mechanism [2.9], the mean time between scattering can be expressed as

$$\langle \tau \rangle = \frac{K}{\sqrt{m^*} \left(\frac{1}{\epsilon_h} - \frac{1}{\epsilon_l} \right)} \quad (2.11)$$

where K is a proportionality constant for all materials and ϵ_h and ϵ_l are the high and low frequency relative dielectric constants. Combining equations (2.10) and (2.11) leads to the mobility

$$\mu_p(N, x) = \frac{\mu_{p2}(N) m_{p2}^{*3/2} \left(\frac{1}{\epsilon_{h2}} - \frac{1}{\epsilon_{l2}} \right)}{m_p^{*3/2} \left(\frac{1}{\epsilon_h} - \frac{1}{\epsilon_l} \right)}.$$

Using the same approximation as for hole mobility, the electron mobility can be obtained by weighing the direct and indirect mobilities by their respective electron populations:

$$\mu_n(N, x) = \mu_d R_d + \mu_i (1 - R_d), \quad (2.12)$$

where

$$R_d = \frac{n_d}{n_d + n_i} = \frac{1}{1 + \left(\frac{m_{ci}^*}{m_{cd}^*} \right)^{3/2} \exp\left(\frac{E_{gd} - E_{gi}}{kT} \right)}, \quad (2.13)$$

$$\mu_d(N, x) = \frac{\mu_{n2}(N) m_{cd2}^{*3/2} \left(\frac{1}{\epsilon_{h2}} - \frac{1}{\epsilon_{l2}} \right)}{m_{cd}^{*3/2} \left(\frac{1}{\epsilon_h} - \frac{1}{\epsilon_l} \right)}, \quad (2.14)$$

and
$$\mu_i(N, x) = \frac{\mu_{n1}(N) m_{c1}^{3/2} \left(\frac{1}{\epsilon_{h1}} - \frac{1}{\epsilon_{l1}} \right)}{m_{c1}^{3/2} \left(\frac{1}{\epsilon_h} - \frac{1}{\epsilon_l} \right)} \quad (2.15)$$

For $\mu_{n2}(N)$ and $\mu_{n1}(N)$ (the mobilities of GaAs and AlAs respectively) we use [2.6, 2.10]

$$\mu_{n2}(N) = \frac{7200 \text{ cm}^2/\text{v} \cdot \text{sec}}{[1 + (5.51 \times 10^{-17} \text{ cm}^3)N]^{0.233}} \quad (2.16)$$

and
$$\mu_{n1}(N) = \frac{165 \text{ cm}^2/\text{v} \cdot \text{sec}}{[1 + (8.1 \times 10^{-17} \text{ cm}^3)N]^{0.13}} \quad (2.17)$$

The minority carrier lifetimes required by the Shockley-Read-Hall model were derived from the mobilities calculated as above and the diffusion lengths (obtained by curve fitting experimental data [2.11, 2.12, 2.13]),

$$L_n \approx \frac{8 \text{ } \mu\text{m}}{1 + N(8 \times 10^{-19} \text{ cm}^3)} \quad (2.18)$$

and
$$L_p \approx \frac{3 \text{ } \mu\text{m}}{1 + N(1.2 \times 10^{-18} \text{ cm}^3)} \quad (2.19)$$

where N is the doping density.

The lifetimes were estimated from the expressions

$$\tau_{no} = \frac{L_n^2}{\frac{kT}{q} \mu_n} \approx 5.3 \text{ nsec} \quad (2.20)$$

and
$$\tau_{po} = \frac{L_p^2}{\frac{kT}{q} \mu_p} \approx 8.5 \text{ nsec.} \quad (2.21)$$

2.2.2.4 Interface Recombination

Interface states due to a lattice mismatch at the heterojunction introduce trapping centers in that region. These trapping centers have been incorporated into the Shockley-Read-Hall model by modifying the minority carrier lifetimes as:

$$\frac{1}{\tau_{no}} = \frac{1}{\tau_{no}} \Big|_{\text{Bulk}} + N_g C_R, \quad (2.22)$$

and
$$\frac{1}{\tau_{po}} = \frac{1}{\tau_{po}} \Big|_{\text{Bulk}} + N_g C_R, \quad (2.23)$$

where C_R is the capture coefficient and N_g is the density of trapping centers. The evaluation of N_g and C_R was done as follows.

The lattice mismatch at a heterojunction can be related to the density of dangling bonds by [2.14]

$$N_h = \frac{K(a_2^2 - a_1^2)}{a_1^2 a_2^2} \quad (2.24)$$

where a_1 and a_2 are the lattice constants of the two materials and $K=4$ for a [100] interface, $K=2\sqrt{2}$ for a [110] interface, and $K=4/\sqrt{3}$ for a

[111] interface. If the composition is gradually varying, the density of trapping centers has been assumed to be

$$N_g = N_h \frac{dc}{dx} \quad (2.25)$$

The capture coefficient C_r can be calculated as [2.10]

$$\frac{1}{C_R} = \frac{0.5 N_h}{S} \quad (2.26)$$

where S is the interface recombination velocity at an abrupt $\text{Al}_{0.5}\text{Ga}_{0.5}\text{As}$ -GaAs heterojunction. We used $S = 8 \times 10^3$ cm/s as obtained by Ettenberg and Kressel [2.15] for this work. Lattice constants a_1 and a_2 for GaAs and AlAs were taken as 5.563×10^{-8} cm and 5.654×10^{-8} cm respectively [2.8].

2.2.3 Computer-Modeling Analysis

Conventional analytical methods used for semiconductor devices are not directly applicable to cascade solar cells because a more precise solar cell relationship for each of the junctions in the cascade structure is required in representation of the total structure. The conventional solar cell analysis solves for minority-carrier concentration over a small wave-length interval $\Delta\lambda$ of the solar spectrum under short-circuit conditions [2.16]-[2.22]. A numerical integration of the short-circuit current distribution over λ is performed to obtain the total short-circuit current. The V-I curve equation is constructed, assuming that superposition is valid, by subtracting the p-n junction forward bias (dark) current from the short-circuit current. This method usually does

not give an accurate representation for even a single-junction solar cell. For example, the method used here and discussed below shows interaction terms which appear in both the short-circuit and dark-current terms [2.23,2.24]. It is only when the interaction terms are included that calculated device characteristics show reasonable agreement with experimental data.

The analytical method used in these studies considers the excitation of the total solar spectrum in the linear continuity equation, given by [2.23], [2.25]-[2.27]

$$\int_0^{\lambda_c} \alpha(1-R)N_o \exp \left(- \int_0^x \alpha dx' \right) d\lambda + D_n \frac{d^2 n_p(X)}{dx^2} + \mu_n E_o \frac{dn_p(X)}{dx} - \frac{n_p(X) - n_{po}}{\tau_n} = 0. \quad (2.27)$$

(See Table 2.1 for definition of symbols.)

A similar equation exists for holes. The solution for the minority-carrier concentration of (2.27) is obtained in closed form by making the assumption that the mobility is independent of position or is an average value in those cases where the bandgap and/or impurity concentration is variable. For example, the error in the electron diffusion length in using the average mobility is ± 4 percent in an $Al_u Ga_{1-u} As$ layer of 10^{17} cm^{-3} donor concentration where the composition is $u = 0$ at one boundary and $u = 0.14$ ($E_g = 1.62 \text{ eV}$) at the other boundary of the layer [2.23]. The effect of this approximation on the device performance

TABLE 2.1. DEFINITION OF SYMBOLS

J_{scn}, J_{scp}	Electron and hole short-circuit current density, respectively, $\text{mA} \cdot \text{cm}^{-2}$.
J_{scT}, J_{scB}	Short-circuit current density of top and bottom cells, respectively, $\text{mA} \cdot \text{cm}^{-2}$.
J_{nOB}, J_{pOB}	Electron and hole saturation current components, respectively, of bottom cell, $\text{mA} \cdot \text{cm}^{-2}$.
J_{nOT}, J_{pOT}	Electron and hole saturation current components, respectively, of top cell, $\text{mA} \cdot \text{cm}^{-2}$.
k	Boltzmann factor, $\text{eV} \cdot \text{T}^{-1}$.
λ	Wavelength, μm .
λ_c	Cutoff wavelength, μm .
α	Absorption coefficient, cm^{-1} .
η	Conversion efficiency, percent.
$\eta(300)$	Conversion efficiency at 300 K, percent.
μ_n, μ_p	Electron and hole mobility, respectively, $\text{cm}^2 \cdot \text{V}^{-1} \cdot \text{s}^{-1}$.
τ_n, τ_p	Electron and hole lifetime, respectively, s.
D_{ni}, D_{pi}	Electron and hole diffusion coefficient, respectively, in region i, $\text{cm}^2 \cdot \text{s}^{-1}$.
$\Delta E_{ci}, \Delta E_{vi}$	Conduction and valence band-edge discontinuity, respectively, at x_i interface, eV.
$E_G(x_i)$	Bandgap at x_i interface, eV.
E_{ci}, E_{vi}	Conduction and valence band-edge, respectively, at x_i interface, eV.
E_{FO}	Equilibrium Fermi level, eV.
E_O	Electric field intensity in window layer, $\text{V} \cdot \text{cm}^{-1}$.
F	V-I solar cell curve fill factor.
J_n, J_p	Electron and hole current density, respectively, $\text{mA} \cdot \text{cm}^{-2}$.
L_{ni}, L_{pi}	Electron and hole diffusion length, respectively, in region i, cm.

TABLE 2.1. DEFINITION OF SYMBOLS (continued)

n_{poi}, n_{pi}	Equilibrium and nonequilibrium ₃ electron concentration, respectively, in region i, cm^{-3} .
N_o	Solar photon flux, $\text{cm}^{-2} \cdot \text{s}^{-1}$.
N_{Ai}, N_{Di}	Acceptor and donor concentration, respectively, in region i, cm^{-3} .
P_{noi}, P_{ni}	Equilibrium and nonequilibrium ₃ hole concentration, respectively, in region i, cm^{-3} .
q	Electronic charge.
Q_{nT}, Q_{pT}	Normalized electron and hole spectral response (i.e., ratio of carriers collected to photons absorbed), respectively, of top cell.
Q_{nB}, Q_{pB}	Normalized electron and hole spectral response, respectively, in region i.
Q_{ni}, Q_{pi}	Normalized electron and hole spectral response, respectively, in region i.
R	Reflectivity at the surface.
R_{ni}, R_{pi}	Electron and hole interaction parameter, respectively, in region i, describing carrier confinement.
s	Surface recombination velocity, $\text{cm} \cdot \text{s}^{-1}$.
T	Temperature, K.
u, v	Alloy composition.
V	Photovoltage, V.
V_{mp}	Photovoltage at maximum power points, V.
$V_{mp}(300)$	Photovoltage at maximum power points at 300 K, V.
V_{oc}	Open-circuit photovoltage, V.
x	Distance into cascade structure, cm.

characteristics is small. For example, the effect on efficiency of changing the thickness of a layer ± 10 percent, which is the equivalent of changing the diffusion length ± 10 percent, in an optimized cell is ± 0.03 percent [2.23]. Equation (2.27) also assumes that either the built-in field is independent of position or it has an average value. In quasi-neutral regions this does not introduce large errors. For electric fields to affect minority-carrier distribution, the field intensity required is usually in excess of 500 V/cm. At field strengths in excess of 1500-2000 V/cm, the influence of the field on efficiency approaches an asymptotic value. Moreover, in the study of single- and two-junction cascade solar cells, the improvement in conversion efficiency due to a built-in field in the window layer is minimal compared to improvement due to the minority-carrier bandedge discontinuity, ΔE_{c1} [2.25].

The other assumptions used in the analysis are that the thermal diffusion contribution to junction current is large compared to space-charge recombination and excess tunnel current components [2.28]; the minority-carrier recombination rate is linearly proportional to excess carrier concentration as given in the last term of (2.27); reflectivity and recombination at heterojunction interfaces are negligible; efficiency is not corrected for grid contact shadowing or for power loss from joule heating arising in the structure's series resistance; and reflectivity at the window surface is 5 percent. In all calculations of carrier concentration, Fermi-Dirac statistics are used.

Alternatively, the solution may be obtained by numerical integration if the mobility, lifetime, or field in (2.27) are position dependent. However, the computer time required for an efficiency calculation

of a complete cascade, seven-layer structure is very much higher using numerical integration rather than the closed-form solution.

The computer calculations for the closed-form analysis are implemented using Fortran IV and an IBM 370/165 computer. Double precision is employed in approximately 60 percent of the calculations required in the program. When the computer modeling program is applied to a seven-layer cascade solar cell, the CPU operating time is typically less than 4 s per run. The number of runs required in a typical study to obtain a practical optimized design of a multilayer device is in the range of 1000 to 2000 runs.

A general solution to (2.26) for electrons is given by [2.23], [2.25]–[2.27].

$$n_p(x) = C_1 \exp(\omega_1 x) + C_2 \exp(\omega_2 x) + \frac{1}{\omega_2 - \omega_1} [G_1(x) \exp(\omega_1 x) + G_2(x) \exp(\omega_2 x)]. \quad (2.28)$$

The functions $G_1(x)$ and $G_2(x)$ are defined by

$$G_1(x) = \frac{1}{D_n} \int_0^x \exp(-\omega_1 x') \int_0^{\lambda_c(x')} \alpha(1-R) N_0 \exp\left(-\int_0^{x'} \alpha dx''\right) d\lambda dx' \quad (2.29)$$

and

$$G_2(x) = -\frac{1}{D_n} \int_0^x \exp(-\omega_2 x') \cdot \int_0^{\lambda_c(x')} \alpha(1-R)N_0 \exp\left(-\int_0^{x'} \alpha dx''\right) d\lambda dx'. \quad (2.30)$$

The constants ω_1 and ω_2 are given by

$$\omega_1 = \frac{\mu_n E_0}{2D_n} + \sqrt{\frac{\mu_n E_0^2}{2D_n^2} + L_n^{-2}} \quad \text{and} \quad (2.31)$$

$$\omega_2 = \frac{\mu_n E_0}{2D_n} - \sqrt{\frac{\mu_n E_0^2}{2D_n^2} + L_n^{-2}}. \quad (2.32)$$

A similar set of equations exists for holes. In the absence of an electric field, the third term in (2.26) vanishes and the general solution under this condition is given by

$$n_p(x) = C_1 \cosh \frac{x}{L_n} + C_2 \sinh \frac{x}{L_n} - \int_0^{\lambda_c} C_3 \exp(-\alpha x) d\lambda \quad (2.33)$$

where

$$C_3 = \frac{\alpha L_n^2 (1-R)N_0}{D_n (\alpha^2 L_n^2 - 1)}. \quad (2.34)$$

A similar set of equations exists for holes.

The nonequilibrium minority-carrier concentration is obtained as a function of position in each of the layers of the structure subject to two boundary conditions. The electron contribution to junction current density arising in p-type material is obtained from the current transport relationship given by [2.16]

$$J_n = q\mu_n n_p E + qD_n \frac{dn_p}{dx} \quad (2.35)$$

Without further assumptions, this results in the solar cell V-I curve given by [2.25]

$$J_n = J_{scn} \left(\frac{x}{L_n}, \alpha x, \frac{\Delta E_c}{kT}, R_n \right) - q \frac{D_n}{L_n} n_p R_n (\exp(qV/kT-1)) \quad (2.36)$$

where R_n is the interaction parameter which describes carrier confinement. The influence of R_n on dark current is manifest through $\Delta E_c/kT$, the normalized thermal barrier in the conduction band, and x/L_n . However, J_{scn} is also an explicit function of $\Delta E_c/kT$ and x/L_n , in addition to its dependence on these factors through R_n . A similar equation exists for holes in n-type material where the interaction term is R_p and the thermal barrier is denoted by ΔE_v . The V-I curve equation for a solar cell obtained from our analysis is given by [2.25]

$$J = J_{scn} + J_{scp} - q \left[\frac{D_n}{L_n} n_p R_n + \frac{D_p}{L_p} p_n R_p \right] (\exp(qV/kT-1)). \quad (2.37)$$

Equation (2.37) contains the parameters that describe internal competing processes and from which other device performance characteristics are

recovered. Equation 2.37 may vary by nearly four decades. It may be shown that the dark current decreases linearly with R_n , but at the same time short-circuit current also decreases. Therefore, the optimum design is not obtained for low or high values of R_n but for a region between these extremes where the efficiency is maximized.

Due to the excellent agreement obtained with experimental results using the closed-form solution (even with the approximations required to linearize the equations), resorting to numerical integration of the set of transport equations is not necessary. Using this solution, a corresponding computer program was written that is modular in concept. The program has been applied to devices containing up to three distinct layers between one junction and an adjacent junction [2.23]-[2.27].

The program has also been applied to the AlGaAs/GaAs single-junction solar cell [2.25]. The agreement with the experimental value of conversion efficiency at 300 K is better than 5 percent [2.29]-[2.32].

Table 2.2 summarizes the optimized design parameters for AlGaAs-GaAs resulting in the maximum BOL* efficiency. Constraints imposed by radiation resistance are not explicitly included in the model leading to the parameters in Table 2.2. The bottom cell bandgap is assigned the value 1.44 eV, corresponding to GaAs. The optimum bandgap of the top cell is found to be 1.94 eV from the optimization procedure, which maximizes efficiency at 300 K and AMO. Setting the tunnel junction bandgap equal to the top cell bandgap results in a design that minimizes the technological difficulties. Window layer parameters used in the analysis are a thickness of 0.1 μm and an acceptor

* Beginning of Life

TABLE 2.2 Summary of Optimum (BOL-Beginning of Life) Design Parameters and Operating Conditions

Optimum (BOL) Design Parameters

top cell bandgap energy	1.94 eV
top cell n-type donor concentration	5×10^{16} to $8 \times 10^{17} \text{ cm}^{-3}$
top cell p-type layer thickness	0.4 μm
top cell n-type layer thickness	1.0 μm
bottom cell n-type donor concentration	5×10^{16} to $7 \times 10^{17} \text{ cm}^{-3}$
bottom cell p-type donor thickness	1.3 μm
bottom cell n-type layer thickness	2.0 μm

Operating Conditions: 300 K, AMO, 1 sun

concentration of $2 \times 10^{18} \text{ cm}^{-3}$. An acceptor concentration of $1 \times 10^{18} \text{ cm}^{-3}$ was chosen for the p-type regions of top and bottom cells. Optimized donor concentrations and layer thicknesses are obtained from the analysis for the active regions. Figure 2.2 depicts the final optimized AlGaAs-GaAs (BOL) cell design resulting from the analysis.

This design yields a calculated AMO, 1 sun efficiency of 27.6% $J_{sc} = 16.1 \text{ mA/cm}^2$, $V_{oc} = 2.6 \text{ V}$, and $FF = 0.89$.

2.3 Experimental Planar Cascade Development

2.3.1 Evolution of the Cascade Structure

Several different structural variations of the optimized AlGaAs-GaAs cell design depicted in Figure 2.2 have been fabricated at RTI. Early experimental cells, such as the original version shown in Figure 2.3a, contained epitaxially grown, abrupt p-n photovoltaic junctions using the nondiffusing impurities Sn for n-type material and Ge for p-type layers. Some devices employed unintentionally doped n-layers ($2 \times 10^{16} \text{ cm}^{-3}$) for the photovoltaic junction. These devices demonstrated good values of V_{oc} (up to 2.2 V), but only modest values of J_{sc} (approximately 5 mA cm^{-2}). Individual $\text{Al}_{0.35}\text{Ga}_{0.65}\text{As}$ top cells were subsequently grown using Be diffusion to form the photovoltaic junction during growth of the $\text{Al}_{0.9}\text{Ga}_{0.1}\text{As}$ window layer; these junctions were characterized by $V_{oc} = 1.25 \text{ V}$ and $J_{sc} = 7 \text{ mA cm}^{-2}$ without AR coating (based on active area). However, when incorporated into the cascade structure, these Be-diffused top cells showed considerable deterioration of open-circuit voltage; this was probably due to the propagation of lattice defects from the degenerately doped tunnel junction, particularly from the Te-doped n^+ -layer.

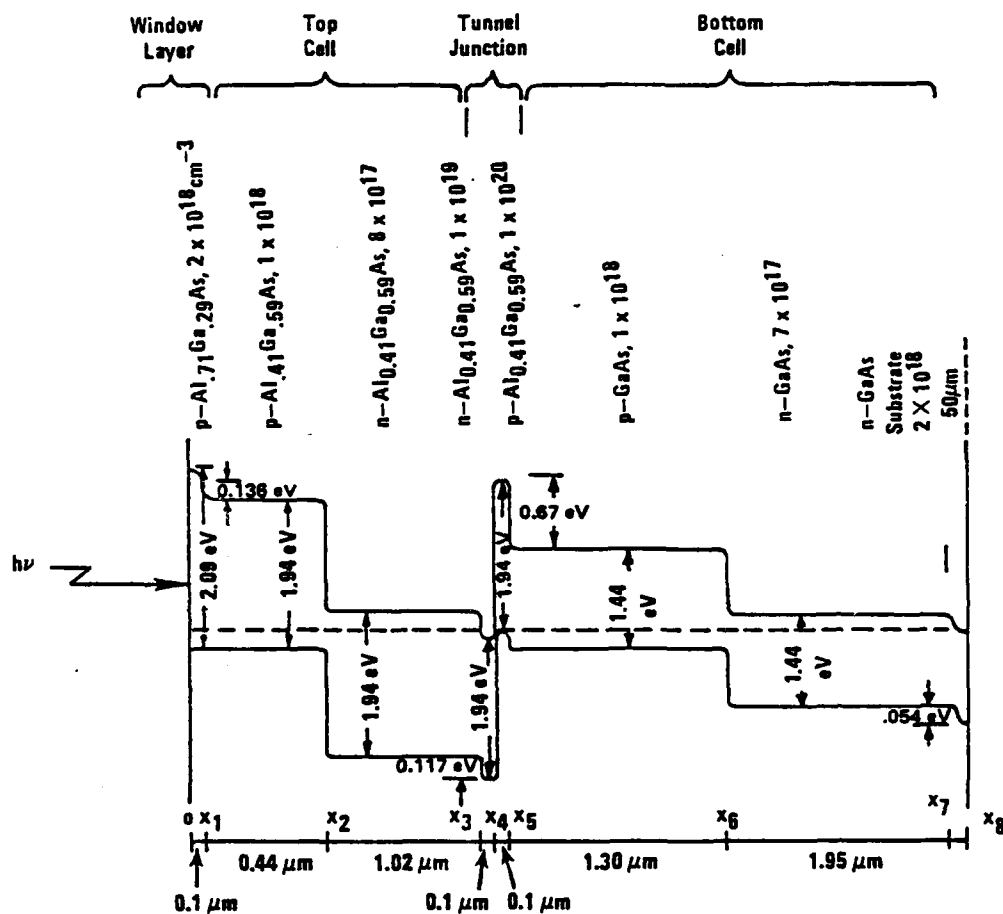


Figure 2.2. Band structure Used in the Study and Parameters Obtained for Optimized Design by Maximizing Conversion Efficiency.

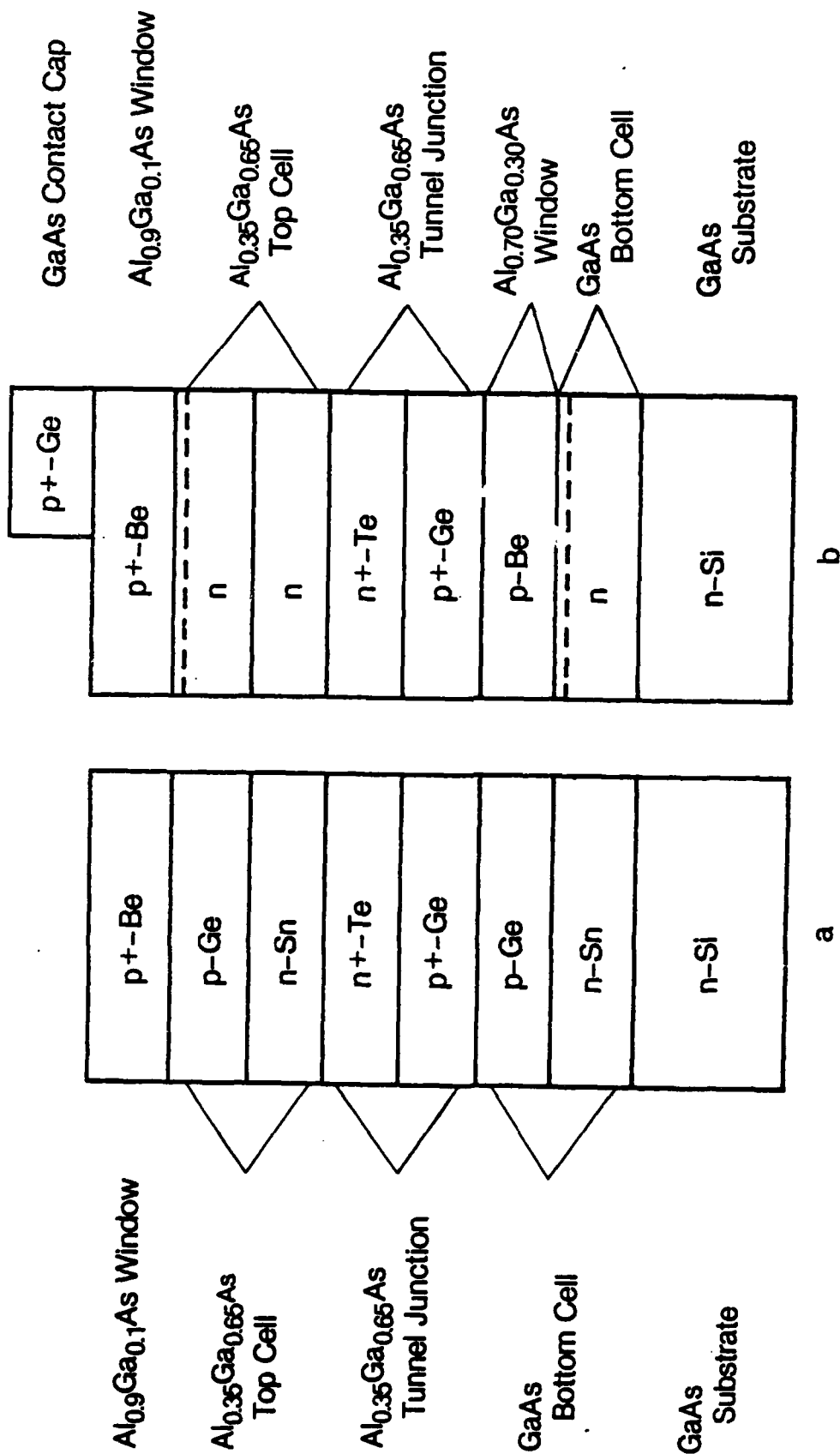


Figure 2.3. AlGaAs Cascade Solar Cell Configuration. (a) Original Structure Using Ge- and Sn-Doped Grown p-n Junction, and (b) Current Structure Using p-n Junction Formed by Be Diffused Into Unintentionally Doped n-Layers.

The modified cascade structure shown in Figure 2.3b was then developed and resulted in small area cells having J_{sc} values up to 13.0 mA cm^{-2} and V_{oc} levels of 2.13 V. When combined with a fill factor of 0.74, the best sample yielded a maximum AMO, 1 sun efficiency of 15.1 percent (active area without AR coating). In comparison with the original structure shown in Figure 2.3a, the modified configuration has several significant features. These included the following:

1. Both photovoltaic junctions are Be-diffused, formed during growth of the $\text{Al}_{0.9}\text{Ga}_{0.1}\text{As}$ layer for the top cell and the $\text{Al}_{0.7}\text{Ga}_{0.3}\text{As}$ layer for the bottom cell. Beryllium was used as the p^+ -dopant for the window layers of both junctions because of its favorable diffusion characteristics and because of its low vapor pressure, which is necessary to prevent cross contamination of melts in the multiwell LPE growth technique. Doping characteristics and electrical properties of Be-doped AlGaAs have been described in some detail [2.33].
2. The GaAs diffused junction is achieved by Be-diffusion from an $\text{Al}_{0.7}\text{Ga}_{0.3}\text{As}$ window layer (see Section 2.2.3.2 for details). Using the window layer as the Be source reduces the hole concentration in the diffused GaAs junction because the diffusion source material, $\text{Al}_{0.7}\text{Ga}_{0.3}\text{As}$, can be grown with a lower Be concentration than GaAs. It is very difficult to obtain a hole concentration less than $\text{mid } 10^{18} \text{ cm}^{-3}$ for Be-doped $\text{Al}_x\text{Ga}_{1-x}\text{As}$ with $x \leq 0.37$ due to the high distribution coefficient of Be (Figure 2.4).

However, for $x > 0.5$, the lower Be distribution coefficient allows hole concentration in the high 10^{17} cm^{-3} to low 10^{18} cm^{-3} to be routinely achieved. SIMS analysis of these layers shows that the reduced hole concentrations correlate with reduced total Be incorporation. This allows the carrier concentration on the p-side of the GaAs junction to be limited to the high 10^{17} cm^{-3} range, thereby maintaining a better electron diffusion length.

3. The active $\text{n-Al}_{0.35}\text{Ga}_{0.65}\text{As}$ layer of the top cell is epitaxially grown on an additional layer of the same composition. This additional layer reduces the propagation of defects originating in the $\text{n}^+(\text{Te})\text{-p}^+(\text{Ge})$ tunnel junction.
4. The technique for preparing the LPE melts for growing the tunnel junction has been changed to reduce defects generated in the Te-doped layer. Properties of the tunnel junctions have been reported previously [2.34].
5. Currently, a $\text{p}^+\text{-GaAs(Ge)}$ cap layer is grown on top of the $\text{Al}_{0.9}\text{Ga}_{0.1}\text{As}$ layer to serve as a p^+ -contact. The excess $\text{p}^+\text{-GaAs}$ is etch-removed using the finger contact metallization as the etch mask.

The growth of this structure will be described in detail in Section 2.3.2 following.

2.3.2 Material Growth by Liquid Phase Epitaxy

The epitaxial reactors used for this project follow conventional design practice, that is, they are of horizontal design with a multibin graphite sliding boat. The heat zone is fitted with either a 24- or 36-

inch sodium filled heat pipe, and the entire heat zone can be "rolled" on and off the reactor tube allowing for rapid heat up and cool down during the growth cycle. The reactor tube and associated gas handling equipment has leak-tight integrity under high vacuum consistent with high purity gas handling and oxygen free growth conditions. The reactors are enclosed in fume hoods compatible with the handling of toxic gases, although no glove box or sample interchange system is used.

2.3.2.1 Overview of Materials Issues

The AlGaAs-GaAs planar cascade structure shown in Figure 2.3b requires growth of eight separate layers. These layers vary widely both in alloy composition and in doping. In particular, the doping requirements are very diverse. The photojunctions are diffused and lightly doped, while the tunnel junction needs to be abrupt and very heavily doped. Along with these constraints, there is the additional requirement for dopants with low vapor pressures to avoid intermelt contamination.

The principle concerns in the growth of this structure have been the following:

- (1) Controlling the depth of the diffused junction in the top and bottom cells.
- (2) Growth of a transparent, low-resistance tunnel junction interconnect.
- (3) Attaining a tunnel junction whose characteristics are thermally stable during growth of the top cell and the top cell window layer.
- (4) Growth of a top cell of high crystalline quality on the degenerately doped tunnel junction epilayers.

These concerns will be discussed at length in the sections following.

2.3.2.2 Bottom Cell and Bottom Cell Window Layer

The LPE boat design used by RTI allows the growth of several device wafers sequentially during a single growth run. For this reason some melts are duplicated to allow for differences in desired layer thicknesses. The growth of the bottom cell reflects this practice. The bottom cell/bottom cell window layer are grown from three melts.

1. Melt (1) may either be unintentionally doped ($n \approx 3 \times 10^{16} \text{ cm}^{-3}$) or Sn-doped ($n \approx 5 \times 10^{17} \text{ cm}^{-3}$). It is found that Sn-doped bottom cells have improved V_{oc} relative to undoped n-layer bottom cells. SEM of cleaved cross sections shows that this is at least partly due to better control of the Be-diffusion front. Not proven, but suspected is that Sn also plays a role in reducing the interaction of Be with dislocations in the formation of shunting paths through the junction.
2. Melt (2) is identical to melt (1) and is present for reasons related to the growth of multiple wafers as described above. Aside from the dopant these melts are made up of ≈ 9 grams of Ga (for 2×2 cm substrates) and an amount of undoped polycrystalline GaAs in excess of the amount needed to saturate the melt. The actual growth is thus a two-phase ramped growth. An initial homogenization and saturation is established by holding at constant temperature for about one hour before initiating the growth ramp. In addition, precursors or "dummy" substrates are used to maintain the bottom of the melts at saturation

during the run. Although the ramp rates used in this work were varied between 0.2°/min and 1.5°/min, most often a ramp of 1°/min was used. The factors governing the selection of the ramp rate will be discussed in the section on the tunnel junction.

3. Melt (3) is used to grow the $p^+-Al_{0.7}Ga_{0.3}As$ window layer. This layer serves as the diffusion source for the formation of the bottom cell junction. Aside from the dopant the melt is made up of (for growth at 800°C) ≈ 9 grams of Ga, 5 mg Al/g Ga and undoped polycrystalline GaAs in excess of the amount needed to saturate the melt.

There are two concerns in the growth of this layer:

- a. The AlAs mole fraction in the layer is sensitive to the thermal history of the melt when excess GaAs is used. For example, if the melt is saturated at a temperature substantially higher than the growth temperature, then AlGaAs will nucleate on the excess GaAs present during cool down to the growth temperature. Aluminum has a large distribution coefficient and will thus be depleted from the melt. Therefore, the time/temperature program must be reproducible from run to run for predictable growths, and the saturation temperature should not be chosen substantially higher than the growth temperature. In spite of these precautions, there is found to be some scatter

in epilayer thickness and Al content due to the somewhat uncertain nucleation area presented by the excess solute in the melt.

- b. The choice of dopant for the bottom cell window layer is critical. Zn and Cd are unacceptable due both to their excessive diffusivities and due to their high vapor pressure which causes intermelt (and overall system) contamination [2.35,2.36]. In addition the diffusion coefficient of Zn in $\text{Al}_x\text{Ga}_{1-x}\text{As}$ increases with x so that the Zn diffuses rapidly upward into the tunnel junction ($\text{Al}_{.35}\text{Ga}_{.75}\text{As}$) [2.37]. Ge is extensively used as a p-type dopant for GaAs and AlGaAs. However, it has been shown to be difficult to obtain high carrier concentrations using Ge in $\text{Al}_x\text{Ga}_{1-x}\text{As}$ with $x > 0.3$ because of strong compensation effects due to Germanium's amphoteric behavior and/or strong dependence of the acceptor ionization energy on Al composition [2.38,2.39]. In addition, Ge p-n junctions show little displacement from the metallurgical interface, and as mentioned earlier (Section 2.3.1) devices with abrupt p-n junctions have poor values of J_{sc} . Mn is another p-type dopant that has been studied [2.40,2.41] however for this application, Mn forms a relatively deep level ($E_A \approx 4kT$ in GaAs) and E_A increases as x increases in $\text{Al}_x\text{Ga}_{1-x}\text{As}$. Mn also forms relatively abrupt

junctions. Mg has been studied as an acceptor in $\text{Al}_x\text{Ga}_{1-x}\text{As}$ [2.42], but it appears that at low concentrations its diffusion coefficient is the same as that of Zn [2.43]. Mg also oxidizes very readily and MgO is a stable insoluble in the melt which interferes with nucleation.

Another candidate acceptor impurity for LPE in the AlGaAs/GaAs system is Be. Be has a low vapor pressure and is known to be a shallow acceptor with $E_A \approx 20$ meV in GaAs [2.44]. In addition Be has been characterized by a diffusion coefficient of less than $10^{-15} \text{ cm}^2/\text{sec}^{-1}$ at 800°C in GaAs [2.45]. Since the behavior of Be as an acceptor in AlGaAs grown by LPE had not been studied previously, we carried out an extensive series of experiments to determine its characteristics [2.33]. The results of that study are summarized as follows.

In a preliminary stage of this work, the distribution coefficient of Be at 800°C in $\text{Al}_x\text{Ga}_{1-x}\text{As}$ with $x < 0.4$ was found to be around 10. Thus this high distribution coefficient produced only heavily doped $\text{Al}_x\text{Ga}_{1-x}\text{As}$ epilayers. In order to obtain epilayers with moderate carrier concentrations suitable for studying the electrical properties, the amount of metallic Be added to the melt should be of the order of 1 μg or less. Therefore an Al:5% Be alloy or a Ga:5% Be alloy was used as the dopant source rather than metallic Be. The Ga:Be alloy has been prepared using a specially designed graphite boat in the LPE system. About 10 g of prebaked Ga and 50 μg of Be were baked at 800°C in a purified hydrogen stream for alloying and then distributed into 15 separate melts, followed by cooling and freezing. These frozen Ga:Be pellets (≈ 0.6 g) were used as the dopant source in an Al-Ga-As melt

with a total weight of about 3 g. Another approach to Be doping was to first grow a Be-doped GaAs epilayer with a hole concentration of about $5 \times 10^{19} \text{ cm}^{-3}$ and with a thickness of about 20 μm . This GaAs layer was then used to saturate the Al:Ga melt and thus a controllable amount of Be was introduced into the melt. It should be mentioned that in all the above approaches extreme care was taken to avoid the formation of BeO. This has been carried out by using a vacuum-tight LPE growth system.

Be diffusion during growth from $\text{Al}_x\text{Ga}_{1-x}\text{As}$ into semi-insulating GaAs substrates is very likely to result in some substrate conduction which affects the measurement accuracy of resistivity and the Hall effect of the epilayers. In order to prevent this undesirable effect, an undoped buffer $\text{Al}_x\text{Ga}_{1-x}\text{As}$ epilayer was first grown on the substrate, followed by growth of the Be-doped epilayer with the same Al composition as the undoped bottom layer. The total thickness of the alloy epilayers was 4-20 μm depending on the Al composition as well as cooling interval, while the thickness of the top layers doped with Be was about half of the total thickness. The epilayer composition was determined using electron microprobe analysis as well as data given by Ref. 2.46 from the chemical composition of the melt. In order to characterize the electrical behavior of Be as a p-type dopant in $\text{Al}_x\text{Ga}_{1-x}\text{As}$, a total of about 100 epilayers with various Al composition and Be concentration have been grown and their electrical measurements have been carried out.

The samples used for electrical measurements were cut with a diamond cutter into square-shaped wafers with dimensions of 5 \times 5 mm. They were lightly etched with 1% Br_2 in methanol before applying Ohmic contacts.

For the samples with Al composition, $x < 0.4$, the contacts were formed by Ag:Mn alloy evaporation, followed by 450°C annealing for 2 min in nitrogen atmosphere, while for Ohmic contacts for higher x than 0.4, Mg ($\approx 50\text{\AA}$), Ti ($\approx 300\text{\AA}$) Pd ($\approx 300\text{\AA}$), and Ag (3000\AA) were successively evaporated, followed by alloying at 550°C for 80 sec in flowing nitrogen. These procedures provided good Ohmic contacts for $\text{Al}_x\text{Ga}_{1-x}\text{As}$ even at low temperature. The Hall voltage and resistivity were measured using the van der Pauw geometry in the temperature range from 77 to 320 K. The magnetic field and the current applied to the samples were typically 9.4 kG and 1 mA, respectively. However, for the samples with high resistivities and mobilities, the measurements were carried out under a magnetic field of 4 kG and a current of 0.1 mA.

The hole concentration, p , in the valence band was calculated from the relation $p = r_H (eR_H)^{-1}$, where e is electronic charge, R_H the Hall coefficient, and r_H the Hall factor which is defined as the ratio of the Hall mobility to the drift mobility. The value of r_H depends on the scattering mechanism involved, temperature and the Al composition in the alloy system. However, for the sake of simplicity the value of 1.3 for r_H has been employed in the present work regardless of temperature and Al composition, according to a recent paper on the electrical properties of Ge-doped p-type $\text{Al}_x\text{Ga}_{1-x}\text{As}$, reported by Zukotynski *et al* [2.47]. As observed in Ref. [2.47], our samples, particularly those with high x values, often showed a voltage offset for diagonal pairs of electrodes in the absence of a magnetic field. The Hall measurements were rejected on the samples for which the offset became one order of magnitude larger than the Hall voltage.

In order to determine the acceptor activation energy ΔE_A and the acceptor concentration N_A in Be-doped $\text{Al}_x\text{Ga}_{1-x}\text{As}$, analyses have been performed using a one-center model from data on the temperature dependence of carrier concentration.

Assuming that donor concentration is negligibly low and the ionized acceptor concentration N_A^- is equal to the hole concentration in the valence band p , we can then obtain the following equation:

$$p = N_A^- = N_A / [1 + g_A \exp[-(E_F - E_A)/k_B T]] \quad , \quad (2.38)$$

where g_A is the degeneracy factor for the acceptor impurity. Other symbols carry their usual meaning. On the other hand, p is also given by

$$p = N_V \exp[-(E_F - E_V)/k_B T] \quad , \quad (2.39)$$

where $N_V = 2(2\pi m_V^* k_B T/h^2)^{3/2}$ and m_V^* is the density-of-states effective mass for holes. From the combination of Eq. (2.38) with (2.39) we can obtain the following equation:

$$p = N_A / [1 + [g_A(p/N_V)] \exp(\Delta E_A/k_B T)] \quad . \quad (2.40)$$

Using this equation, parameters of $\Delta E_A (= E_A - E_V)$ and N_A were determined by a least-square curve fitting method. In this equation, $g_A = 4$ was used owing to the fourfold degeneracy of the valence-band edge in $\text{Al}_x\text{Ga}_{1-x}\text{As}$, and also $m_V^* = (0.62 + 0.17x)$ was employed as the compositional

dependence of the effective mass for holes in the alloy system. This value for m_v^* was derived by taking the contribution of heavy and light holes in GaAs and AlAs into account and also by linearly interpolating between those density-of-state masses, reported by Lawaetz [2.40].

For reference purposes, the estimation of error in determining ΔE_A and N_A has been made using another expression for m_v^* , i.e., $m_v^* = (0.48 + 0.31x)$. As a result, for example, for the samples with an x of 0.8, the values of ΔE_A decrease by less than 1%, whereas those of N_A increase at most by 4%, compared with those values calculated using $m_v^* = (0.62 + 0.17x)$. Therefore the use of the two expressions on m_v^* described above did not make a significant difference in determining the parameters. However, it should be noted that if the value of r_H is taken as unity instead of 1.3 employed in this work, ΔE_A increases by 10% while N_A decreases by as much as 30%. Therefore in order to determine these parameters with more accuracy, the dependency of r_H described in the previous section should be considered.

The dependence of room-temperature hole concentration and resistivity on Al composition x in the epilayers grown at Be doping level X_{Be}^L between 1 and 8×10^{-3} at.% is shown in Figure 2.4. The hole concentration is seen to decrease with increasing x value though there is strong scatter among the data points. This dependence is considered to be related to the formation of deeper levels with higher Al composition. The increase in acceptor activation energy with increasing x value has been observed on $Al_xGa_{1-x}As$ doped with other p-type dopants such as Ge [2.47,2.49], Zn [2.50,2.51], and Mg [2.52]. In our experiments, however, the samples with $x < 0.4$ usually showed degenerate properties, and it was quite difficult to obtain nondegenerate p-type epilayers with $x < 0.4$.

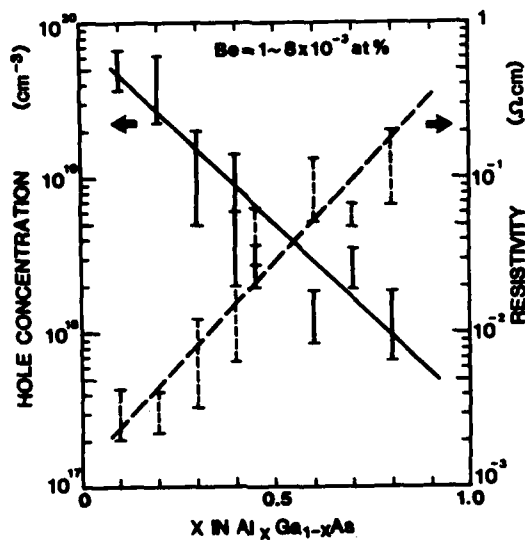


Figure 2.4. The Dependence of Hole Concentration and Resistivity at Room Temperature on Al Composition in Be-doped $\text{Al}_x\text{Ga}_{1-x}\text{As}$. X_{Be}^{L} is approximately between 1 and 8×10^{-3} at.% in all the samples.

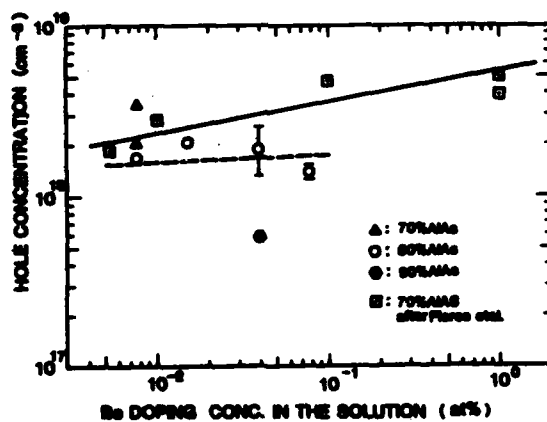


Figure 2.5. The Variation of Hole Concentration at Room Temperature with Be Concentration in the Ga Solution.

even if the doping level was lowered to about 4×10^{-4} at.%, suggesting that the distribution coefficient of Be is very high, which is in agreement with the doping behavior of Be in GaAs.

From a practical point of view, it is important to know the variation of hole concentration of the epilayers at a constant value of x with X_{Be}^{L} . Figure 2.5 shows the results obtained on the epilayers with $x = 0.8$, which were grown varying X_{Be}^{L} from 8×10^{-3} to 8×10^{-2} at.%. In this figure, the results reported by Flores *et al.* [2.53] are also indicated for comparison. It is seen from this figure that hole concentration in $\text{Al}_{0.8}\text{Ga}_{0.2}\text{As}$ are approximately between 1 and $3 \times 10^{18} \text{ cm}^{-3}$ independent of the Be concentration studied in this work, though there is considerable scatter among the data. Although Flores' results have a tendency for the hole concentration in $\text{Al}_{0.7}\text{Ga}_{0.3}\text{As}$ to slightly increase with increasing X_{Be}^{L} , it is thought that there is no significant difference between the two results. These doping characteristics of Be in AlGaAs are quite different from those of Zn in GaAs [2.54] where the hole concentrations in the solids have been reported to increase with the square root of X_{Zn}^{L} . This behavior is based on the existence of equilibrium between the liquid and semiconductor bulk on account of the high diffusion coefficient of Zn. On the other hand, in the case of a low diffusion coefficient like Te in GaAs, the carrier concentration is known to vary linearly with dopant concentration in the liquid [2.55]. To date, there are no data available for the diffusion coefficient of Be in $\text{Al}_x\text{Ga}_{1-x}\text{As}$. However, even if the value of the diffusion coefficient of Be, D_{Be} , $\text{Al}_x\text{Ga}_{1-x}\text{As}$ would be approximated by either $D_{\text{Be}} < 1 \times 10^{-15} \text{ cm}^2/\text{sec}$ at 800°C for GaAs [2.45] or $D_{\text{Be}} > 1 \times 10^{-10} \text{ cm}^2/\text{sec}$ at 800°C for GaP [2.51], the results shown in Figure 2.5 could not be explained in terms of the difference in the diffusion coefficient. This anomalous behavior is

likely to arise from the formation of electrically inactive complexes as observed in GaAs doped with Te and Se [2.57,2.58]. Another possibility responsible for this behavior is a substantial reduction of X_{Be}^{I} due to BeO produced by the reaction with background oxygen in the open tube LPE system.

Figure 2.6 shows the variation of the distribution coefficient of Be with x in $\text{Al}_x\text{Ga}_{1-x}\text{As}$. It is seen that the distribution coefficient decreases exponentially with increasing x and is larger than unity over a wide range of x . It should be pointed out that the scatter of the data in Figure 2.6 is due to the difficulty in weighing accurately and handling the minute quantities of Be used in melt preparation. Nevertheless, this figure does show the trend of high-distribution coefficients at low Al concentrations and vice versa. This high distribution coefficient results in considerable difficulty in growing low-carrier concentration epilayers particularly with low x values, even if the dilute dopant sources such as GaAs:Be, Al:Be, and Ga:Be alloys are used for the LPE growth.

Be Electrical Properties. This section mainly describes the temperature dependence of electrical properties of the $\text{Al}_x\text{Ga}_{1-x}\text{As}$ epilayers with $x > 0.4$ since it was difficult to control Be doping concentration in obtaining nondegenerate epilayers with $x < 0.4$, as mentioned in the previous section. In measuring the dependence of hole concentration as a function of temperature, a number of samples showed impurity-band conduction at low temperature, as shown in Figures 2.7 and 2.8, similar to that observed in the Ge-doped $\text{Al}_x\text{Ga}_{1-x}\text{As}$ reported in Refs. [2.47] and [2.49]. Therefore data in this temperature region were rejected in determining ΔE_{A} and N_{A} . The results thus obtained from temperature dependences of hole concentrations are listed in Table 2.3.

TABLE 2.3. Summary of Results.

Sample No.	χ^a	Be conc. $\times 10^3$ (at.%)	$P_{300K} \times 10^{-18b}$	ν_H at 300 K	$N_A \times 10^{-18}$ (cm $^{-3}$)	ΔE_A (meV)
114-2	0.45	1.5	3.6	62	7.1	8.4
115-2	0.36	0 ^c	0.49	72	0.64	14
55-C	0.6	40	2.2	39	3.8	9.0
146-B	0.7	8	3.5	36	8.5	14
146-C	0.7	8	2.0	50	3.8	13
154-C	0.8	16	0.80	91	0.98	33
161-C	0.8	80	1.5	47	8.1	74
167-D	0.8	16	0.46	72	3.0	97
169-C	0.8	8	1.6	49	6.6	51
169-D	0.8	40	1.3	68	7.5	79
183-C	0.8	8	1.8	34	6.3	43
185-C	0.45	1.5	2.0	47	3.6	9.6
185-D	0.45	0.75	0.42	51	0.72	45
189-C	0.4	0.6	1.3	51	2.0	11
189-D	0.4	1.2	1.4	48	2.3	12
190-D	0.8	40	2.6	38	9.0	34
127-B	0.45	...	0.86	50	1.3	20
128-B	0.9	40	0.58	90	3.5	91
130-C	0.7	40	1.9	32	4.5	24

^aAl mol fraction, each value contains error within $\pm 2\%$.^cGrown with residual Be for previous run.^b $p = 1.3/qR_H$.^dGaAs:Be with $p = 5 \times 10^{19} \text{ cm}^{-3}$ as a dopant.

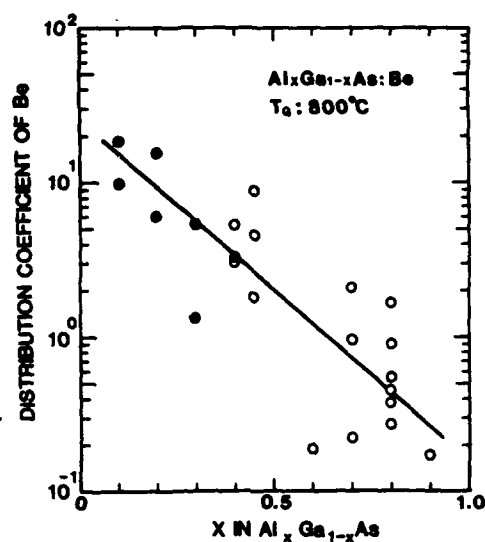


Figure 2.6. The variation of the distribution coefficient of Be, K_{Be} , at $800^\circ C$ in $Al_xGa_{1-x}As$ as a function of Al composition. $K_{Be} = C_{Be}^S / C_{Be}^L$, where C_{Be}^S and C_{Be}^L are the concentration of Be in the solid and liquid phases, respectively. The solid circles show the results when C_{Be}^S for the acceptor impurity is taken to be equal to the hole concentration at room temperature because of degeneracy of these samples, whereas the open circles are the results when $C_{Be}^S = N_A$.

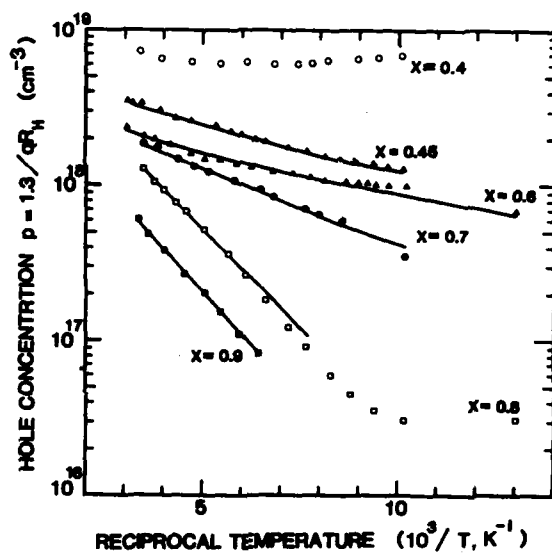
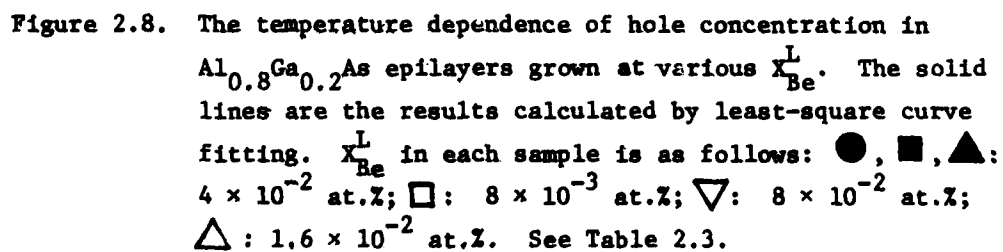


Figure 2.7. The temperature dependence of hole concentration in $\text{Al}_x\text{Ga}_{1-x}\text{As}$ epilayers with various Al compositions. The doping level X_{Be}^{L} in the epilayers is about 4×10^{-2} at.% with the exception of $x = 0.45$, where $X_{\text{Be}}^{\text{L}} = 1.5 \times 10^{-3}$ at.%. The solid lines are the results calculated by least-square curve fitting.



A typical temperature dependence of hole concentration on x is shown in Figure 2.7. These epilayers were grown with X_{Be}^L of about 4×10^{-2} at.%, with the exception of the epilayer with $x = 0.45$, where X_{Be}^L was about 1.5×10^{-3} at.%. Because of the large scatter among N_A in these epilayers with various x values, it is impossible to derive an explicit expression for the dependence of ΔE_A on Al composition. However, ΔE_A is seen to increase with increasing x value and we can roughly estimate $\Delta E_A \approx 10$ meV at low x (0.45-0.6) and $\Delta E_A \approx 50-90$ meV at high x (0.8-0.9) at this Be doping concentration. Furthermore, a significant feature is that the hole concentrations at room temperature of more than 10^{18} cm^{-3} can easily be achieved at $X_{Be}^L \approx 10^{-3}-10^{-2}$ at.% regardless of the Al composition, with the exception of an epilayer with $x = 0.9$.

It is of significance to estimate the effect of N_A on ΔE_A for a given constant x value in order to elucidate the electrical behavior of Be in $\text{Al}_x\text{Ga}_{1-x}\text{As}$. For this purpose, ΔE_A and N_A in $\text{Al}_x\text{Ga}_{1-x}\text{As}$ with a constant x value were determined from the temperature dependence of hole concentration and this is shown in Figure 2.8, where the results on $\text{Al}_{0.3}\text{Ga}_{0.2}\text{As}$ are given as an example. Although there is poor correlation between N_A and X_{Be}^L , it is possible to estimate the dependence of ΔE_A on N_A . In general, the impurity ionization energy is known to be a function of impurity concentration and the relationship between the two parameters is given by the following empirical expression [2.59,2.60]:

$$\Delta E_A = E_{AO} - \bar{a} N_A^{1/3}, \quad (2.41)$$

where E_{AO} is the ionization energy for infinite dilution and \bar{a} is a constant. The results obtained using least-square curve fitting from

the data on ΔE_A and N_A for $\text{Al}_{0.8}\text{Ga}_{0.2}\text{As}$ and $\text{Al}_{0.45}\text{Ga}_{0.55}\text{As}$ are shown in Figure 2.9. Calculated values for E_{AO} and \bar{a} are 190 meV and $7.3 \times 10^{-5} \text{ meV cm}^{-1}$ for $\text{Al}_{0.8}\text{Ga}_{0.2}\text{As}$, and 63 meV and $3.1 \times 10^{-5} \text{ meV cm}^{-1}$ for $\text{Al}_{0.45}\text{Ga}_{0.55}\text{As}$, respectively. Undoubtedly, these values may be modified by additional data points which are needed to determine them more accurately. However, the values of E_{AO} are clearly seen to increase with increasing Al composition. Such a trend is in agreement with the increase of the ionization energy roughly estimated using available data on Al compositional dependence of effective density-of-state hole mass and dielectric constant in the AlAs-GaAs ternary system.

Figure 2.10 shows the temperature variation of hole Hall mobilities with different N_A in the epilayers with a given constant Al composition of 0.8. All the samples shown in this figure are the same as those in Figure 2.8. The mobilities at room temperature are less than $10^2 \text{ cm}^2/\text{v sec}$ regardless of the N_A values, similar to those observed in $\text{Al}_x\text{Ga}_{1-x}\text{As}$ doped with other dopants [2.47], and are found to have an increasing tendency with decreasing N_A though the data are fairly scattered. As temperature is lowered, one can see all the samples exhibit a maximum mobility followed by a steep reduction. Evidently, the temperature dependence in the low-temperature region is much greater than that expected from ionized impurity scattering. This rapid reduction in the mobility may arise from the onset of the impurity-band conduction as shown in Figure 2.8. The room-temperature Hall mobility as a function of impurity concentration is most commonly used to characterize the material properties. Figure 2.11 shows the relationship of N_A or p versus hole Hall mobility at room temperature for $\text{Al}_{0.8}\text{Ga}_{0.2}\text{As}$ epilayers.

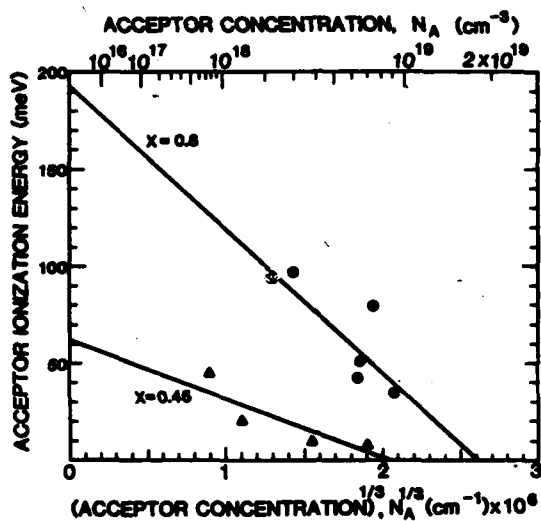


Figure 2.9. The relationship of ΔE_A vs N_A for Be-doped $\text{Al}_x\text{Ga}_{1-x}\text{As}$ with $x = 0.8$ and 0.45 . The solid lines are calculated by least-square curve fitting.

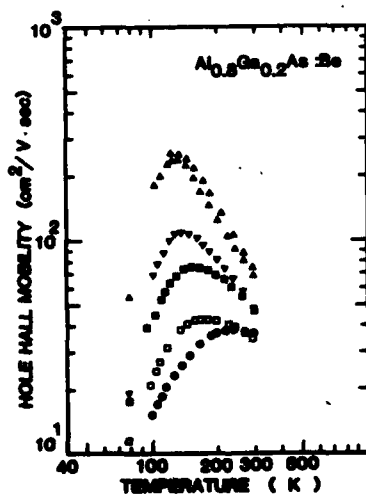


Figure 2.10. The temperature dependence of hole Hall mobility in $\text{Al}_{0.8}\text{Ga}_{0.2}\text{As}$ with various N_A values. The symbols identifying the samples are the same as those in Figure 2.8.

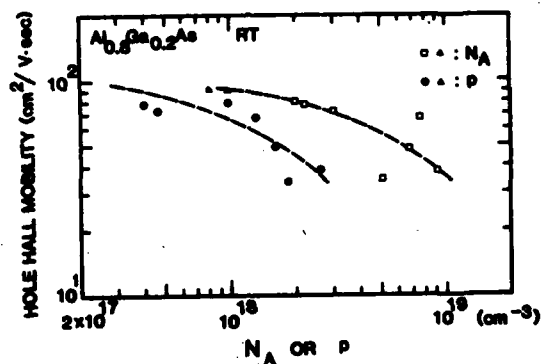


Figure 2.11. The variation of hole Hall mobility with N_A or p in $\text{Al}_{0.8}\text{Ga}_{0.2}\text{As}$ doped with Be. The open and solid triangles indicate the results for $x \approx 0.85$.

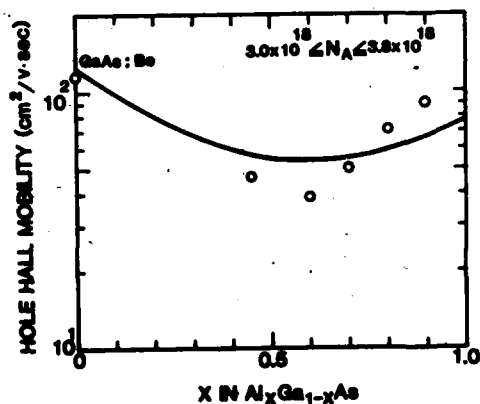


Figure 2.12. The variation of hole Hall mobility with x value in $\text{Al}_x\text{Ga}_{1-x}\text{As}$ with the acceptor concentration $3.0 \times 10^{18} < N_A < 3.8 \times 10^{18} \text{ cm}^{-3}$. The solid line shows the result from calculations using an expression for alloy scattering rate in Ref. [2.61].

Clearly, the increase of N_A or p leads to reduced values of mobility. Similar tendency is observed for the epilayers with other x values. The variation of the room-temperature hole mobility with x value has also been examined for the samples with a constant N_A . [Actual N_A among the samples, however, is not constant, but in the range $(3.0 - 3.8 \times 10^{18} \text{ cm}^{-3})$.] As a result, the mobility is observed to show a minimum at about $x = 0.6$ as shown in Figure 2.12, where data of MBE GaAs:Be with a hole concentration of $3.5 \times 10^{18} \text{ cm}^{-3}$, reported in Ref. [2.45], are also indicated for comparison. In general, the random potential alloy scattering mechanism is known to play an important role as a factor which limits the mobility in alloy semiconductors [2.61]-[2.63]. Then, the Al compositional dependence of the hole mobility was calculated on the basis of the relaxation time due to scattering in a random alloy [2.61], and the result obtained is indicated by the solid line in Figure 2.12. These calculations were made using the Monte Carlo method, and included polar optical, piezoelectric, ionized impurity, and acoustic mode scattering in addition to alloy scattering. The alloy scattering potential was based on the electron affinity difference between GaAs and AlAs [2.63].

The experimental results obtained through the present work have provided useful information on doping characteristics and electrical properties of Be in $\text{Al}_x\text{Ga}_{1-x}\text{As}$ using an LPE technique. Using Be as a dopant, high hole concentrations of more than 10^{18} cm^{-3} can easily be achieved in $\text{Al}_x\text{Ga}_{1-x}\text{As}$ with x values up to 0.9. This is believed to be a unique feature of Be dopant compared with Ge or Zn dopant in this material. The distribution coefficient of Be in $\text{Al}_x\text{Ga}_{1-x}\text{As}$ is very high, which results in difficulty in doping controllable amounts of Be

in $\text{Al}_x\text{Ga}_{1-x}\text{As}$ particularly with low x values. Although ΔE_A increases with increasing x in agreement with results on $\text{Al}_x\text{Ga}_{1-x}\text{As}$ doped with other p-type dopants, the values of ΔE_A obtained here seem comparable with or slightly higher than those of Zn- [2.51] or Mg-doped [2.52] $\text{Al}_x\text{Ga}_{1-x}\text{As}$ which are lower than those of Ge-doped $\text{Al}_x\text{Ga}_{1-x}\text{As}$ [2.47, 2.49]. The relationship of ΔE_A vs N_A for the epilayers with a given constant x shows that ΔE_A decreases with increasing N_A . The hole Hall mobility at room temperature is less than $10^2 \text{ cm}^2/\text{V sec}$ regardless of the x value and is observed to decrease with increasing N_A for a constant x value. The results of the Al compositional dependence of the mobility suggest that the mobility may be controlled by alloy scattering.

Based on these experiments, Be seemed to be an excellent window layer dopant capable of providing highly doped, low resistivity window layers and controllable diffused junction formation for both top and bottom cells. The controllability as mentioned in Section 2.3.1 is due to the pronounced variation of the Beryllium distribution coefficient with x in $\text{Al}_x\text{Ga}_{1-x}\text{As}$. From Figure 2.6 we see that

$$K_{\text{Be}}(800^\circ\text{C}) \approx 24 \exp[-5.0752 \cdot x]. \quad (2.42)$$

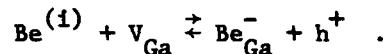
This allows us to control the amount of Be incorporated in the window layer both by controlling the amount of Be added to the melt and also by increasing the amount of Al in the window layer. Since the window layer acts as a solid state diffusion source for the formation of the bottom cell p-n junction, by controlling the Be content of the window layer and

by varying the Sn doping of the underlying GaAs epilayers, we can exercise substantial control over the junction depth and the carrier concentration of the p-type diffused layer. This latter point is important in maintaining acceptable minority carrier diffusion lengths.

There are two additional points relevant to the behavior of Be in this device structure. The total incorporation of Be in the window layer was explored using secondary ion mass spectroscopy SIMS [2.64]. It was found that in the doping range relevant to this work the Hall carrier concentration resulting from Be doping correlates well with the total Be incorporation in the layer. This is an important point since it is the total Be concentration that is relevant to the diffusion process. The diffusion characteristics of Be profiles from as-grown LPE layers is somewhat surprising. A comparison of Be-SIMS profiles from As grown, Be-doped layers and similar layers treated at 800°C for 2 h showed no significant differences. However, Be implanted to high concentration exhibits significant redistribution and anomalous diffusion effects (i.e., $D = f(\text{conc.})$) upon annealing at 800°C. This LPE result is consistent with the low diffusion coefficient ($10^{-15} \text{ cm}^2/\text{s}$) of Be in AlGaAs prepared by MBE techniques [2.45]. The differences observed in the annealing properties of implanted Be and Be incorporated during growth may be associated with the interstitial nature of implanted Be.

It should also be noted that the diffusion coefficient of Be in GaAs grown by MBE is about two order of magnitude lower than that observed for implanted Be [2.65]. It seems likely that the diffused junction forms by interstitial diffusion during growth of the Be-doped window layer. However, the interstitially diffusing Be will interact with vacancies resulting in substitutional Be that is relatively immobile

($D \approx 10^{-15} \text{ cm}^2/\text{sec}$). The simplest such reaction is



Of course there are many other possible reactions involving divacancies, intermediate products, split interstitials, etc. nevertheless, regardless of the details of this reaction, it seems as if such a model qualitatively describes the observed behavior. A Be diffusion profile is rapidly established during growth however the profile does not continue to broaden during the growth of subsequent layers.

In summary, by combining light (Sn) doping of the underlying GaAs layers with the use of Be doping in the $\text{Al}_x\text{Ga}_{1-x}\text{As}$ window layer ($x = 0.7$), a diffused junction bottom cell can be formed in GaAs with a p-layer thickness of 1-2 μ (SEM/EBIC determinations).

2.3.2.3 Tunnel Junction

The fabrication of a high quality tunnel interconnect is in many ways the most demanding aspect of producing a cascade cell. This is at least partly due to the diverse constraints that the tunnel interconnect must satisfy:

- (a) The tunnel junction (TJ) needs to act as a low resistance interconnect at the current densities required for high efficiency operation.
- (b) The TJ needs to be transparent to the radiation not absorbed by the top cell.
- (c) The TJ must be of high crystalline quality since it serves as the epitaxial pattern for the top cell growth.

Taken together, these constraints pose a difficult materials problem.

As was the case for the diffused junction of the bottom cell, the dopant choice is critical. Based on a classical band-to-band tunneling mechanism [2.66], we need an abrupt interface between degenerately doped p^+ and n^+ regions. As will be shown below, a simple band-to-band mechanism does not correspond to the observed behavior, nevertheless, these criteria for dopant selection are still valid. The p-type dopant selection is severely restricted by the requirements of an abrupt dopant profile. Zn, Cd, Mg and Be do not form a sufficiently abrupt interface by LPE. Mn is sufficiently non-diffusing, however, Mn has a value of $E_a \approx 4KT$ in GaAs and E_a increases with x in $Al_xGa_{1-x}As$. Thus Mn will not produce degenerate doping levels in the 1.9 eV bandgap AlGaAs needed in the tunnel junction. Ge is virtually the only remaining choice; Ge has been shown to produce substantial compensation in LPE layers [2.67] and E_a for Ge also increases with AlAs mole fraction, but for $x = .35$, Ge has a value of $E_a \approx 70 \text{ meV}$ ($< 3KT$) which is acceptable [2.68].

The n-type dopant choice offers similarly restricted selection. Sn, the common n-type LPE dopant, has a very low distribution coefficient in the AlGaAs alloy system, and for degenerate doping levels the large quantities of Sn required in solution prevent the achievement of a planar interface [2.69].

Si is amphoteric and has limitations imposed by limited solubility in the melt. S has a large diffusion coefficient [2.68] and its high vapor pressure causes intermelt contamination. Se and Te appeared to be the only choices. Te had been studied most extensively [2.38] and was used in the bulk of this work, some work was carried out using Se.

These Se results will be discussed later in this section. A series of experiments was carried out on isolated tunnel junction structures. The results of those experiments are described here. These results were previously published in Ref. [2.34]. The mole percentages of Ge and Te in the p^+ and n^+ melts were held constant at 20% and 4%, respectively.

For bandgaps up to 1.6 eV, carrier concentrations in the low $10^{19}/\text{cm}^3$ range were obtained (Hall measurements) for both n^+ and p^+ layers grown on Cr-doped substrates. For bandgaps around 1.9 eV the highest carrier concentration obtained was in the low $10^{18}/\text{cm}^3$ range. Increasing the mole fractions of Ge and Te in the p^+ or n^+ melts did not result in any appreciable increase in the carrier concentration in the epitaxial layers.

Figure [2.13] shows the room-temperature I-V characteristics of a p^+-n^+ AlGaAs diode with a bandgap of 1.65 eV. The total resistance of the structure, including the measuring probe resistance, is 0.8Ω . The resistance of the measuring probe is 0.22Ω ; thus the diode resistance plus the resistance of the ohmic contacts is 0.58Ω . For the cascade solar cell structure, the tunnel diode is forward biased. Thus from Figure 2.13, when correction for the measuring probe is included, a current density of 18 A/cm^2 results in a voltage drop of 100 mV. This is the anticipated solar cell current density for more than 500 suns concentration. When the tunnel diode was heated to about 200°C , no change in the diode resistance was observed. The negative resistance portion of the I-V characteristic, however, completely disappears due to the exponential temperature dependence of the excess current. Cooling to liquid-nitrogen temperature improves the peak-to-valley current

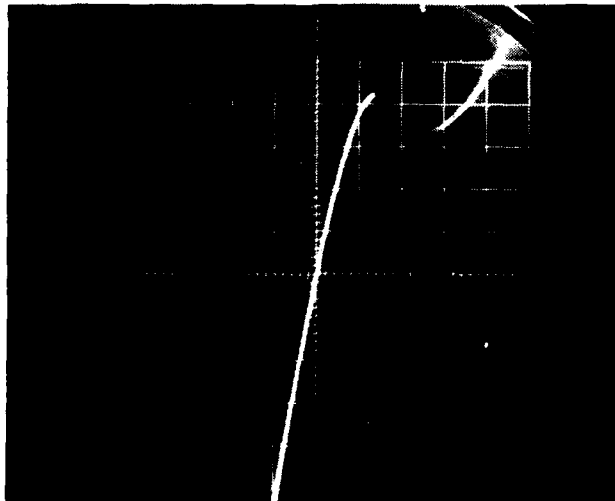


Figure 2.13. Voltage Current Characteristics of AlGaAs Tunnel Diode; the Diode Area is $3 \times 10^{-2} \text{ cm}^2$. Scale: 0.1 V/div and 10 mA/div.

ratio, and a second hump starts to appear as shown in Figure [2.14]. The significance of this I-V characteristic is the appearance of two well-resolved negative resistance regions.

Such a secondary hump had been previously observed [2.20], with lower resolution in Ge, Si, and GaAs tunnel diodes, especially after electron bombardment [2.21]. These diodes, however, had been formed using a metal alloy for the top, heavily doped layer. The second hump was then attributed to tunneling from the conduction or valence bands to impurity bands within the forbidden bandgap. Because of the nature of the alloying process, the origin of these impurity bands was not identified. However, in the present study, using a planar diode, the origin of these impurity bands can be directly related to either the $n^+(\text{Te})$ or $p^+(\text{Ge})$ dopants.

The first hump in Figure [2.14] peaks at about 0.15 V (correction for probe resistance is included) and is a result of the tunneling process between the degenerate levels in the conduction and valence bands of the n and p sides of the junction, respectively. For AlGaAs with a carrier concentration in the upper $10^{18}/\text{cm}^3$ range on both sides of the junction, there will be a very slight penetration of the Fermi level in the valence band. Thus the position of this 0.15-V peak is mainly a result of the penetration of the Fermi level in the n-side conduction band.

The second hump current starts at about 0.38 V and stops at about 0.62 V (corrections for probe resistance are included). The second hump can be attributed to tunneling of electrons from the n side of the junction to a deep level band on the p side. Thus the second hump starts when the Fermi level in the n side starts to cross this deep impurity band in the p side (i.e., from Figure [2.14]). This result is

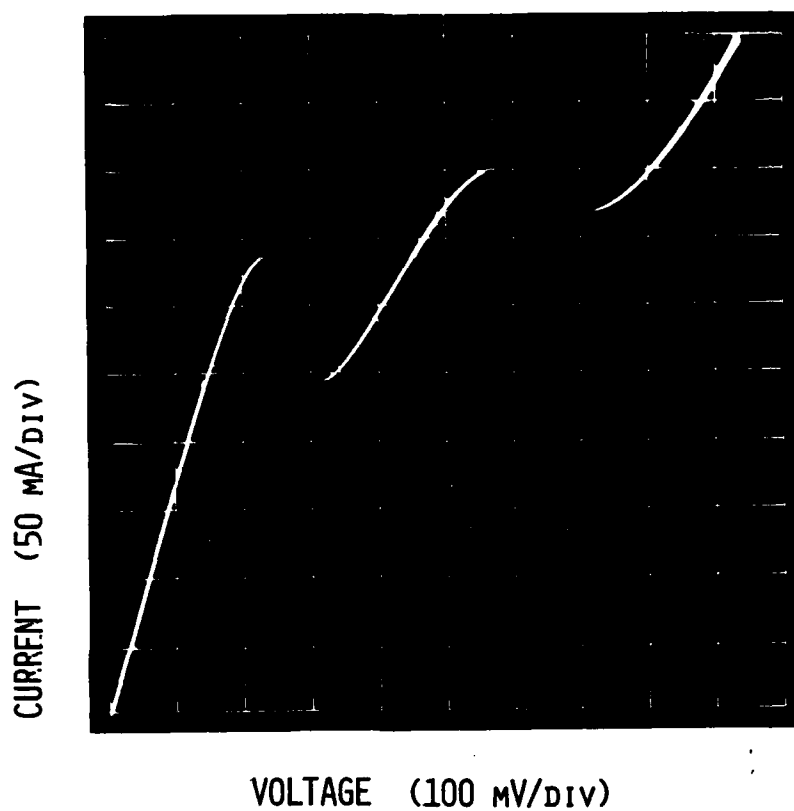


Figure 2.14. Forward current-voltage characteristics at 78°K of $\text{Al}_{0.17}\text{Ga}_{0.83}\text{As}$ tunnel diode. The diode area is $5 \times 10^{-2} \text{ cm}^2$.

consistent with the photoluminescence emission spectra of Ge-doped AlGaAs. At liquid-nitrogen temperature the spectra have a broad peak at about 1.52 eV for an alloy with a bandgap of 1.716 eV [2.72]. It has been suggested that this peak results from a deep center complex involving Ge, which forms a band 0.2 eV above the valence-band edge. Predictions of these deep level bands both by photoluminescence measurements and by the tunneling process are in good agreement.

The presence of an impurity band with energy levels deep in the bandgap is generally an undesirable effect owing to its contribution to the excess current. However, the effect can be used as a form of tunnel spectroscopy to determine the energy levels of the impurity, as demonstrated in the present results. Such deep levels may dominate device performance, especially in high bandgap materials. The width of the band that gives the second hump can also be estimated. The width of the second hump equals the sum of the width of the deep level and the penetration of the Fermi in the conduction band. Since the latter is about 0.15 V seen from Figure [2.14], the width of the deep level band is about 0.1 eV and is located about 1.5 eV below the conduction band.

For higher bandgaps at liquid-nitrogen temperature, the forward I-V trace still shows the presence of these two humps, although with lower resolution, as shown in Figure [2.15]. The first hump appears to peak at about 0.08 V, indicating that the penetration of the Fermi level in the n-side conduction band is less than Figure [2.14] for lower bandgaps. This is due to the decrease in the maximum carrier concentration that could be obtained with an increase in the bandgap. The separation between the two humps in Figure [2.15] is about 0.35 V, i.e., the deep

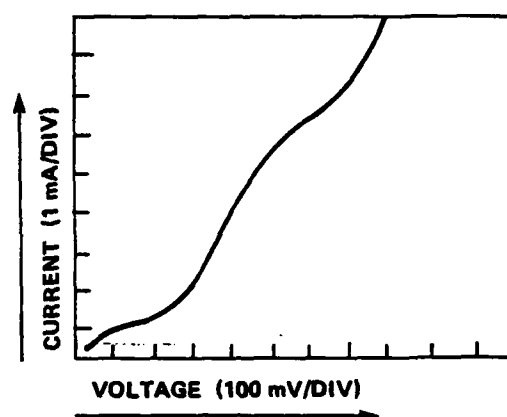


Figure 2.15. Forward current-voltage characteristic at 78°K of $\text{Al}_{0.26}\text{Ga}_{0.74}\text{As}$ tunnel diode. The diode area is $1.5 \times 10^{-2} \text{ cm}^2$.

level band is located about 1.55 eV below the conduction band of the p-type layer. Thus, from Figures [2.14] and [2.15], the location of this impurity band is nearly independent of the Al concentration in the p^+ layer. This result is consistent with the photoluminescence measurement of Ge-doped AlGaAs [2.72], where the wavelength of the emission peak resulting from this deep level band is almost independent of Al concentration in the layer.

As reported previously, the maximum achievable doping levels decreased as the alloy bandgap increased. For bandgaps above 1.85 eV, at room temperature, the doping concentration on the p and n sides of the junction have been found to be nearly (but not quite) degenerate. The resulting I-V characteristic was that of a backward diode, as shown in Figure [2.16]. This characteristic is typical of those observed for diodes with bandgaps in the range 1.85-1.95 eV. It should be mentioned that the doping levels required to obtain this AlGaAs backward diode are being self-adjusted. This is because these doping levels correspond to the maximum concentration that could be attained in this wide bandgap material when Ge and Te are being used. However, for backward diodes fabricated from low bandgap materials such as GaAs or Si, the doping levels have to be carefully controlled to prevent band-to-band tunneling.

These experiments showed that AlGaAs p^+-n^+ diodes could be fabricated for alloy compositions in the direct bandgap range. Tunnel diodes were fabricated up to bandgaps of about 1.83 eV. The I-V characteristics show a second current hump which is believed to be due to tunneling from the conduction band on the n side of the junction to an impurity band lying about 1.5 eV below the conduction band of the p side of the junction.

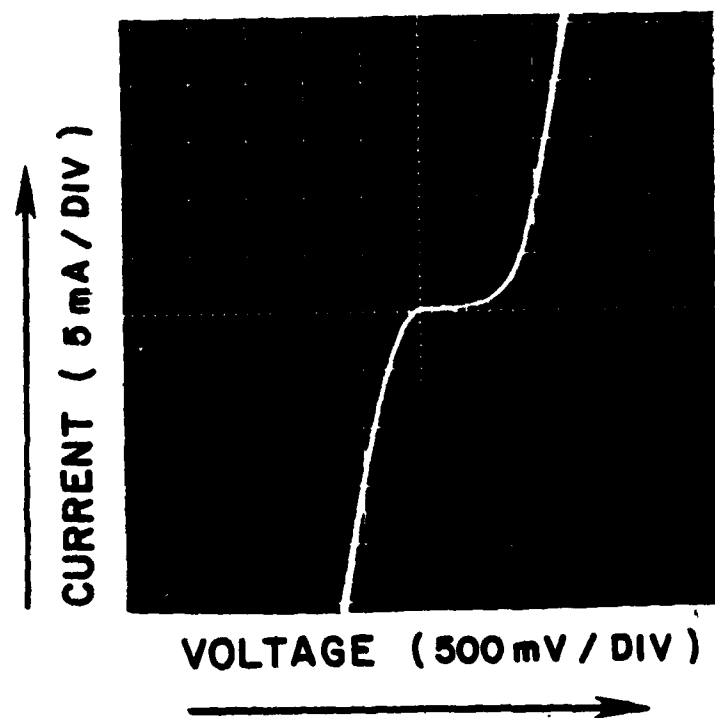


Figure 2.16. Current-voltage characteristics at room temperature of $\text{Al}_{0.35}\text{Ga}_{0.65}\text{As}$ backward diode. The diode area is $1.1 \times 10^{-2} \text{ cm}^2$.

The deep level results from the Ge doping of AlGaAs and has also been identified by photoluminescence measurements. For alloys with bandgaps in the range 1.85-1.95 eV, backward diodes were obtained. These results for AlGaAs tunnel junctions were a significant achievement of the program. In particular, the excellent characteristics obtained for the 1.65 eV bandgap junction shown in Figure 2.13. It should be remembered that the ideal bandgap combination at 1 sun and AMO is 1.6/0.95 eV. Thus, this tunnel junction would be ideal in the AlGaAs (window)/AlGaAs (tunnel junction, top cell)/InGaAs (bottom cell) structure discussed in Appendix I.

Subsequent development of the AlGaAs/AlGaAs/GaAs structure (ideally 1.94/1.42 eV) has been impeded by marginal tunnel junction performance. There are four problem areas. These areas are of varying importance and will be discussed below in order of importance, beginning with the least important concern.

- (1) The tunnel junctions reported above were grown without top cells. Thus, the growth was terminated immediately after the growth of the p^+ layer. This minimizes any thermal degradation of the junction's electrical characteristics. High temperature annealing ($\sim 900^\circ\text{C}$) of tunnel junction structures results in severe degradation of the electrical characteristics. In the cascade structure, the growth continues for the top cell, window layer, and contact layer. This represents additional time-at-temperature (~ 20 min). In order to avoid excessive tunnel junction deterioration during this period, the growth temperature has been kept low ($\sim 800^\circ\text{C}$) and the cooling rate used

for the two-phase growth is kept high ($\sim 1^\circ/\text{min}$). These issues will be discussed further in the last part of this section dealing with the crystalline quality of the tunnel junction.

- (2) The structures reported in the first part of this section were p^+ on n^+ junctions. This tunnel junction arrangement requires n on p photojunctions. This would present no particular problem if an abrupt photojunction would suffice. Unfortunately, this is not the case; as discussed above, we have found that diffused junctions give superior performance. The available dopants do not offer the converse of the Be/Sn combination (i.e., we do not find an n-type dopant with suitable diffusion characteristics).

As a result, the tunnel junction must be grown n^+ on p^+ . These junctions do not perform as well as the p^+ on n^+ structures. This may be due to the generation of defects in the Te-doped layer (see below). The presence of these defects threading through the tunnel junction in the p^+ on n^+ case may be favorable to the defect tunneling mechanism. In the n^+ on p^+ case, the dislocation loops formed in the Te-doped layer do not extend through the tunnel junction. This explanation is speculative, although the dislocation generation has been verified.

- (3) A considerably more important problem is due to the insufficient bandgap of the tunnel junction. As presented

in Section 2.2.3, the ideal bandgap combination for the AlGaAs/GaAs cell is 1.94/1.42 eV. Tunnel junctions with bandgaps greater than 1.85 eV have not been demonstrated, and the resistance of tunnel junction structures with $1.65 \text{ eV} < E_g < 1.85 \text{ eV}$ increases with bandgap (compare Figures 2.13 and 2.15). A further consideration along these lines is the concentration dependence of the absorption coefficient [2.73], this effectively reduces the bandgap from the value deduced from microprobe data. The density of states in band tail formation is fairly small; nevertheless the interactive nature of the loss mechanisms associated with photoabsorption in the tunnel junction makes the cascade structure very sensitive to tunnel junction collection. Thus, if anything, the undoped bandgap of the tunnel junction layers should slightly exceed the top cell bandgap.

- (4) The high levels of Ge and Te needed in the tunnel junction melts (~ 20 a/o and ~ 4 a/o, respectively) cause several problems both in the epilayers and in the melt. First, for the Te case, the substitutional component for n-type doping (Te residing on an As lattice site) produces a substantial dilation of the AlGaAs lattice, due to the relative difference in covalent radii of Te and As versus the relative radii of Al, Ga, and As (Table 2.4a). The resulting strain field causes misfit formation and, more importantly, enhances the flux of point defects to the growth interface, which aids the propagation of

TABLE 2.4a. Rationalized Tetrahedral Radii According to Phillips [2.79]

Al 1.230	Si 1.173	P 1.128	S 1.127
Ga 1.225	Ge 1.225	As 1.225	Se 1.225
In 1.405	Sn 1.405	Sb 1.405	Te 1.405

TABLE 2.4b. Tetrahedral Covalent Radii According to Pauling [2.80]

(in Å)

Al 1.26	Si 1.17	P 1.10	S 1.04
Ga 1.26	Ge 1.22	As 1.18	Se 1.14
In 1.44	Sn 1.40	Sb 1.36	Te 1.32

NOTE: Table 2.4a accounts for differences in atomic core size neglected in Table 2.3b. Neither accounts for dopant ion coulombic effects, or for free-hole effects.

existing defects. Second, and more significantly, these high molar percentages of dopant result in precipitation of other phases both in the melt and in the solid. For high Te-doping levels in AlGaAs [2.13] and GaAs [2.14], precipitation of GaTe, Ga_2Te_3 , and Al_2Te_3 has been studied. The strain fields surrounding these precipitates punch out dislocation loops. These dislocations propagate from the tunnel junction and through subsequent epilayers grown for the top cell, dramatically limiting the performance of the structure. The problems posed by precipitate formation can be thought of as two separate issues: (1) precipitate formation and (2) dislocation growth and propagation. It has been shown [2.11, 2.15] that the dislocation growth and propagation can be minimized by growth at temperatures greater than the melting point of the precipitate. In AlGaAs grown in an oxygen-free environment, the chief precipitate is Al_2Te_3 (melting point 886.8°C). Unfortunately, growth at temperatures $\sim 900^\circ\text{C}$ will compromise the abruptness of the dopant profiles necessary for tunnel junction operation. It should be noted that growths carried out above the melting point of the precipitate do not completely avoid precipitate formation. Precipitation will still occur during cool-down, but the dislocation loops formed will not be at high temperatures long enough to propagate into overlying epilayers. This corresponds to the Ge case in the present tunnel junction;

the Ge-containing precipitates, GeAs_2 and GeAs , are unstable above 730°C [2.78]. Thus the degradation of subsequent epilayers due to the $\text{p}^+(\text{Ge})$ epilayer is found to be minimal.

The presence of high levels of Te in the melt can also cause nonplanar epilayer morphology as shown in Figure 2.17. These conical "hills" were often observed in the initial stages of this work. They are believed to be a nucleation phenomena associated with the presence of a precipitate particle at the growing interface. The following procedure was developed to significantly reduce this effect.

The Ga and excess GaAs are first baked together at 900°C overnight and then cooled to room temperature before the addition of Te and Al to the melt. Upon reheating the melt to the deposition temperature of 800°C followed by epitaxial growth, a smooth, specular AlGaAs layer is obtained. A possible explanation of this method for reducing Te-related defects is that when the prebaked Ga melt (saturated with GaAs) is quenched to room temperature, GaAs crystallites are formed. These solid crystallites in the melt may act as nucleation sites for the Te compounds during the process of melt saturation at 800°C . It appears that the GaAs crystallites are of sufficient number to trap most of the Te compounds that will otherwise disturb the epitaxial layer. A contributing mechanism



82.5 X

Figure 2.17. Conical Hills Representative of Those Observed for Heavy Te- or Se-Doping of AlGaAs. (Te = 0.4 atomic percent) Magnification 82.5. Sample L-274-B.

may also depend on the prebake resulting in a reduced oxygen concentration in the melt [2.81]. Russian workers have identified Ga_2TeO_6 in LPE material grown in an H_2 stream containing trace amounts of O_2 [2.82]. Our work has indicated that the problems associated with high levels of Te-doping are accentuated by system leaks. However, the problems are reduced but not eliminated in a leak-tight system.

Some experiments were carried out using Se as the n^+ dopant or with mixed Se-Te doping. Se has a much higher distribution coefficient than does Te which allows much smaller atomic fractions of Se in the melt. Se also has a closer match to Arsenic's covalent radius (Table 2.3). However, Se has a much higher vapor pressure than does Te which can result in intermelt contamination, and most significantly, the selenides of Al and Ga have greater (more negative) enthalpies of formation and higher melting points than do the corresponding tellurides (Table 4.1). This last factor dominates and Se-doped tunnel junction cascade cells are inferior to similar structures doped with Te. Section 4 will discuss an approach to the cascade structure that circumvents many of the difficulties discussed here.

Typical melt compositions used for the tunnel junction epilayers in this study were:

Melt 4 - Aluminum 1.2 mg per g. Ga, Ge 250 mg per g. Ga, and GaAs in excess of the amount needed to saturate the melt.

Melt 5 - Aluminum 1.2 mg per g. Ga, Te 8 mg per g. Ga, and GaAs in excess of the amount needed to saturate the melt.

2.3.2.4 Top Cell

The primary difficulty in the growth of the top cell is in minimizing the effects of crystalline imperfections originating in the Te-doped n^+ tunnel junction layer (see Section 2.3.2.3). These dislocations propagate upward during growth and seem to act as shunting paths in the top cell junction. This drastically reduces top cell performance. For this reason, the top cell n-type layers are grown much thicker than the top cell modeling results call for (5-6 μ vs. $\sim 2 \mu$). This buffer region reduces but does not eliminate the effect of the Te-doped layer on top cell performance. Also, this extra thickness places the top cell p-n junction several diffusion lengths and several absorption lengths from the tunnel junction. This effectively prevents collection of photocarriers by the tunnel junction, so that an explicit minority carrier barrier layer is not required.

The actual growth of the top cell is virtually the same as for the bottom cell (Section 2.3.2.2) with the addition of Al to the top cell melts. As was mentioned in regard to the bottom cell window layer, care must be taken to anticipate Al depletion from the melt due to nucleation of AlGaAs on the excess solid GaAs present on the melt. The make up of the melts for the top cell growth is as follows:

Melt 6 - 1.10 mg Al per g. Ga, 50 mg Sn per g. Ga, and GaAs in excess of the amount required to saturate the melt.

Melt 7 - This melt is identical to Melt 6. As was mentioned in Section 2.3.2.2, the use of two melts for the top and bottom cell n-type layers permits growth on several substrates in one run.

The top cell p-type layer is formed by Be diffusion from the top cell window layer.

2.3.2.5 Top Cell Window Layer

This layer performs the same functions as does the bottom cell window layer (see Section 2.3.2.2). This window layer requires a bandgap in excess of 2 eV thus the problems of Al depletion from this melt are especially severe. In addition, since this is the next to last layer grown, there is at least a 30 degree drop in temperature during the ramped growth of the preceding layers. If excess GaAs is used, there will be substantial growth on the excess solid phase during this time period. There will also be some Al losses due to spontaneous nucleation in the melt and due to nucleation on the precursors. Therefore, the window layer melt should not use excess GaAs, but should have an overall composition giving a liquidus temperature only a few degrees higher than the temperature at which the substrate contacts this melt.

Melt 8 - 10 mg Al per g. Ga, 50 μ g Be per g. Ga, and GaAs as required for saturation (see above).

2.3.2.6 GaAs Contact Layer

This growth is straightforward. The areas of this epilayer that are not actually covered by the contact metallization will be removed during processing. For this purpose, a thin epilayer is needed ($\sim 0.5 \mu$).

Melt 9 - 50 mg Ge per g. Ga and GaAs in excess of the amount needed for saturation.

2.3.3 Cell Fabrication

Fabrication of the cascade wafers into photovoltaic devices consists of photoresist patterning and e-beam deposition of contacts to the p^+ -GaAs followed by e-beam deposition of a broad-area contact to the n^+ -substrate. Removal of the photoresist from the front surface is followed by sintering the contacts in purified hydrogen at 485°C for 2 minutes. Additional details of electrical contact fabrication are given below.

2.3.3.1 Electrical Contacts

A variety of ohmic contact technologies for the p^+ front surface of the cascade cell were examined to reduce the cell series resistance and to improve metal adhesion. These approaches are basically separated into methods for applying contacts directly to the p^+ - $Al_{0.9}Ga_{0.1}As$ window layer versus forming the contacts on a p^+ -GaAs cap layer. All contacts formed on the GaAs cap layer have yielded lower resistance and better metal adhesion than those formed on the $Al_{0.9}Ga_{0.1}As$.

The p^+ -GaAs cap contact is included in the growth and fabrication of complete cascade solar cells. The p^+ -GaAs contacting layer is approximately 0.5 μm thick and is doped with Ge to $p > 1 \times 10^{18} cm^{-3}$.

A photolithographic process is used to define openings for the p^+ -contact. This is followed by e-beam evaporation of 1200Å of Ag-Mn alloy (5% Wt Mn) followed by 1200Å of Al. Contact to the n^+ -substrate is then fabricated by e-beam evaporation of 200Å Sn followed by 2000Å Ag. The n^+ -GaAs contact reproducibly has a specific resistance, R_s , of

$\sim 1 \times 10^{-6} \Omega\text{-cm}^2$. The p^+ -GaAs contact has a specific resistance, R_s , of $\sim 1 \times 10^{-4} \Omega\text{-cm}^2$. However, the p^+ contact is somewhat variable; contacts with $R_s = 2 \times 10^{-5} \Omega\text{-cm}^2$ have been measured, as have contacts with $R_s = 1 \times 10^{-3} \Omega\text{-cm}^2$. The n^+ contact area is also 10X larger than the p^+ contact area so that the series resistance due to contact effects is dominated by the p^+ contact. Contact fabrication is completed by sintering the wafer at 485°C in purified hydrogen for 2 minutes.

Contacts deposited directly to the $\text{Al}_{0.9}\text{Ga}_{0.1}\text{As}$ window layer were used to quickly evaluate new experimental structures using an abbreviated, but effective, fabrication process. In this case, a metallization consisting of e-beam evaporated 50Å Al, 200Å Mn, 300Å Pd, followed by 1500Å Au yields contacts that are ohmic immediately following evaporation. Following deposition of the n^+ -substrate contact, the wafer is alloyed at 480°C in purified hydrogen for 60 seconds, which maintains the p^+ -contact ohmicity and reduces its specific resistance. These contacts have very consistent values of R_s , with $R_s = 4 \times 10^{-4} \Omega\text{-cm}^2$.

2.3.3.2 Antireflection Coating

A broad-band, two-layer AR coating has been successfully applied to the AlGaAs-GaAs cascade cell to increase the short-circuit current densities by as much as 28 percent compared to the same cells prior to coating (Figures 2.18 and 2.19). The process used is similar to a process first described by Sahai et al. [2.83]. These AR layers consist of 560Å of Ta_2O_5 followed by 800Å of SiO_2 deposited by e-beam evaporation. Results of a theoretical analysis performed to calculate optimum thicknesses of the Ta_2O_5 and SiO_2 layers as a function of the

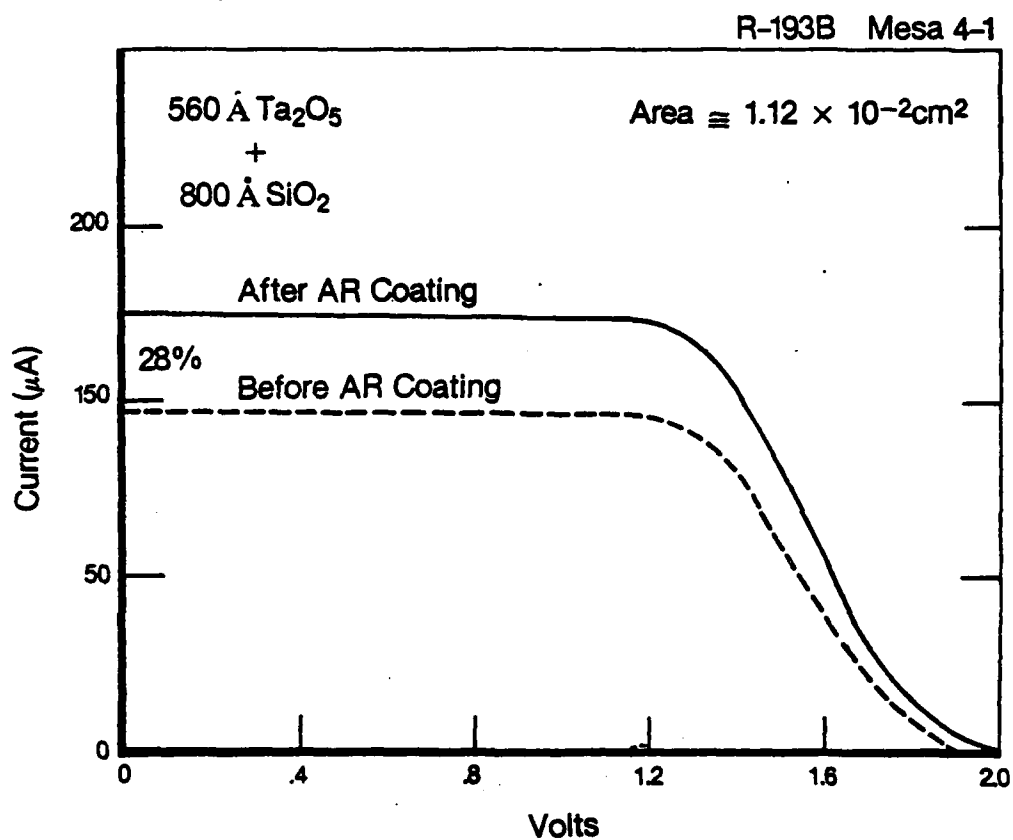


Figure 2.18. Current-Voltage Characteristic for an Illuminated AlGaAs-GaAs Cascade Solar Cell Before and After AR Coating.

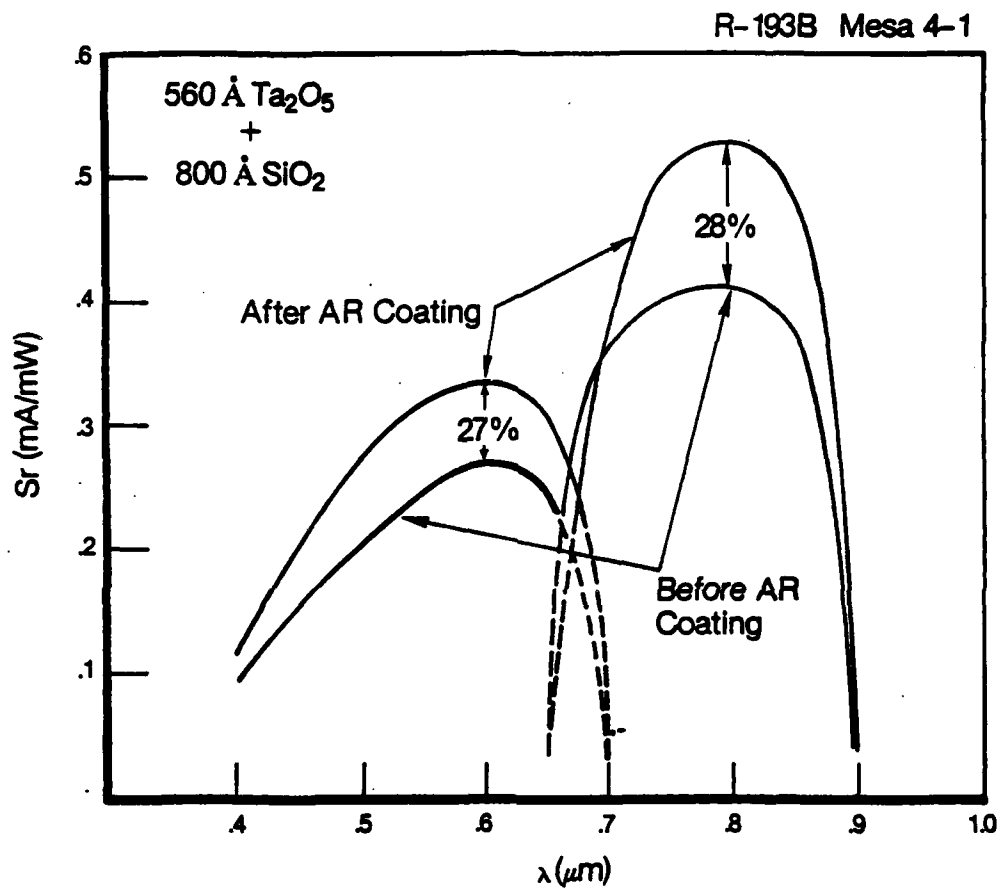


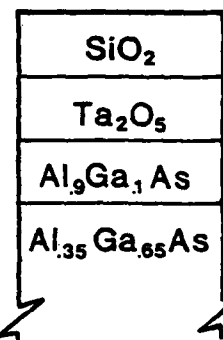
Figure 2.19. Spectral Response for an Illuminated AlGaAs-GaAs Cascade Solar Cell Before and After AR Coating.

$\text{Al}_{.9}\text{Ga}_{.1}\text{As}$ window layer thickness are shown in Table 2.5. The unique feature of this analysis is that the fraction of light transmitted through the window was maximized; other analyses consider and maximize light transmitted through the AR coat. Results given in Table 2.5 show that for an AMO spectrum (wavelengths between 0.30 and 1.20 μm) the total light transmitted through the $\text{Al}_{.9}\text{Ga}_{.1}\text{As}$ window layer is greater than 90 percent for window thicknesses of 0.3 μm . These data also illustrate the importance of minimizing the thickness of the window layer.

In the AR coating work performed, it was assumed that the indices of refraction of the e-beam deposited films correspond to their respective "bulk" values. Of course it was realized that this would not be the case since the films are not perfectly stoichiometric and are more accurately denoted as SiO_x and Ta_2O_x . Experiments are needed to determine the index of refraction as a function of controlled experimental conditions. This would provide the model with more accurate parameters. Because of this uncertainty, we have observed that in some cases AR coating decreased the cell's performance. Although this result could be somewhat influenced by the natural oxide on the $\text{Al}_{.9}\text{Ga}_{.1}\text{As}$ layer, with adequate preparation procedures, this oxide is only about 50 Å thick. This would imply that the variability observed is due to the evaporated oxides, and not due to the native oxide.

TABLE 2.5. Theoretical Analysis for Two-Layer AR Coating.

Layer Composition	Layer Thickness - μm				
$\text{Al}_9\text{Ga}_1\text{As}$.3	.4	.5	.8	1.0
Ta_2O_5	.054	.054	.055	.058	.063
SiO_2	.100	.117	.115	.115	.111
Transmission (%) Thru $\text{Al}_9\text{Ga}_1\text{As}$	90.9	89.4	89.1	87.3	87.1
Reflection (%)	3.3	3.9	3.5	3.7	3.3
Absorption in $\text{Al}_9\text{Ga}_1\text{As}$ (%)	5.8	6.7	7.4	9.0	9.7



3.0 EXPERIMENTAL CELL PERFORMANCE

3.1 Experimental Techniques

3.1.1 Current-Voltage Characteristics

The dark I-V characteristic of a solar cell is equal in analytical importance to the photocurrent. It serves as a probe of the basic mechanism controlling the solar cell operation, since the quality of the p-n junction is intimately related to the performance of the cell, and the dark current characteristic is very sensitive to junction quality. The dark I-V characteristics of the devices were measured point by point with the experimental apparatus shown in Figure 3.1. The current source supplied currents ranging from 10^{-10} amp to 0.09 amp. The current meter consisted of an Analog Devices Model 310K operational amplifier and a digital multimeter, Keithley Model 160. The voltage was read from a Keithley Model 602 electrometer, which is a solid state, battery-operated instrument capable of measuring voltages from 10^{-5} volts to 10 volts with an input impedance of 10^{14} ohm.

All devices were tested under AMO illumination produced by a solar simulator employing a 1 KW Xenon arc lamp. The AMO source was calibrated to assure accuracy of the measurements. Since it is not easy to duplicate the solar spectrum with an artificial light source, the effective intensity of the artificial light was adjusted to be the same as that of the sun as determined by a radiant power measuring device, a pyrheliometer. The intensity of light was also adjusted by calibrating the short circuit current using a NASA Lewis standard p-n junction silicon solar cell. Figure 3.2 shows the block diagram for I-V measurement under AMO, where the concentrator lens (6X) was used for the study of high intensity effects. Some measurements were performed on samples in

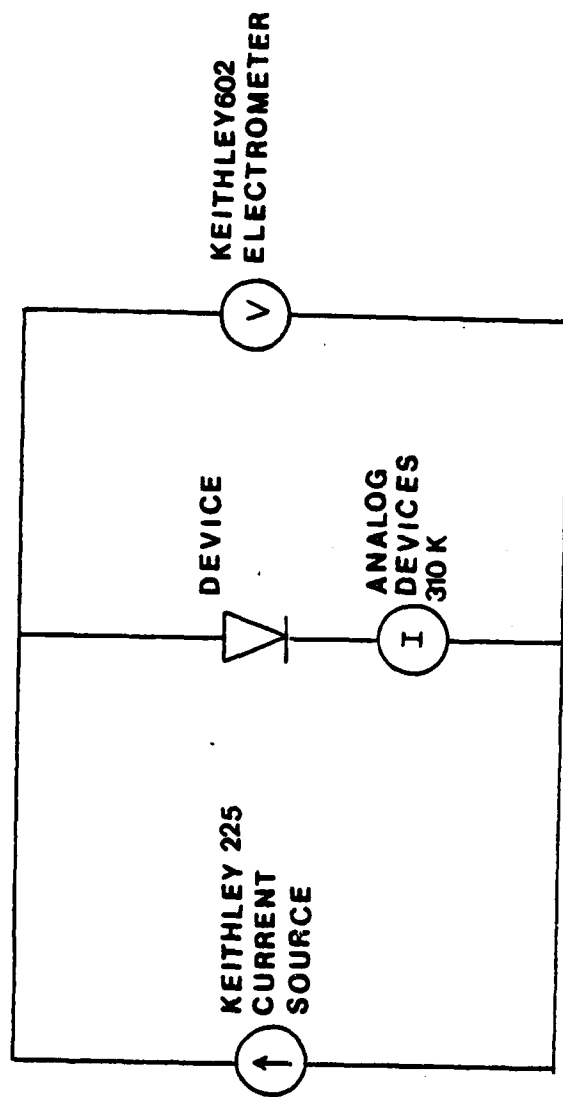


Figure 3.1. Schematic Representation of the Set-up for Dark I-V Measurements.

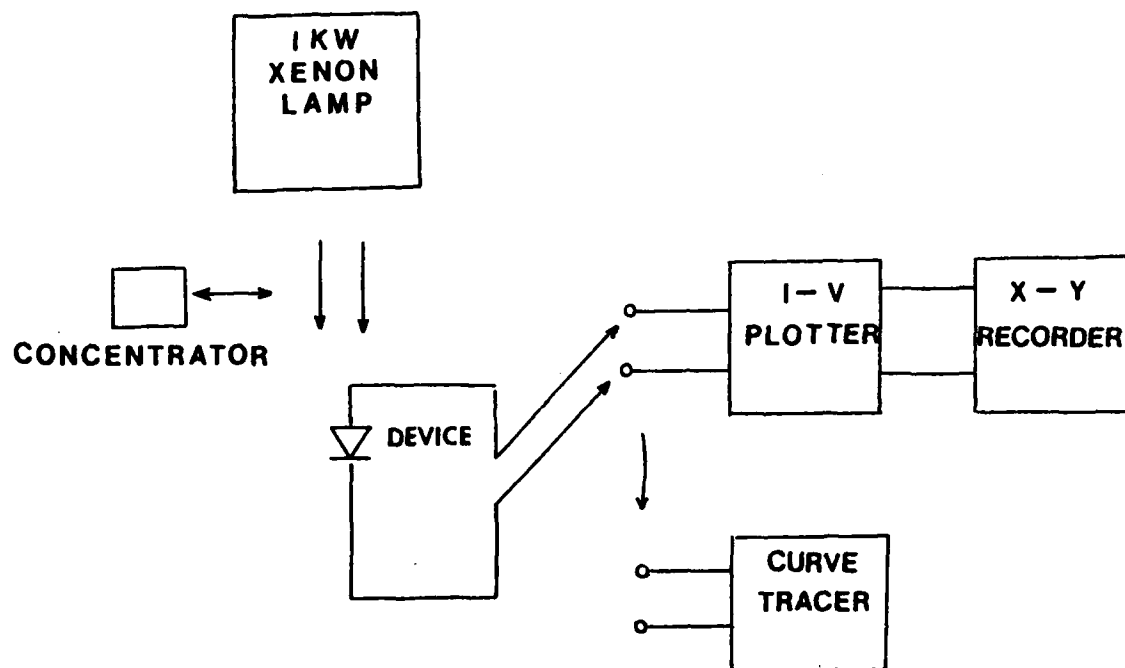


Figure 3.2. Block Diagram of the Set-up for I-V Measurements under AMO Illumination.

the sunlight outside the laboratory. From the intensity of the sunlight as measured by a thermopile (Eppley Laboratories Pyranometer), all data were corrected to the standard AMO illumination for comparison with theoretical values.

3.1.2 Spectral Response

The schematic diagram for the spectral response measurements is shown in Figure 3.3. The light source was a 500 W quartzline lamp together with a set of narrow bandpass filters (bandwidth = 100Å) to produce monochromatic beams. To increase the signal-to-noise ratio of the response, a low frequency beam-chopper and a lock-in amplifier were used to detect the short circuit current of the illuminated cell. The short circuit current was converted to a voltage input to the lock-in amplifier by loading with a small resistor. The intensity of the monochromatic beam at each wavelength was calibrated using a standard Si-cell obtained from NASA Lewis Research Center. After the system was calibrated excellent agreement was obtained between the data taken at NASA Lewis and the present results, as seen in Figure 3.4.

A second light source along with two filters was used to measure cascade cells. During the measurement of the top cell in the cascade structure, the bottom cell was turned on to act as a conductor by passing light through a low-pass filter with a cutoff wavelength at 7000Å (1.77 eV). In a similar way, a narrow band filter was employed to turn on the top cell when measuring the bottom cell.

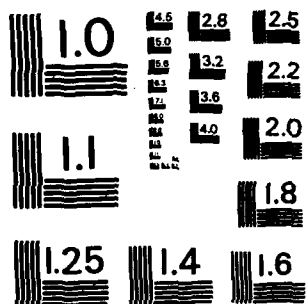
AD-A126 588 DEVELOPMENT OF HIGH EFFICIENCY STACKED MULTIPLE BANDGAP
SOLAR CELLS. (U) RESEARCH TRIANGLE INST RESEARCH
TRIANGLE PARK NC S M BEDAIR ET AL. SEP 82

AD-A126 588 DEVELOPMENT OF HIGH EFFICIENCY STACKED MULTIPLE BANDGAP
SOLAR CELLS. (U) RESEARCH TRIANGLE INST RESEARCH
TRIANGLE PARK NC S M BEDAIR ET AL. SEP 82

2/3

UNCLASSIFIED R11/1678/00-F-VOL-2 AFAPL-TR-79-2116-VOL-2 F/G 10/2

NL



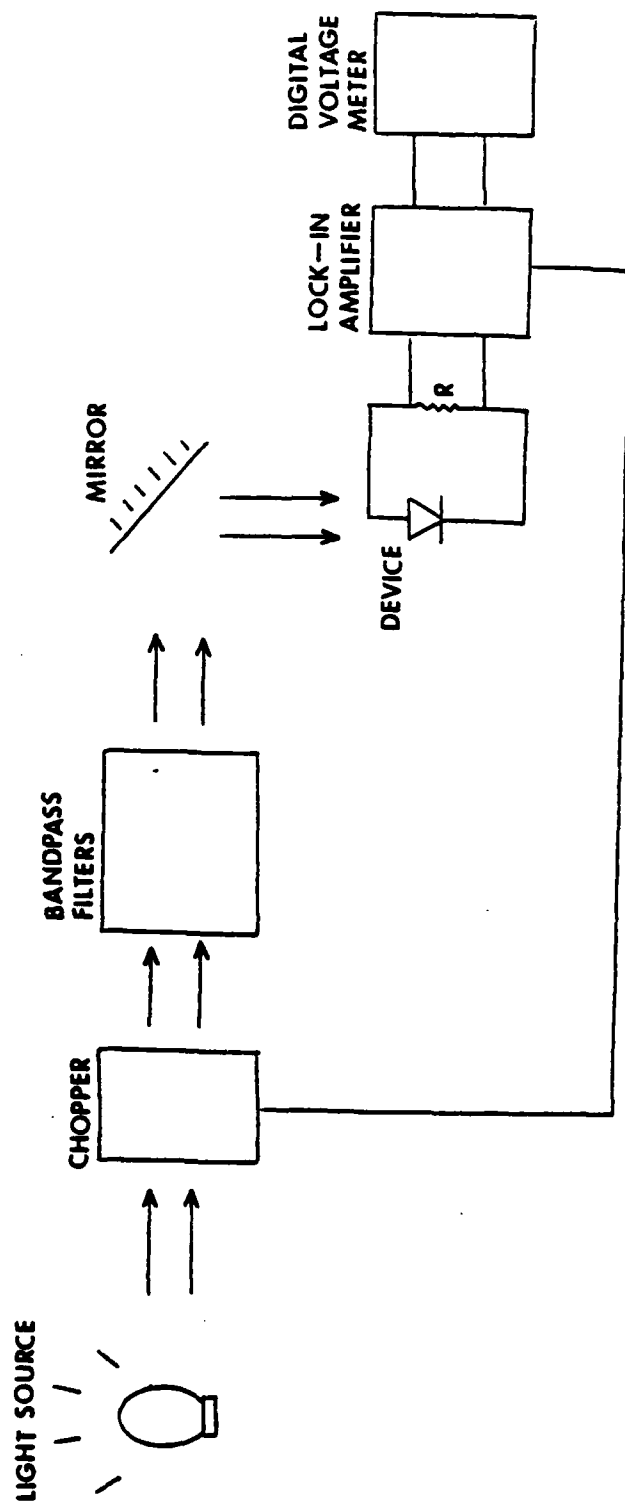


Figure 3.3. Schematic representation of the Experimental Arrangement for Spectral Response Measurements.

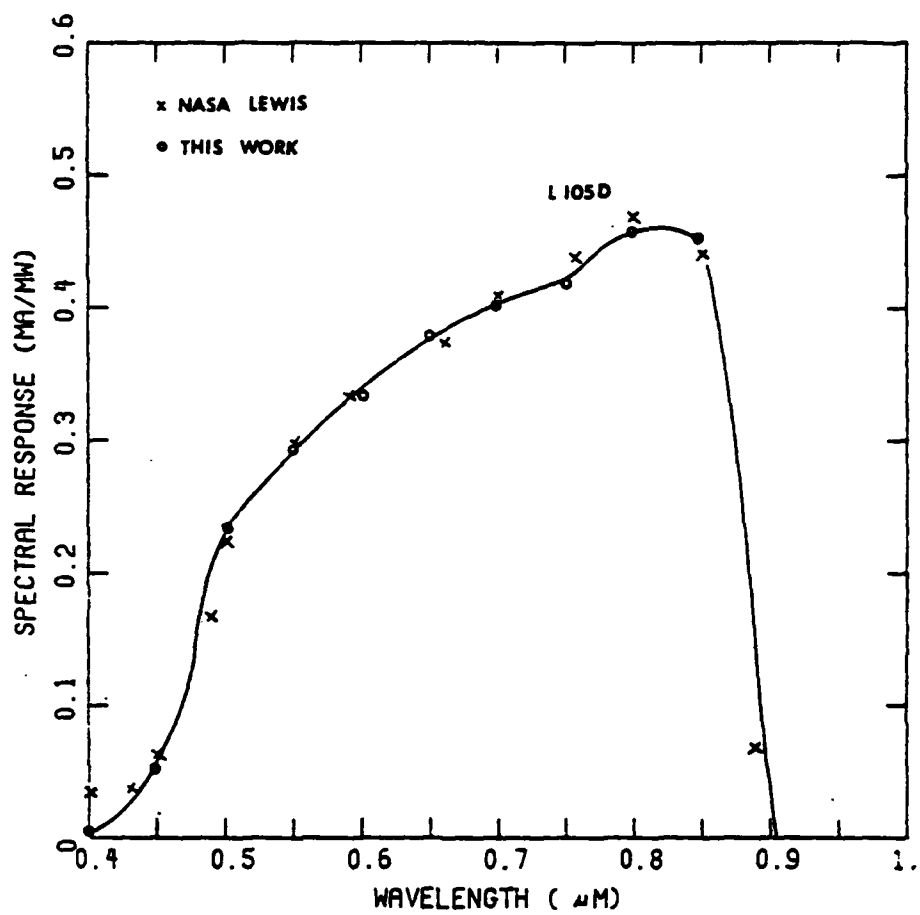


Figure 3.4. Comparison of the Calibrated System and the Standard System for Spectral Response Measurements.

3.1.3 Diffusion Length

The minority carrier diffusion length in the base region of a solar cell is one of the most important parameters determining the long wavelength response. This quantity is a measure of the average distance that a carrier may diffuse before recombination occurs. A variety of experimental techniques have been applied to measure the diffusion length [3.1,3.2,3.3]. The technique described here is to determine diffusion lengths from the measurement of the short circuit current induced by strongly ionizing radiation. Advantages of this technique over others are its simplicity and speed. While the use of electrons, photons, X-rays, or γ -rays will adequately provide a uniform carrier generation throughout the device, the γ -ray method was used because no particle accelerator and flux monitor are required once the γ -ray source is calibrated.

In this study, the sample was uniformly illuminated with γ -ray from a Co^{60} source. The generated carriers were then collected at the p-n junction just as in solar cell operation. The diffusion length was then obtained from the measured short circuit current and the dose rate of the Co^{60} source [3.1]. For a device with a junction near the surface and a thickness of several diffusion lengths or more, the relationship between the short circuit current and the diffusion length is simply

$$J_{sc} = qg(L + W), \quad (3.1)$$

where q is the electronic charge, g is the carrier generation rate and

W is the junction depletion width. If W is negligible compared with L, the expression reduces to

$$J_{sc} = qgL. \quad (3.2)$$

Figure 3.5 shows a schematic of the experimental arrangement. The Co^{60} source is a "Gammacell 220" manufactured by Atomic Energy of Canada Limited. The differential operational amplifier (LH0052C) used to measure the current has an extremely low input offset voltage so that the precise short circuit current can be obtained.

3.1.4 Resistance

3.1.4.1 Series Resistance

The solar cell has components of series resistance due to the metal contacts, the metal-semiconductor barrier, and the emitter and base thicknesses. This series resistance, represented by R_s , is very important in determining the short circuit current and especially the fill factor of the solar cell. The series resistance has been measured by a practical approach as presented in Figure 3.6. The current difference between the short circuit current and the current at point P is chosen to be the same for all curves under various illuminations. The I-V relations are related to the difference through the following relations:

$$\begin{aligned} \Delta I &= I_o \left(e^{\frac{q(V_1 - I_1 R_s)}{nkT}} - 1 \right), \\ &= I_o \left(e^{\frac{q(V_2 - I_2 R_s)}{nkT}} - 1 \right), \\ \text{and} \quad &= I_o \left(e^{\frac{q(V_3 - I_3 R_s)}{nkT}} - 1 \right). \end{aligned} \quad (3.3)$$

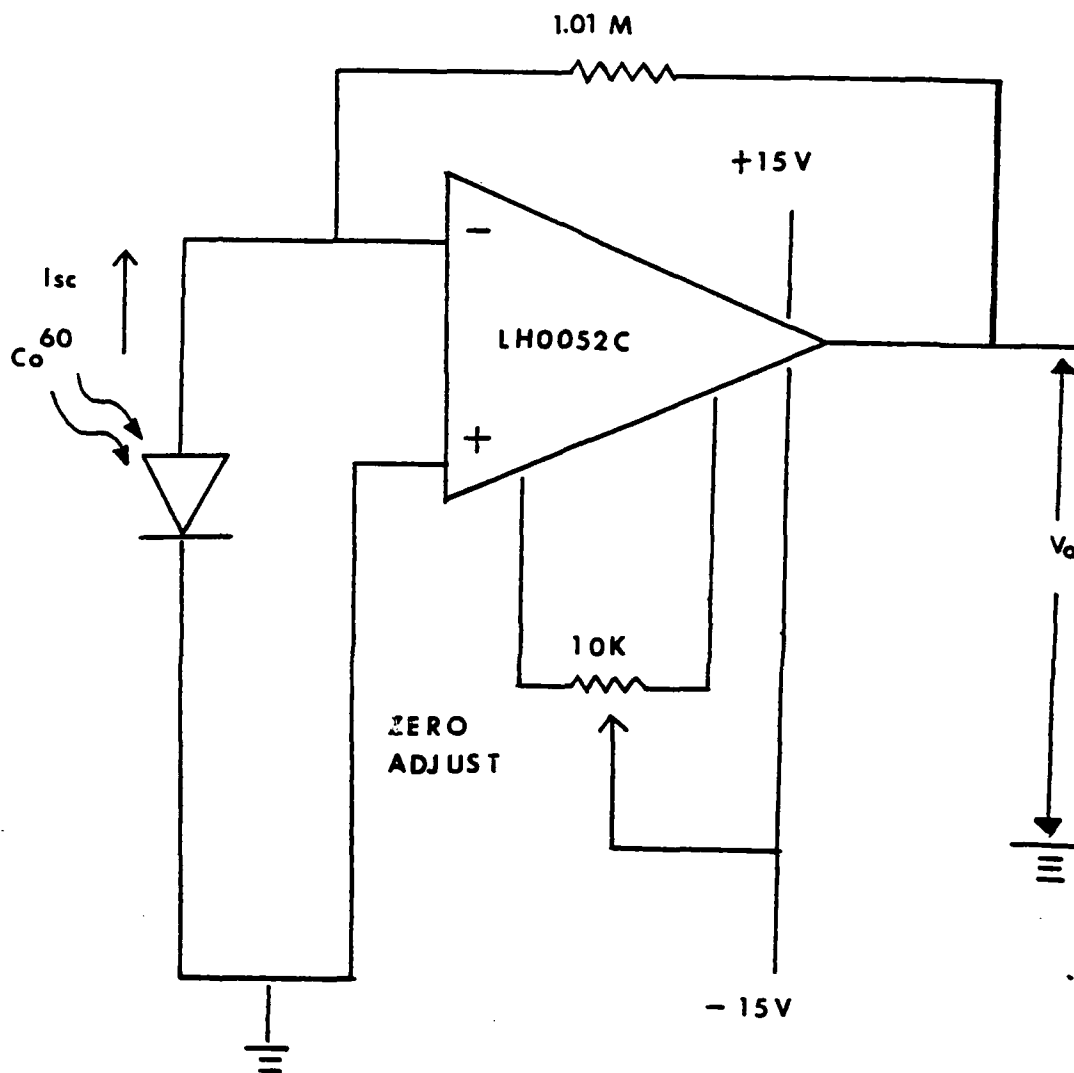


Figure 3.5. Schematic Representation of the Set-up for Diffusion Length Measurements.

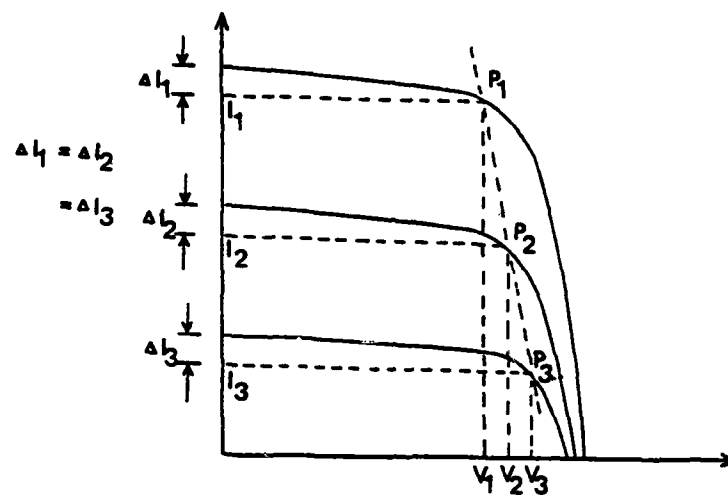


Figure 3.6. Schematic Illustration for the Calculation of the Series Resistance of a Solar Cell.

It is obvious from these expressions that

$$\begin{aligned} V_1 - I_1 R_s &= V_2 - I_2 R_s \\ &= V_3 - I_3 R_s \end{aligned} \quad (3.4)$$

and

$$\begin{aligned} R_s &= \frac{V_2 - V_1}{I_1 - I_2} \\ &= \frac{V_3 - V_2}{I_3 - I_2} . \end{aligned} \quad (3.5)$$

The slope of the line connecting the P points is the series resistance of the solar cell. It has been found that a major contribution to the series resistance of the cascade solar cell is due to the resistance of the metallic contact to the p-type epilayer. For this reason, a separate approach for measuring the contact resistance has been carried out as described in the following section.

3.1.4.2 Contact Resistance

To measure the contact resistance, contributions from the spreading resistance, bulk resistance and residual resistances have to be separated from the total resistance. Cox and Strack [3.4] developed a technique to evaluate the specific contact resistance on epitaxial layers. Contacts of different diameters are deposited on the top of the epitaxial layer while a large area back side contact was fabricated on the heavily doped substrate. The separation was then achieved by

measuring the total resistance and employing an expression relating the dependence of the spreading resistance to the contact diameter. Although this technique is quite commonly used in studying contact resistance, it is not appropriate for the present work since it requires a conducting substrate with the same type of majority carrier as in the epitaxial layer. The measurement of contact resistance on an epitaxial layer with an insulating, semi-insulating or different type substrate needs another approach. The method of measuring the contact resistance used in this work is discussed in the following.

Figure 3.7 shows a pattern consisting of rectangular bars which was employed to evaluate the contact resistance. The total resistance between two metal bars is given by equation (3.6),

$$R_T = 2R_c + R_1, \quad (3.6)$$

where R_T = total resistance ,

R_c = metal-semiconductor resistance ,

and R_1 = spreading and bulk resistance.

The contact resistance R_c can be obtained by measuring sequentially the resistance between adjacent bars and extrapolation to the origin as shown in Figure 3.8. This linear relationship of assuming the spreading resistance and the bulk resistance being proportional to the spacing between two bars is approximately true as long as the spacing is considerably larger than the width of the metal bar.

3.1.4.3 Shunt Resistance

The shunt resistance of the solar cell can be due to surface leakage along the edges of the cell or to junction leakage resulting from

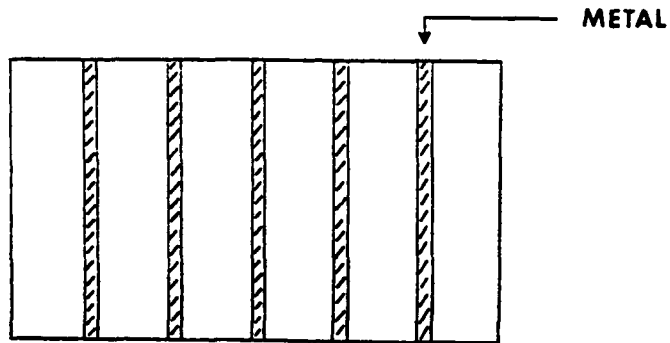


Figure 3.7. Contact Pattern for Contact Resistance Measurements.

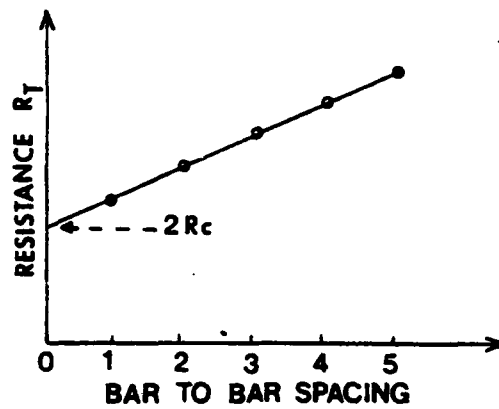


Figure 3.8. Resistance Versus Contact Spacing.

lattice defects or other inhomogeneities in the vicinity of the junction. This lowers the open circuit voltage, the fill factor and ultimately the efficiency of the cell. The shunt resistance, represented by R_{sh} , has been characterized by measuring the I-V relationship at reverse bias and at small forward bias.

3.2 Experimental Results

3.2.1 Introduction

In order to better understand the performance of cascade cells, experimental and theoretical studies have been carried out to examine top cells, bottom cells and cascade cells individually. Bottom cells referred to here are GaAs cells with window layers, with tunnel junctions and window layers, or with tunnel junctions only.

Figures 3.9a and 3.9b show SEM and EBIC pictures of the cross section of a cascade solar cell. Layer thicknesses have typically been in the range of 0.5 to 3.0 μm . Carrier concentrations determined by Hall measurements at room temperature have varied from 10^{17} cm^{-3} to 10^{18} cm^{-3} . Uniform doping has been found in the epitaxial layers by capacitance-voltage measurements with a Schottky contact. The doping profile is approximately Gaussian for the diffused layers.

The structure employed for computer simulation is shown in Figure 3.10 with all junctions assumed abrupt for simplicity. The mole fraction, x , of AlAs in $\text{Al}_x\text{Ga}_{1-x}\text{As}$ layers measured by the electron microprobe is approximately 0.35 and 0.9 for the top cell and the window layer respectively. Bandgaps of the top cell and the tunnel junction determined by photoluminescence measurements range from 1.8 eV to 1.9 eV. The experimental results presented in the following sections are typical values for these cells, not necessarily the best values, so that by

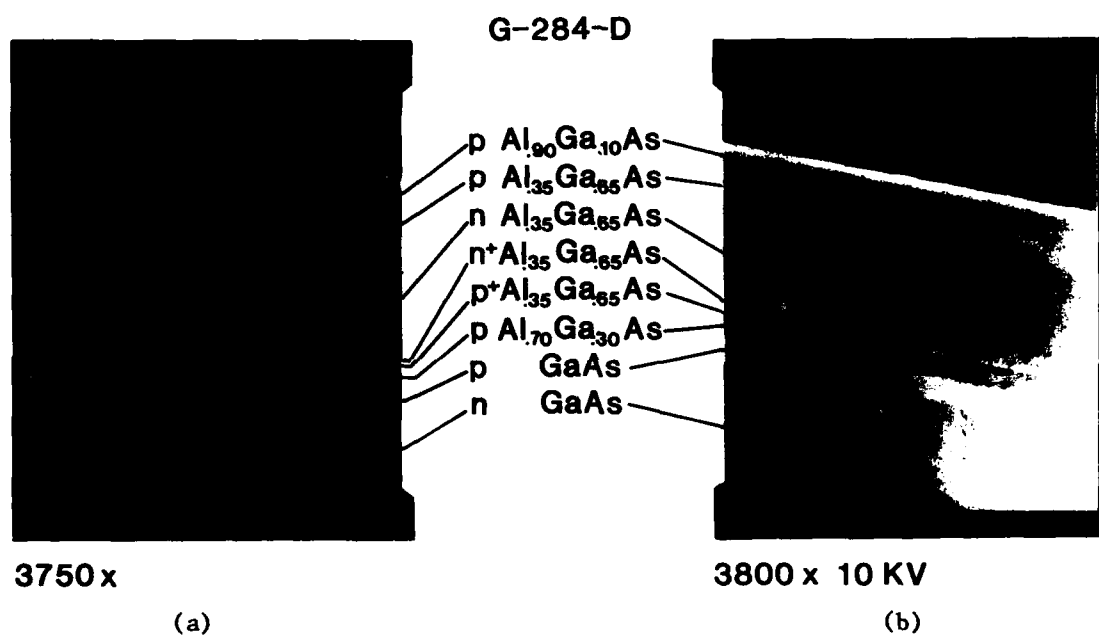


Figure 3.9. Scanning electron micrographs of an AlGaAs-GaAs cascade solar cell cross-section. (a) Combined secondary-emission and electron-beam-induced-current modes, and (b) secondary emission mode only.

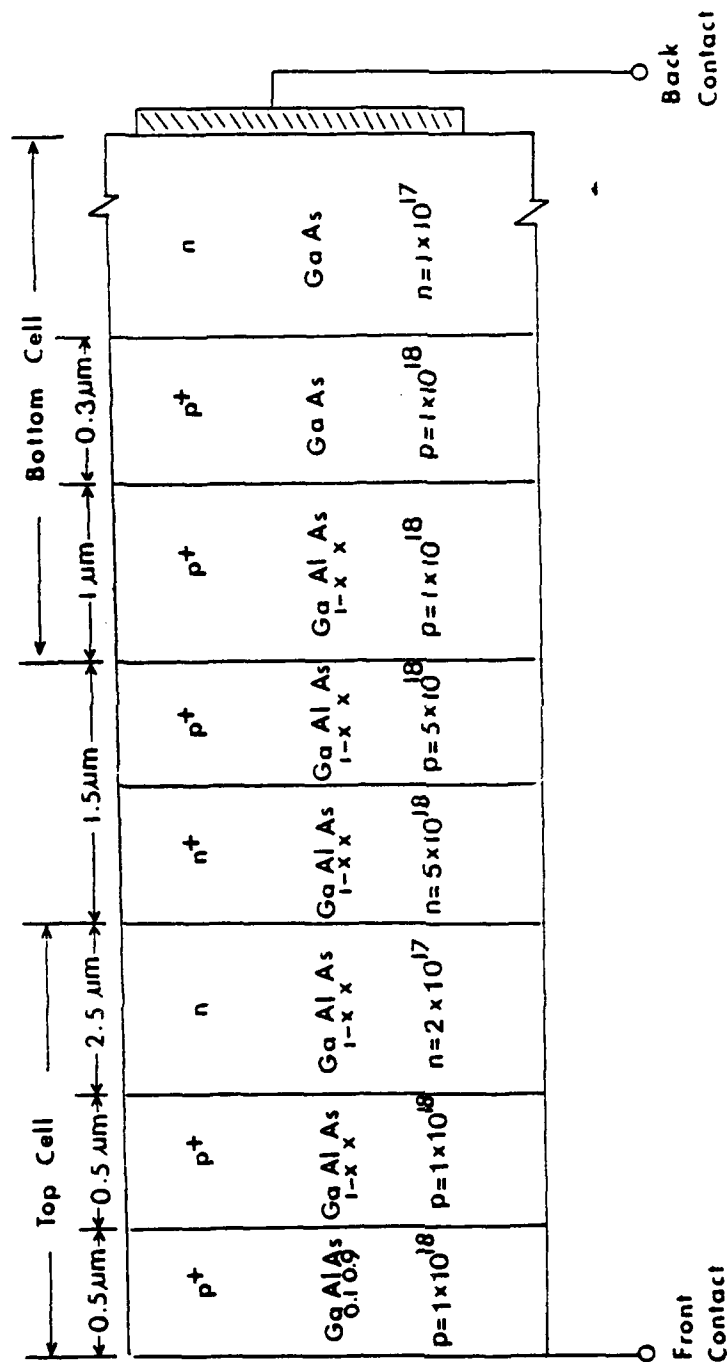


Figure 3.10 Composition profile and structure of a cascade cell for the computer simulation.

comparing these results with the computer modeling results we can explore the problems encountered in the process of materials growth and device fabrication.

3.2.2 Dark Current-Voltage Characteristics

3.2.2.1 Diode Factor

Figures 3.11a and 3.11b show the dark I-V characteristics of a top cell, bottom cell and cascade cell. The I-V relations obey $I = I_0 \exp(qV/nKT)$, where I_0 and n are approximately constant. The values of n typically ranged from $1.5 \rightarrow 2$ over most of the voltage region for a single-junction cell indicate the dominance of non-ideal current recombination mechanisms in the solar cell operation. Henry, et al. [3.5] have attributed the origin of $n \approx 2$ to surface recombination as shown in Figure 3.12. In the cited work on studies of AlGaAs heterojunctions, it was observed that electrons and holes bypassing the p-n junction recombine at etched surfaces where surface imperfection introduces many recombination centers. In an attempt to verify this, the structure shown in Figures 3.13a and 3.13b was used in the present work to separate the current around the sides of the sample from the total current. Log I-V plots for the surface recombination current and the junction current of a sample shown in Figure 3.14, however, indicate that the two diode factors are almost the same. Although the difference is noticeable, it is too small to attribute the excess current in the present cells to surface recombination.

Another critical factor affecting the determination of n is series resistance. The diode equation including the series resistance is

$$I = I_0 \left[e^{\frac{q(V - IR_s)}{nKT}} - 1 \right]. \quad (3.8)$$

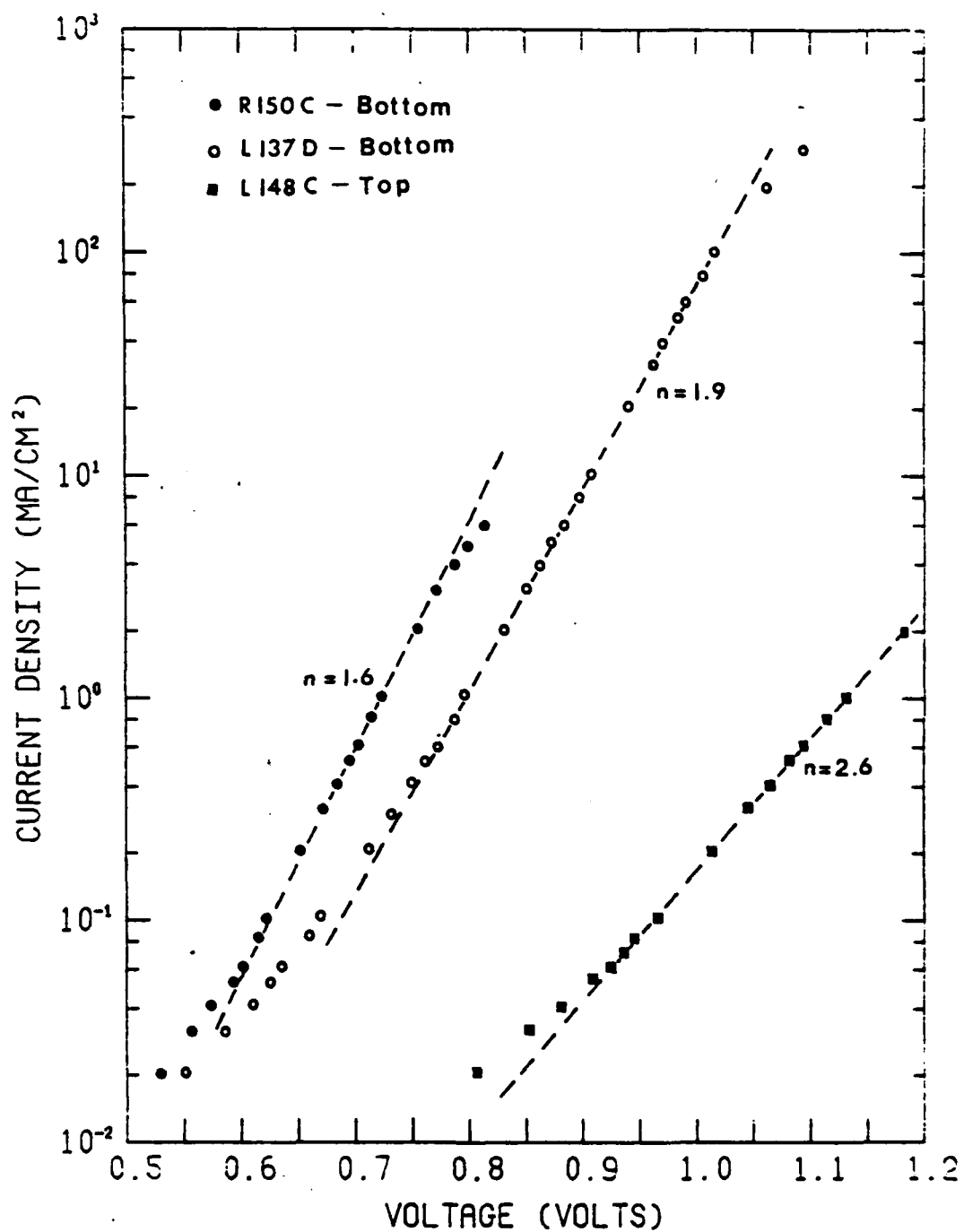


Figure 3.11(a) Dark I-V measurements of top and bottom cells.

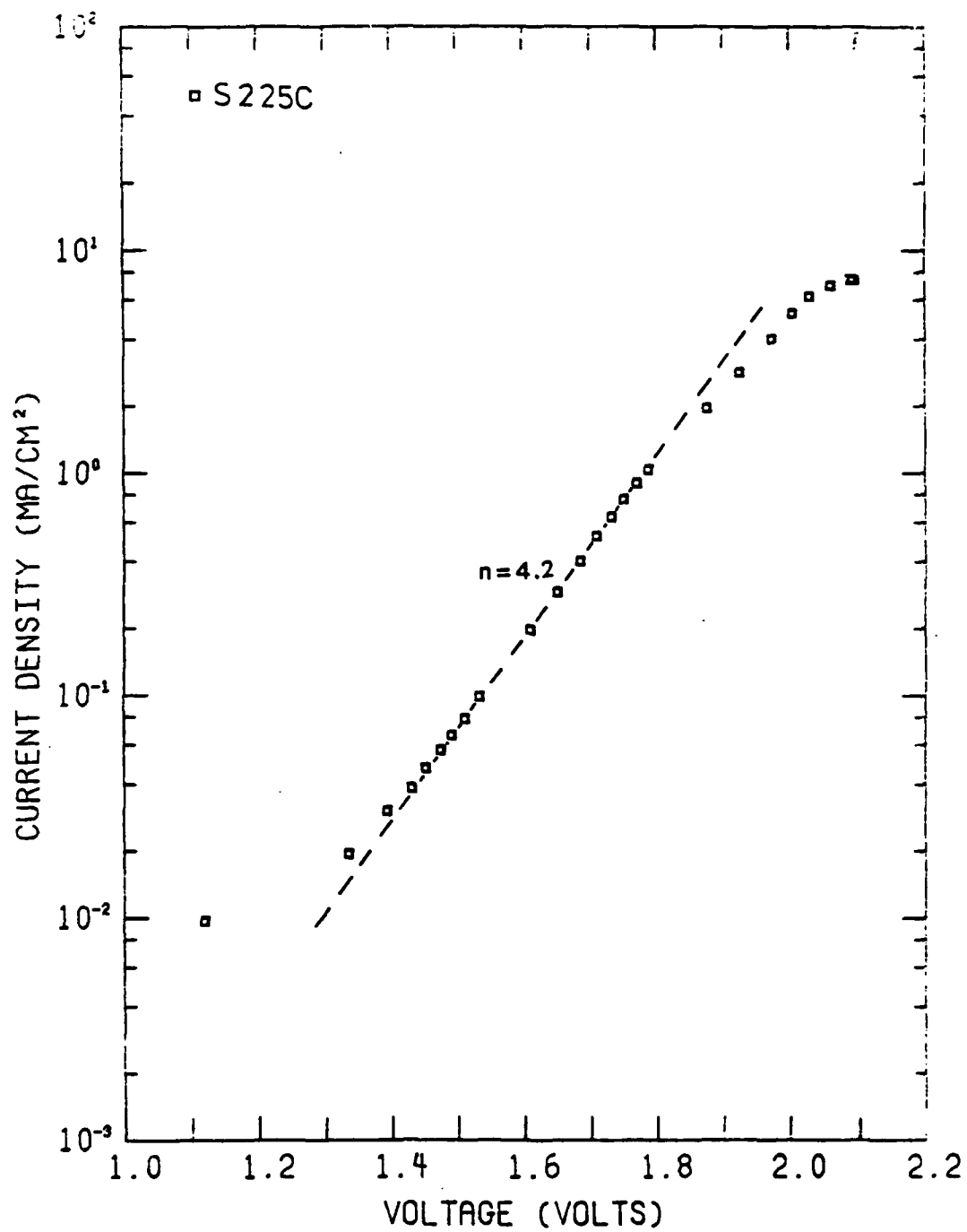


Figure 3.11(b) Dark I-V measurements of a cascade cell.

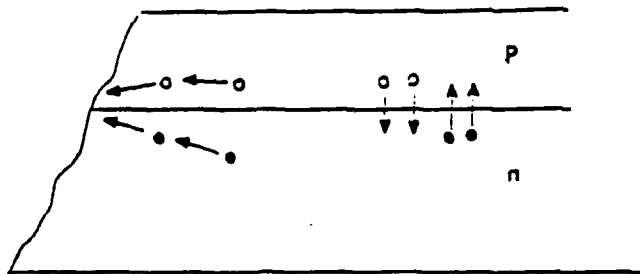


Figure 3.12 Model of minority carrier flow around the junction at the edge.

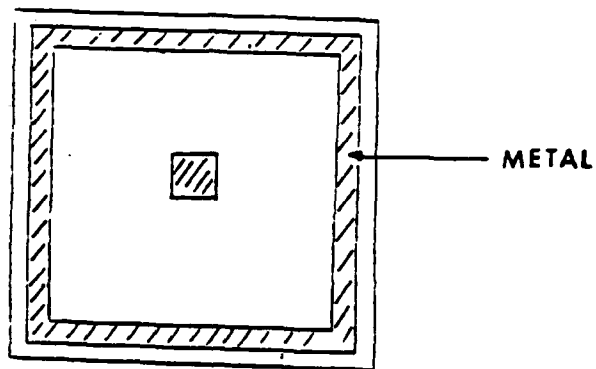


Figure 3.13(a) Contact pattern for the separation of the edge current from the total current.

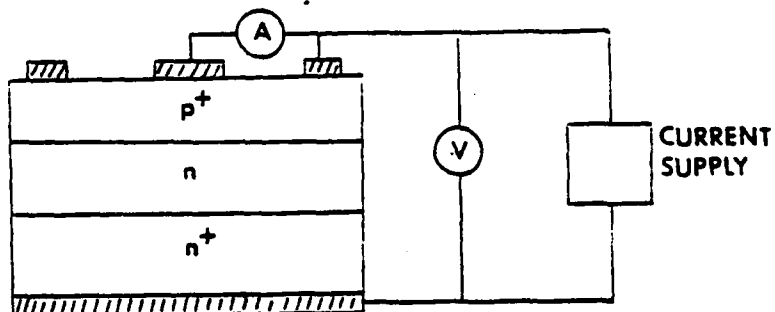


Figure 3.13(b) Schematic representation of the set-up for the separation of currents through the center and the circumference.

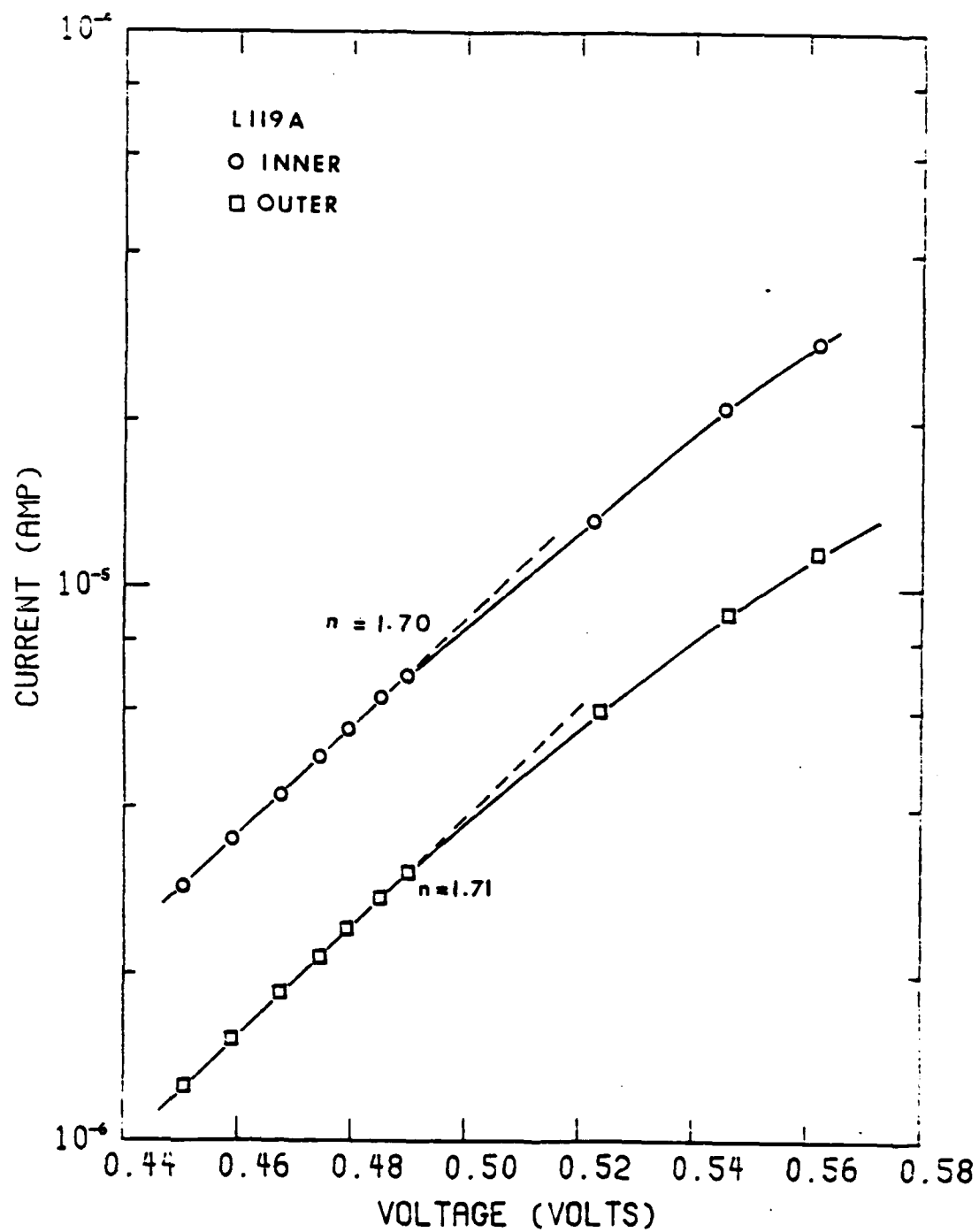


Figure 3.14 I-V measurements of inner and outer diodes.

If the resistance is too large to be neglected, it will influence the measurement of the n value. A log I - V plot will not resemble a straight line with a slope of q/nKT . A more sophisticated method, described as follows, has been used to eliminate the effect of series resistance.

The I - V relationship for the equivalent circuit of a solar cell with some finite series resistance is

$$I = I_o \left[e^{\frac{q(V - IR_s)}{nKT}} - 1 \right] - I_{sc}, \quad (3.9)$$

where I_{sc} is approximately equal to the short circuit current and is proportional to the light intensity. The expression for the open circuit voltage is obtained by setting the output current I in equation (3.9) equal to zero. Thus

$$I_{sc} = I_o \left[e^{\frac{qV_{oc}}{nKT}} - 1 \right]. \quad (3.10)$$

In this way, the term containing the series resistance, R_s , vanishes and a true value of n can be obtained by the log $I_{sc} - V_{oc}$ plots of equation (3.10) with varying light illumination. In comparison with Figures 3.11a and 3.11b, results in Figures 3.15a and 3.15b show some improvement in the measured diode factor. The major assumption made in utilizing equation (3.10) to determine n is the constancy of I_o under different illumination levels. This assumption can be justified by the coincidence of the higher voltage parts of the log $(I + I_{sc})$ vs V plots under various illumination levels as shown in Figure 3.16. This will be discussed in the next section. Another advantage of this method is in the determination of n in the diffusion dominated region (if any), since it measures the solar cell at the highest output voltage, where the effect of non-ideal recombination which dominates at low voltage should be limited.

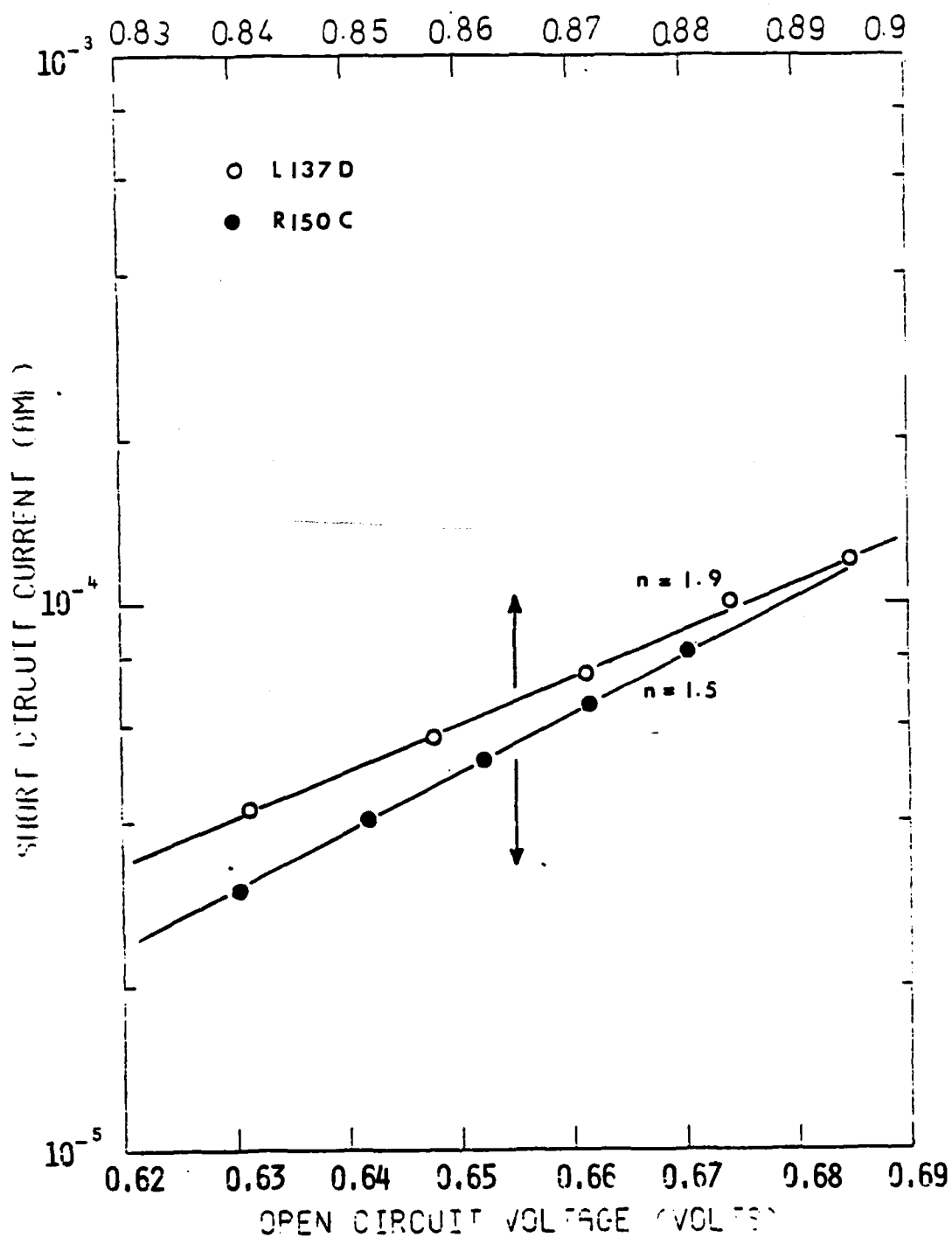


Figure 3.15(a) Short circuit current versus open circuit voltage for bottom cells.

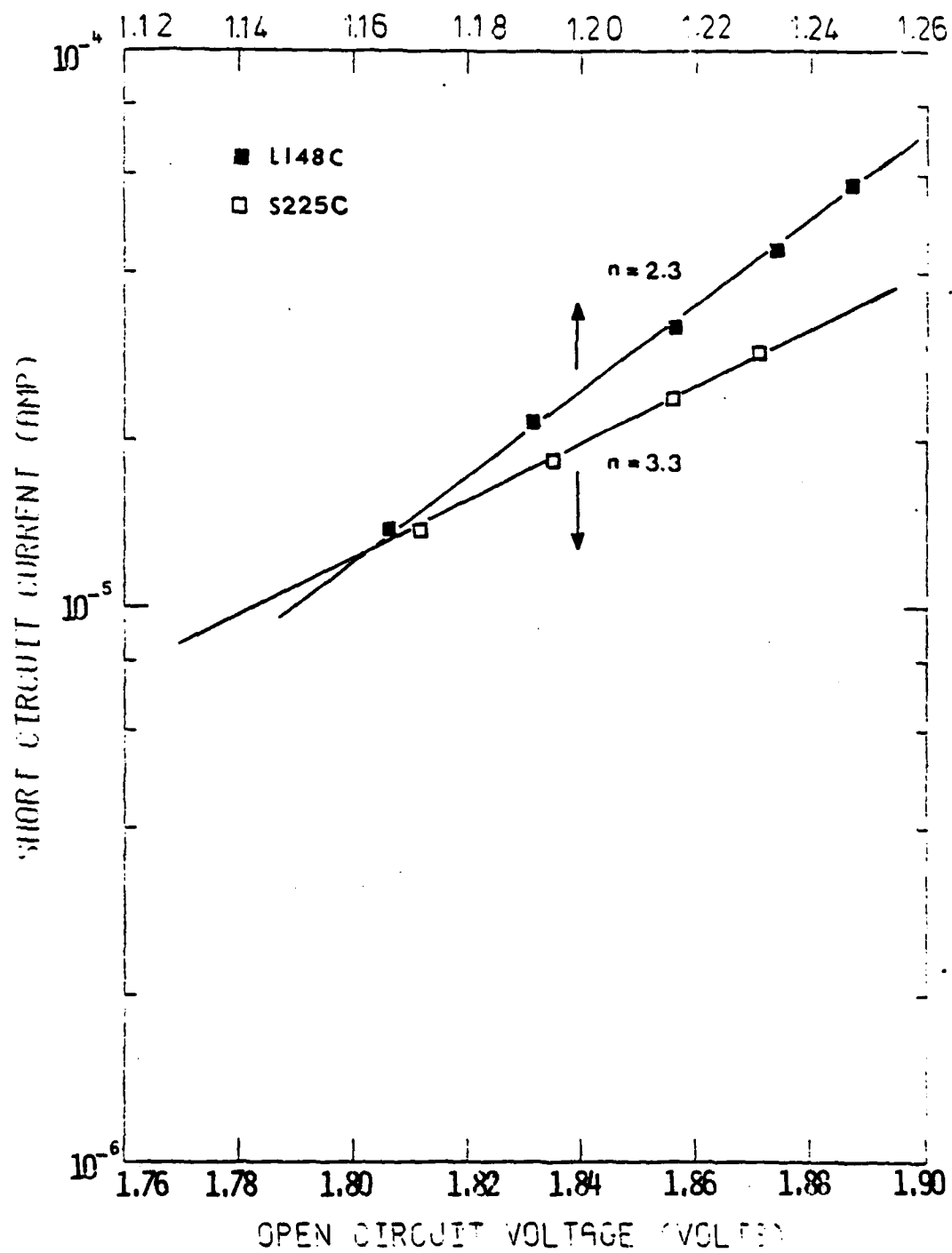


Figure 3.15(b) Short circuit current versus open circuit voltage for top and cascade cells.

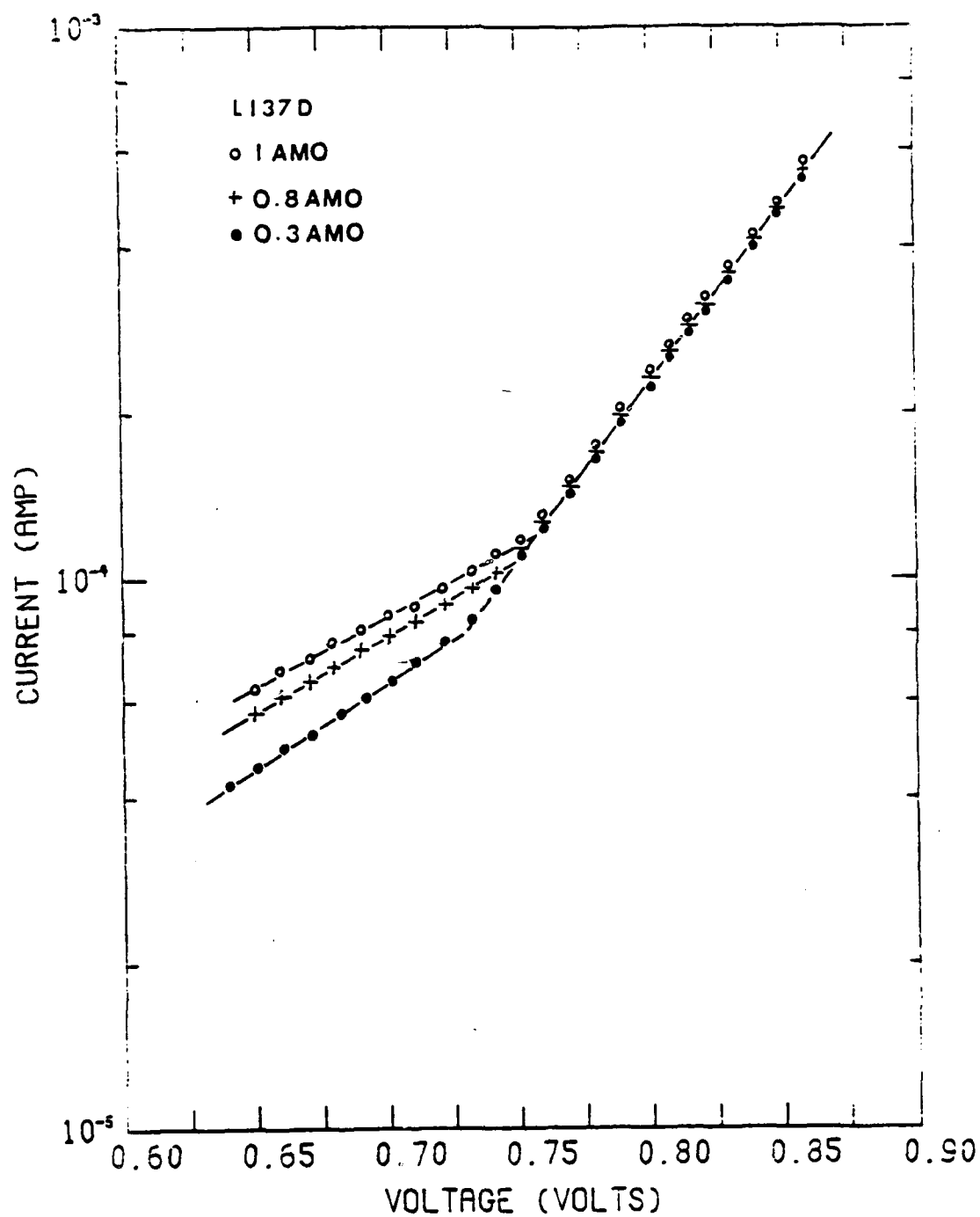


Figure 3.16 $\log (I + I_{sc})$ versus voltage plots for a bottom cell under various AMO illumination levels.

Diode factors of most cascade cells are within the range of 3 ~ 4. The origin of these values can be seen as follows:

$$V_{\text{Top}} = \frac{n_1 KT}{q} \ln \left(\frac{I}{I_{o1}} \right) \quad (3.11)$$

and

$$V_{\text{Bot}} = \frac{n_2 KT}{q} \ln \left(\frac{I}{I_{o2}} \right) . \quad (3.12)$$

Assuming $I_{o1} = I_{o2}$, the diode equation for the cascade structure can be expressed as

$$\begin{aligned} V &= V_1 + V_2 \\ &= \frac{KT}{q} (n_1 + n_2) \ln \left(\frac{I}{I_o} \right) . \end{aligned} \quad (3.13)$$

Therefore, the diode factor, $n_1 + n_2$, will be between 3 and 4 since n_1 and n_2 are between 1.5 and 2.

In order to further examine the mechanism determining the diode factor, studies were also performed on the effect of the light on the value of n . Figure 3.16 shows a family of I-V characteristics after subtraction of the short circuit current. Values of n can be obtained from equation (3.14),

$$I + I_{sc} = I_o \left(e^{\frac{qV}{nKT}} - 1 \right) . \quad (3.14)$$

The n -values remain approximately constant for all illumination conditions in the high voltage region. The observed differences at low voltage can

be understood from equation (3.9), incorporating the series resistance into the ideal diode equation, shown again below for convenience,

$$I + I_{sc} = I_o \left[e^{\frac{q(v-IR_s)}{nKT}} - 1 \right]. \quad (3.9)$$

The effect of R_s is maximum in the region near the short circuit current which corresponds to the lower voltage region in the $\log(I + I_{sc}) - V$ plots. On the contrary, R_s has no effect at the open circuit voltage, where the current I is zero. The opposite effects of the series resistance in the dark and the light can be seen in Figure 3.17.

3.2.2.2 Reverse Saturation Current

Figures 3.18a, 3.18b, and 3.18 c show I-V characteristics in the current region where solar cells normally operate. The measured saturation currents I_o 's are about 1 ~ 2 orders of magnitude larger than the calculated values. The variation of saturation current I_o calculated as a function of the carrier lifetime is shown in Figure 3.18a. The current in a p-n junction has usually been described by the sum of the diffusion current and the recombination current,

$$I = I_1(e^{qV/KT} - 1) + I_2(e^{qV/2KT} - 1), \quad (3.15)$$

where I_1 , I_2 are the diffusion component and the recombination component (respectively) of the reverse saturation current and are given by [3.6]

$$I_1 = qn_1^2 \left(\frac{1}{N_D} \sqrt{\frac{D_p}{\tau_p}} + \frac{1}{N_A} \sqrt{\frac{D_n}{\tau_n}} \right) \quad (3.16)$$

and
$$I_2 = \frac{qn_1 w}{\tau_{po} + \tau_{no}} \quad (3.17)$$

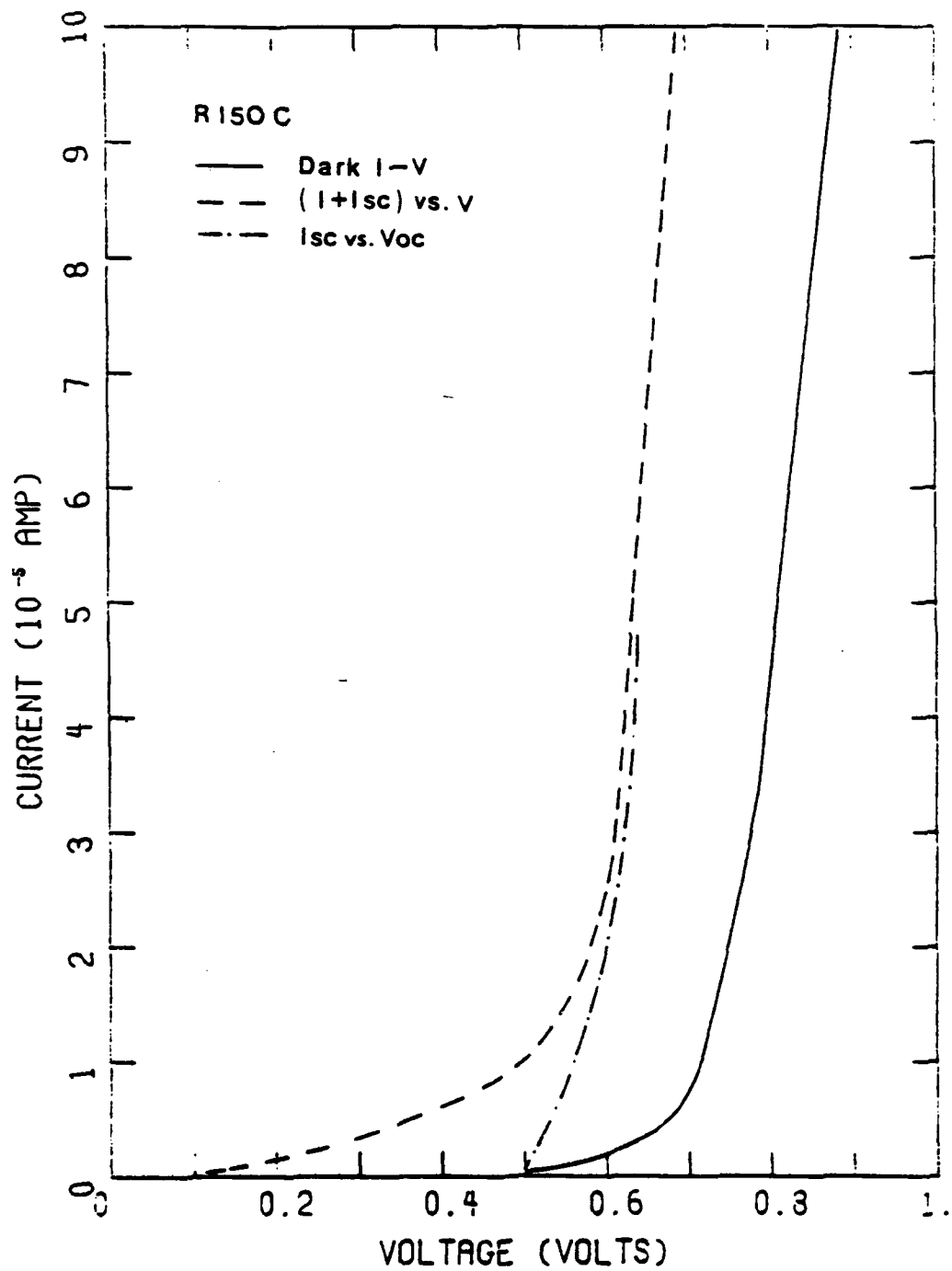


Figure 3.17 Comparison of I-V measurements using various approaches.

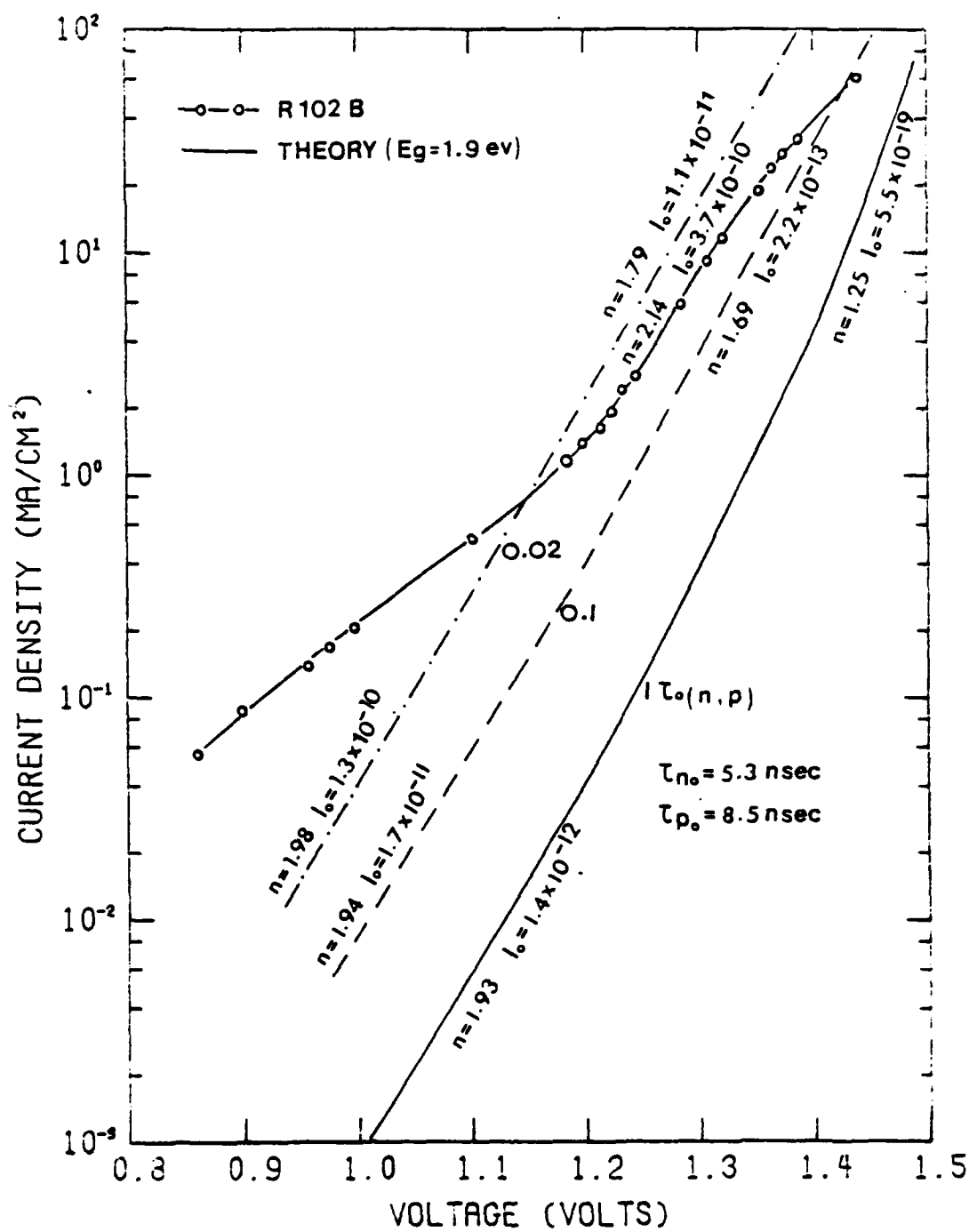


Figure 3.18(a) Dark I-V characteristics of the top cell as a function of the minority carrier lifetimes.

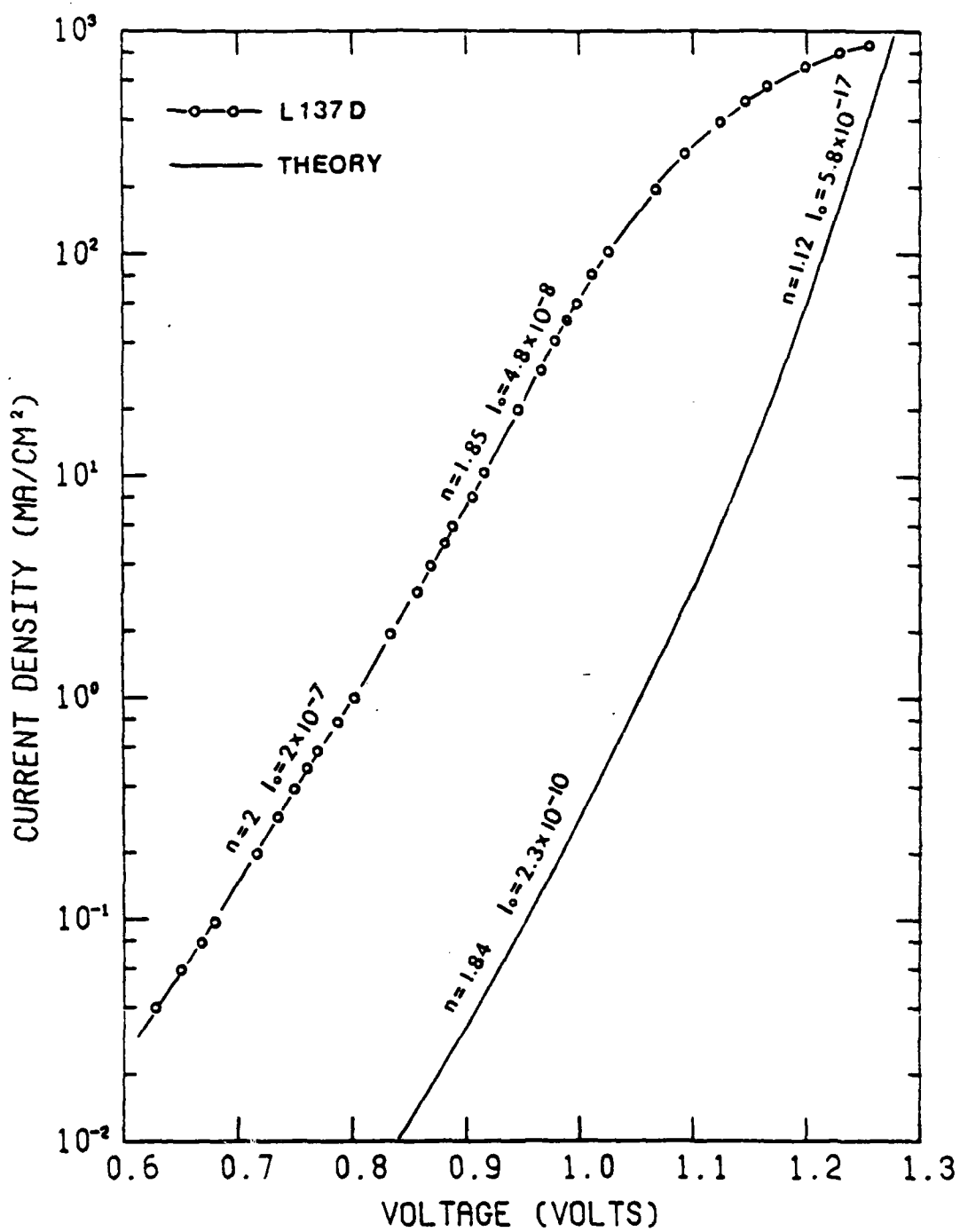


Figure 3.18(b) Comparison between the calculated and measured reverse saturation currents of the bottom cell.

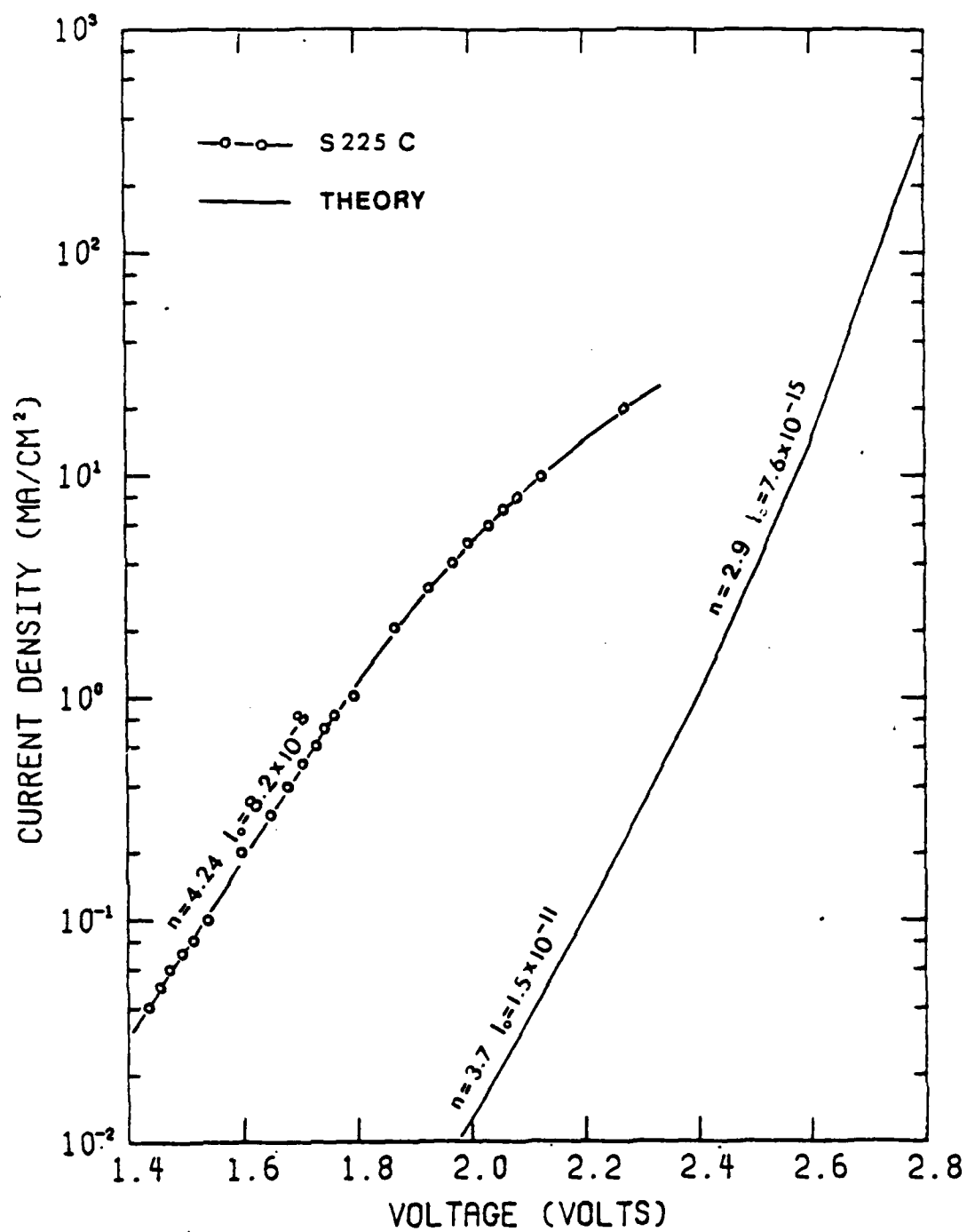


Figure 3.18(c) Comparison between the calculated and measured reverse saturation currents of the cascade cell.

The ratio I_1 to I_2 indicates that the relative significance of these current mechanisms is proportional to the intrinsic carrier concentration n_i as

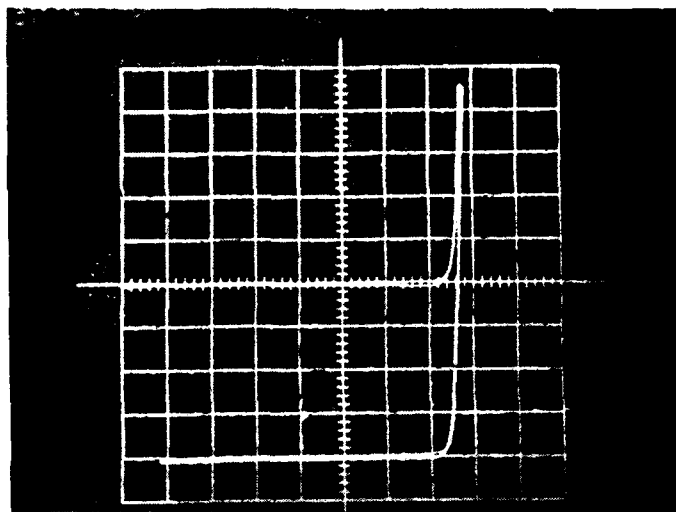
$$\frac{I_1}{I_2} = \frac{n_i \left(\frac{1}{N_D} \sqrt{\frac{D_p}{\tau_p}} + \frac{1}{N_A} \sqrt{\frac{D_n}{\tau_n}} \right) (\tau_{po} + \tau_{no})}{W} \quad (3.18)$$

Equation (3.18) indicates that the current recombination mechanism in the depletion region tends to dominate over a major portion of the I-V characteristics for high bandgap material, since n_i decreases exponentially with increasing bandgap.

3.2.3 Current-Voltage Characteristics Under Illumination

3.2.3.1 Introduction

I-V data have been taken for numerous cells under AMO illumination. Results presented here refer to cells without antireflection coatings. Figures 3.19a, 3.19b, and 3.19c illustrate some results of the better cells. Calculated results are shown in Figures 3.20a through 3.20h for comparison with the experimental data. Calculated dependence of the efficiency of cascade cells on the bandgap of the top cell is shown in Figure 3.21. Open circuit voltages, short circuit currents, fill factors and efficiencies will be examined in the following sections.



Sample No. L162C

Scale

Ver. 0.1 mA/div

Hor. 0.5 V/div

Illumination: 1 AMO

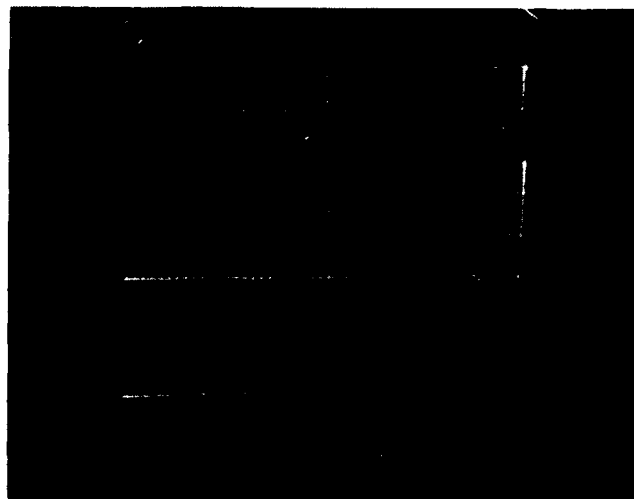
$V_{oc} = 1.31 \text{ V}$

$I_{sc} = 13.6 \text{ mA/cm}^2$

FF = 0.83

$\eta = 10.9\%$

Figure 3.19(a). I-V measurements of a top cell under AMO illumination.



Sample No. L137D

Scale

Ver. 0.5 mA/div

Hor. 0.2 V/div

Illumination: 1 AMO

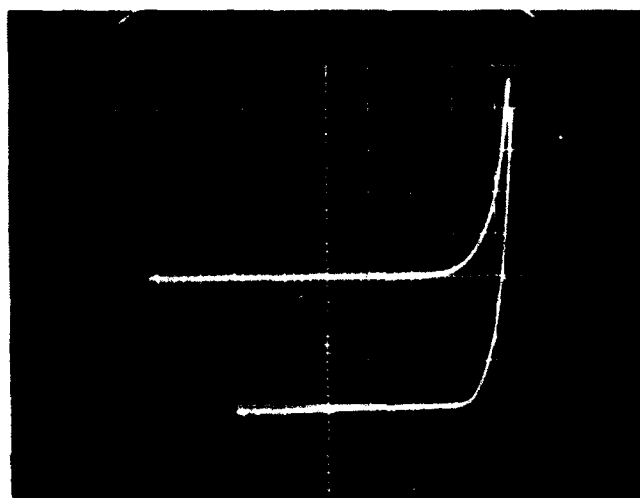
$V_{oc} = 0.88 \text{ V}$

$I_{sc} = 18.6 \text{ mA/cm}^2$

FF = 0.76

$\eta = 9.2\%$

Figure 3.19(b). I-V measurements of a bottom cell under AMO illumination.



Sample No. G239C

Scale

Ver. 0.02 mA/div

Hor. 0.5 V/div

Illumination: 1 AMO

$V_{oc} = 2.17 \text{ V}$

$I_{sc} = 12.3 \text{ mA/cm}^2$

FF = 0.75

$\eta = 14.8\%$

Figure 3.19(c). I-V measurements of a cascade cell under AMO illumination.

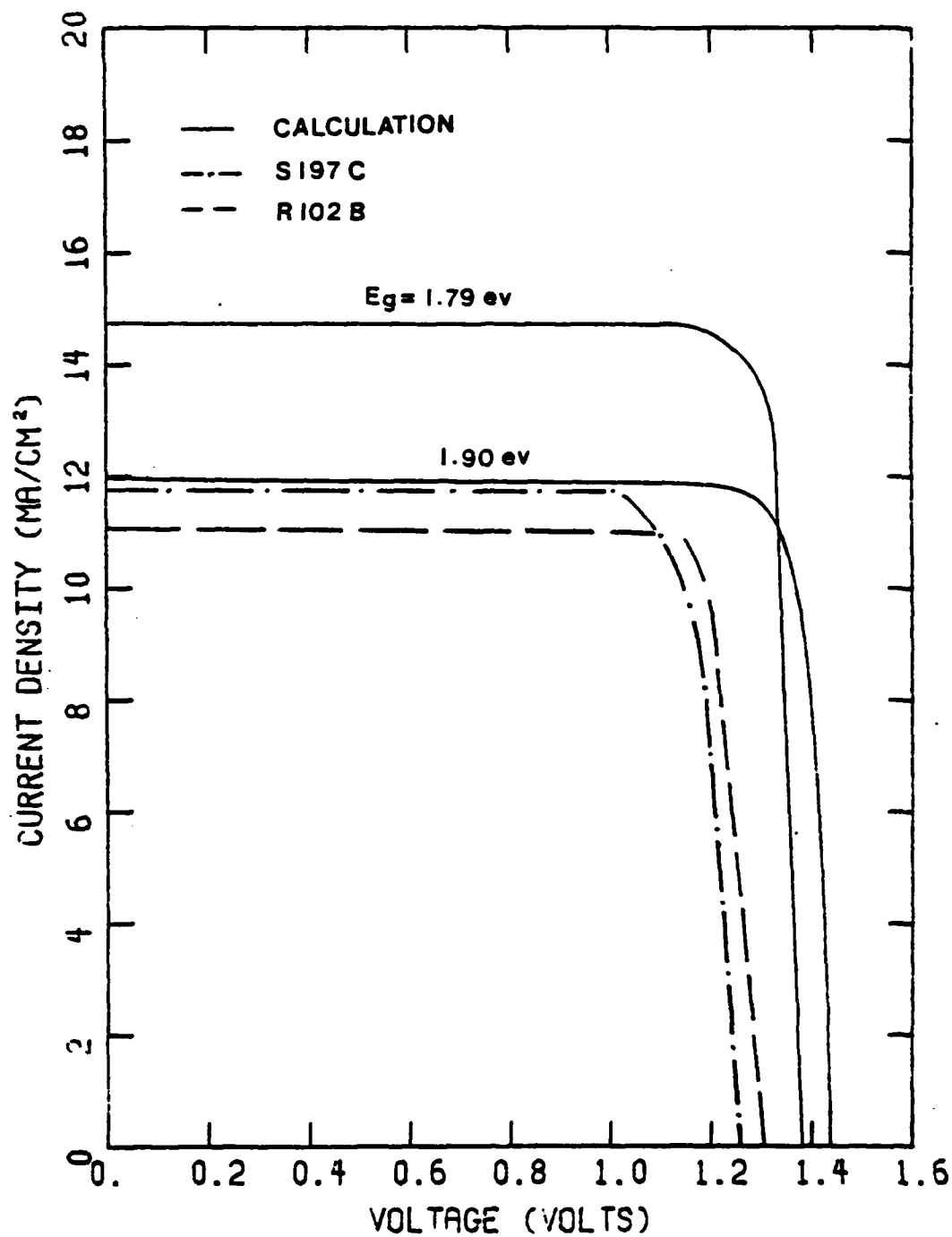


Figure 3.20(a) I-V characteristics of the top cell under AMO illumination.

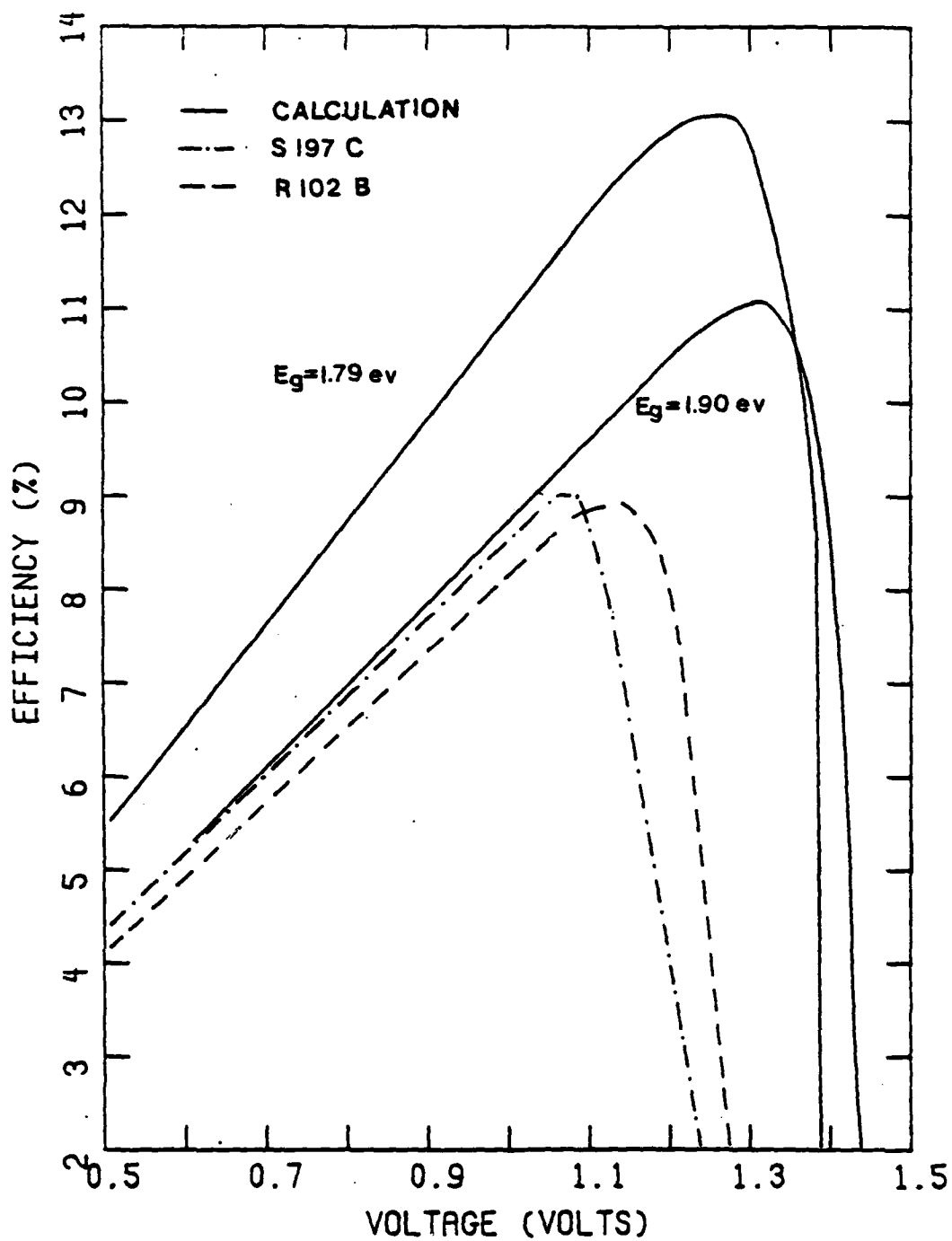


Figure 3.20(b) Dependence of efficiency on the terminal voltage for the top cell.

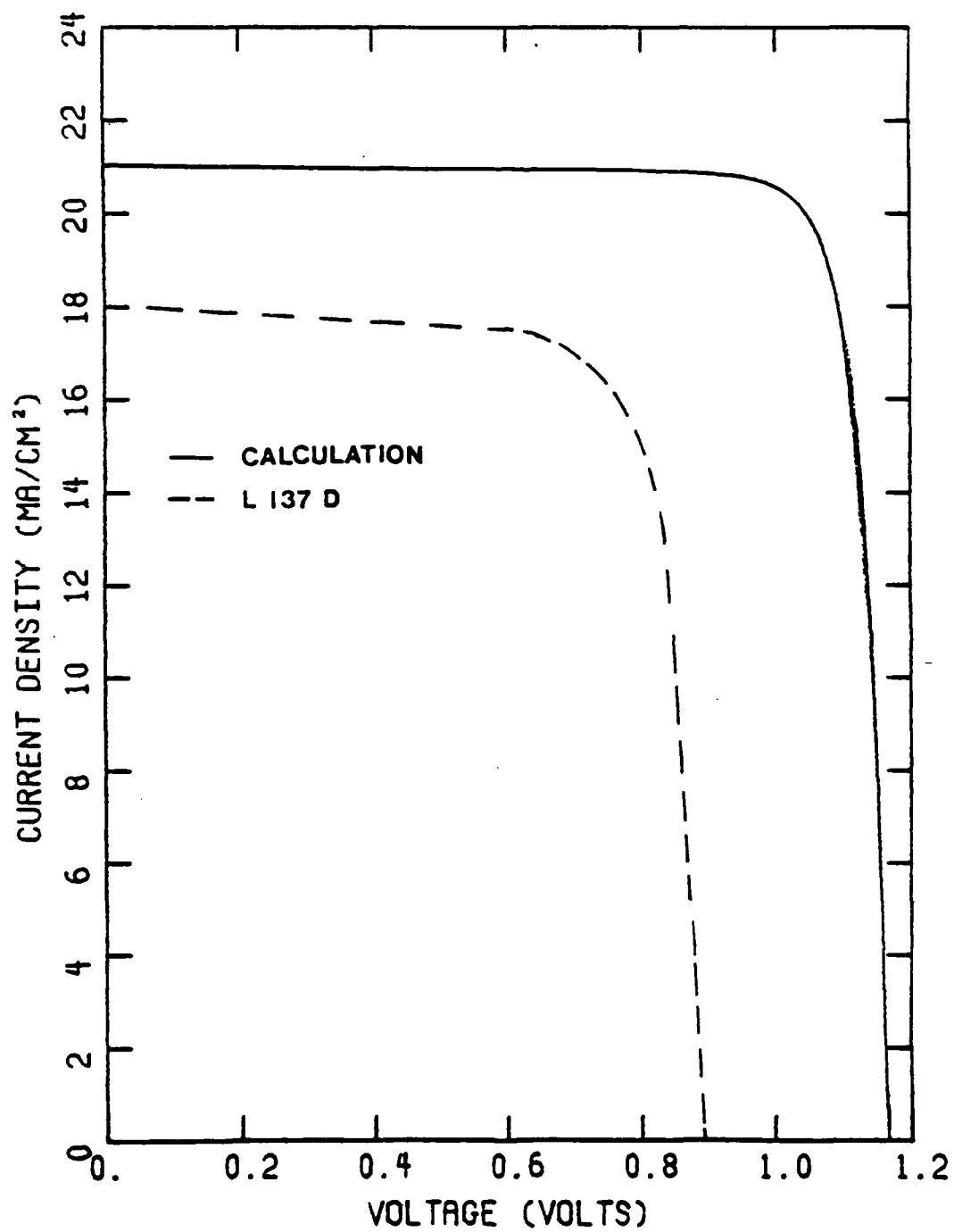


Figure 3.20(c) I-V characteristics of the bottom cell under AMO illumination.

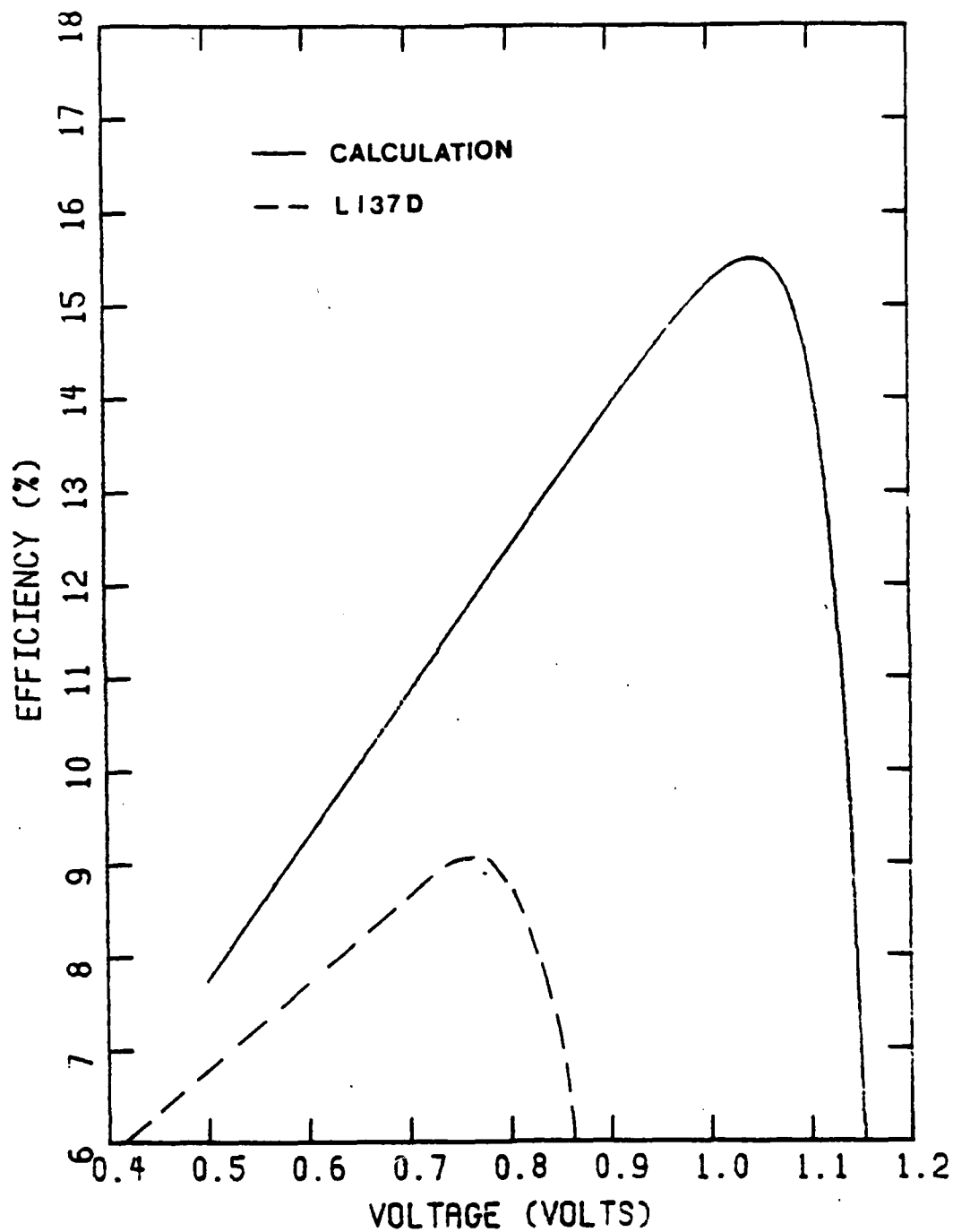


Figure 3.20(d) Dependence of efficiency on the terminal voltage for the bottom cell.

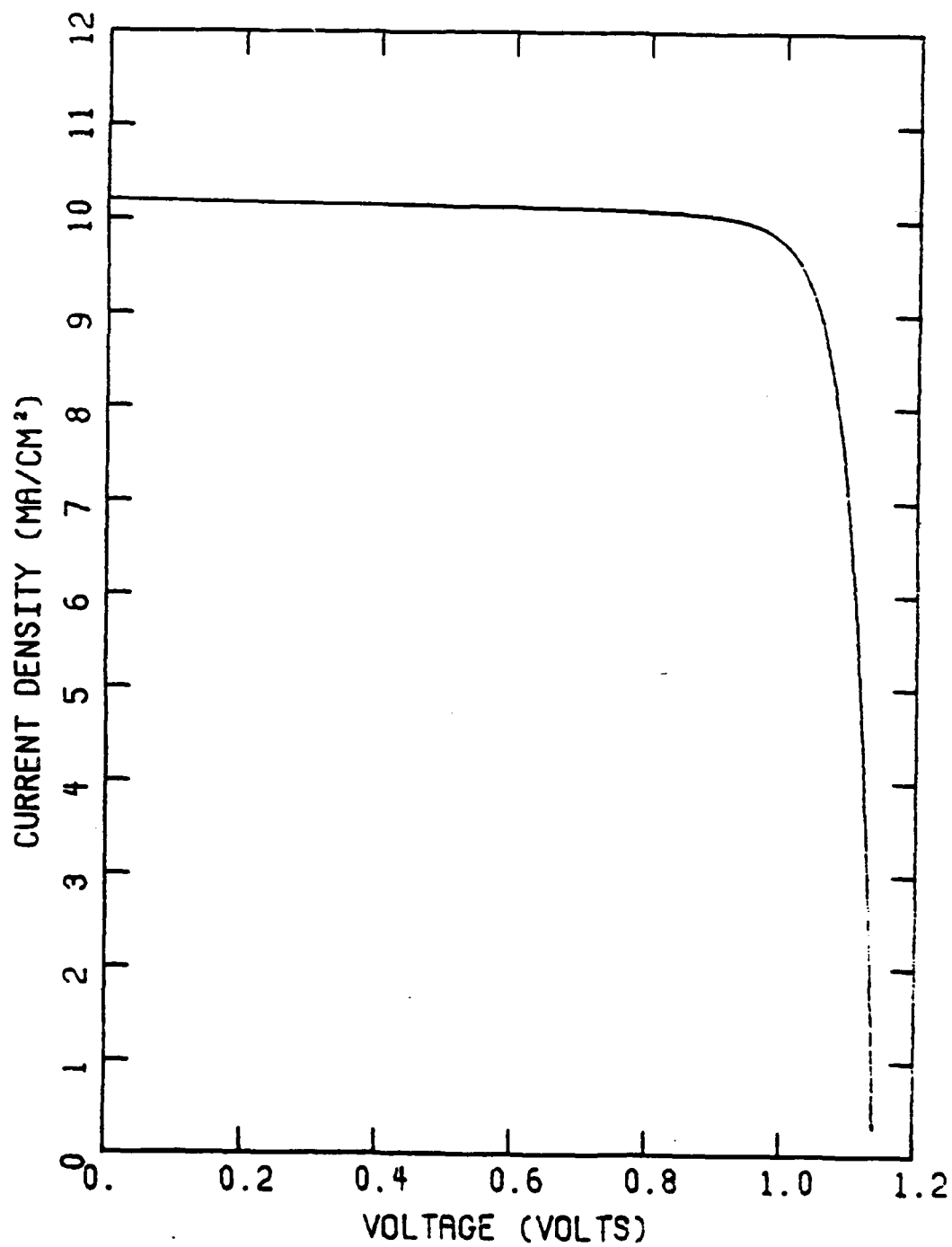


Figure 3.20(e) I-V characteristics of the bottom cell with a top cell under AMO illumination.

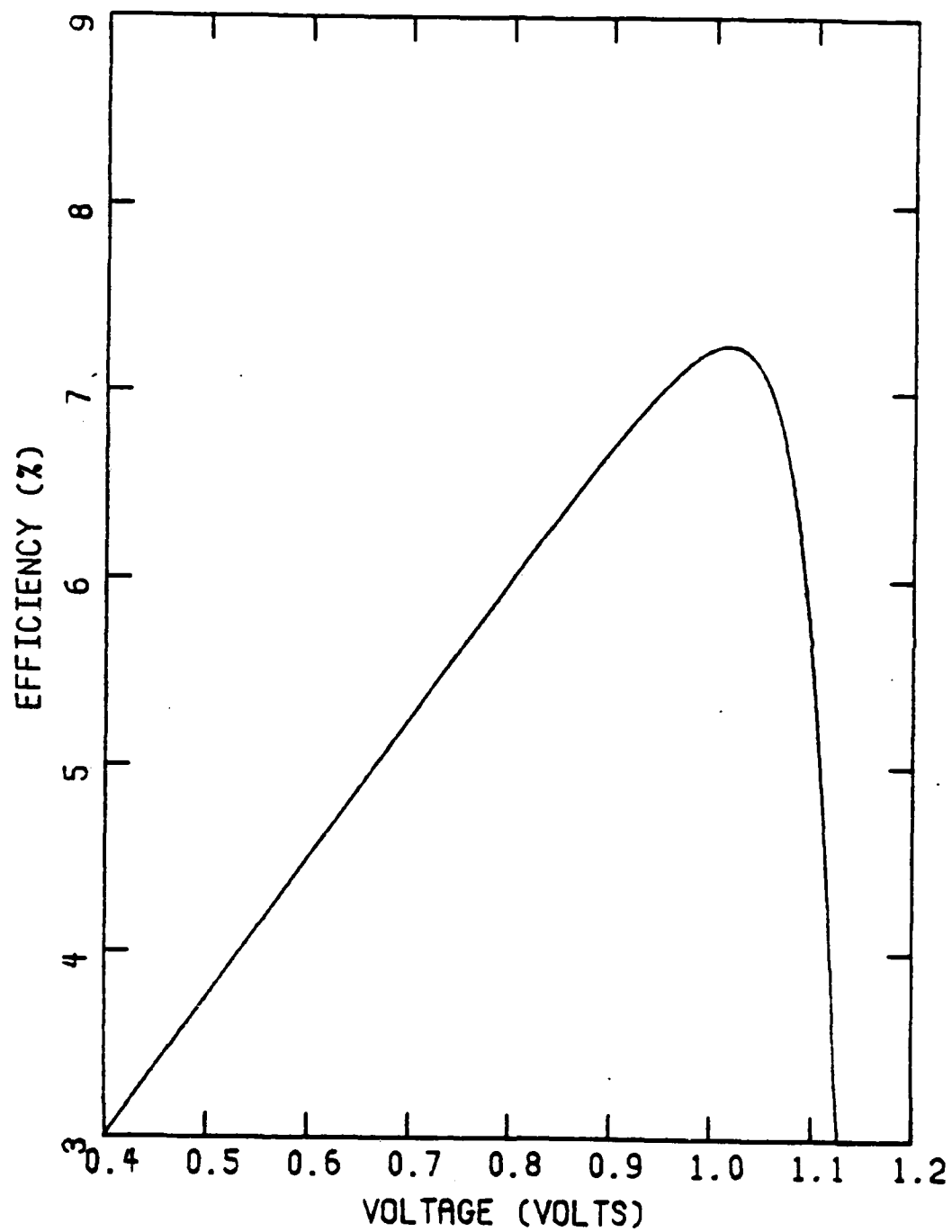


Figure 3.20(f) Dependence of efficiency on the terminal voltage for the bottom cell with a top cell.

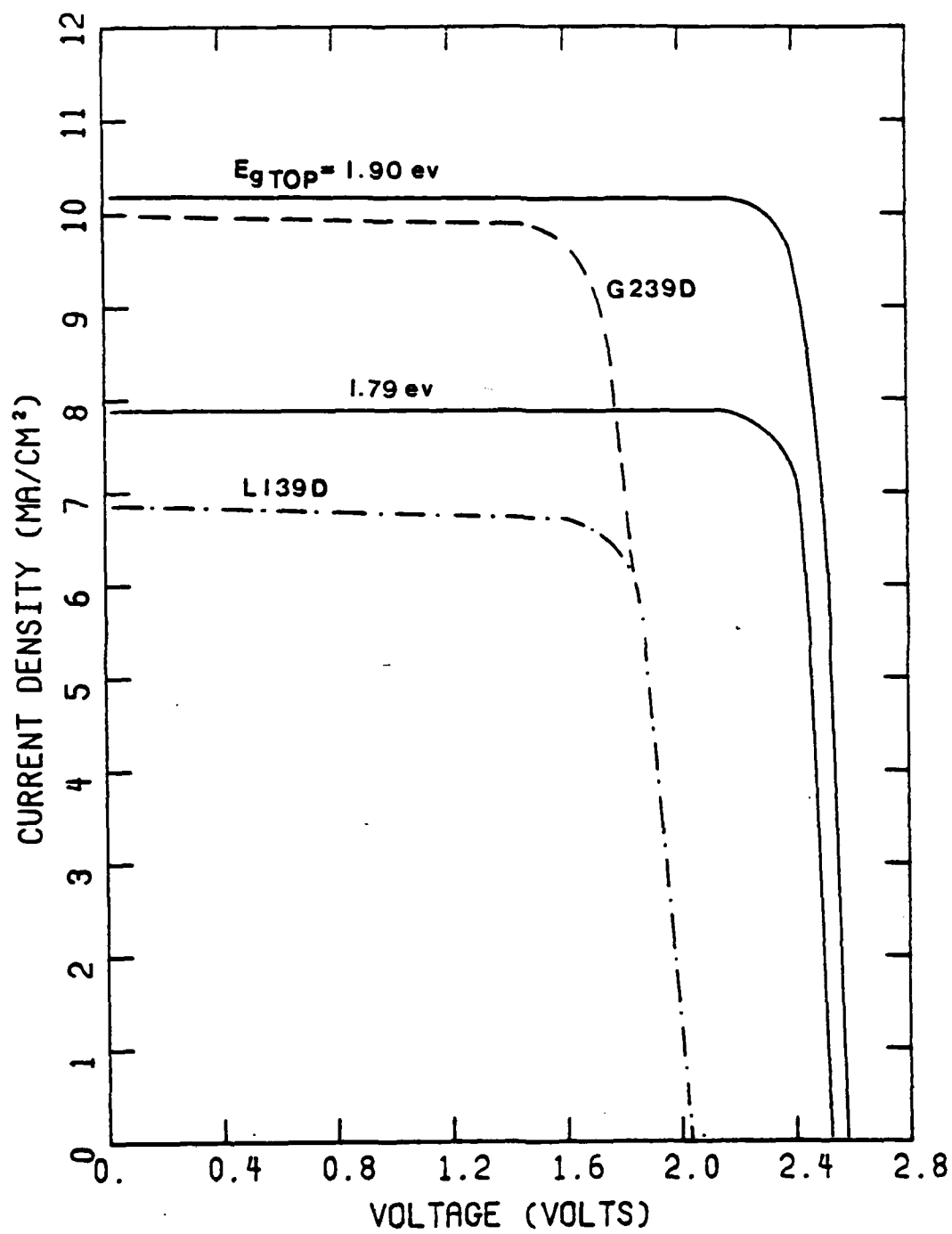


Figure 3.20(g) I-V characteristics of the cascade cell under AMO illumination.

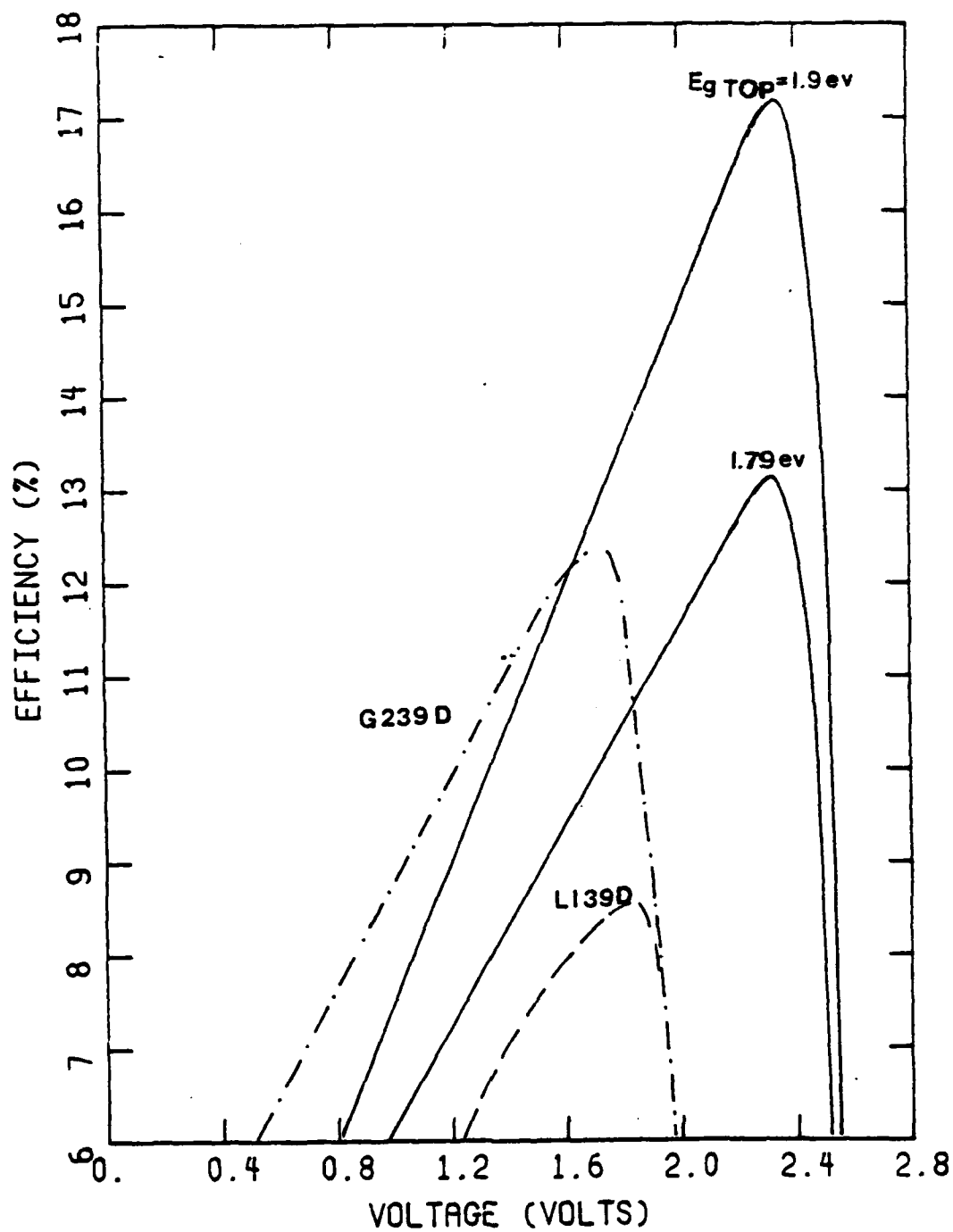


Figure 3.20(h) Dependence of efficiency on the terminal voltage for the cascade cell.

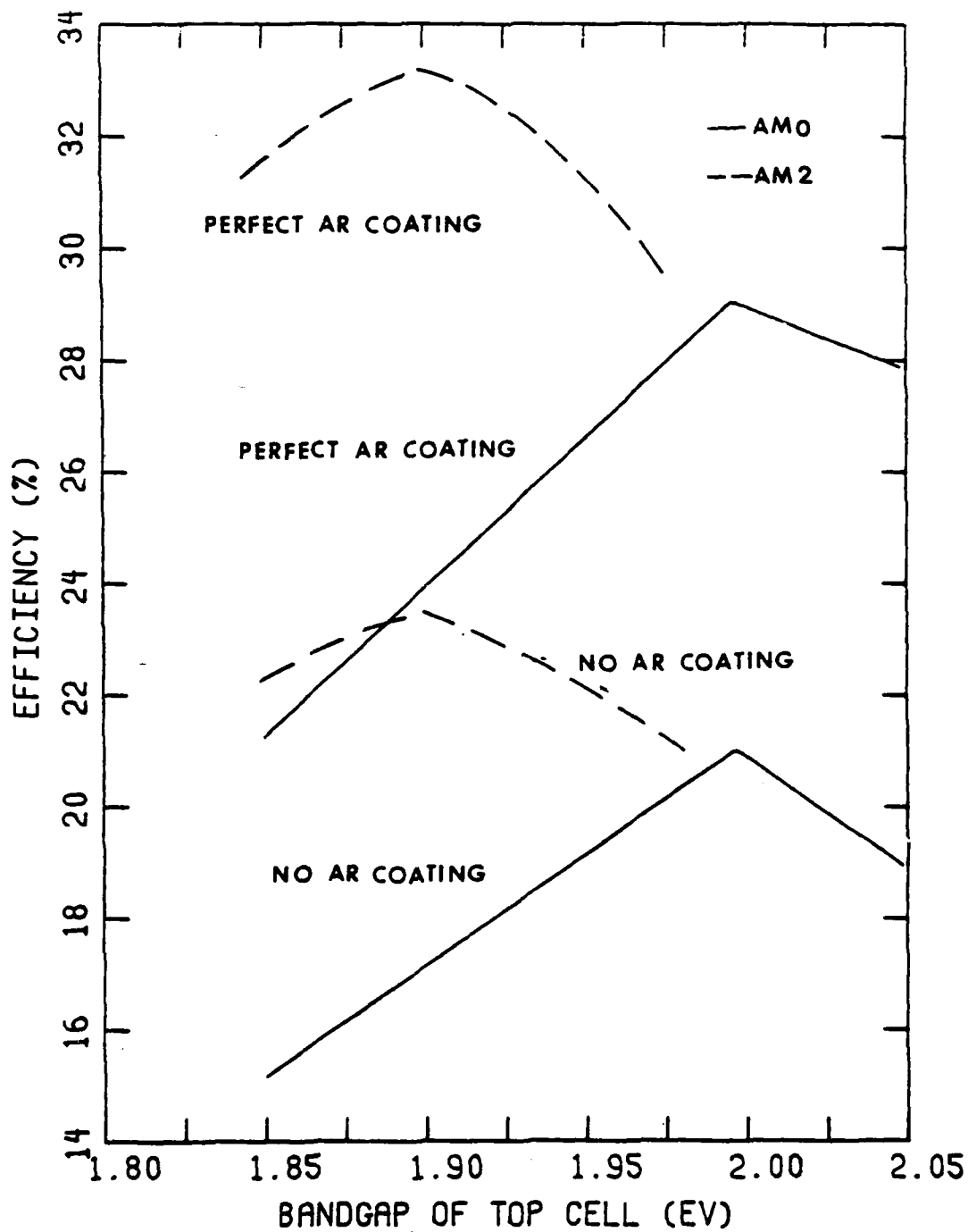


Figure 3.21 Dependence of efficiency on the bandgap of the top cell in a cascade structure.

3.2.3.2 Open Circuit Voltage

The disagreement between calculated and measured open circuit voltage is due to the high dark current resulting from small minority carrier lifetimes. The discrepancy can be quantitatively described by Equation (3.19),

$$V_{oc} = \frac{nKT}{q} \ln \left(\frac{I_{sc}}{I_o} \right) . \quad (3.19)$$

The saturation currents I_o 's, which are 1 to 2 orders of magnitude higher than the theoretical values (as discussed in Section 3.2.2.2) will reduce the open circuit voltages of single-junction cells by 0.12 - 0.24 volts according to Equation (3.19). The reduction of short circuit current I_{sc} ($\sim 15\%$) will further lower V_{oc} by about 8.4 millivolts. The combined effects of short circuit current and saturation current result in an open circuit voltage deviation ΔV_{oc} of 0.13 - 0.25 volt for top cells and bottom cells. For the cascade cell ΔV_{oc} will be 0.26 - 0.50 volt since the diode factor n is approximately twice as much as that of a single-junction cell. The high saturation currents that reduce the V_{oc} values for these cascade cells are due to the degraded quality of the epitaxial layers. As discussed in Section 2, this is primarily due to the degenerately doped AlGaAs tunnel junction layers.

3.2.3.3 Short Circuit Current

The measured short circuit currents varied over a wide range. A number of factors affect the value of I_{sc} such as the bandgap, the diffusion length and the lifetime of the minority carrier, the thickness of the window layer, the junction depth and the series resistance.

The theoretical dependence of the short circuit current of the cascade cell on the bandgap of the top cell is shown in Figure 3.22. In Figure 3.23 current mismatch between the top cell and the bottom cell due to insufficient carrier collection or unoptimized bandgaps leads to a lower cascade cell short circuit current. A better match obtained by adjusting bandgaps can be seen in Figure 3.24. Carrier generation rate profiles are shown in Figures 3.25a through 3.25d. The effect of the window layer can be seen in separating the region of maximum carrier generation from region of high recombination velocity at the surface.

The spectral current distribution over various regions in a cascade solar cell is shown in Figure 3.26 as a function of the thickness of the window layer. While the window layer and the top cell are competing for high energy photons, the current of the bottom cell is virtually constant. The fact that the bottom cell consists of a GaAs layer grown on a high quality GaAs substrate and has lessened sensitivity to the thickness of the epitaxial layers, suggests that the top cell governs the measured short circuit current of these cascade cells. Since the performance of the cascade cell is directly associated with that of the top cell, it is necessary to more closely examine the top cell.

Optimization of the p-n junction depth of the top cell for short circuit current is shown in Figure 3.27. This adequately describes general trends of the effect of device geometry on short circuit current for top cells with several bandgaps. For cells with the same bandgaps (e.g., 1.97 eV) and different window thickness, the optimum placement of the p-n junction is almost the same (0.4 - 0.5 μm). A slight drop in the current for shallower junctions is caused by insufficient collection

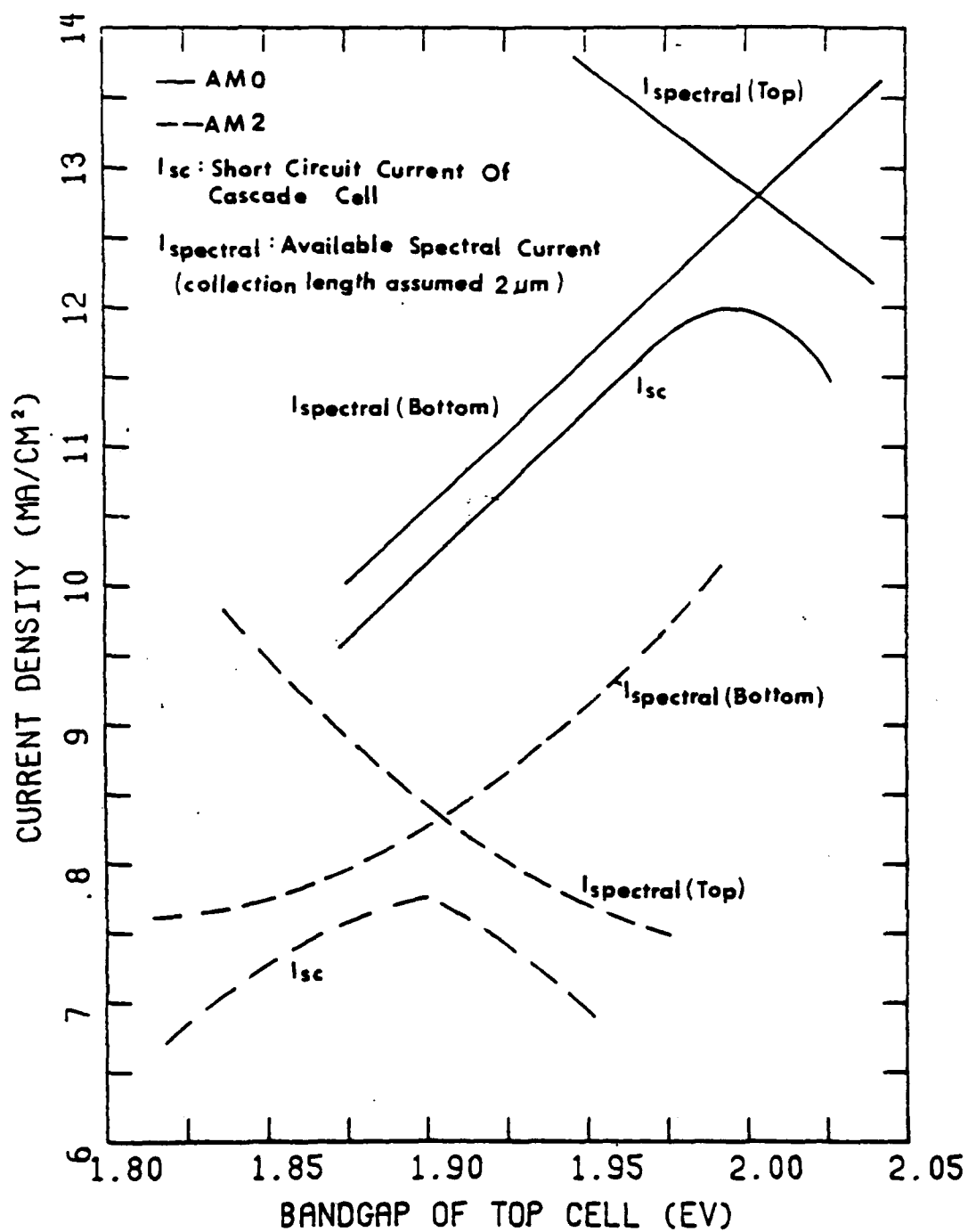


Figure 3.22 Dependence of short circuit current on the bandgap of the top cell in a cascade structure.

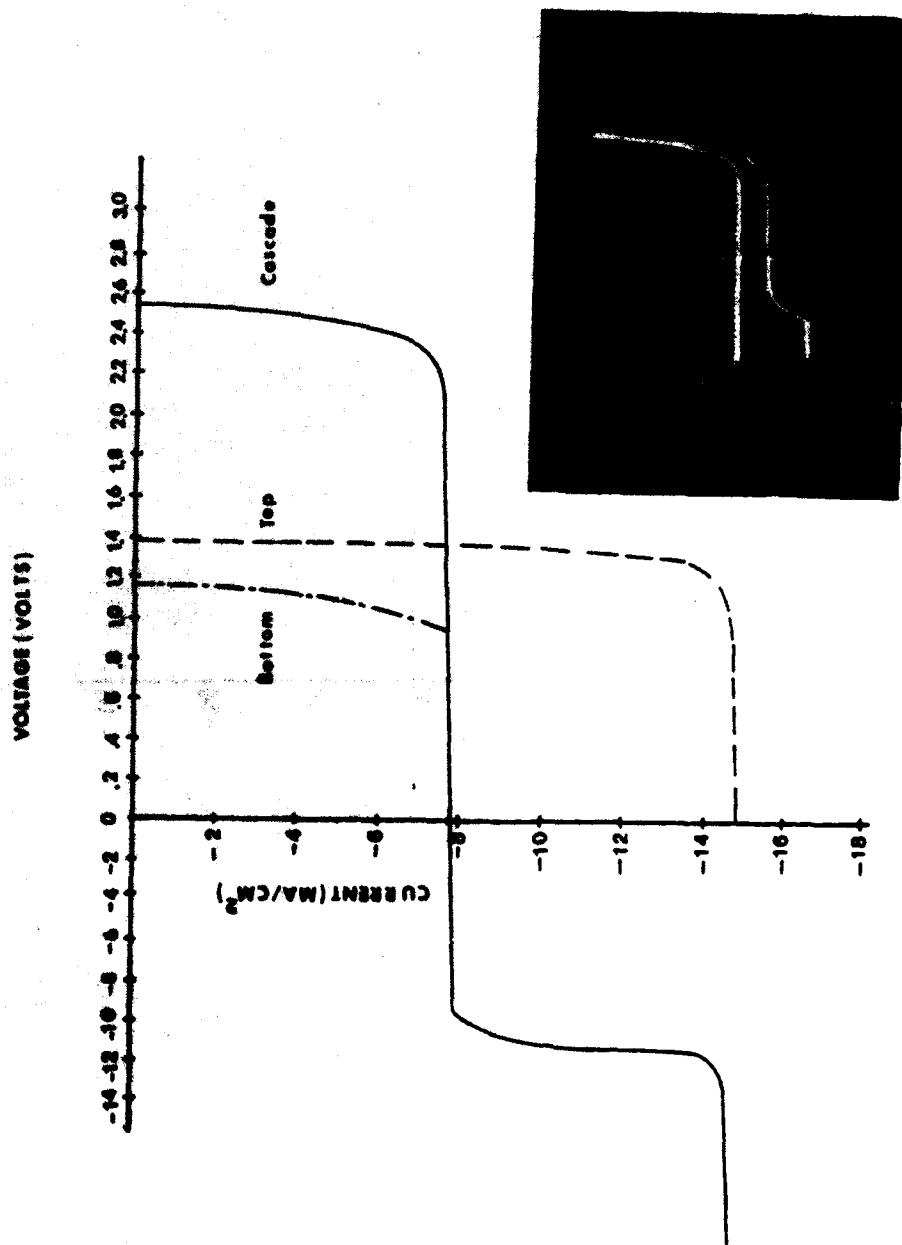


Figure 3.23. I-V characteristics of a cascade cell showing the current mismatch between the top cell and the bottom cell.

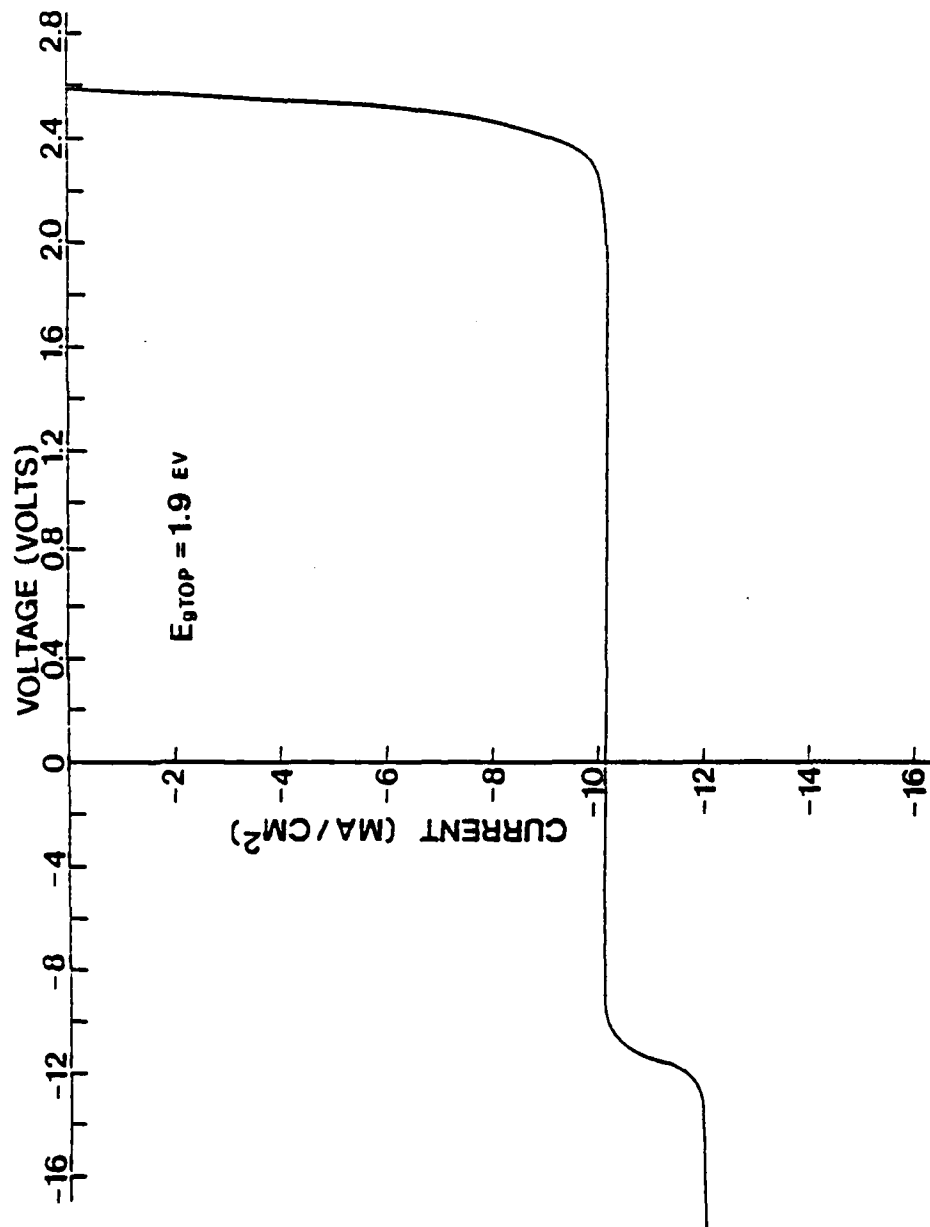


Figure 3.24 I-V characteristics of a cascade cell with an improved current matching between the top cell and the bottom cell.

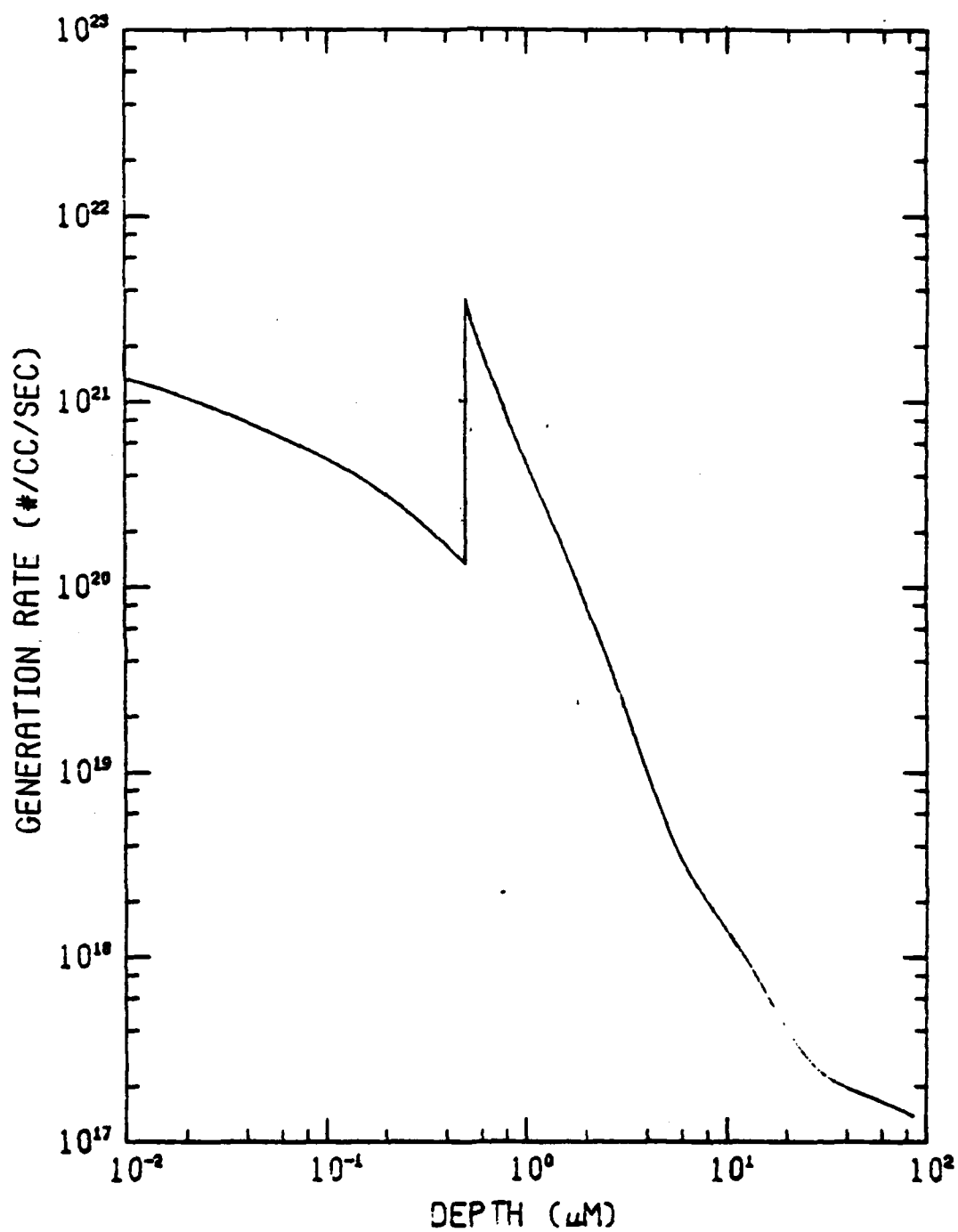


Figure 3.25(a) Carrier generation rate profile of the top cell.

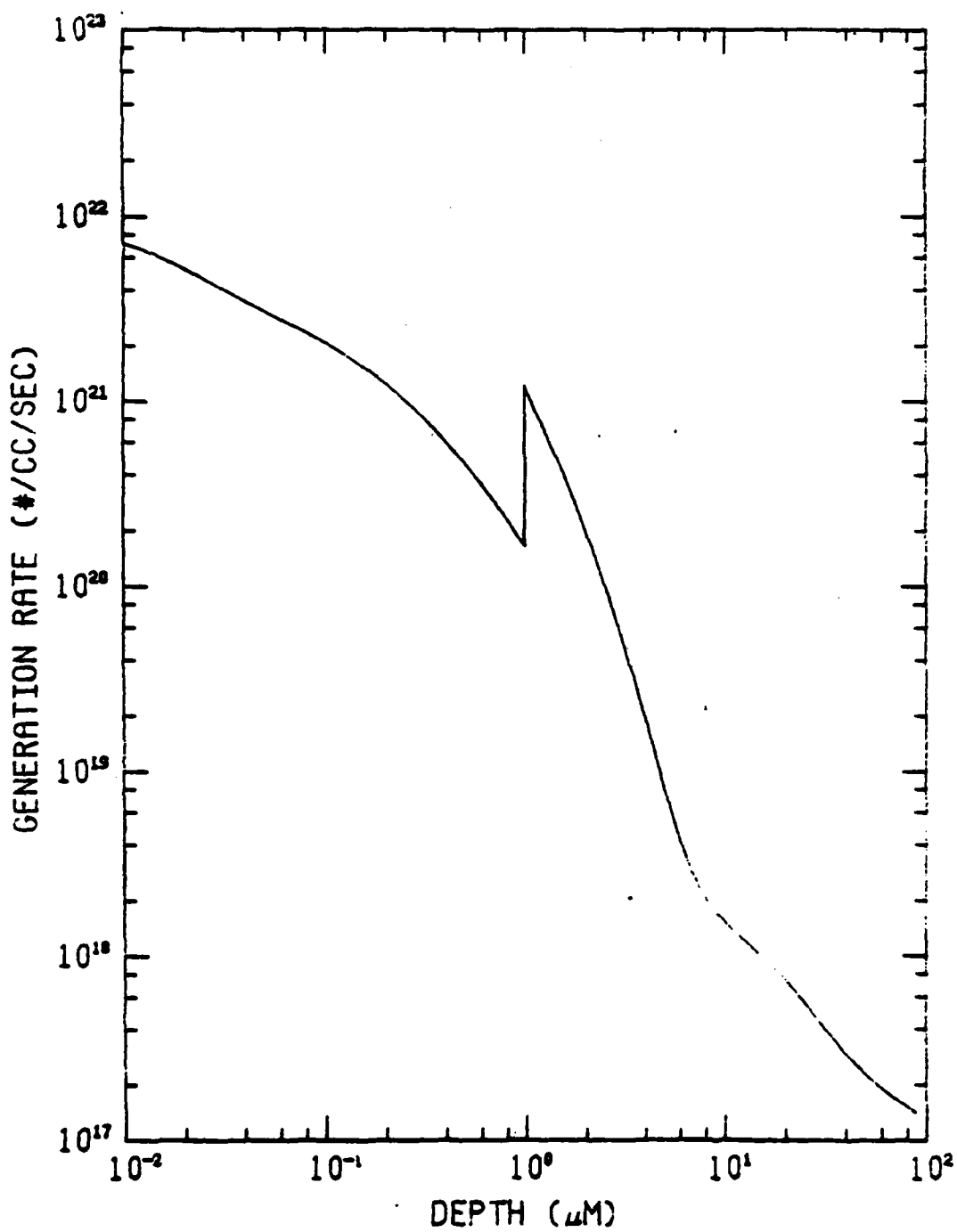


Figure 3.25(b) Carrier generation rate profile of the bottom cell.

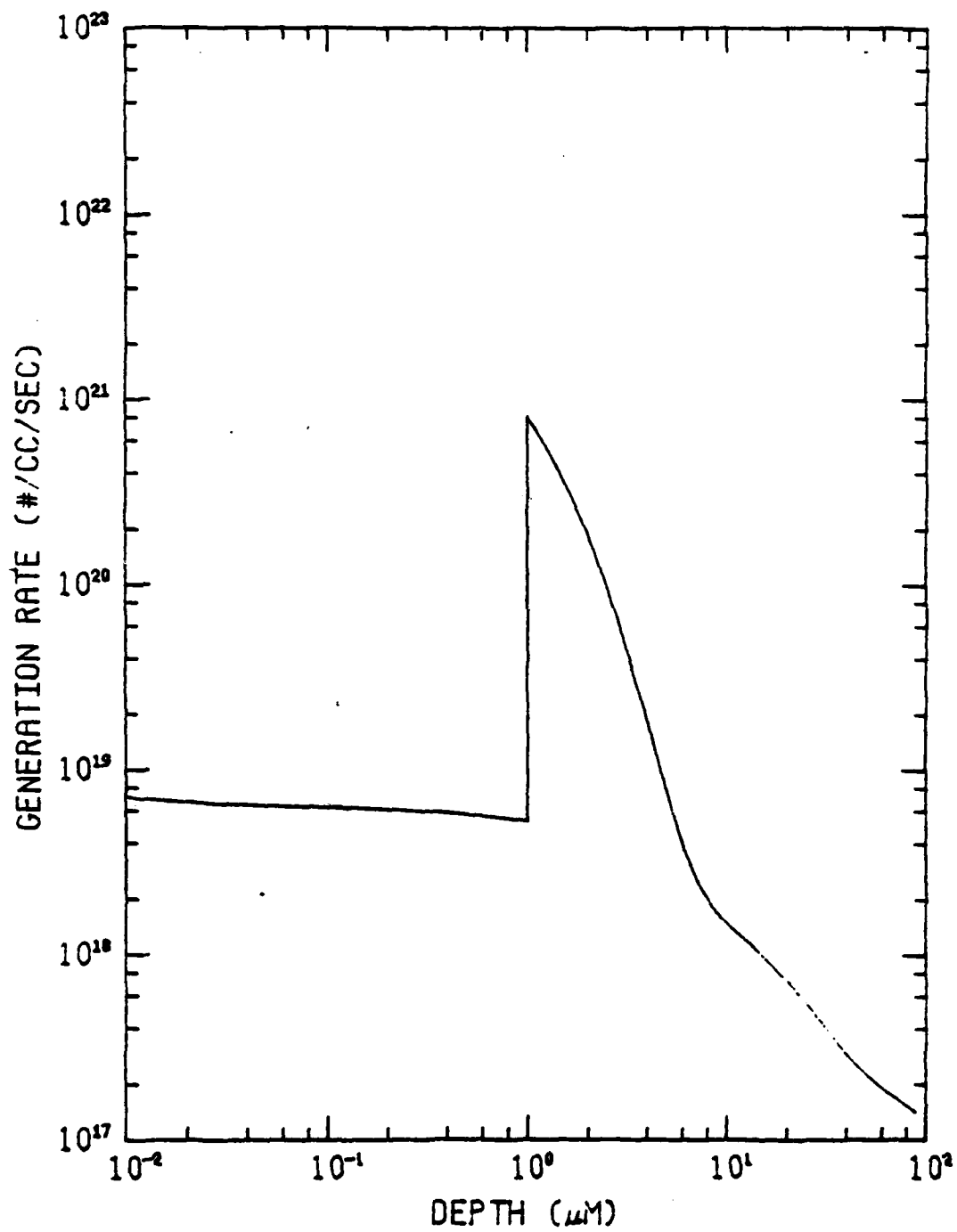


Figure 3.25(c) Carrier generation rate profile of the bottom cell with a top cell.

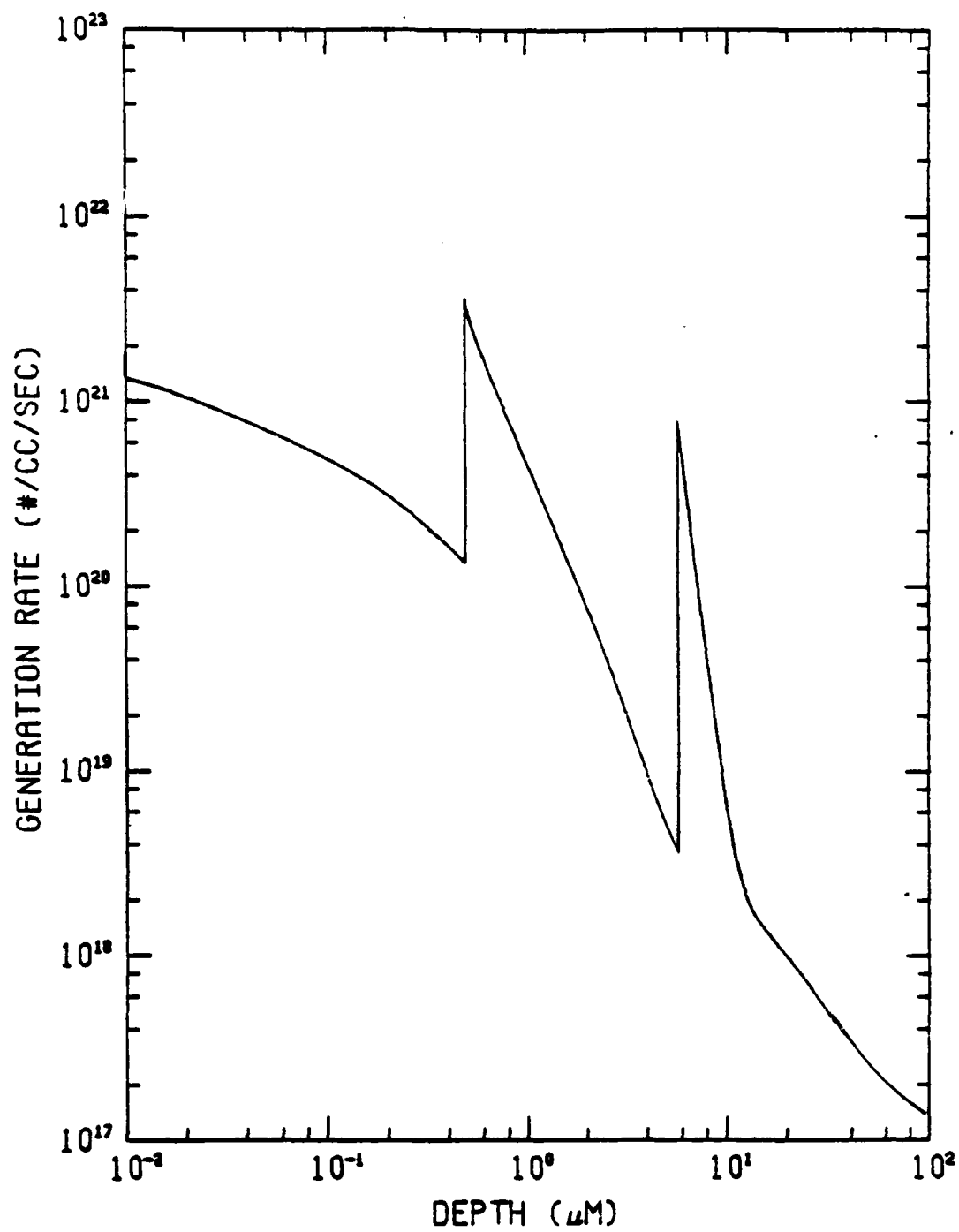


Figure 3.25(d) Carrier generation rate profile of the cascade cell.

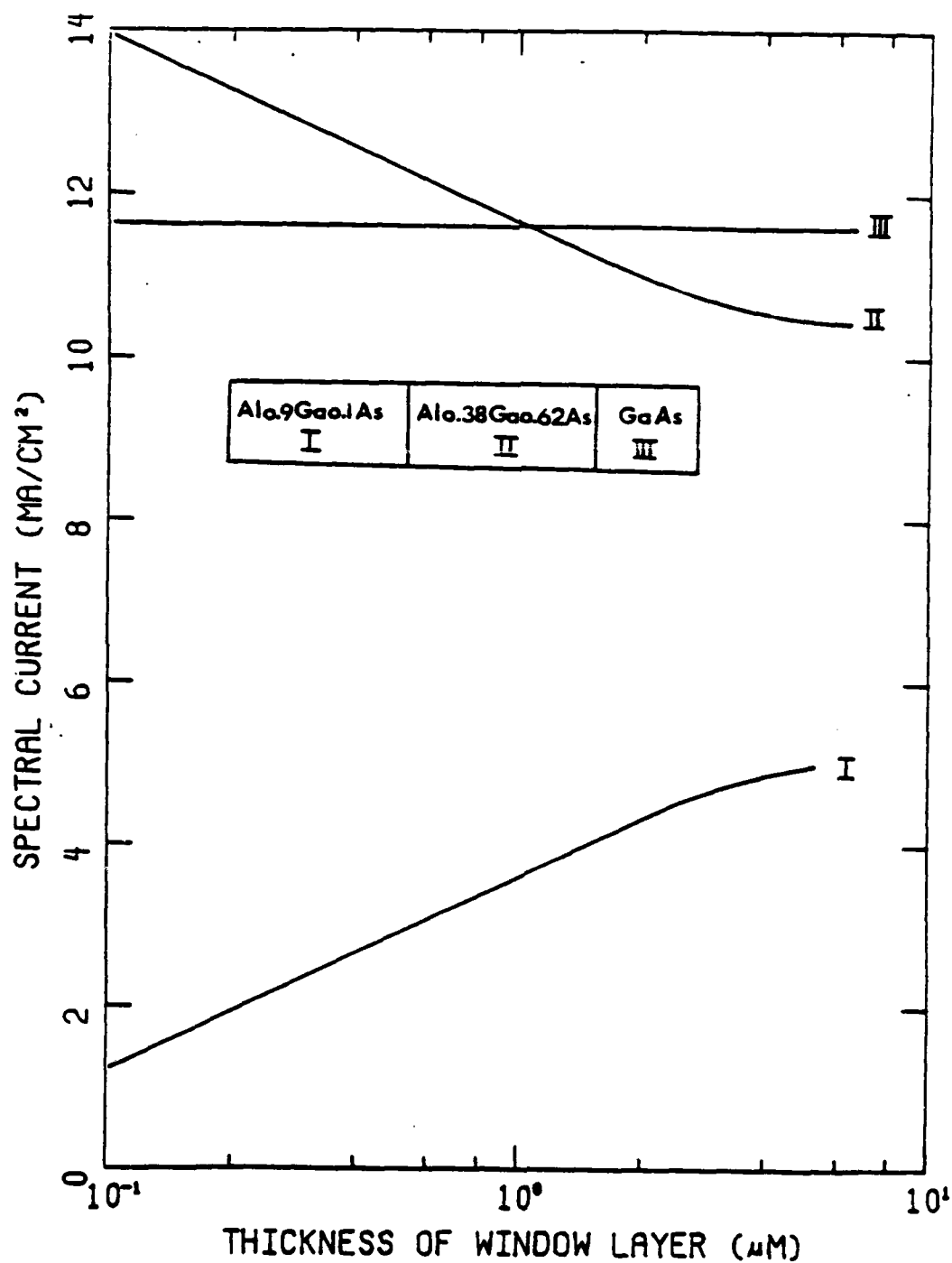


Figure 3.26 Dependence of spectral currents within various regions of a cascade cell on the thickness of the window layer.

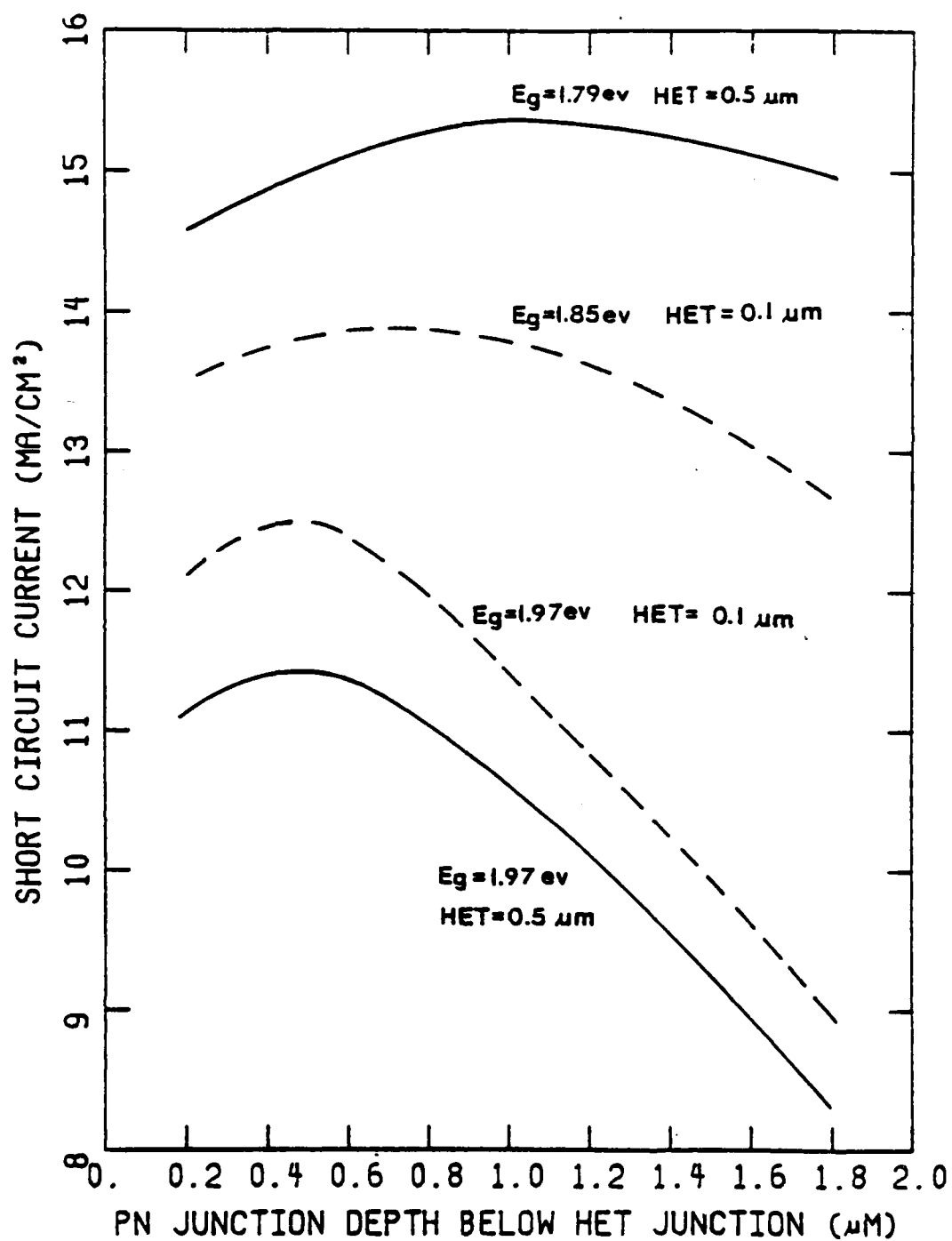


Figure 3.27 Dependence of short circuit current on pn junction depth.

of the carriers generated below the p-n junction. The overall increase of current at a given depth for the 0.1 μm window is due to the utilization of those high energy photons which are otherwise almost all lost in a 0.5 μm window. The lost contribution of carriers generated in the window layer to the short circuit current is more important for the case of higher bandgap cells, since the total current is smaller. Short circuit current for lower bandgap cells, however, should be less influenced by the location of the p-n junction (see Figure 3.27). Furthermore, the optimum location moves closer to the heterojunction when the bandgap increases. These calculated results indicate that more precise control of the device geometry is required for cells of higher bandgaps. Effects of window layer thickness on the performance of the cascade cell are shown in Figures 3.28a and 3.28b. The effect of diffusion length on short circuit current is shown in Figure 3.29. Results of the detailed calculation for the top cell with an optimum bandgap (1.97 eV) are shown in Figure 3.30. Once again, cells with higher bandgaps can be seen to be more sensitive to the quality of the material. Since the short circuit current of the cascade cell is smaller than that of a single-junction cell, a small amount of current loss results in a large drop of efficiency.

3.2.3.4 Fill Factor

The measured fill factors which are around 0.1 lower than predicted values reduce efficiencies about one percentage point. The fill factor is determined by the magnitude of the saturation current, the diode factor, the open circuit voltage, the series resistance and

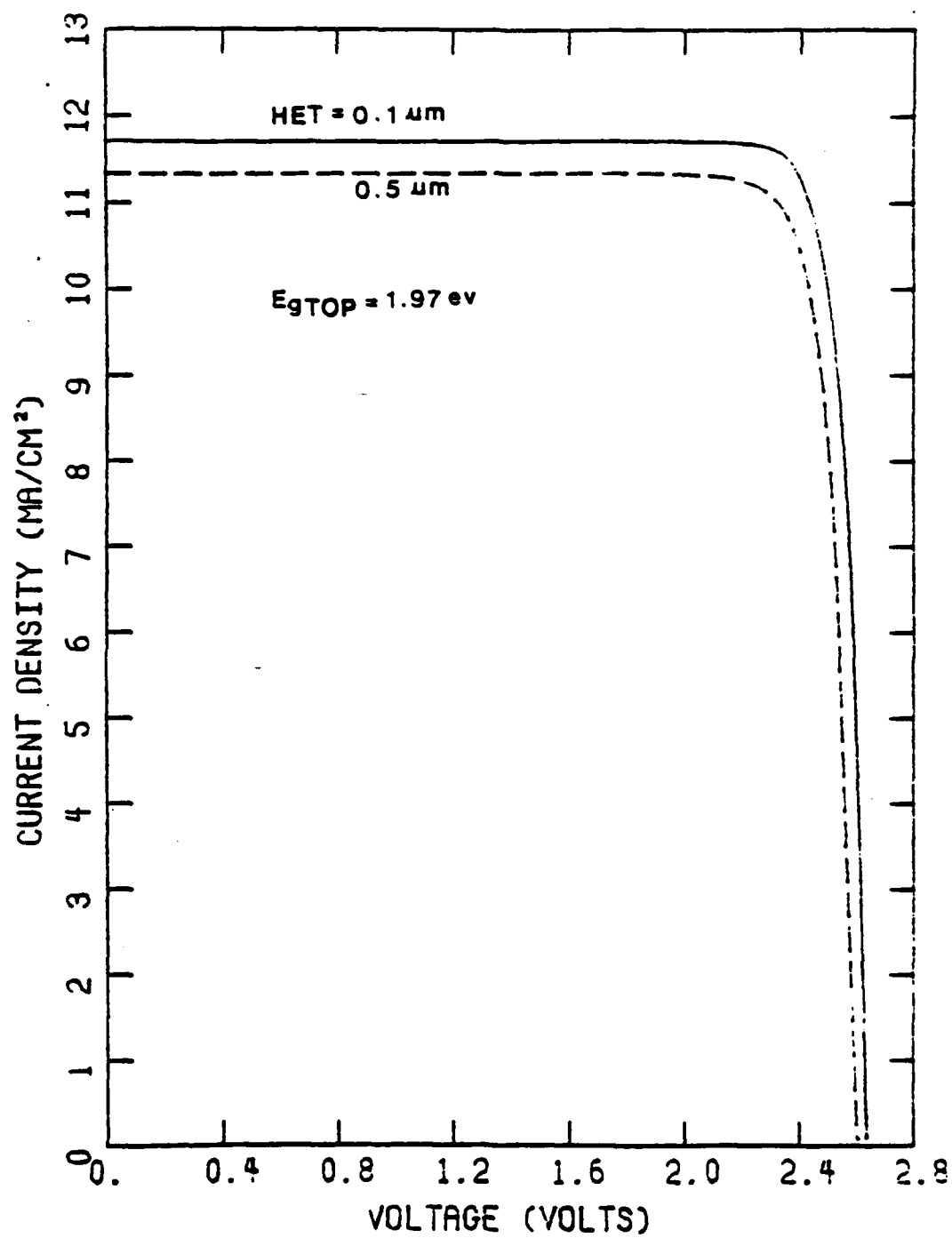


Figure 3.28(a) Effect of window layer thickness on I-V characteristics of the cascade cell.

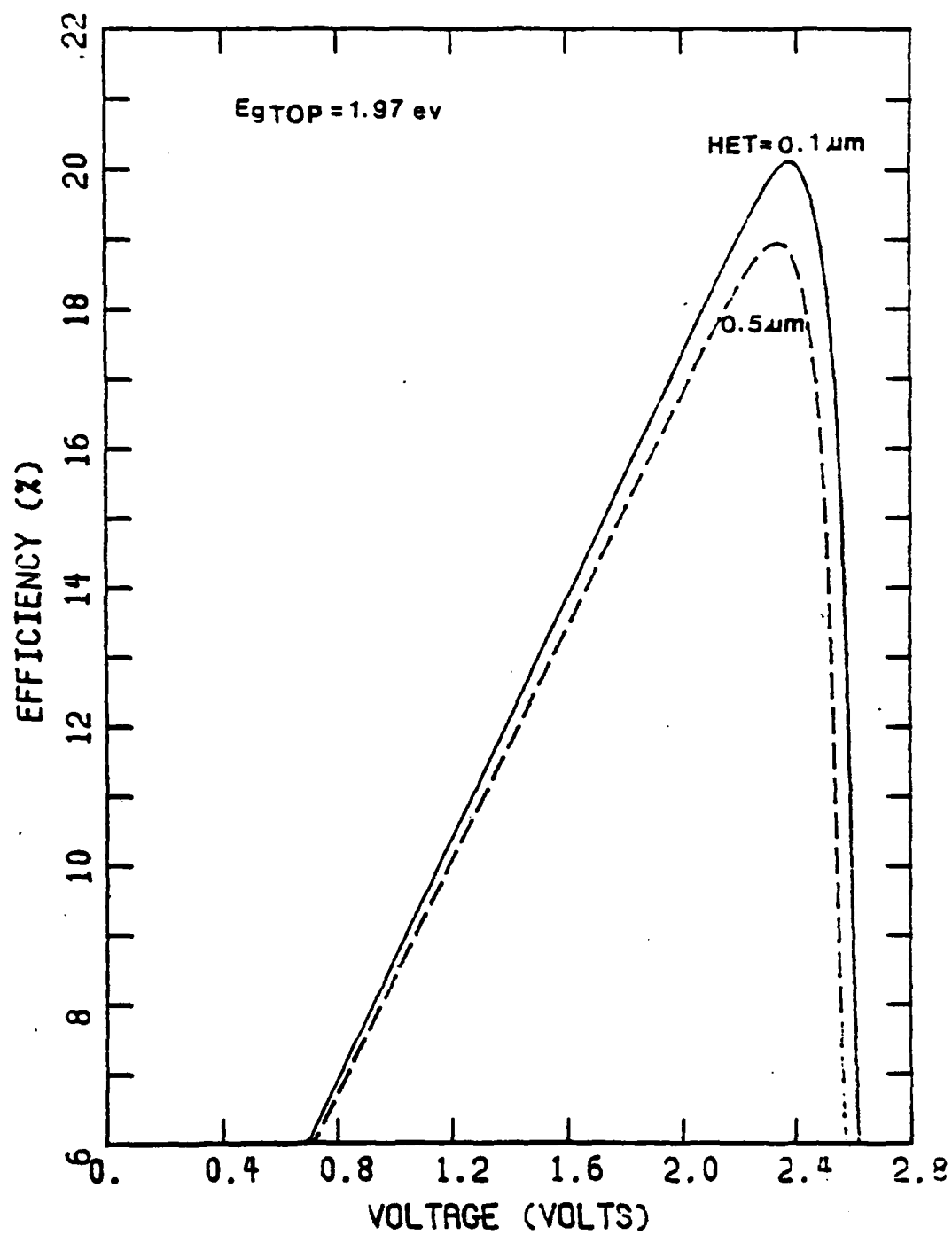


Figure 3.28(b) Effect of window layer thickness on the efficiency of the cascade cell.

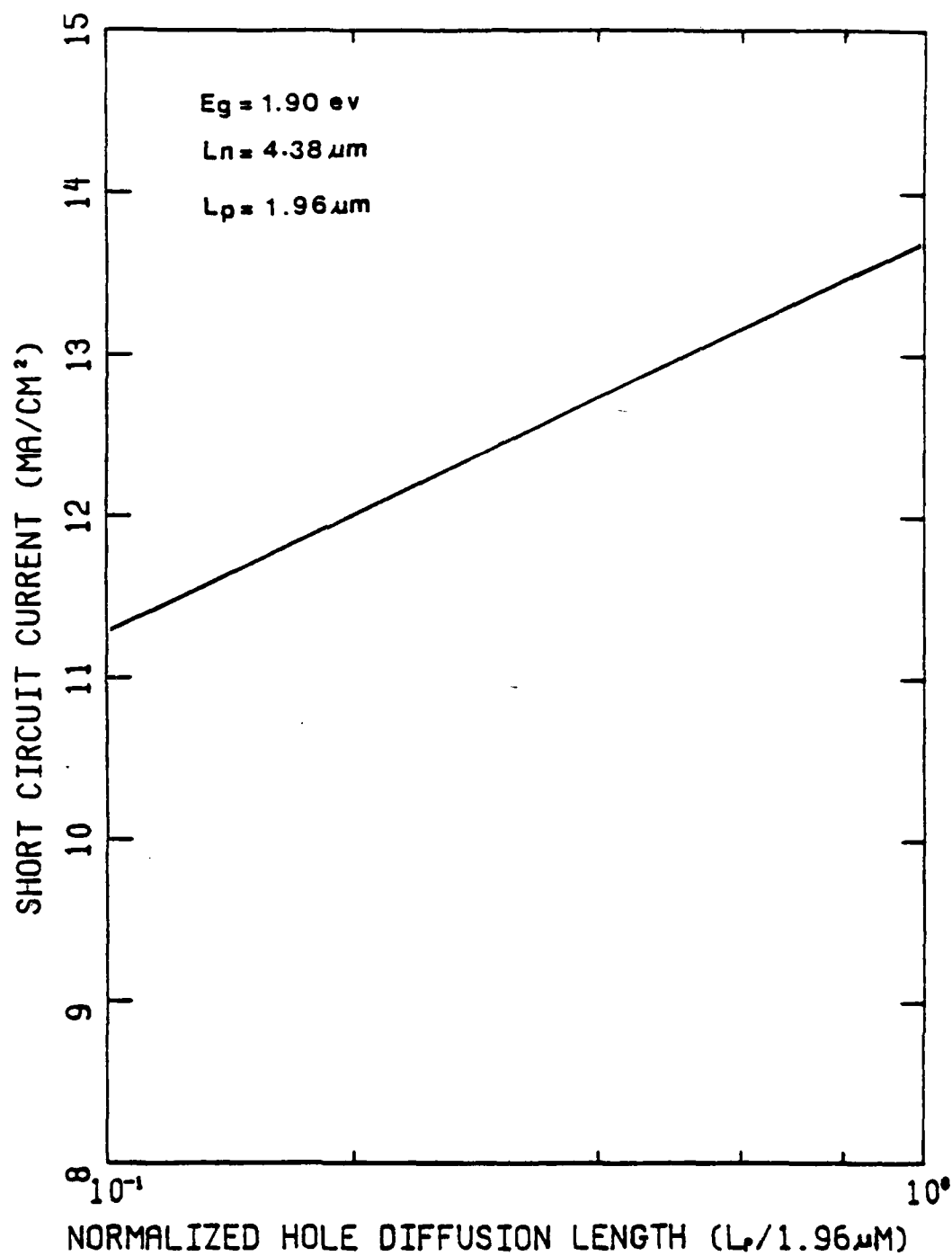


Figure 3.29 Dependence of short circuit current on hole diffusion length for a top cell with a bandgap of 1.90 eV.

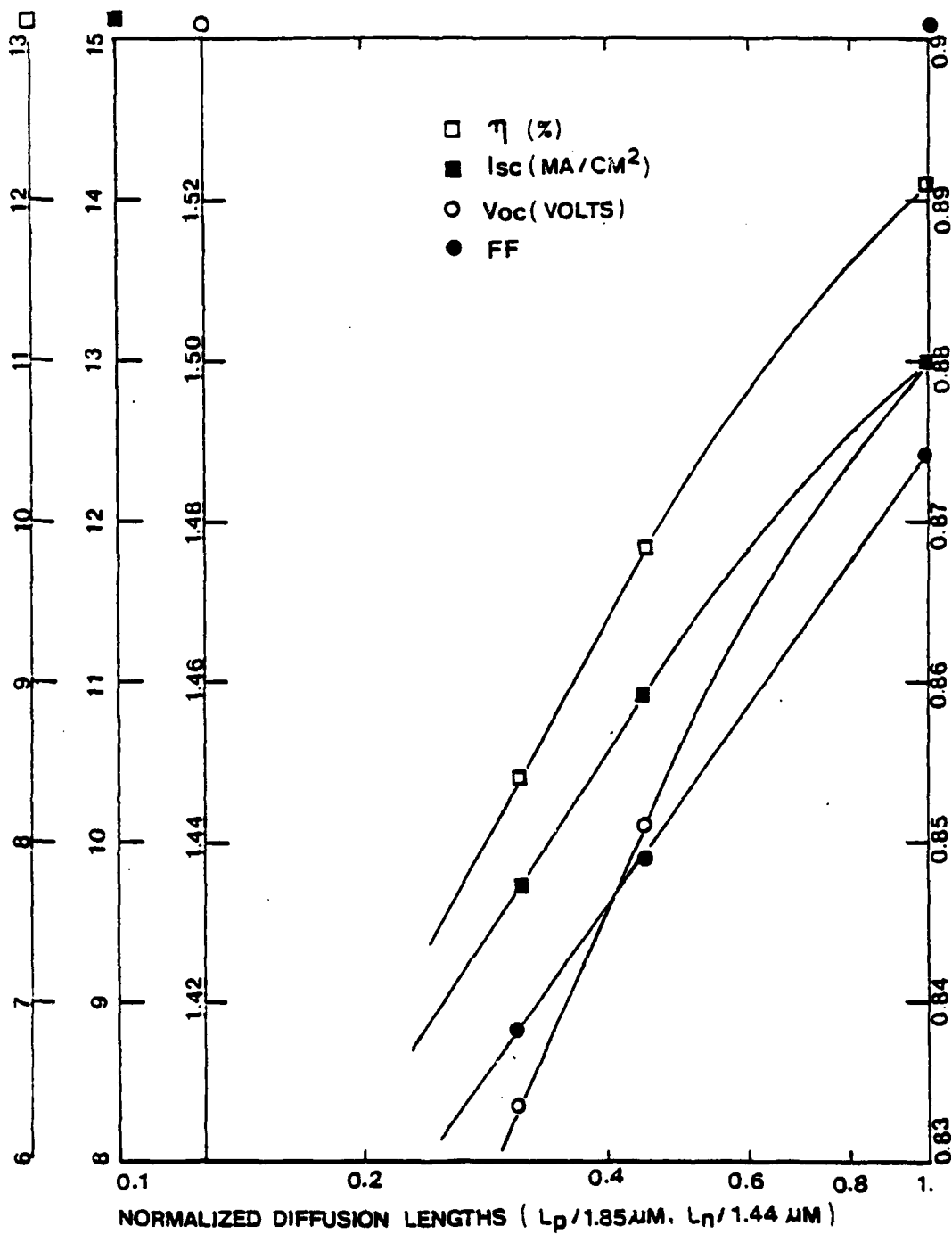


Figure 3.30 Dependence of parameters on diffusion lengths for a top cell with a bandgap of 1.97 eV.

the shunt resistance. Since there are so many parameters affecting the fill factor, it is perhaps better to analyze one parameter at a time while neglecting the influence of other effects.

Without considering series resistance and saturation current, Lindmayer [3.7] suggested that the high depletion-region recombination current reduces the fill factor. At a given series resistance, Green [3.8] pointed out that the fill factor is reduced by a higher value of diode factor, while Pulfrey showed that the fill factor is mainly determined by the saturation current [3.9]. The expression of fill factor without considering series and shunt resistance effects can be derived as

$$FF = \frac{V_m}{V_{oc}} \left[1 - \frac{[\exp(qV_m/nKT) - 1]}{[\exp(qV_{oc}/nKT) - 1]} \right] \quad , \quad (3.20)$$

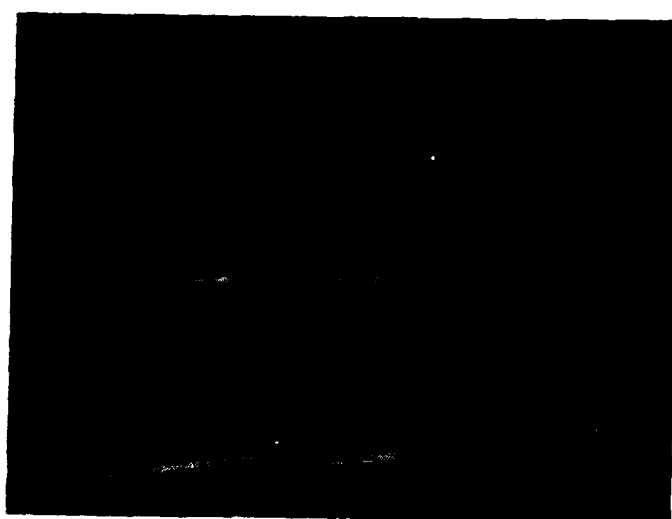
where V_m is the voltage output at maximum power. Table 3.1 shows the calculated dependence of the fill factor on the minority carrier lifetimes for a top cell with a bandgap of 1.97 eV.

Table 3.1. Dependence of Fill Factor on Carrier Lifetimes for a Top Cell with a Bandgap of 1.97 eV

τ ($\tau_{no} = 5.3$ nsec $\tau_{po} = 8.5$ nsec)		V_m (V)	V_{oc} (V)	$\frac{V_m}{V_{oc}}$	FF
$\tau_n = \tau_{no}$	$\tau_p = \tau_{po}$	1.364	1.5	0.909	0.874
0.2 τ_{no}	0.2 τ_{po}	1.290	1.442	0.895	0.849
0.1 τ_{no}	0.1 τ_{po}	1.248	1.407	0.887	0.838
0.02 τ_{no}	0.02 τ_{po}	1.142	1.302	0.877	0.807

Comparing the results in Table 3.1 with the relationship expressed in Equation (3.20) we see that the effect of smaller carrier lifetime is to move the voltage V_m to a range where the diode factor, n , is larger. This results in a reduction of the fill factor. Effects of series resistance and shunt resistance will be discussed in later sections (Sections 3.2.6.1 and 3.2.6.2). According to the discussion in Section 3.2.6.2., the shunt resistance of these cells is large enough to have a negligible effect at one solar intensity. Conversely, the fill factor decreases quite rapidly with increasing series resistance as will be shown in Figure 3.48. The series resistance of the present cascade cells ranges from 5 to 30 ohms and this leads to a reduction in the fill factor of 0.01 to 0.08. It has been found that the high series resistance and the small carrier lifetime are primarily responsible for the fill factor reduction of the solar cells in this study.

An anomalous I-V characteristic (Figure 3.31) was observed for several samples. From a first order approximation, the I-V curves of diodes with and without illumination should have the same degree of sharpness around the knees. Instead, the curve of the illuminated diode is sharper. The possibility of this effect arising from series resistance has been ruled out after the I-V characteristics and the resistance values were carefully measured. Although the cause of this phenomenon is not known, it is believed to be related to the presence of deep levels of unknown origin, possible related to defects in the AlGaAs. The reason why this observed effect varies from sample to sample is probably due to the varying densities of these deep levels which are sensitive to the fabrication conditions. GaAs-based devices have been notorious for their numerous deep impurity and defect centers [3.10]. LPE grown AlGaAs epitaxial layers generally exhibit some deep levels within the bandgap. These levels are responsible for enhancing the free carrier recombination rate by acting as recombination centers. One effect due to these deep levels is evident when the tunnel junction is characterized at liquid nitrogen temperature, as shown in Figure 3.32. Two regions of negative resistance appear corresponding to band-to-band tunneling and band-to-impurity tunneling respectively. Illuminating a diode can increase carrier lifetimes by filling these deep levels. As a result, carrier recombination rates can be reduced leading to an improvement of the sharpness of the I-V curve. If this is the case, then a very low level of illumination appears to drastically reduce the recombination enhancement due to these levels.



Sample No. R139D

Scale

Ver. 0.01 mA/div

Hor. 0.5 V/div

Illumination: 1 AMO

Figure 3.31. I-V characteristics of a cascade cell with a poor dark I-V curve.

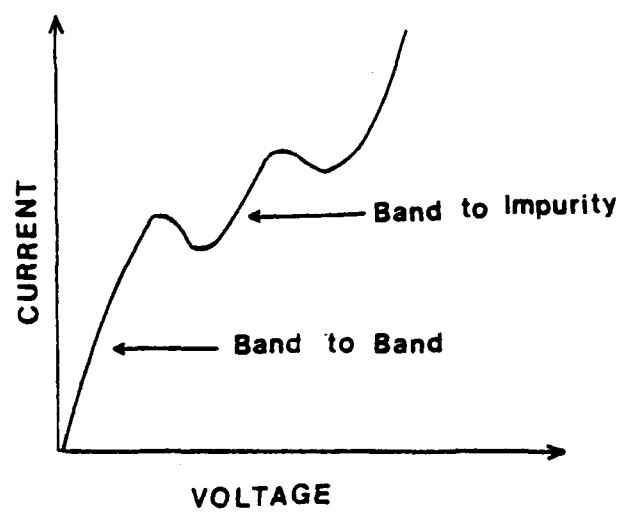


Figure 3.32 I-V characteristics of the AlGaAs tunnel junction at temperature 77°K.

I-V measurements under various solar intensities for a cascade solar cell are shown in Figure 3.33, where the maximum power point is identified by an open circle in each of the curves. Effects of light intensity on open circuit voltage, fill factor and efficiency for several cascade cells are shown in Figures 3.34a, 3.34b, and 3.34c for conditions of unconcentrated sunlight. Along with the linear dependence of the short circuit current on intensity the open circuit voltage increases logarithmically with increasing intensity as predicted by Equation (3.19). Fill factor is relatively insensitive to illumination level. The gain in fill factor contributed by the increasing open circuit voltage as expected by Equation (3.19) is largely cancelled out by the series resistance effect due to the increasing current in the presence of a high series resistance. The effects of high illumination on cascade solar cells was not a task to be systematically investigated in this work. The initial results shown in Figures 3.35a and 3.35b, however, are useful for cell characterization. Both short circuit current and open circuit voltage increase with increasing light intensity as expected [3.11]. The expected increase of fill factor is not found in these particular samples. The decrease in fill factor is attributed to the series resistance which causes a significant voltage drop under the high current condition.

A negative resistance region due to the tunnel junction is observed in the I-V characteristics shown in Figure 3.36. The short circuit current in this case has exceeded the peak current (I_p) of the AlGaAs tunnel junction as shown in Figure 3.37 [3.12]. This decreases the fill factor and consequently the efficiency. By using high intensity illumination, we can readily determine the current handling

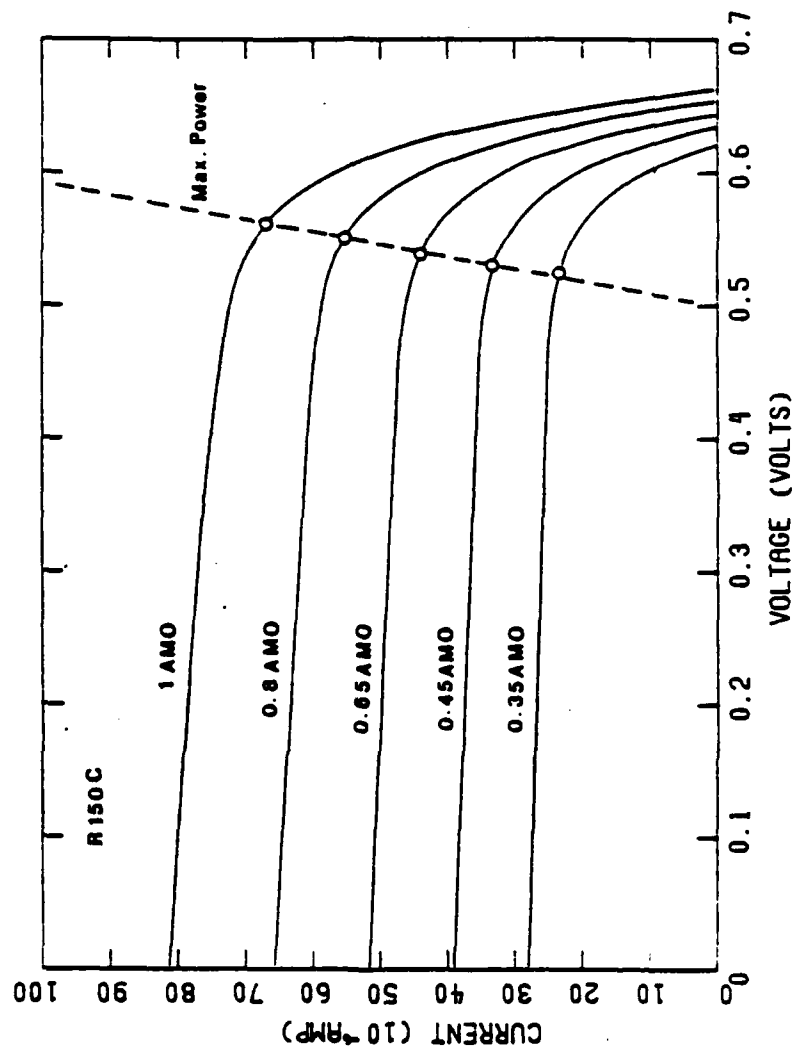


Figure 3.33 I-V characteristics of a bottom cell under various AMO illuminations.

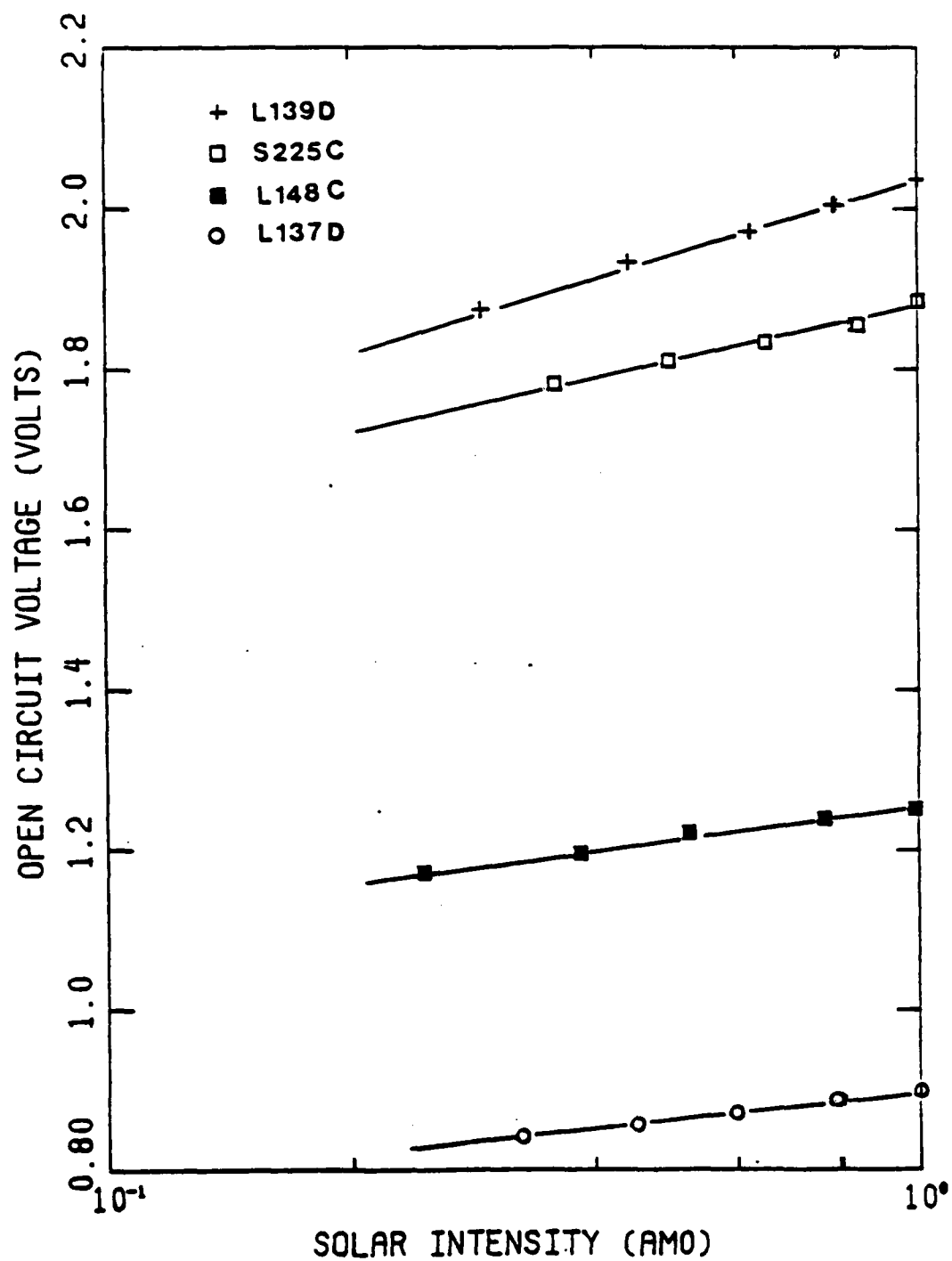


Figure 3.34(a) Dependence of open circuit voltage on light intensity.

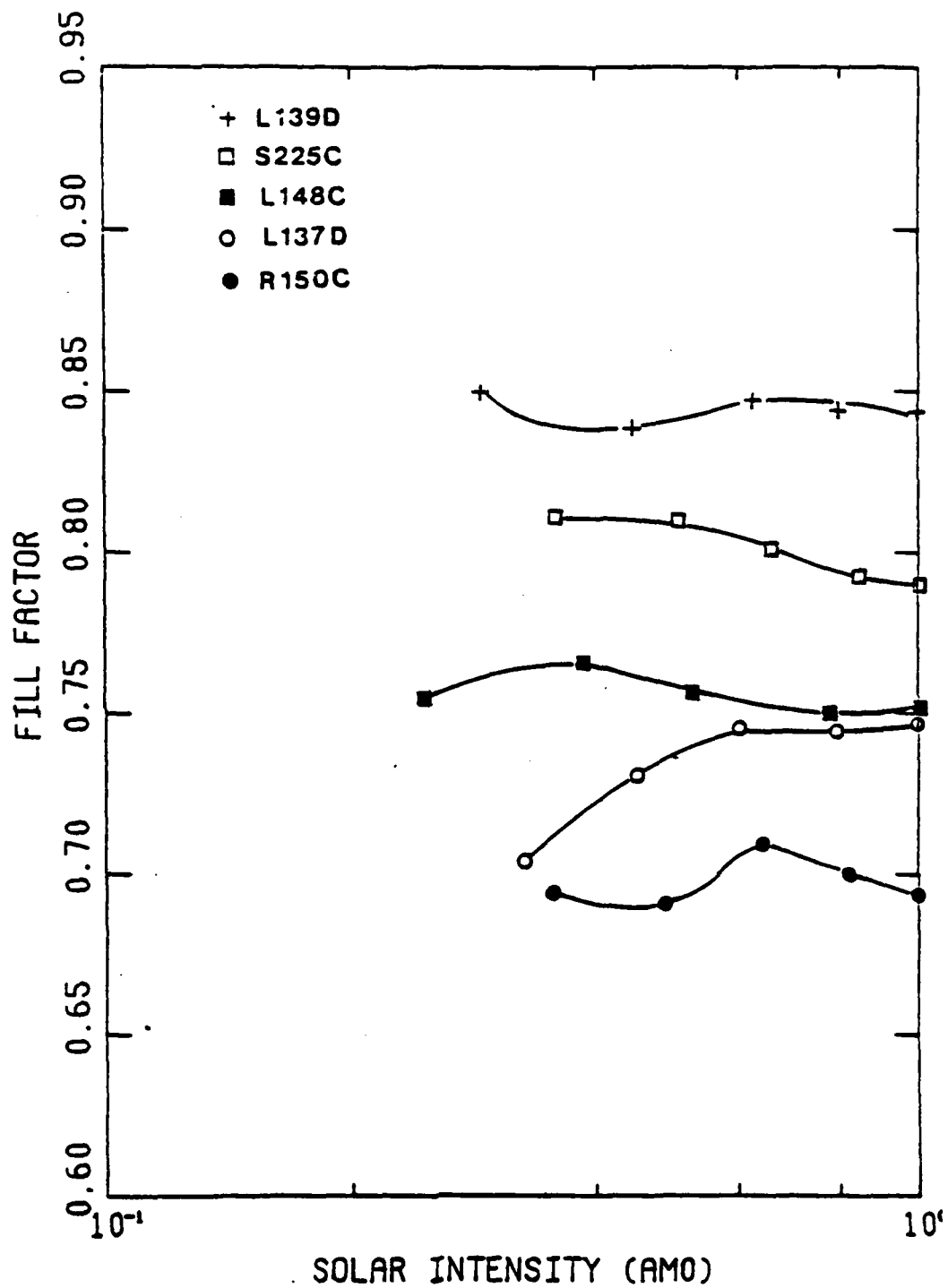


Figure 3.34(b) Dependence of fill factor on light intensity.

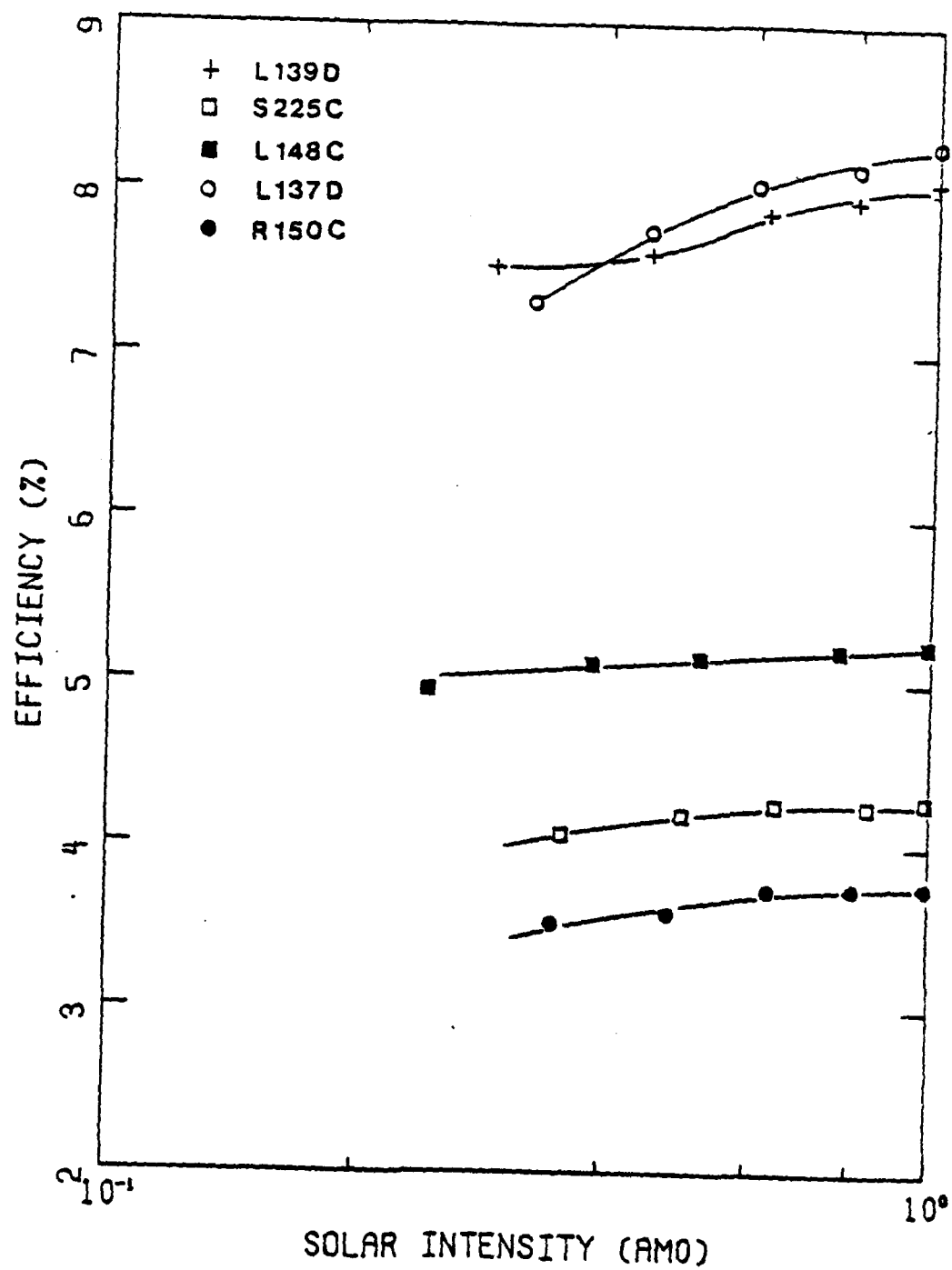
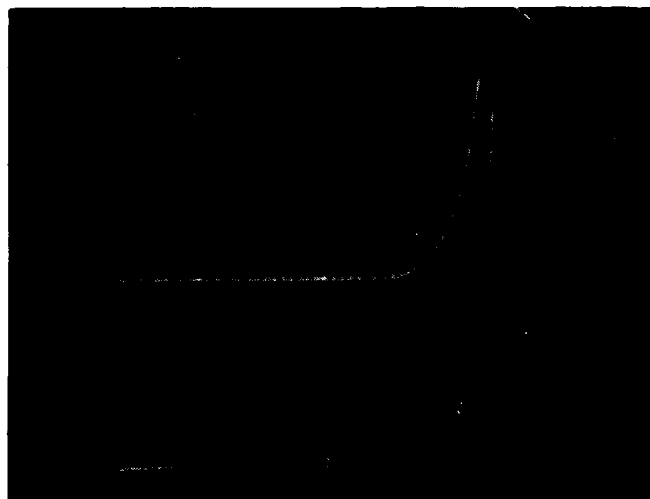


Figure 3.34(c) Dependence of efficiency on light intensity.



Sample No. G222D

Scale

Ver. 0.01 mA/div

Hor. 0.5 V/div

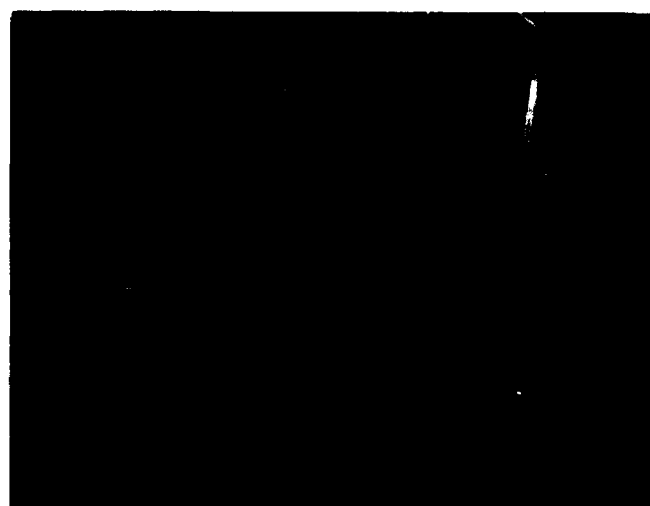
Illumination: 1 AMO

$V_{oc} = 1.9 \text{ V}$

$I_{sc} = 5.73 \text{ mA/cm}^2$

FF = 0.74

$\eta = 5.95\%$



Sample No. G222D

Scale

Ver. 0.1 mA/div

Hor. 0.5 V/div

Illumination: 9 AMO

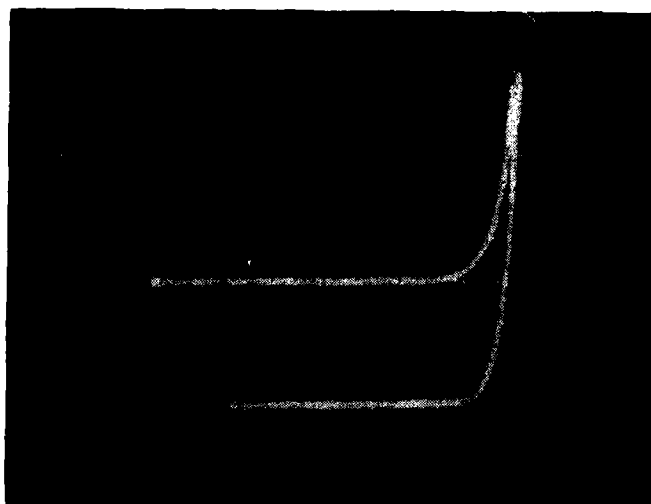
$V_{oc} = 2.1 \text{ V}$

$I_{sc} = 53.3 \text{ mA/cm}^2$

FF = 0.73

$\eta = 6.71\%$

Figure 3.35(a). Comparison of I-V characteristics of a cascade cell under 1-sun and multi-sun illuminations.



Sample No. G239C

Scale

Ver. 0.02 mA/div

Hor. 0.5 V/div

Illumination: 1 AMO

$V_{oc} = 2.1 \text{ V}$

$I_{sc} = 11.6 \text{ mA/cm}^2$

FF = 0.77

$\eta = 13.9\%$



Sample No. G239C

Scale

Ver. 0.2 mA/div

Hor. 0.5 V/div

Illumination: 13 AMO

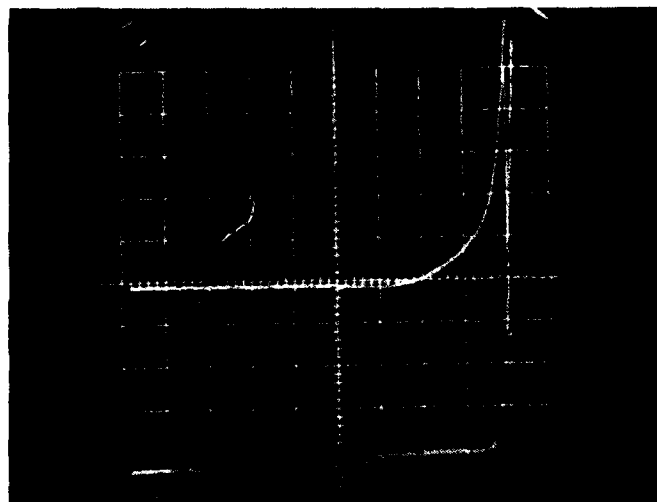
$V_{oc} = 2.26 \text{ V}$

$I_{sc} = 152 \text{ mA/cm}^2$

FF = 0.65

$\eta = 12.7\%$

Figure 3.35(b). Effect of tunnel junction on the performance of a cascade cell operated at high solar intensity.



Sample No. G222D

Scale

Ver. 0.01 mA/div

Hor. 0.50 V/div

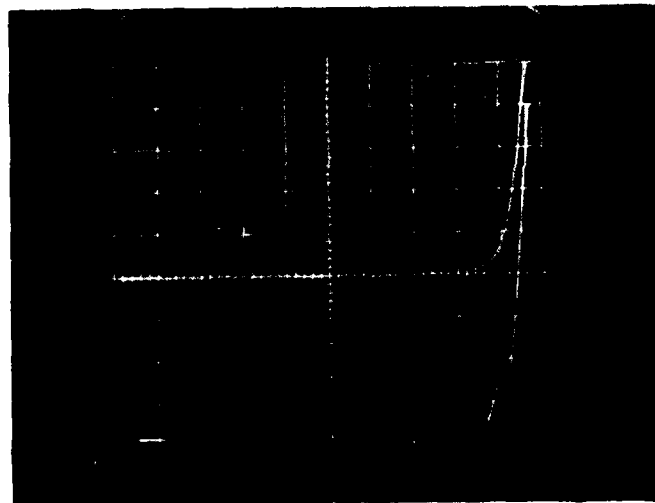
Illumination: 1 AMO

$V_{oc} = 2.0 \text{ V}$

$I_{sc} = 5.60 \text{ mA/cm}^2$

FF = 0.84

$\eta = 6.95\%$



Sample No. G222D

Scale

Ver. 0.1 mA/div

Hor. 0.5 V/div

Illumination: 9 AMO

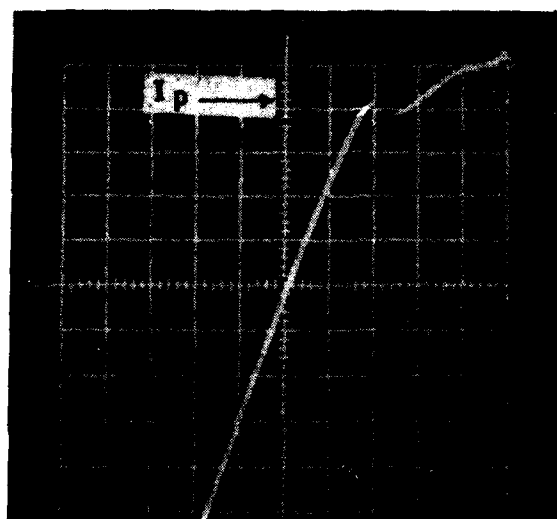
$V_{oc} = 2.2 \text{ V}$

$I_{sc} = 50.7 \text{ mA/cm}^2$

FF = 0.77

$\eta = 7.05\%$

Figure 3.36. Negative resistance region on I-V characteristics of a cascade cell under multi-sun illumination.



Scale

Ver. 100 mA/div

Hor. 0.1 V/div

Figure 3.37. I-V characteristics of AlGaAs tunnel diode.

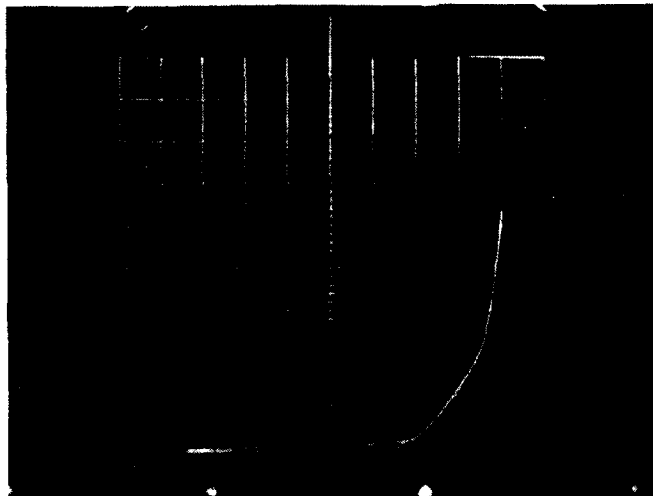
capacity of the tunnel junction. However, improvements in fill factors under multi-sun conditions for cascade cells with poor fill factors at one sun illumination can be seen in Figures 3.38a and 3.38b. This improvement is believed to be due to the filling of traps and the reduction of the recombination rate under illumination as previously discussed.

3.2.3.5 Efficiency

The measured photovoltaic conversion efficiencies for these cascade cells are approximately 10% for AMO illumination and 14% under AM2 conditions. Ratios of typical experimental data to theoretical values are shown in Table 3.2. It might appear from this table, that the bottom cell degrades the cascade cells more than the top cell, but this is actually not the case, since losses measured for bottom cells shown here partly contain the loss of high energy photons, which are absorbed by the top cell and are unavailable to the bottom cell in a cascade structure.

Table 3.2. Ratios of Experimental Data and Theoretical

TYPE	V_{oc}	I_{sc}	FF	η
TOP	0.87	0.84	0.95	0.69
BOTTOM	0.78	0.86	0.90	0.60
CASCADE	0.81	0.78	0.92	0.58



Sample No. G246C

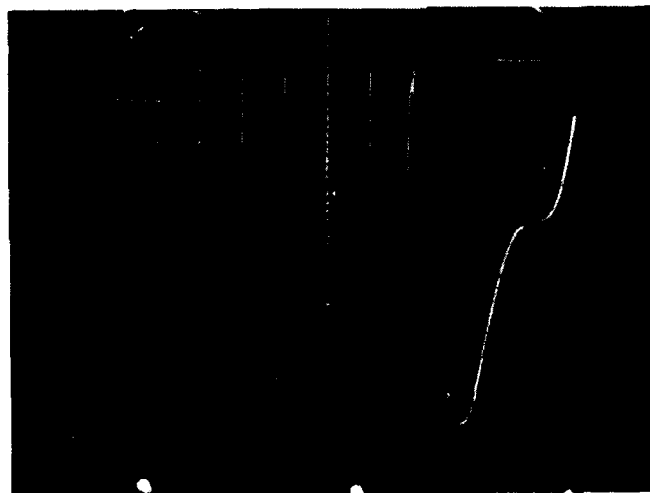
Scale

Ver. 0.02 mA/div

Hor. 0.5 V/div

Illumination: 1 AMO

FF = 0.54



Sample No. G246C

Scale

Ver. 1.0 mA/div

Hor. 0.5 V/div

Illumination: 44 AMO

FF = 0.79

Figure 3.38. Improvement of fill factors under multi-sun condition for cascade cells with poor fill factors at one sun illumination.

In other words, the bottom cell is expected to perform better when it is only responsible for the collection of the lower energy photons in the operation of the cascade cell. It has also been found that bottom cells with a window layer perform better than bottom cells with a tunnel junction. The diffused junction in the GaAs is deeper for the latter case due to a longer growth time. Diffused layers tend to have smaller minority carrier lifetimes which reduce both open circuit voltage and short circuit current. In this case with the tunnel junction grown directly on the bottom cell and with no top cell overgrowth we observe satisfactory ohmicity. The high temperature during the top cell growth on the tunnel junction generally broadens the tunnel junction doping profiles and the diffused junction degrades the performance of the tunnel junction and the bottom cell in the cascade device.

3.2.4 Spectral Response

The experimental and theoretical studies reported above were on samples without antireflection coatings. Calculated reflectance of light incorporated into the computer modeling is shown in Figure 3.39. Spectral response, when normalized to unity at the wavelength of maximum response, is shown in Figures 3.40a and 3.40b. The response begins at the bandgap energy, reaches a peak, and decreases with increasing energy due to losses in the window layer. A short diffusion length and a thick window layer result in insufficient collection of the carriers generated near the surface by high energy photons. This results in a discrepancy between the experimental and the theoretical values of top cells for short wavelengths as shown in Figure 3.40a. It is important to keep the window layer and diffused layer very thin in order to achieve high quantum yields at short wavelengths.

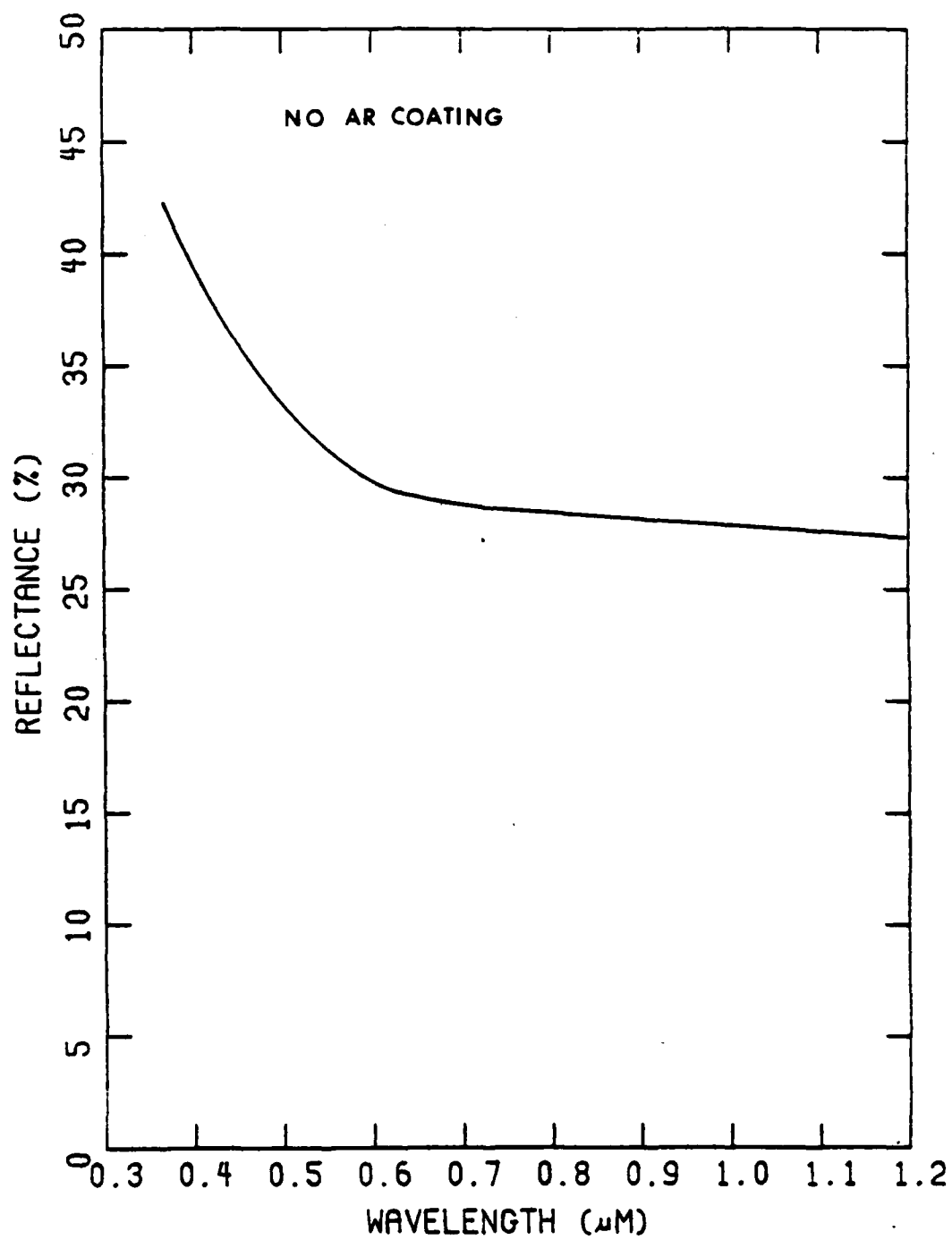


Figure 3.39 Reflection of light on the surface of AlGaAs cascade solar cell.

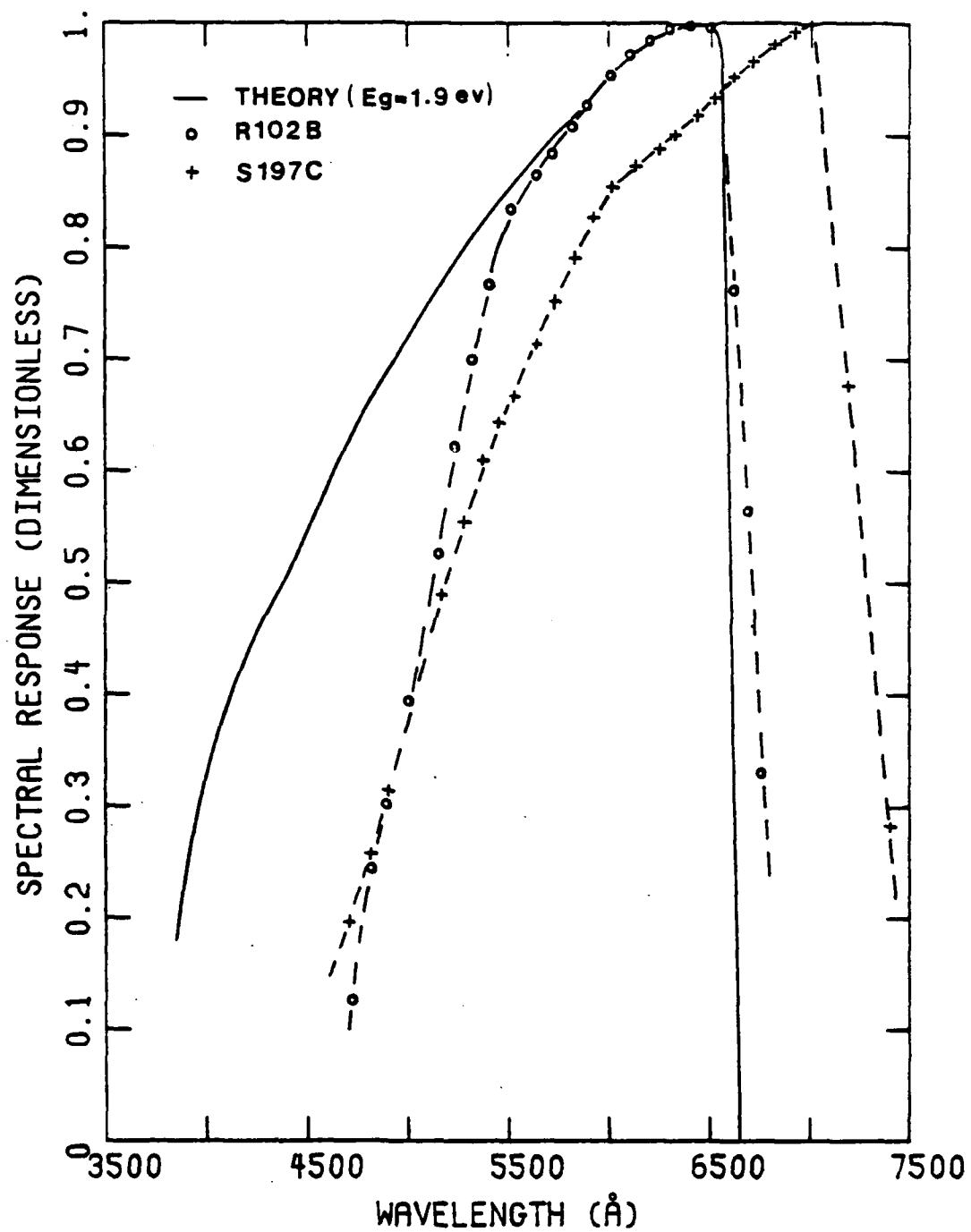


Figure 3.4C(a) Comparison of calculated spectral responses and experimental measurements for top cells.

Reasonably good agreement between theory and experiment is seen for the bottom cell in Figure 3.40b. The deviation of the response in the short wavelength region is due to the absorption by the tunnel junction atop the bottom cell. The gradual increase of the measured response near the band edge may be due to impurity absorption which was not considered in the theoretical analysis. The measured quantum efficiencies are shown in Figures 3.41a and 3.41b along with calculated values. The quantum efficiency, as defined here, is the number of electron-hole pairs collected under short circuit conditions relative to the number of photons incident on the surface of the cell. Typical results for most cascade cells as shown in Figure 3.41b indicates that the top cell limits the short circuit current of the cascade cell.

3.2.5 Mobility and Diffusion Length

3.2.5.1 Mobility

Hall measurements have been carried out to determine the carrier mobility with emphasis on hole mobility, since in this structure with thin p-layers the hole mobility in the thicker n-regions will be intimately related to the short circuit current. The measured hole mobilities range from 60 to 120 $\text{cm}^2/\text{v-sec}$ with varying Al composition and doping density. The dependence of hole mobility as a function of doping and Al composition in AlGaAs is shown in Figures 3.42a and 3.42b. Comparisons with other data are shown in Figures 3.43a and 3.43b. Reasonably good agreement can be seen for the measurements on $\text{Al}_{0.8}\text{Ga}_{0.2}\text{As}$, especially in the range where the doping densities are below 10^{18} cm^{-3} . The justification of the approximation taken in the present work of

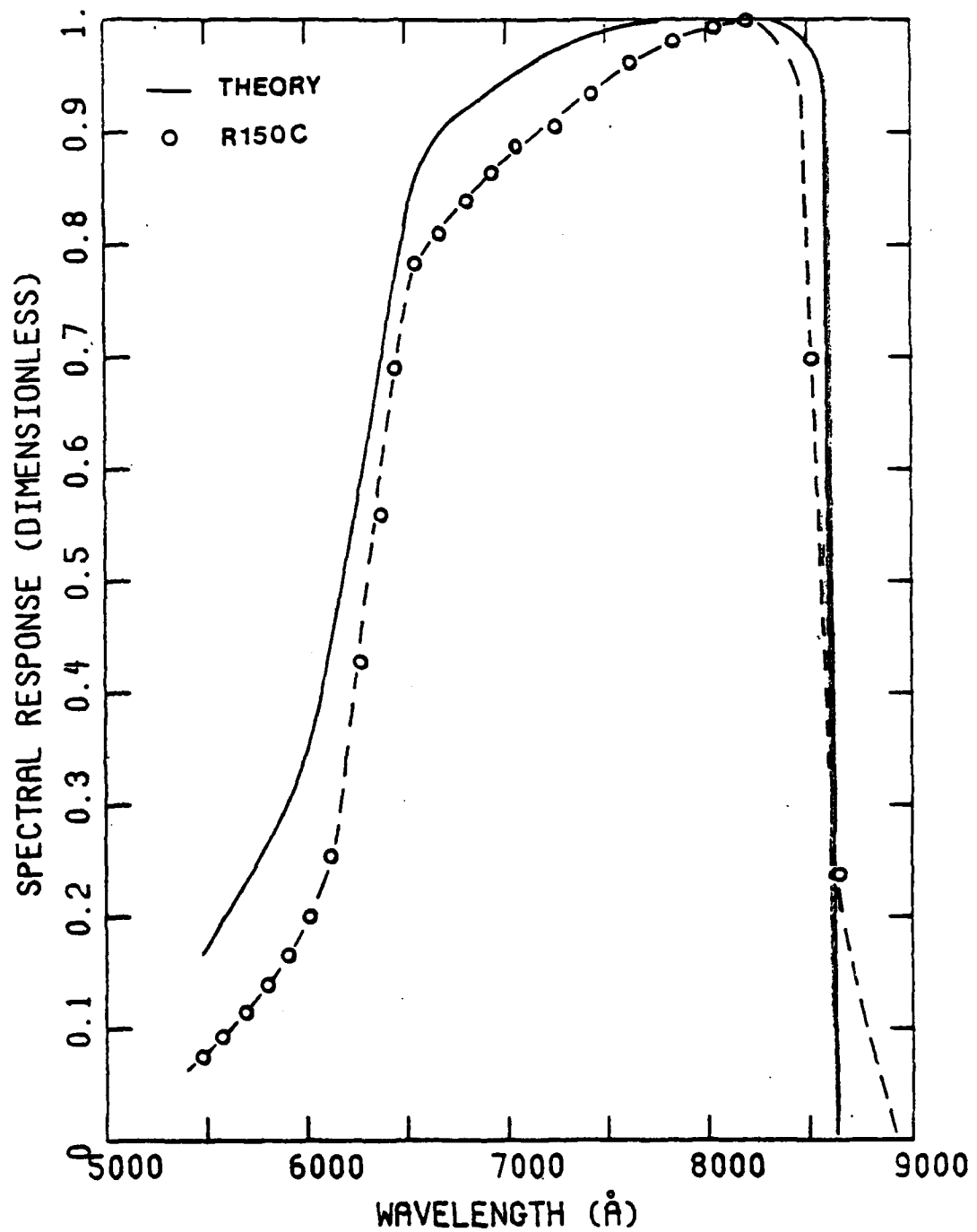


Figure 3.40(b) Comparison of calculated spectral responses and experimental measurements for a bottom cell with a tunnel junction.

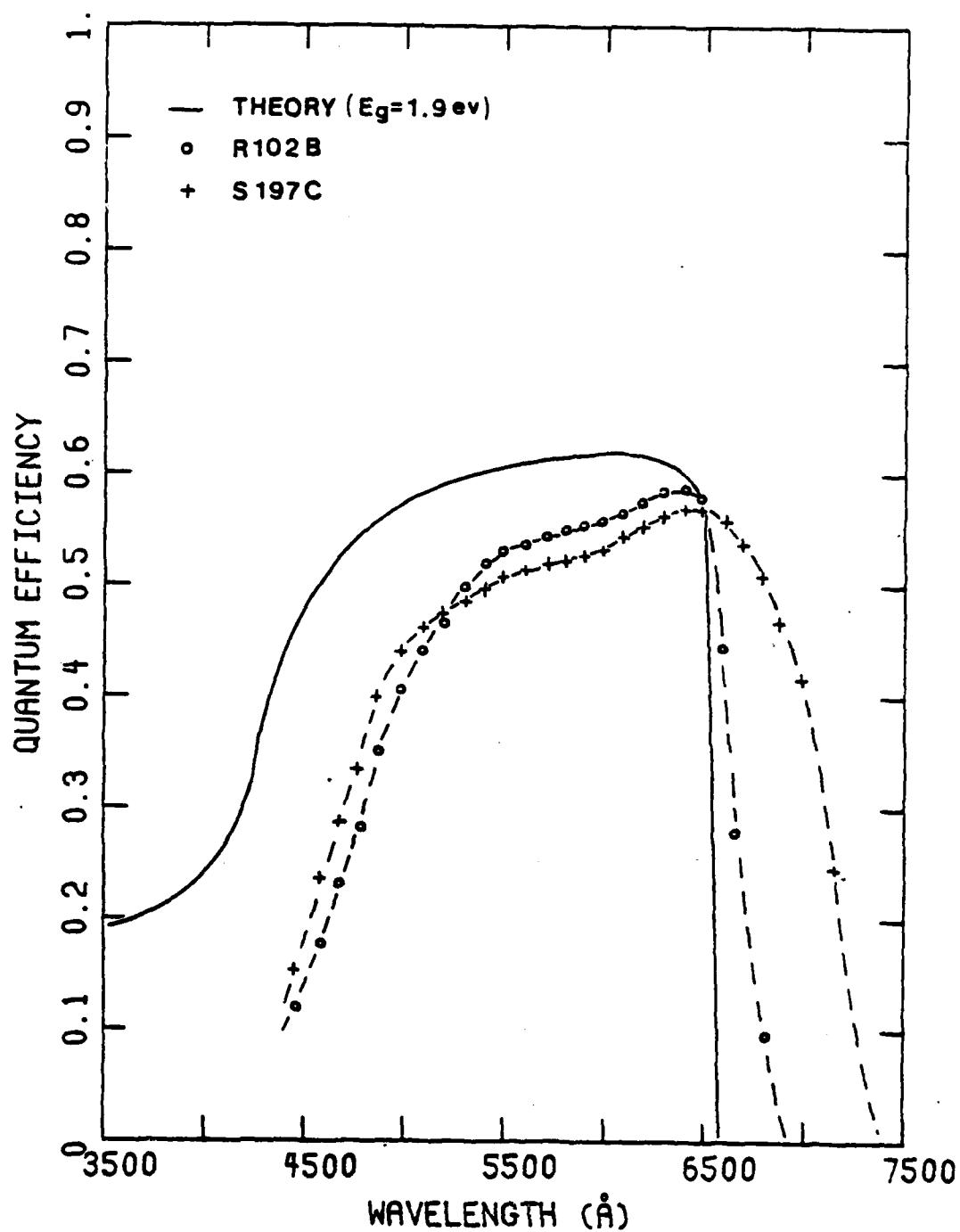


Figure 3.41(a) Comparison of calculated quantum efficiencies and experimental measurements for top cells.

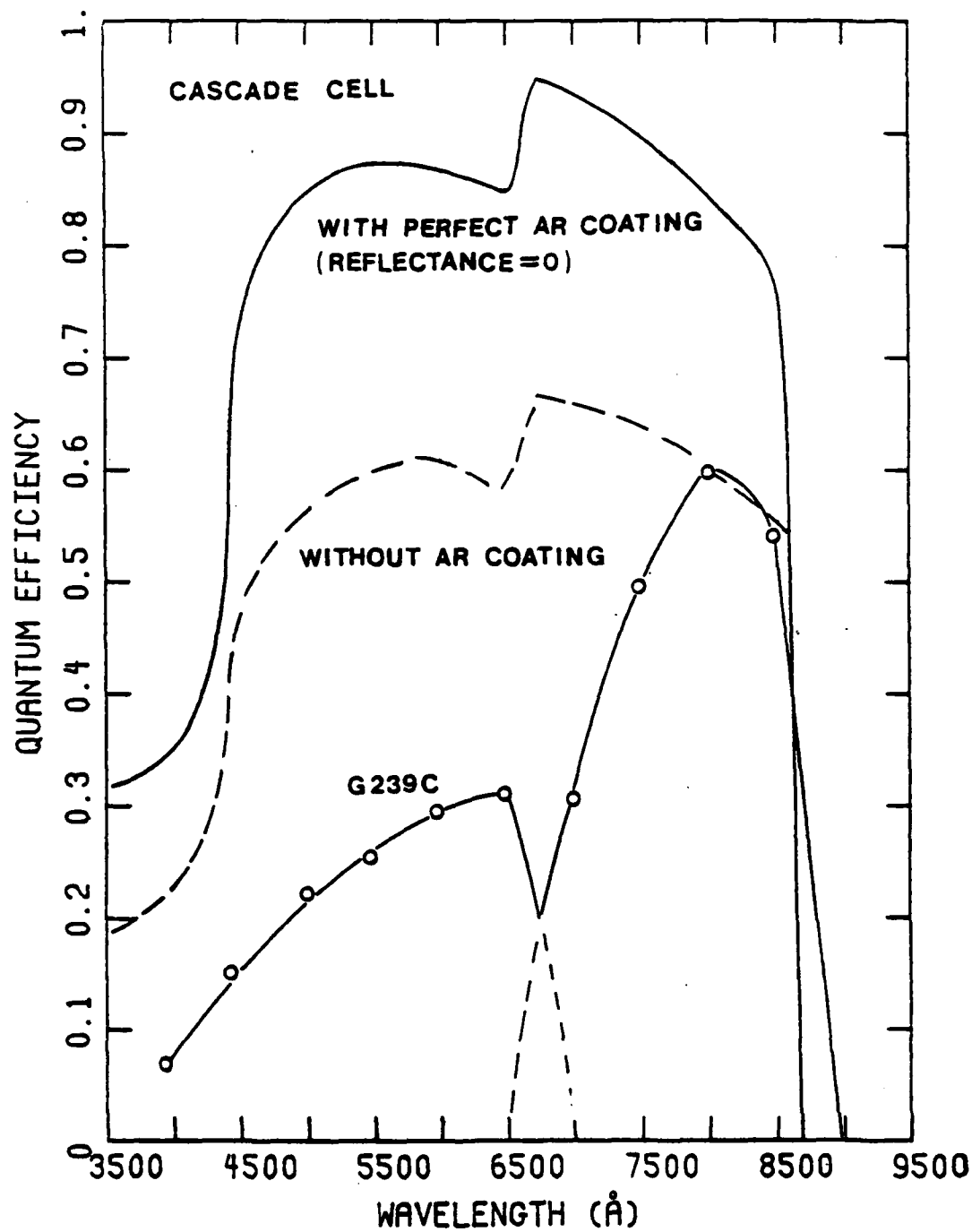


Figure 3.41(b) Comparison of calculated quantum efficiencies and experimental measurements for cascade cells.

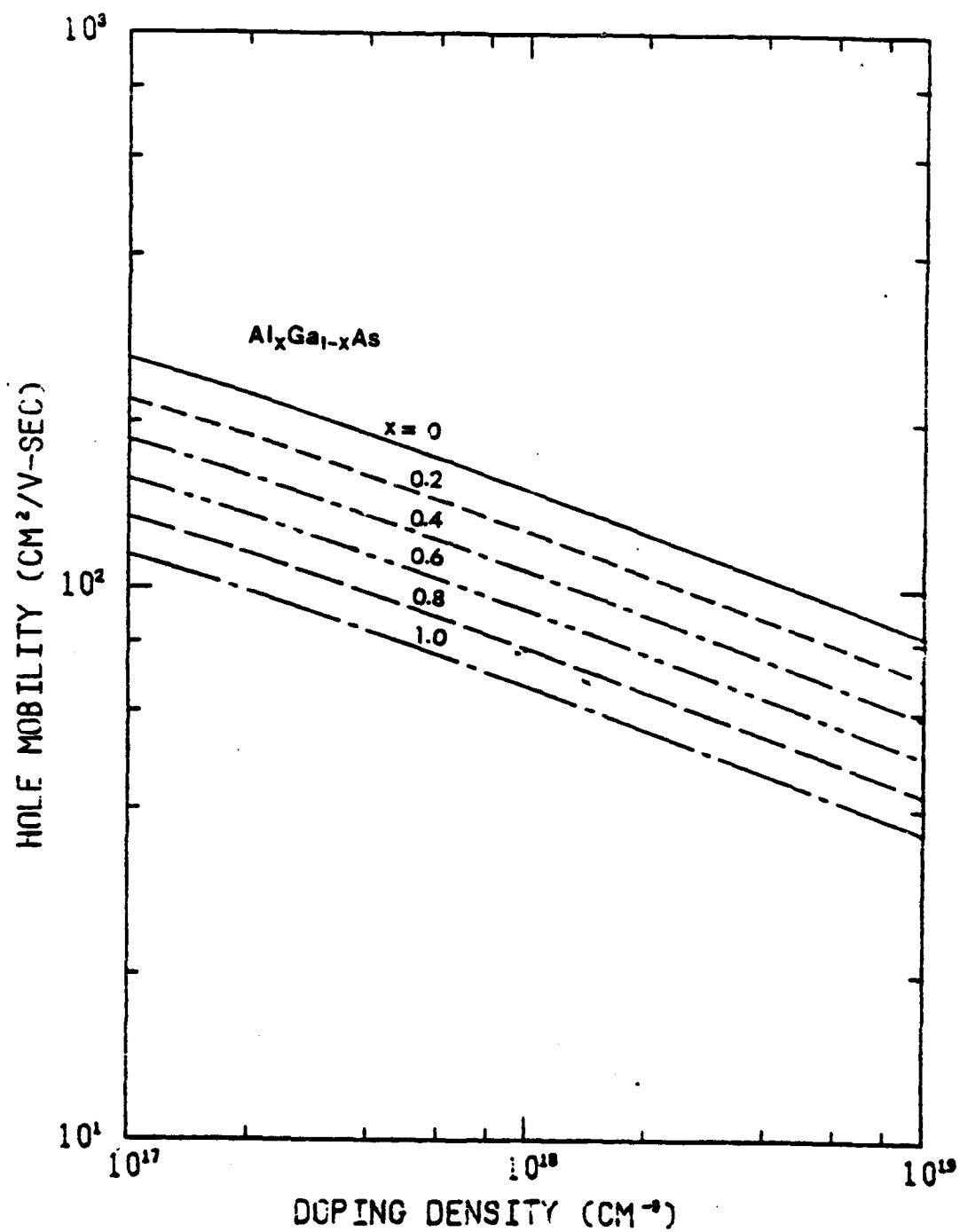


Figure 3.42(a) Relationship between hole mobility and doping density in AlGaAs.

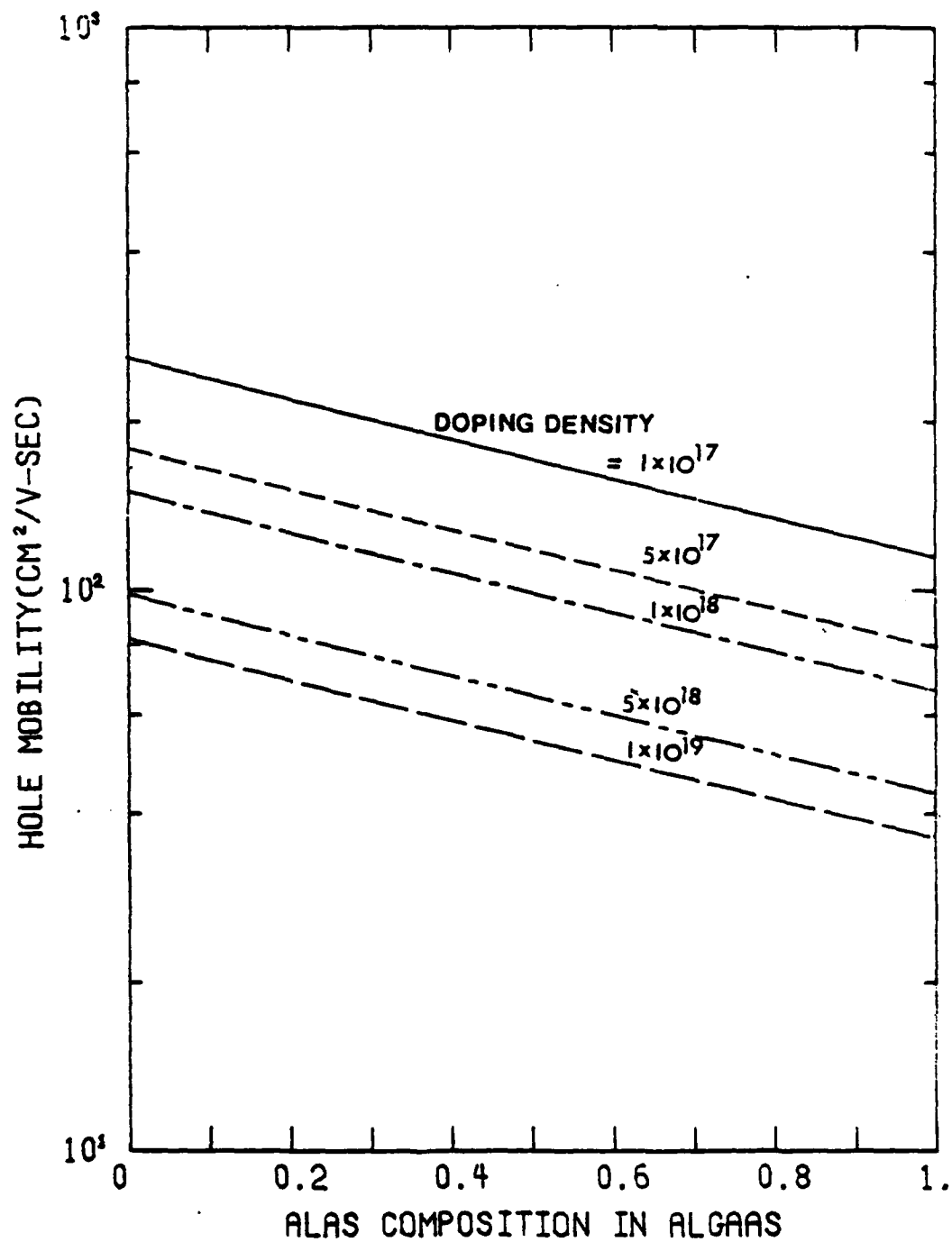


Figure 3.42(b) Relationship between hole mobility and AlAs composition in AlGaAs.

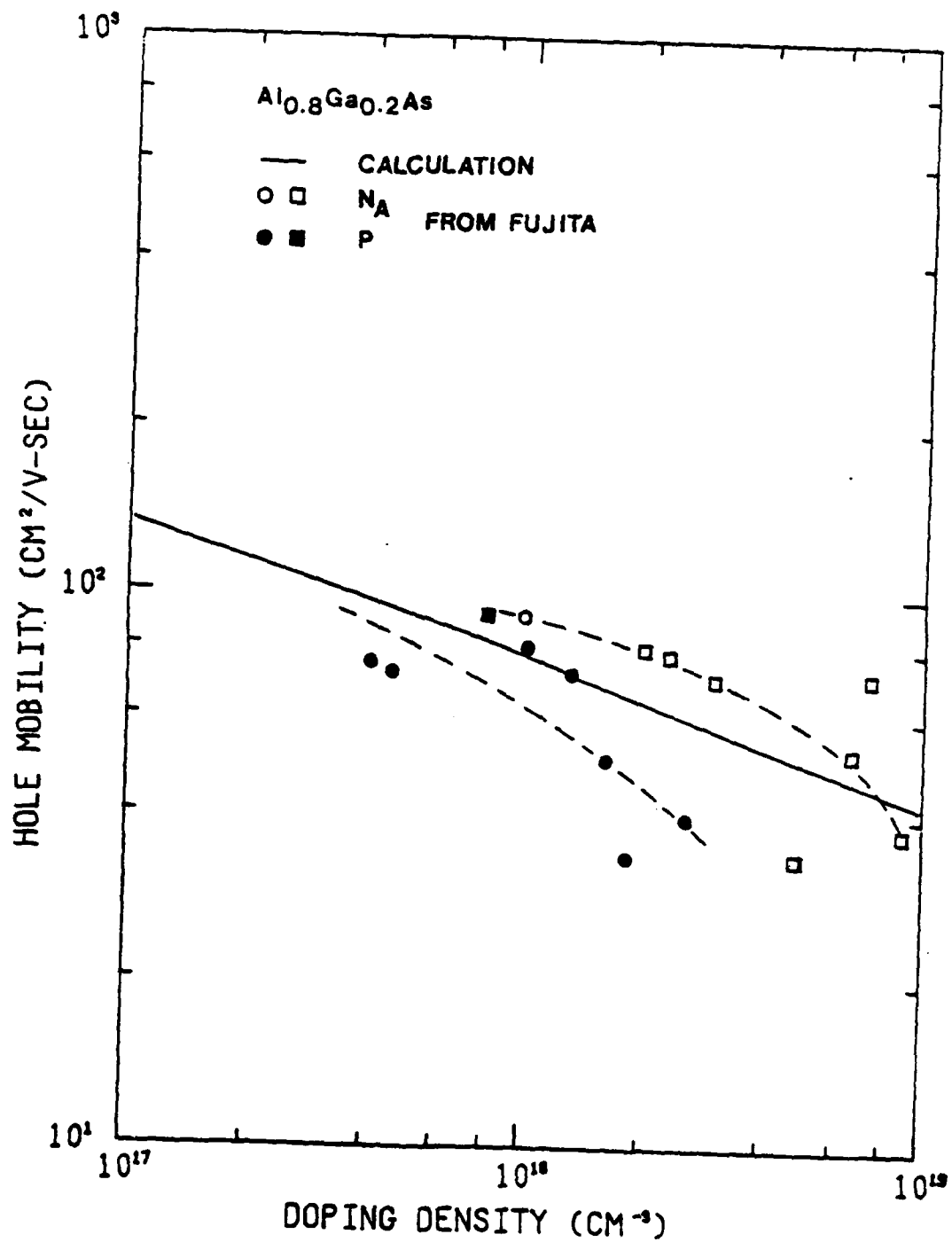


Figure 3.43(a) Relationship between hole mobility and doping density in Al_{0.8}Ga_{0.2}As.

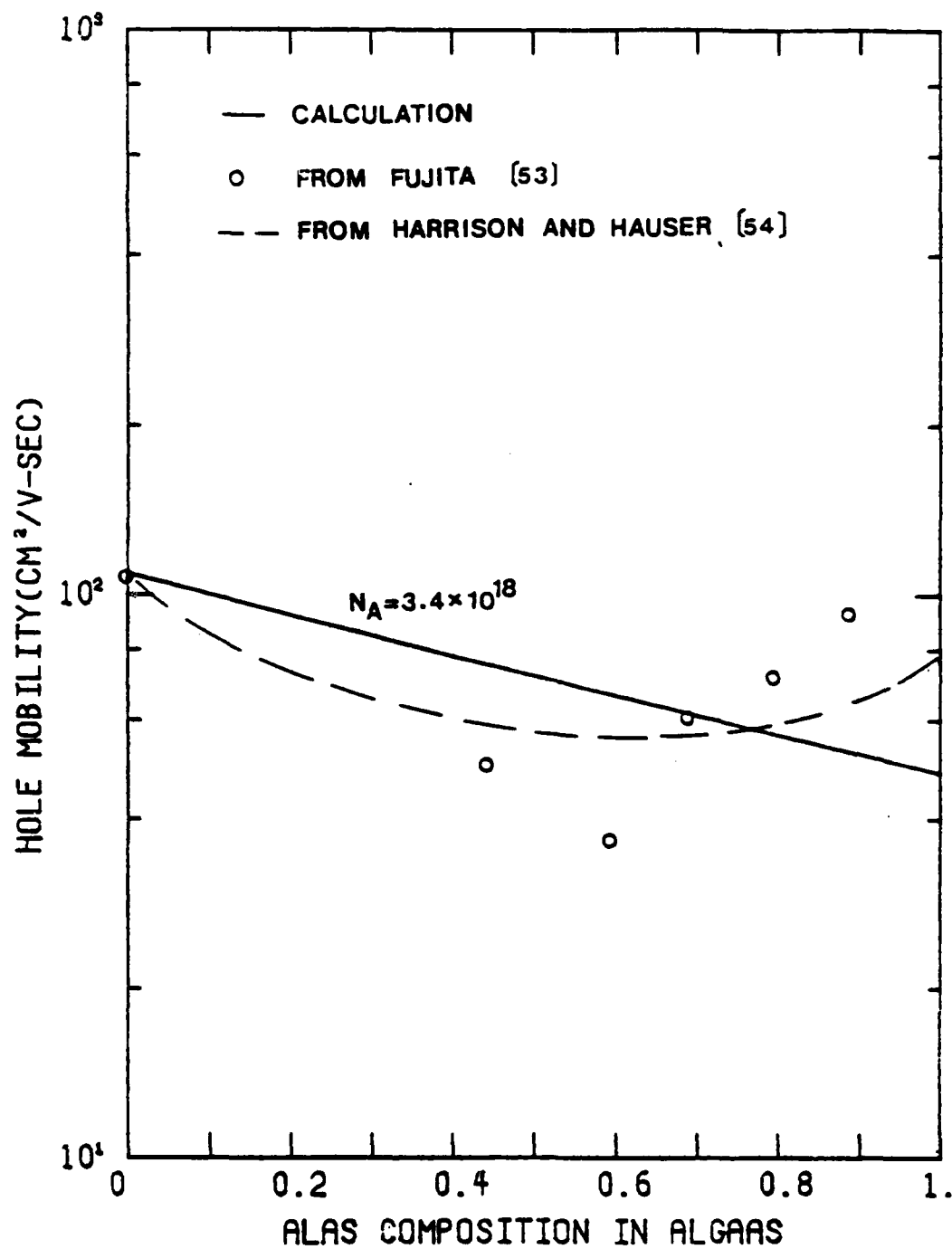


Figure 3.43(b) Relationship between hole mobility and AlAs composition in AlGaAs with a doping density $3.4 \times 10^{18}/\text{cm}^3$.

assuming the optical phonon scattering being the major scattering mechanism becomes more uncertain for the case of high doping density, where ionized impurity scattering is important, and for the case of $\text{Al}_x\text{Ga}_{1-x}\text{As}$ ($x \sim 0.5$), where alloy scattering cannot be neglected [3.13,3.14].

3.2.5.2 Diffusion Length

As given in Equations (2.18) and (2.19), diffusion lengths used to estimate the lifetimes are shown in Figure 3.44. The hole diffusion length measured by the γ -ray technique were around one micron with some uncertainty attributed to the finite thickness of the emitter layer. This diffusion length corresponds to a carrier lifetime one to two orders of magnitude smaller than that used in the theoretical calculation.

3.2.6 Resistance

3.2.6.1 Series Resistance

The I-V characteristics of several samples with high series resistance are shown in Figures 3.45a and 3.45b. Figure 3.46 shows the measured series resistance of a cascade cell as determined by the method described in this section. The series resistance has ranged from 5 to 50 ohms, considerably larger than the 0.2 - 0.25 ohms of conventional Si solar cells. This high series resistance has been found to be due to contact resistance and resistance of the tunnel junction. The resistance due to the tunnel junction can be estimated from the expression derived by Kane [3.15]

$$R^{-1} = \frac{q^2 \sqrt{2m^*}}{4n^2 w} E_g^{1/2} \exp\left(\frac{-4\sqrt{2m^*} E_g^{1/2} w}{3\pi}\right), \quad (3.21)$$

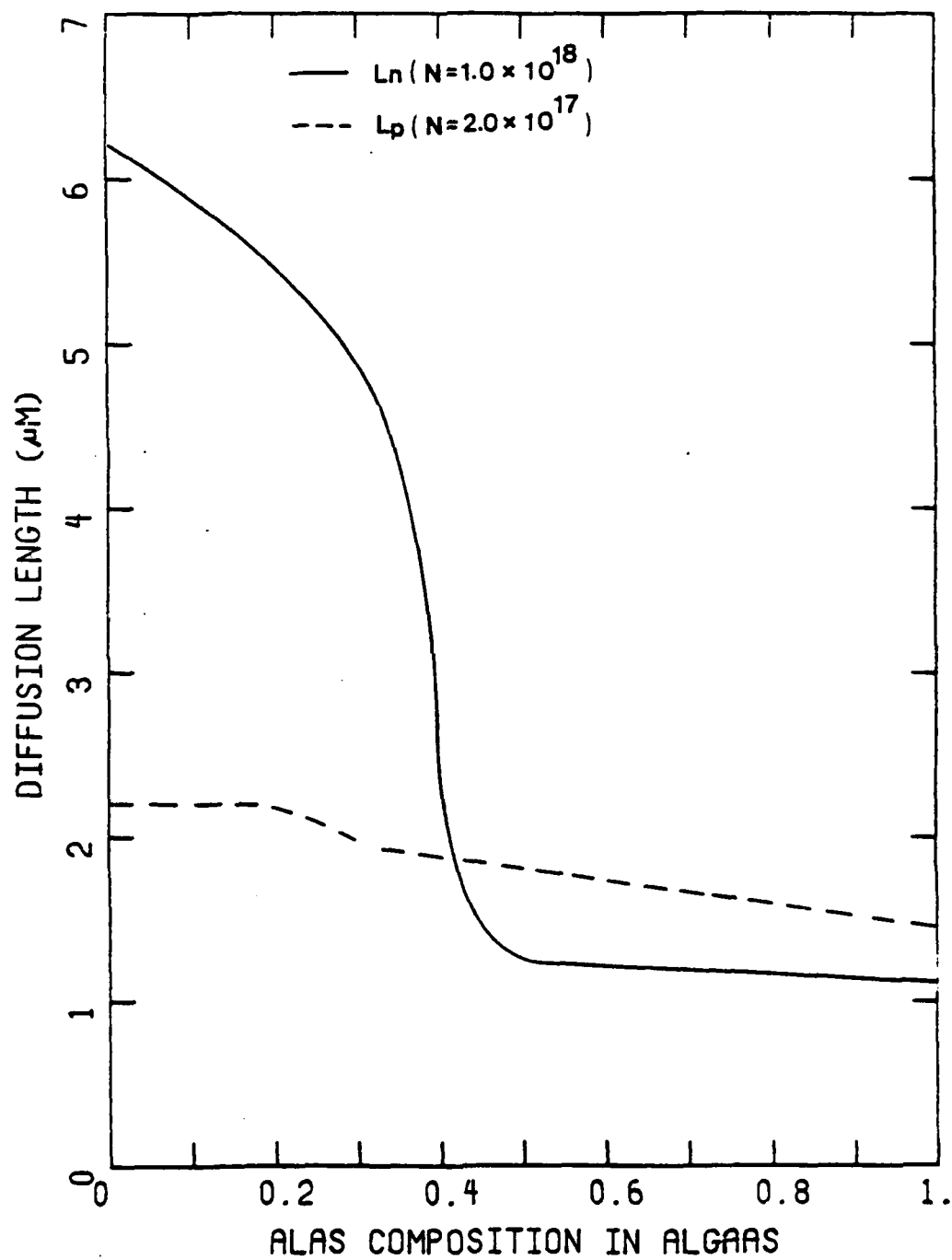
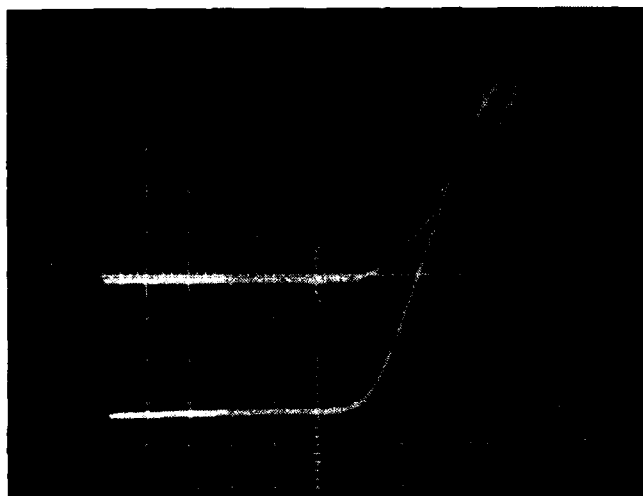


Figure 3.44 Dependence of diffusion lengths on AlAs composition in AlGaAs.



Sample No. G220D

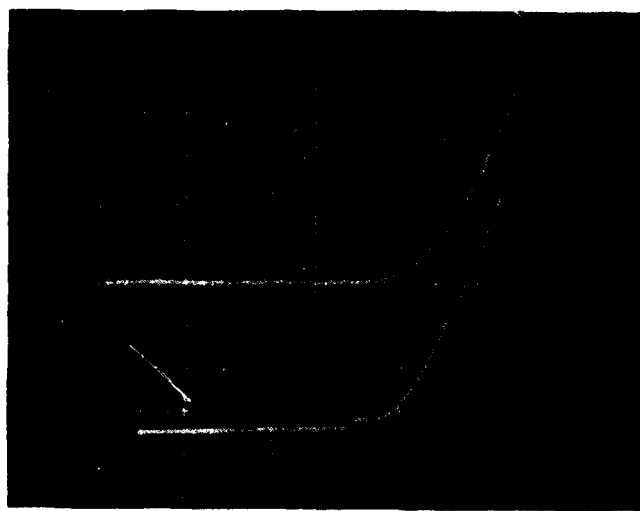
Scale

Ver. 0.02 mA/div

Hor. 0.5 V/div

Illumination: 1 AMO

Figure 3.45(a). Effect of high series resistance on I-V characteristics of a cascade cell.



Sample No. G220D

Scale

Ver. 0.02 mA/div

Hor. 0.5 V/div

Illumination: 1 AMO

Figure 3.45(b). Effects of high series resistance on I-V characteristics of cascade cells.

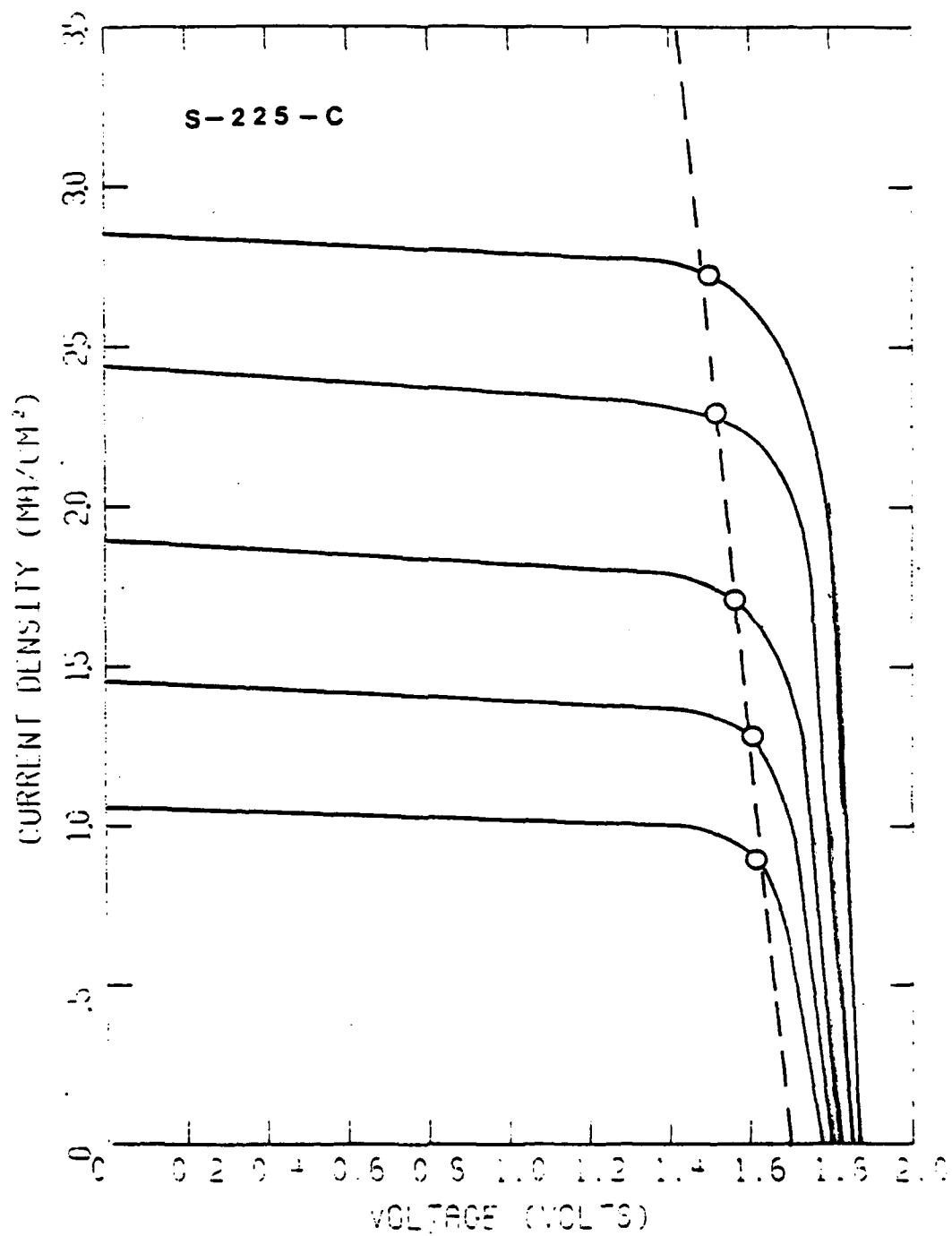


Figure 3.46 Series resistance measurement for a cascade cell.

where m^* is the tunneling particle mass, E_g is the bandgap and w is the junction depletion width, and the other symbols have their usual meanings. Using this expression to calculate the junction resistivity of GaAs tunnel diodes, Fraas and Knechtli [3.16] noticed that the resistance was so sensitive to depletion width w that it varied by one order of magnitude as w varying by 20Å. AlGaAs tunnel junction diodes with a bandgap of 1.6 eV have been reported to have a resistance of less than 0.78 ohm (see Section 2.3.2.3). The increase in resistance with increased bandgap can be understood from the exponential dependence on E_g as given in Equation (3.21). The difficulty of achieving a heavily doped layer for the high bandgap material results in a wider depletion width. This wide depletion width further increases the resistance of the tunnel junction.

Figures 3.47a, 3.47b, and 3.47c show the theoretical effect of series resistance on the I-V characteristics of three illuminated cells. The open circuit voltage remains unchanged by the reduction of short circuit current when the series resistance is so large that the voltage drop across the diode causes a significant amount of dark current in opposition to the photocurrent.

The fill factor is seriously reduced due to series resistance as shown in Figure 3.48. As shown in Figures 3.49a, 3.49b, and 3.49c, the voltage V_m at the maximum power point shifts to lower voltages as the series resistance increases. Since the fill factor is proportional to the voltage V_m at a given open circuit voltage, the decrease of V_m results in a reduction of fill factor. The reduction of efficiency as a result of series resistance effects is shown in Figure 3.50. From this figure, it can be seen that a series resistance of 30 ohms, as measured for most cascade cells, results in a one percentage point loss in efficiency.

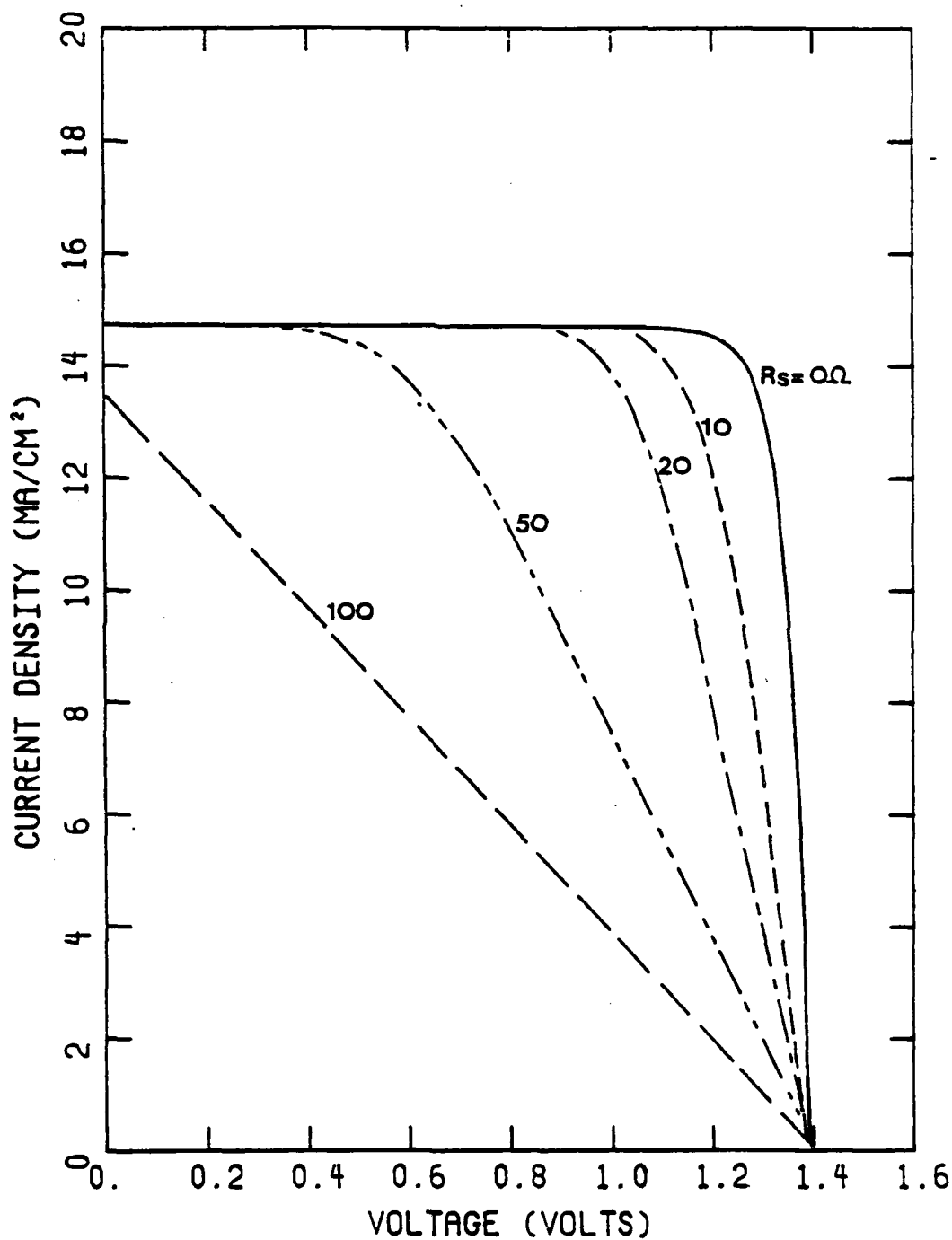


Figure 3.47(a) Series resistance effect on I-V characteristics of the top cell under AMO illumination.

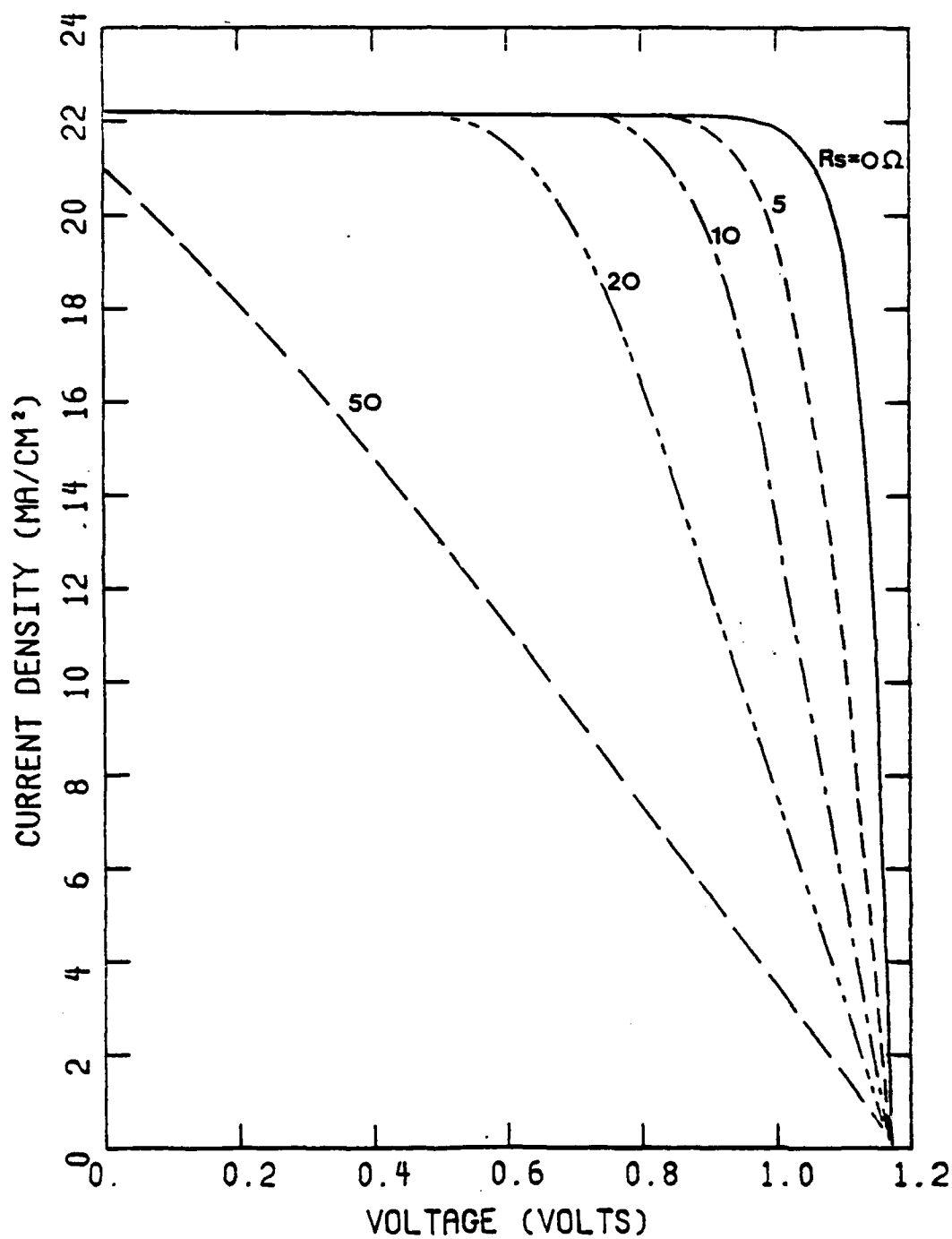


Figure 3.47(b) Series resistance effect on I-V characteristics of the bottom cell under AMO illumination.

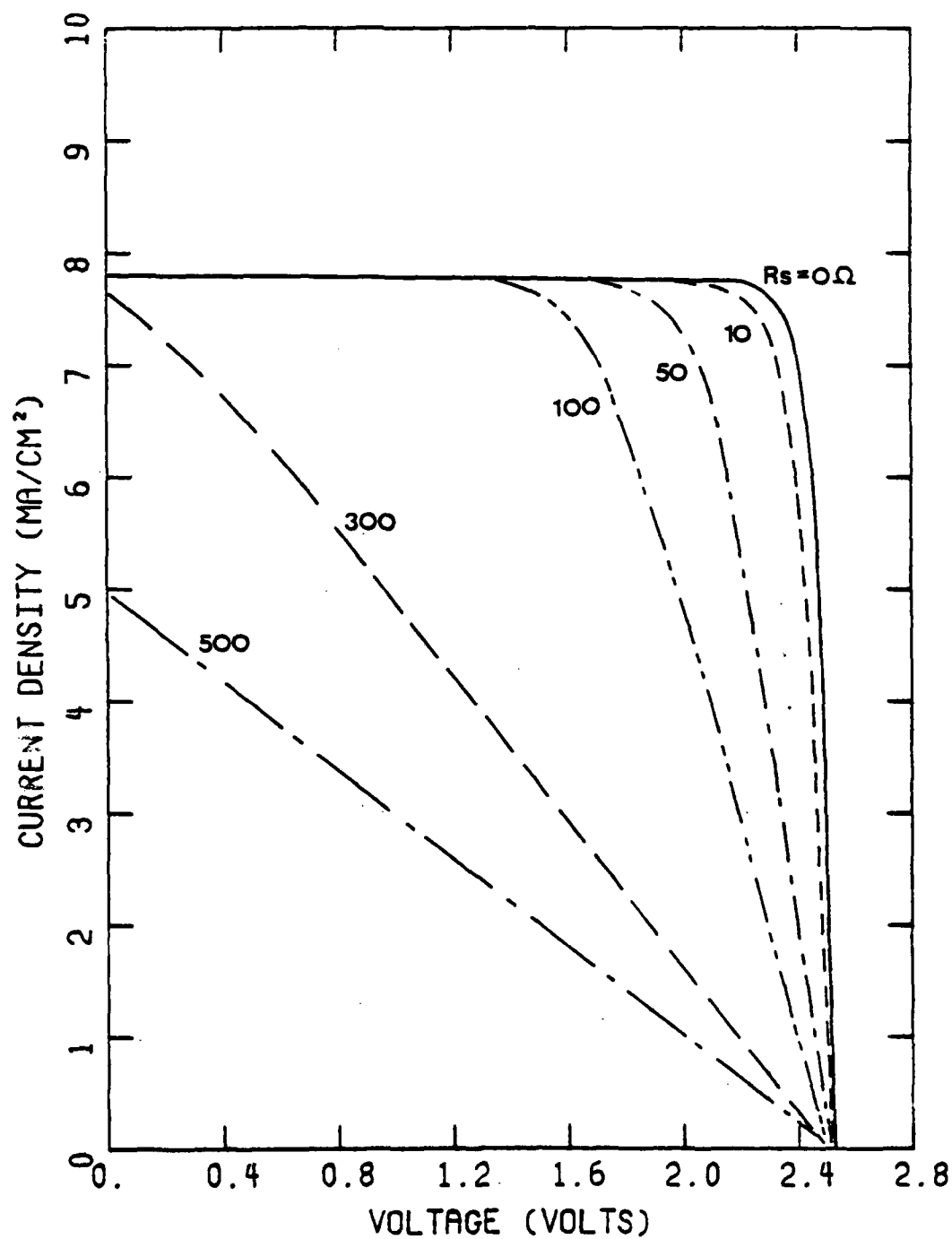


Figure 3.47(c) Series resistance effect on I-V characteristics of the cascade cell under AMO illumination.

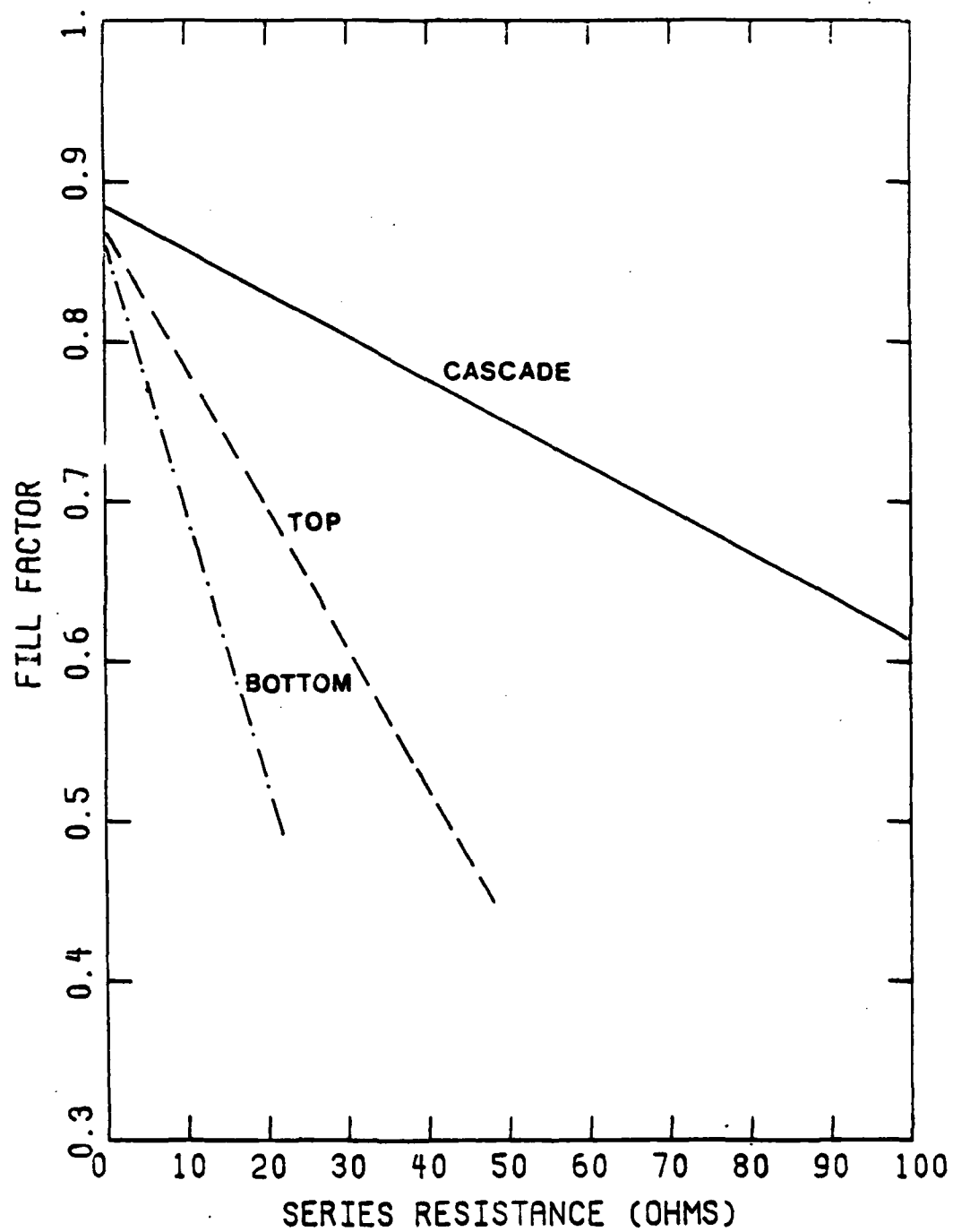


Figure 3.48 Series resistance effect on fill factors of solar cells.

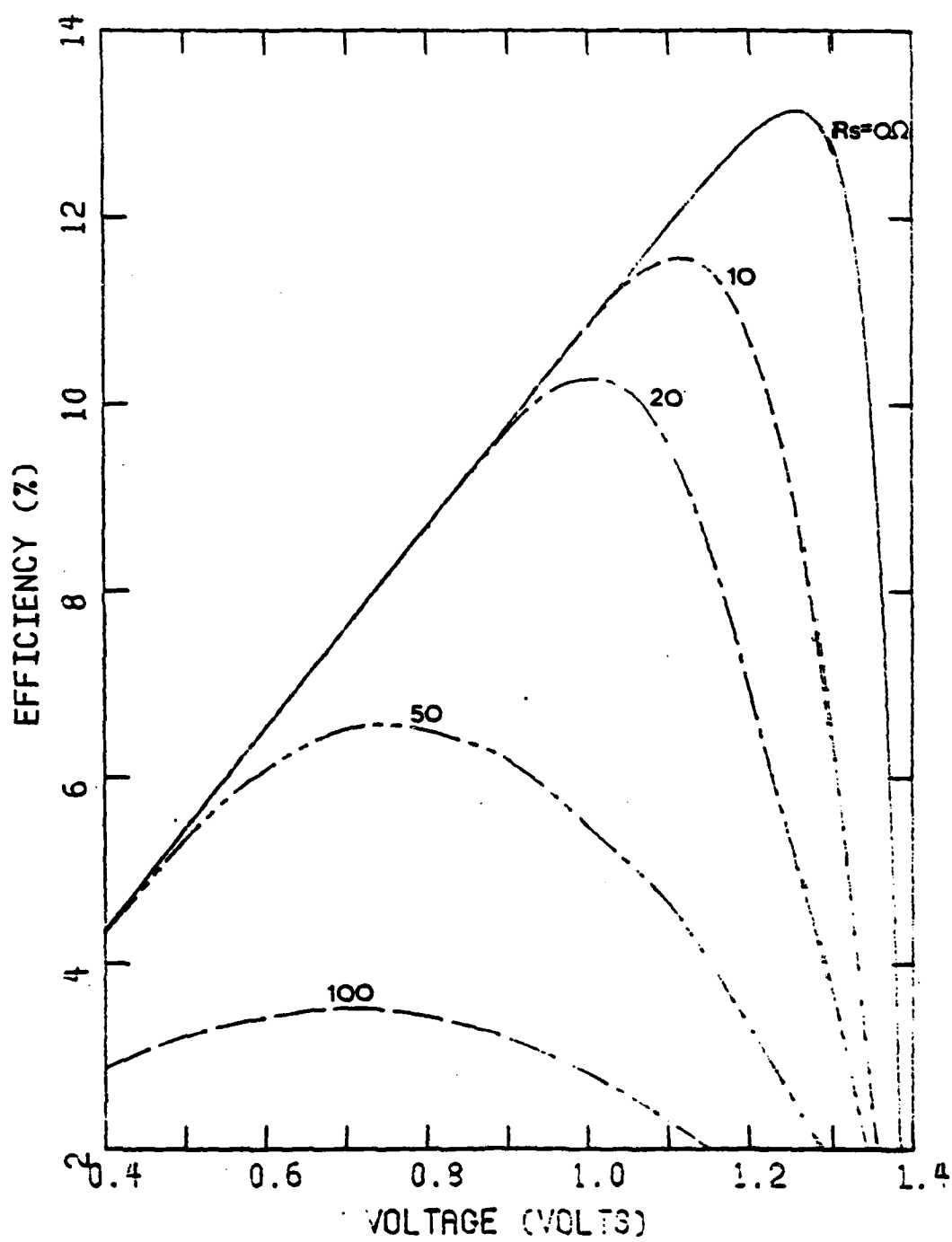


Figure 3.49(a) Series resistance effect on efficiency of the top cell under AM0 illumination.

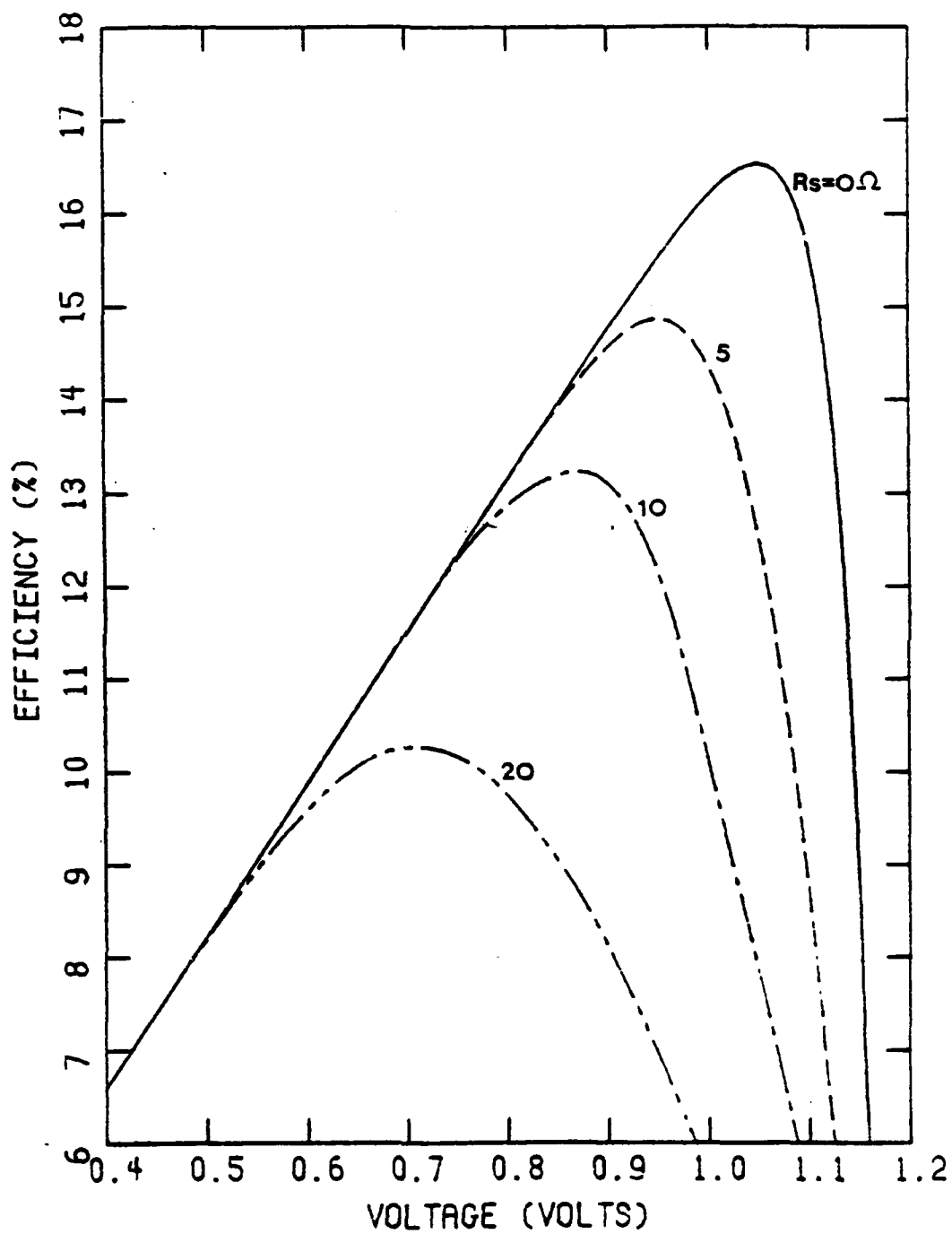


Figure 3.49(b) Series resistance effect on efficiency of the bottom cell under AMO illumination.

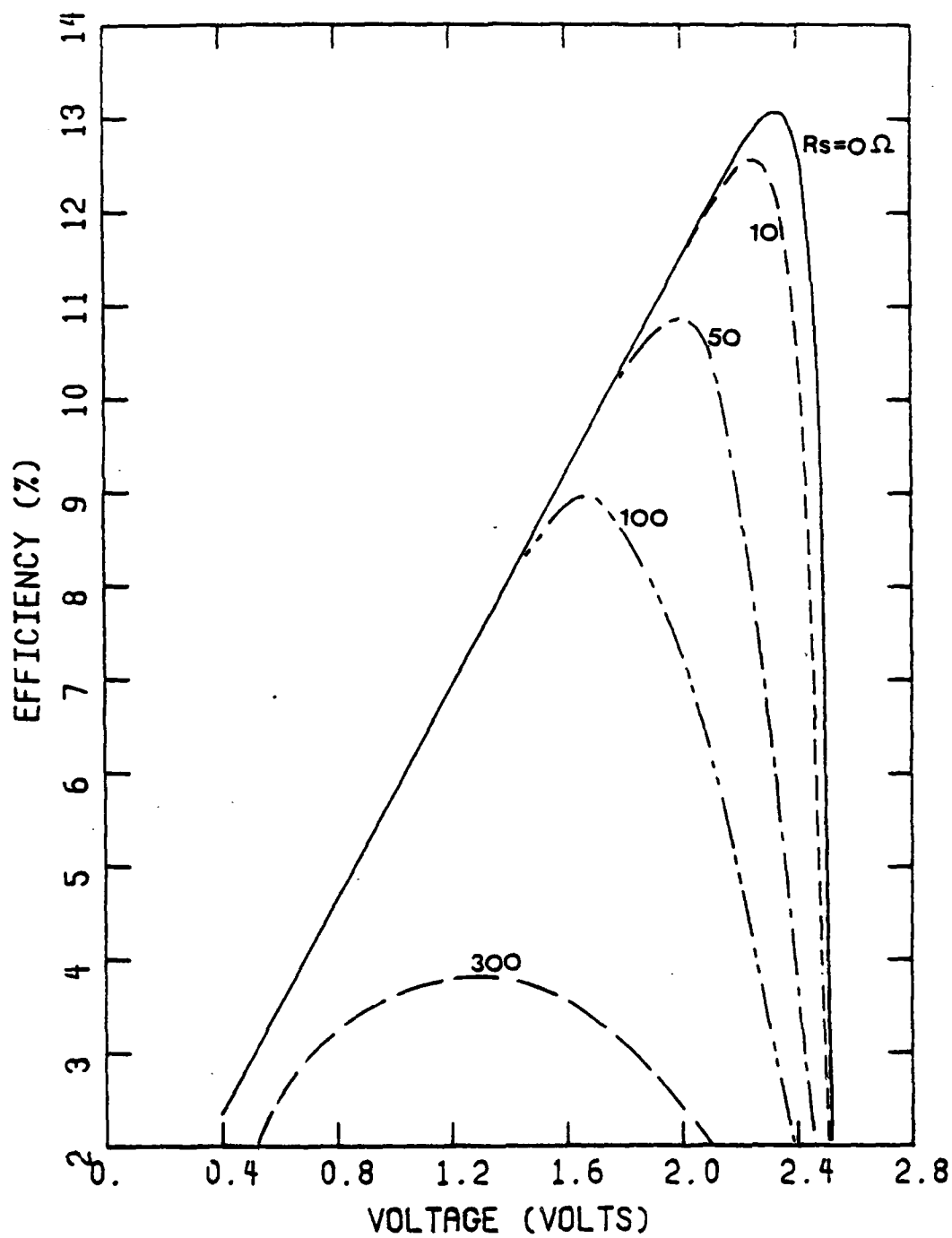


Figure 3.49(c) Series resistance effect on efficiency of the cascade cell under AMO illumination.

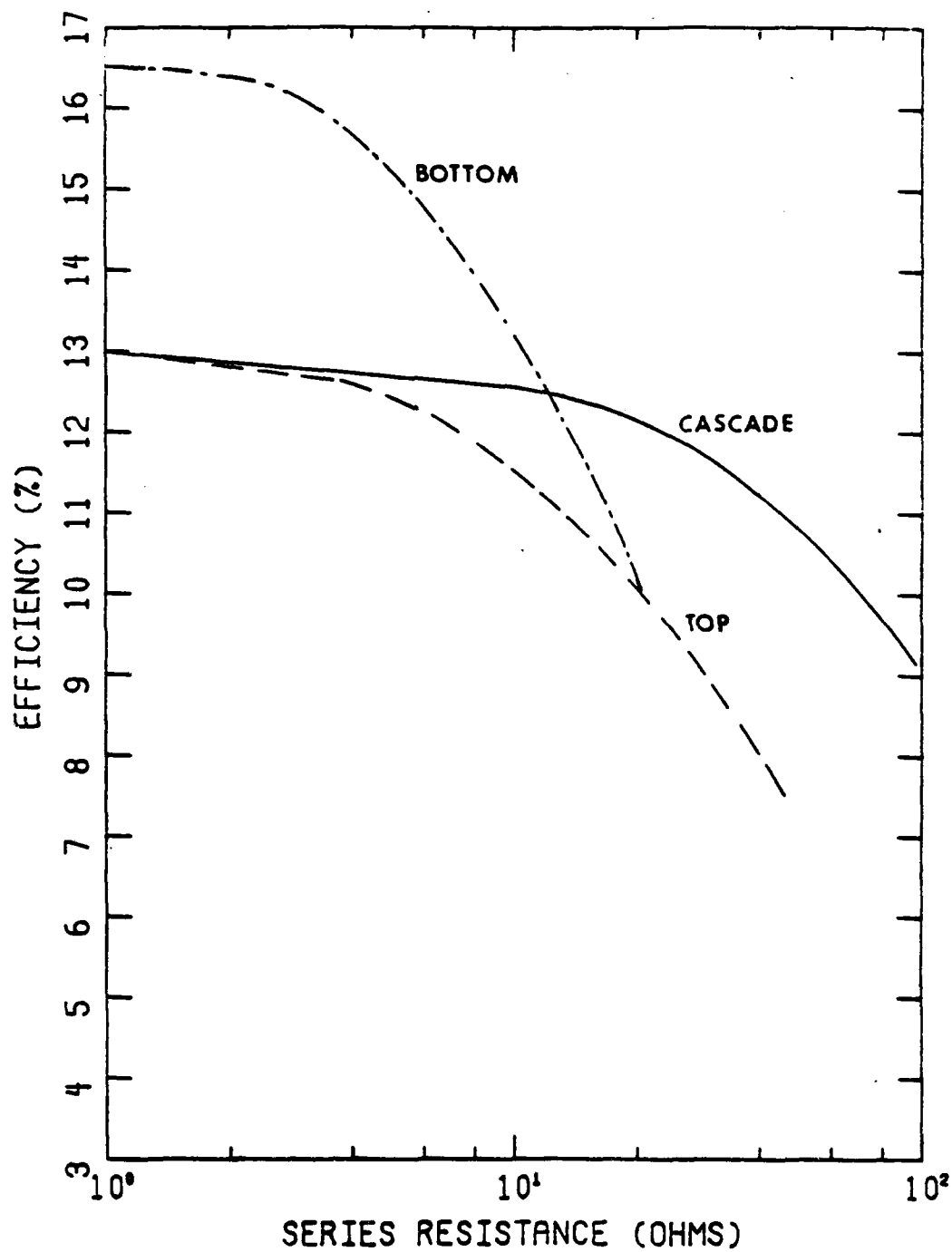


Figure 3.50 Series resistance effect on efficiencies of solar cells.

AD-A128 588

DEVELOPMENT OF HIGH EFFICIENCY STACKED MULTIPLE BANDGAP
SOLAR CELLS..(U) RESEARCH TRIANGLE INST RESEARCH
TRIANGLE PARK NC S M BEDAIR ET AL. SEP 82

3/3

UNCLASSIFIED

RTI/1878/00-F-VOL-2 AFAPL-TR-79-2116-VOL-2 F/G 10/2

NL

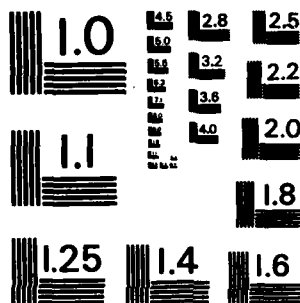
END

DATE

FILED

089

DTIC



MICROCOPY RESOLUTION TEST CHART
NATIONAL BUREAU OF STANDARDS-1963-A

The calculated results for series resistance effects on the dark I-V characteristics are shown in Figures 3.51a, 3.51b, and 3.51c. The series resistance effect becomes increasingly important at high forward bias where the diffusion current should be dominant. This indicates that in the determination of the diode factor from dark I-V measurements, a region dominated by the diffusion current cannot be found unless the series resistance is relatively small.

3.2.6.2 Shunt Resistance

The effect of shunt resistance on the I-V characteristics is shown in Figures 3.52a, 3.52b, and 3.52c. A low shunt resistance reduces the open circuit voltage and the fill factor, but the short circuit current is virtually unaffected. The dependence of efficiency on the terminal voltage with various shunt resistances is shown in Figures 3.53a, 3.53b, and 3.53c. The effect on peak efficiency is shown in Figure 3.54. As the calculated results indicate, shunt resistance effects are not very significant unless the value of the shunting resistance becomes less than 10^3 ohm for individual top and bottom cells, or less than 10^4 ohm for cascade cells. The effect of a shunt resistance is larger in cascade cells due to the higher output voltage. This results in a larger leakage current for the same shunting resistance. The measured shunt resistance for good cells is 10^6 ohm which is large enough to have little effect on the cell performance at one solar intensity. Some cells, however, show resistances less than 10^4 ohm due to junction leakage. The junction leakage is mainly due to crystal defects. Figures 3.55a, 3.55b, and 3.55c show the effects of shunt resistance on dark I-V characteristics.

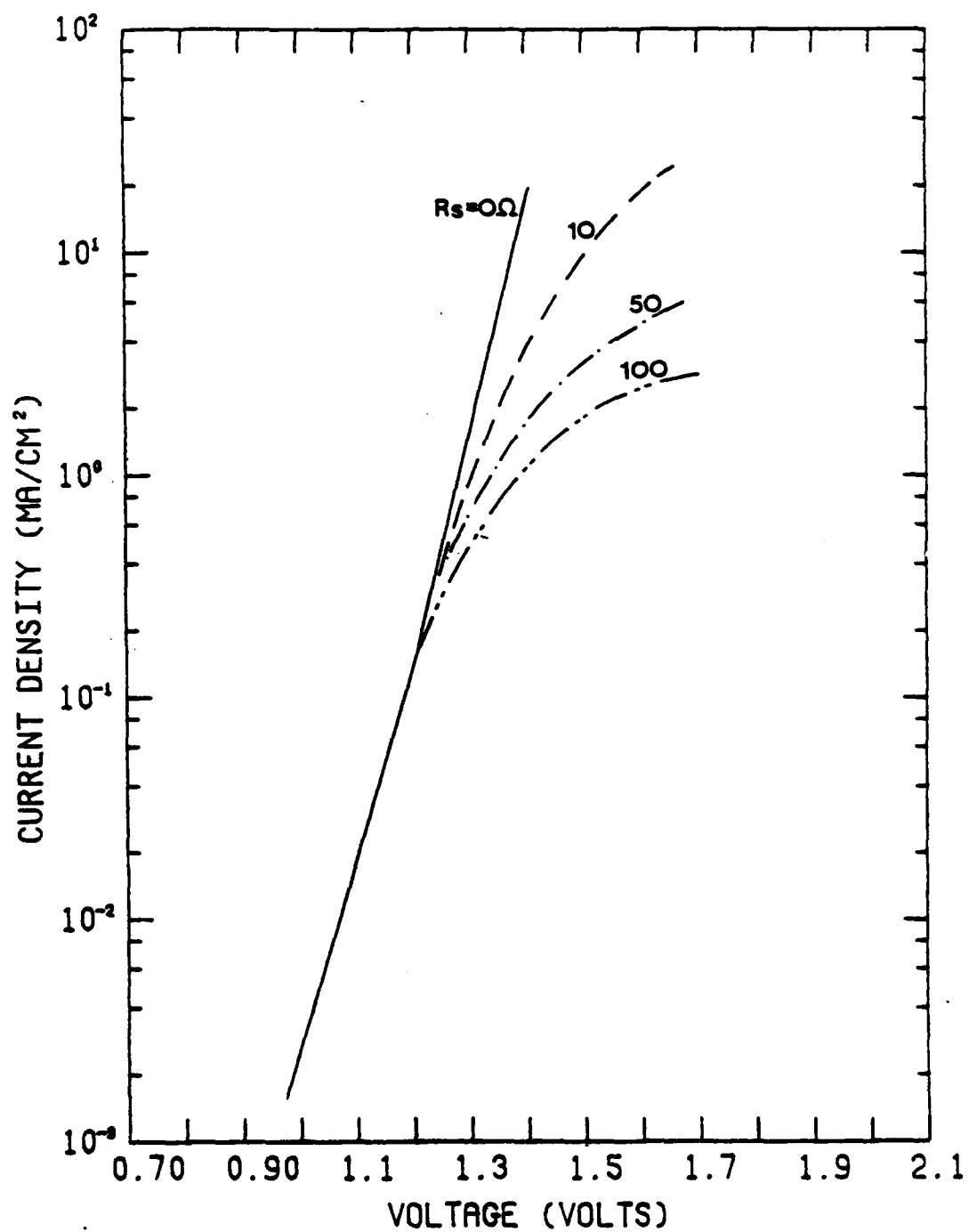


Figure 3.51(a) Series resistance effect on dark I-V characteristics of the top cell.

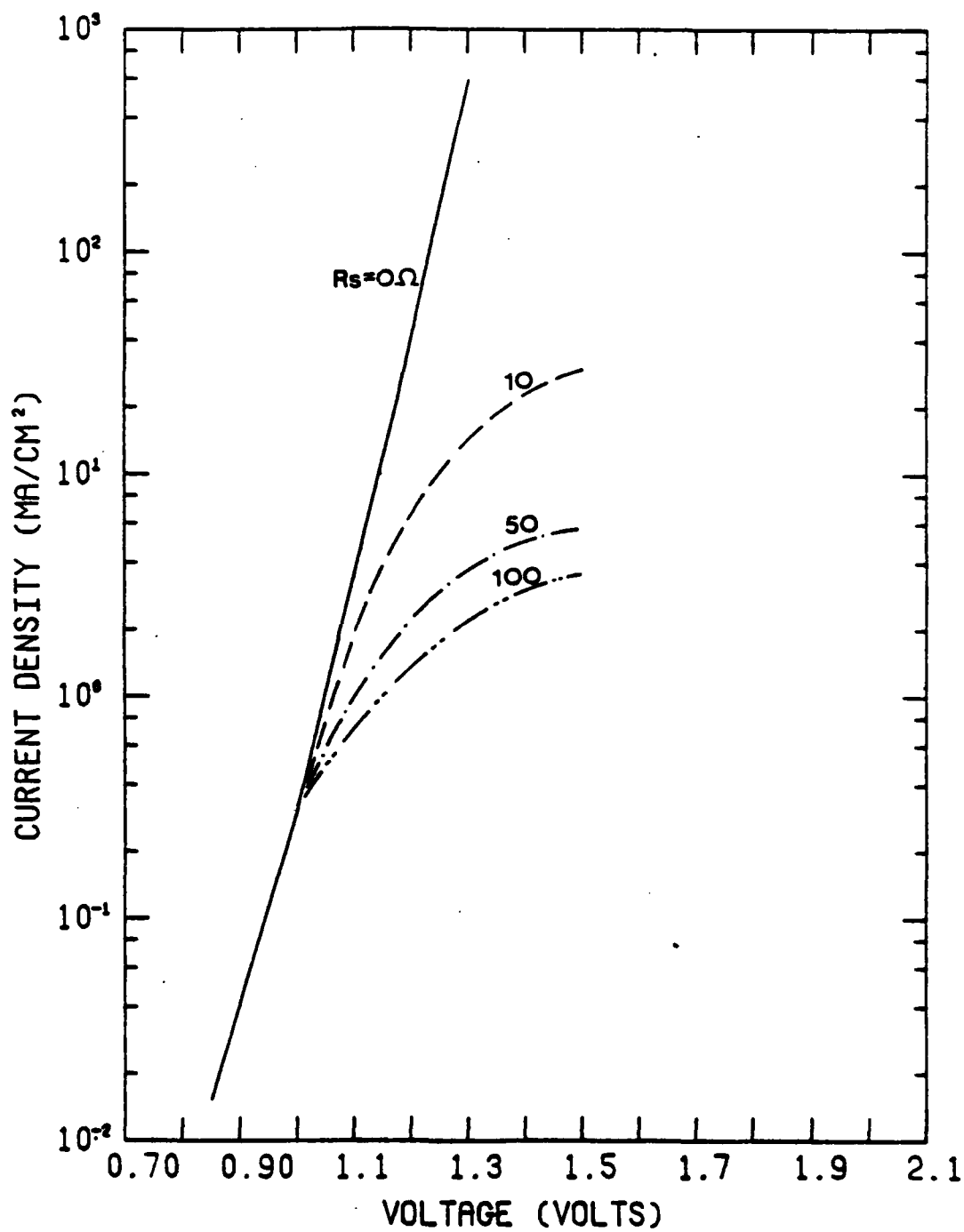


Figure 3.51(b) Series resistance effect on dark I-V characteristics of the bottom cell.

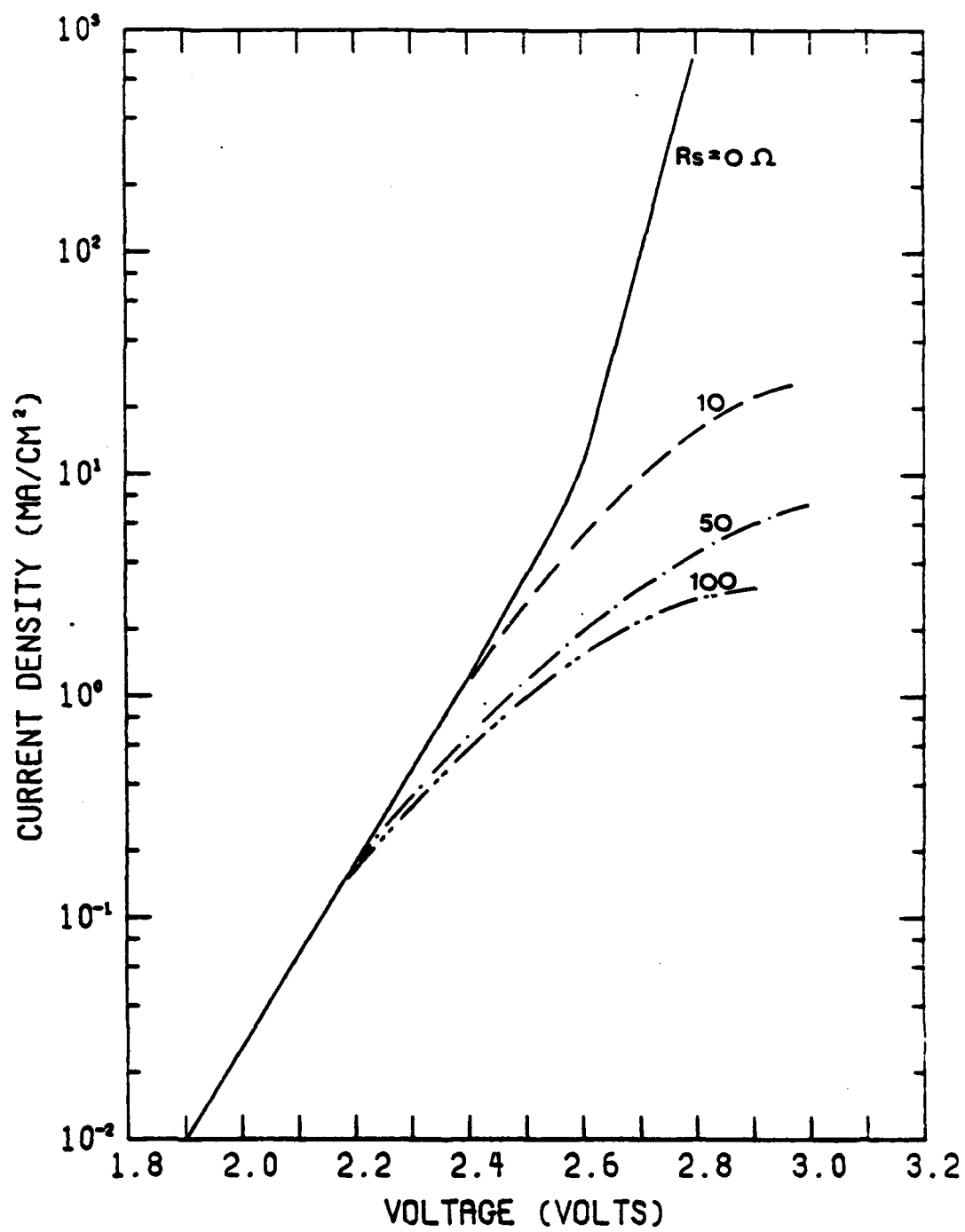


Figure 3.51(c) Series resistance effect on dark I-V characteristics of the cascade cell.

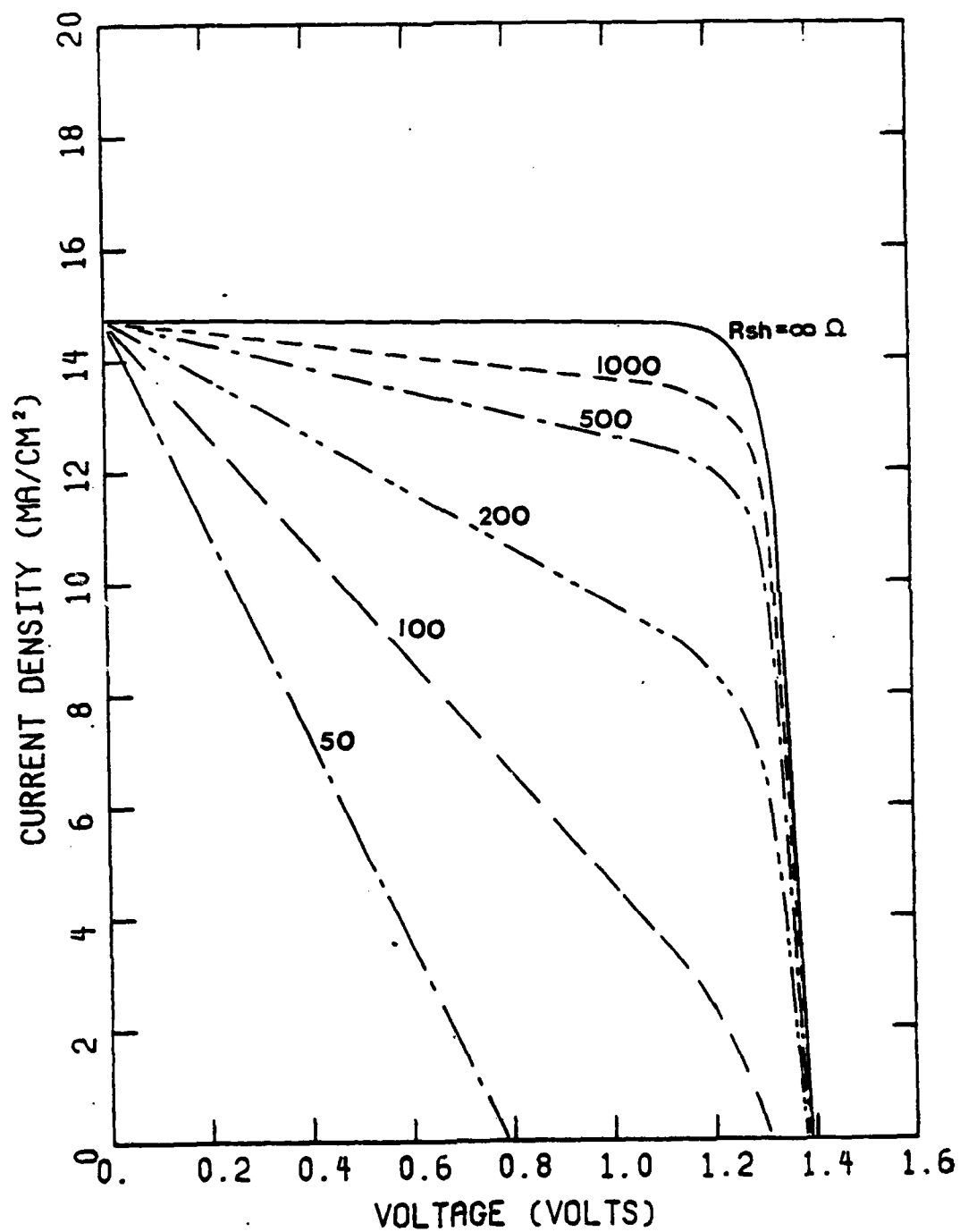


Figure 3.52(a) Shunt resistance effect on I-V characteristics of the top cell under AM0 illumination.

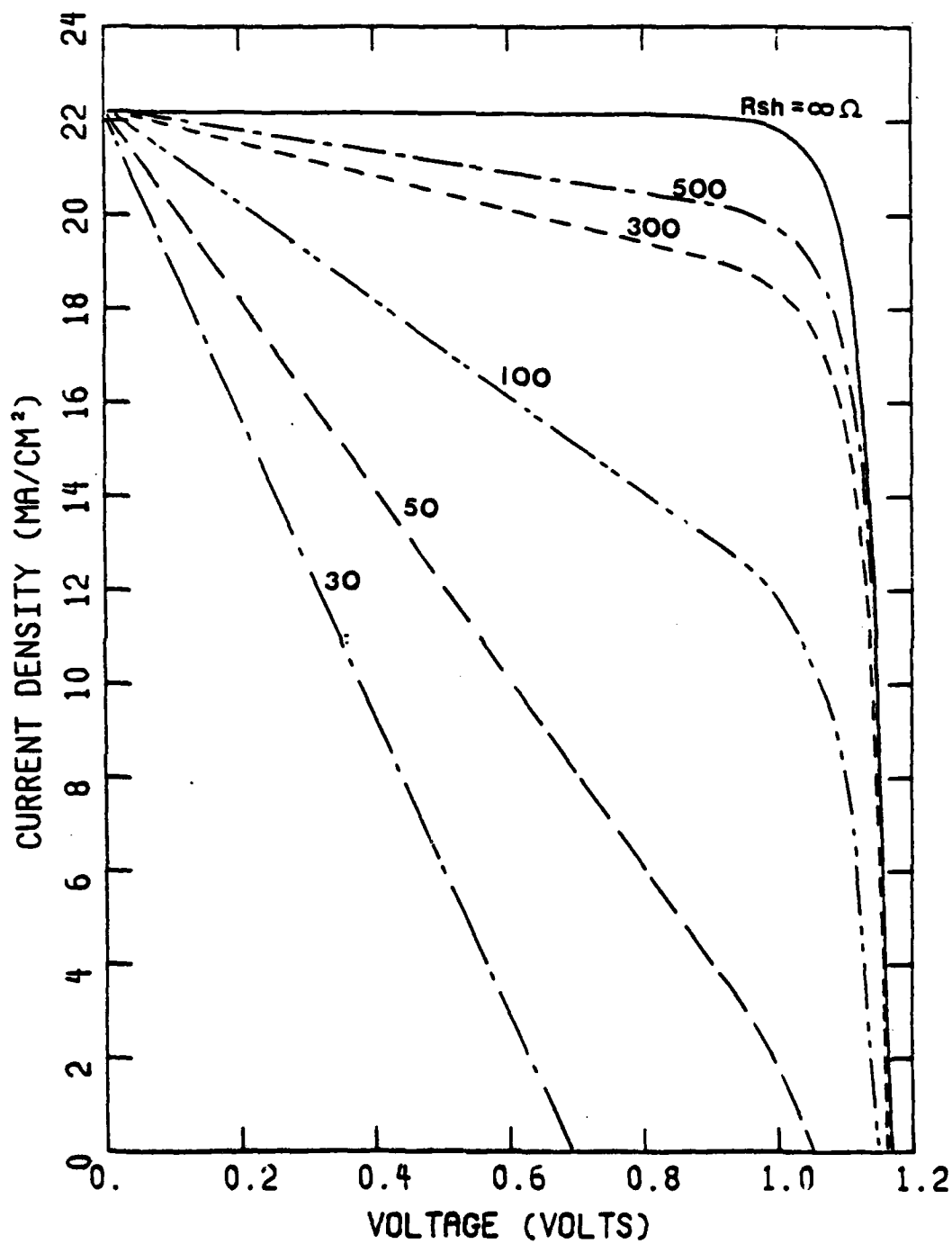


Figure 3.52(b) Shunt resistance effect on I-V characteristics of the bottom cell under AMO illumination.

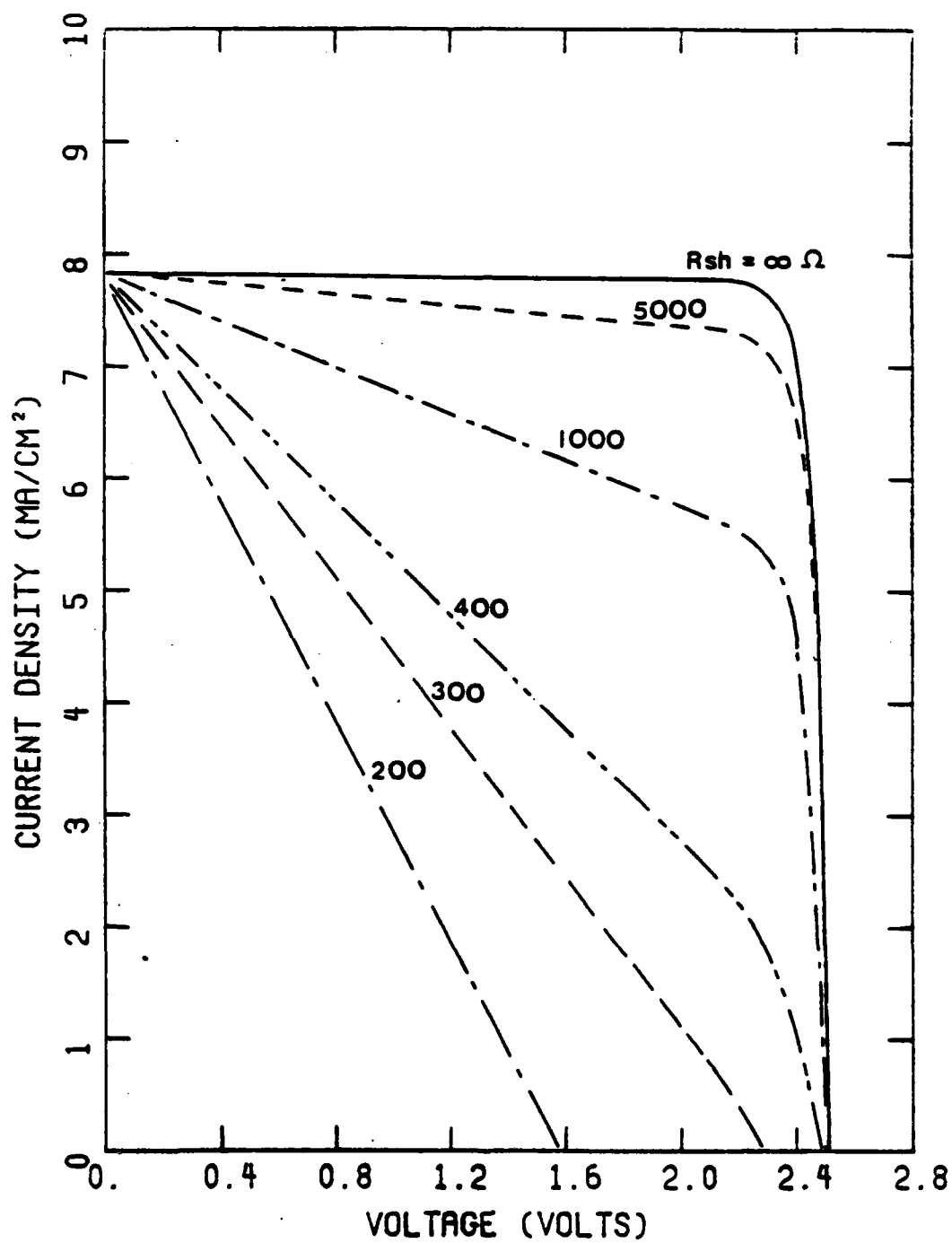


Figure 3.52(c) Shunt resistance effect on I-V characteristics of the cascade cell under AMO illumination.

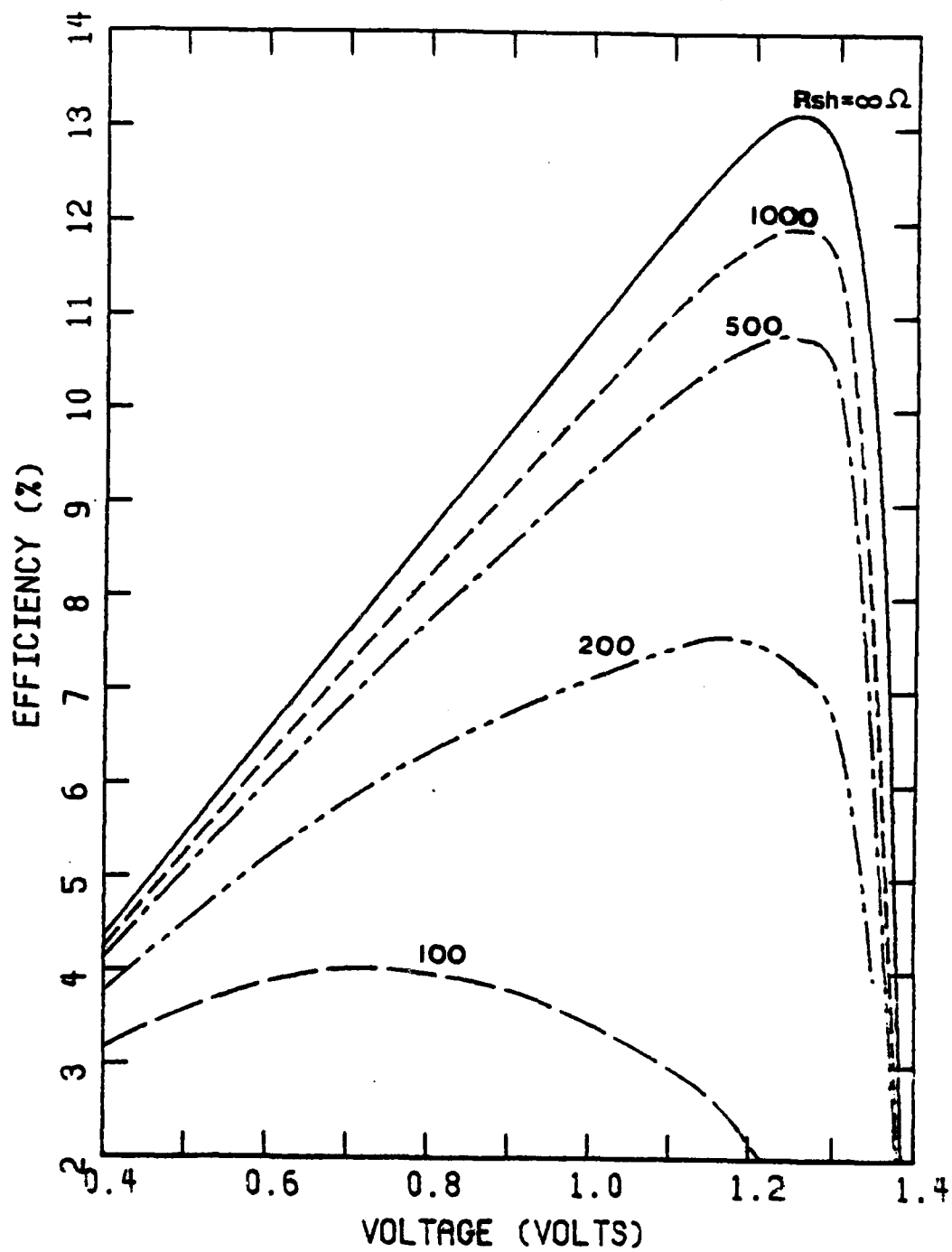


Figure 3.53(a) Shunt resistance effect on efficiency of the top cell under AMO illumination.

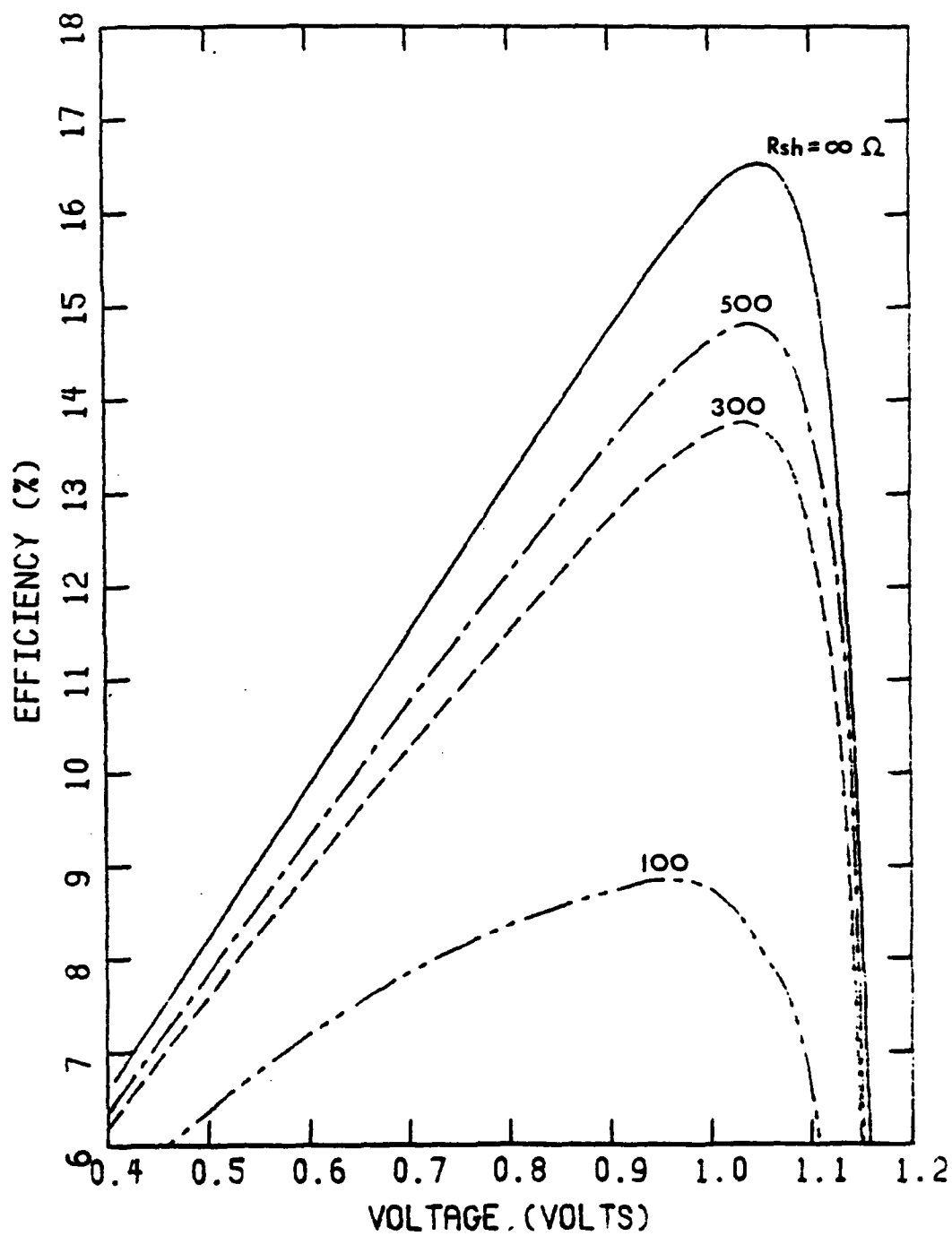


Figure 3.53(b) Shunt resistance effect on efficiency of the bottom cell under AMO illumination.

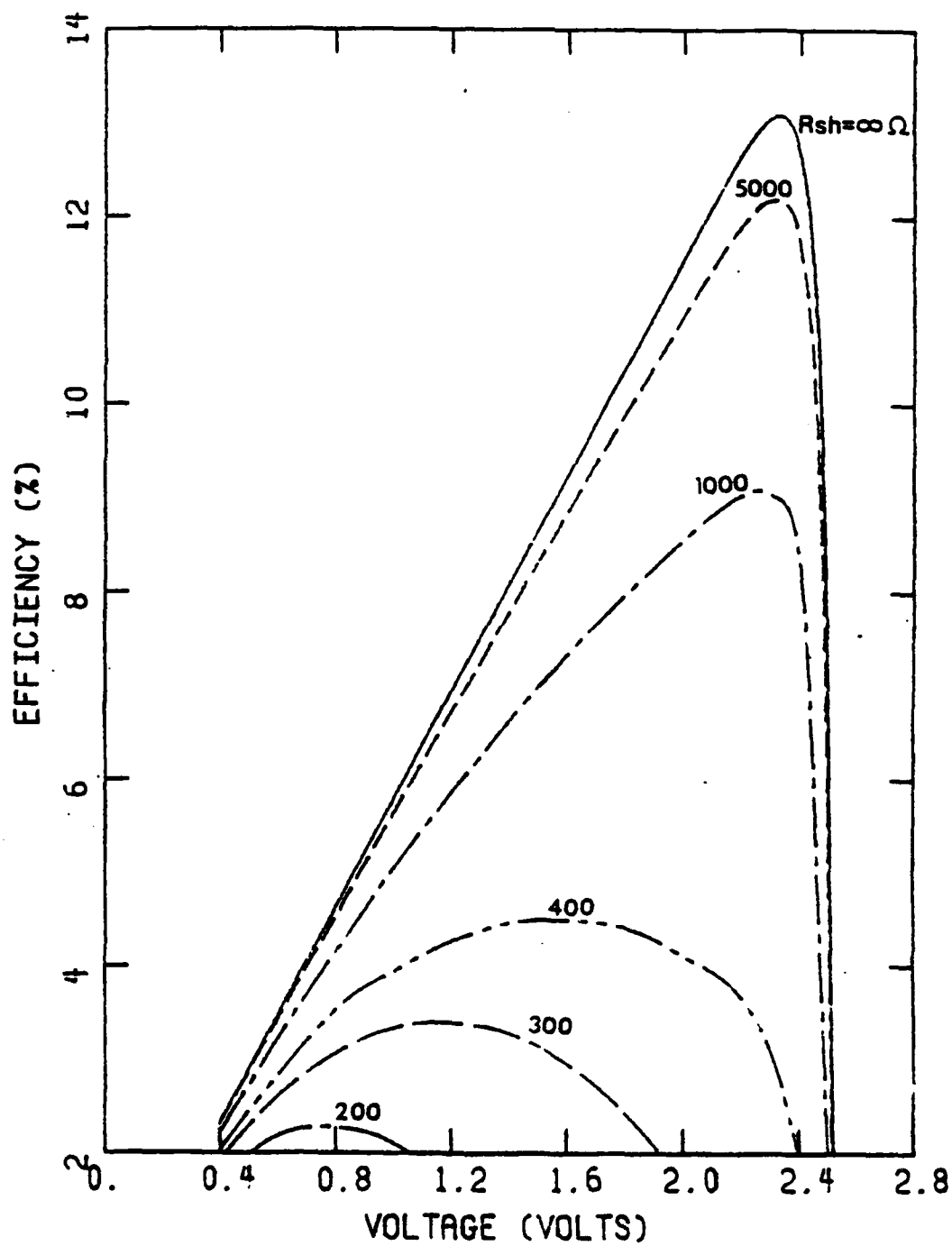


Figure 3.53(c) Shunt resistance effect on efficiency of the cascade cell under AMO illumination.

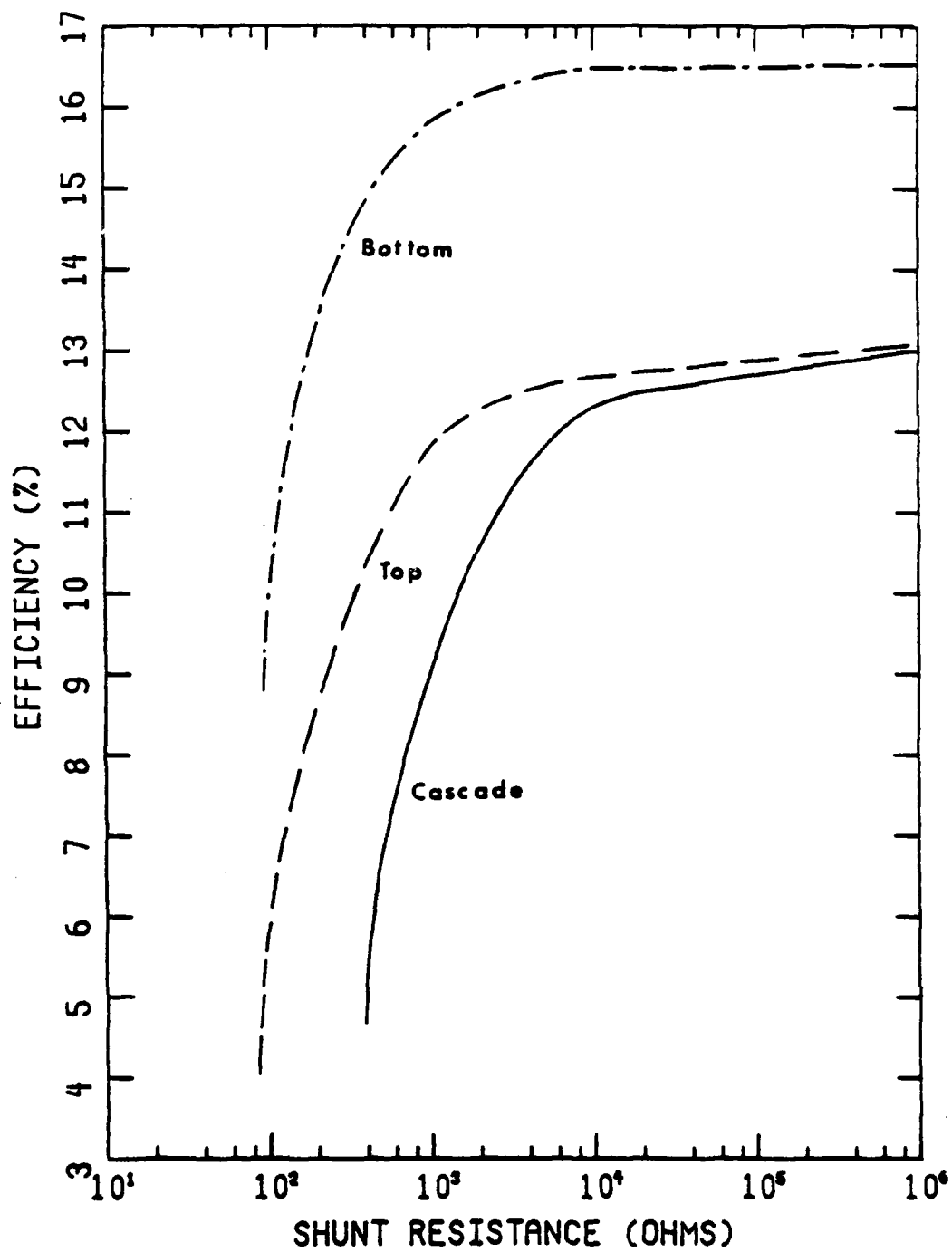


Figure 3.54 Shunt resistance effect on efficiencies of solar cells.

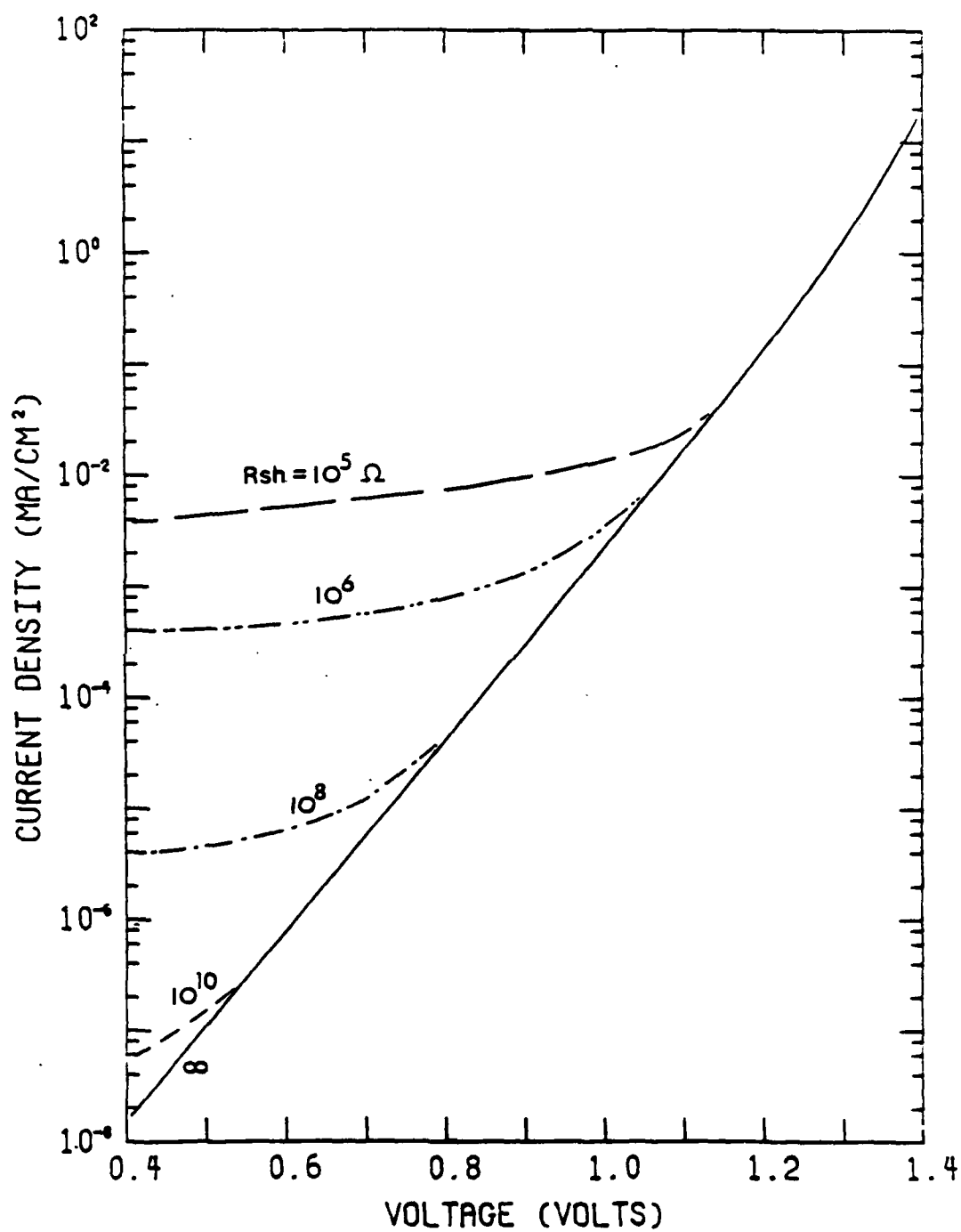


Figure 3.55(a) Shunt resistance effect on dark I-V characteristics of the top cell.

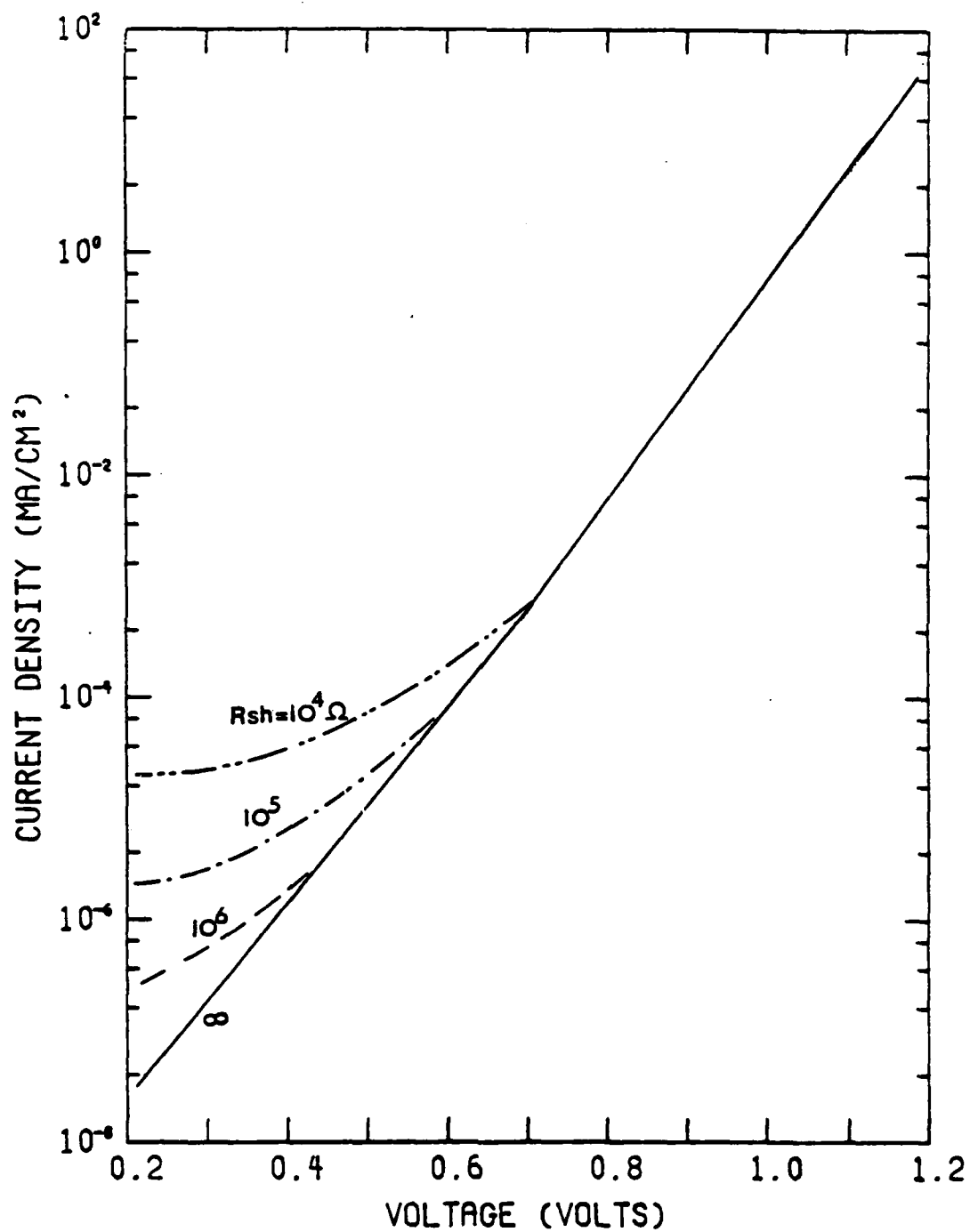


Figure 3.55(b) Shunt resistance effect on dark I-V characteristics of the bottom cell.

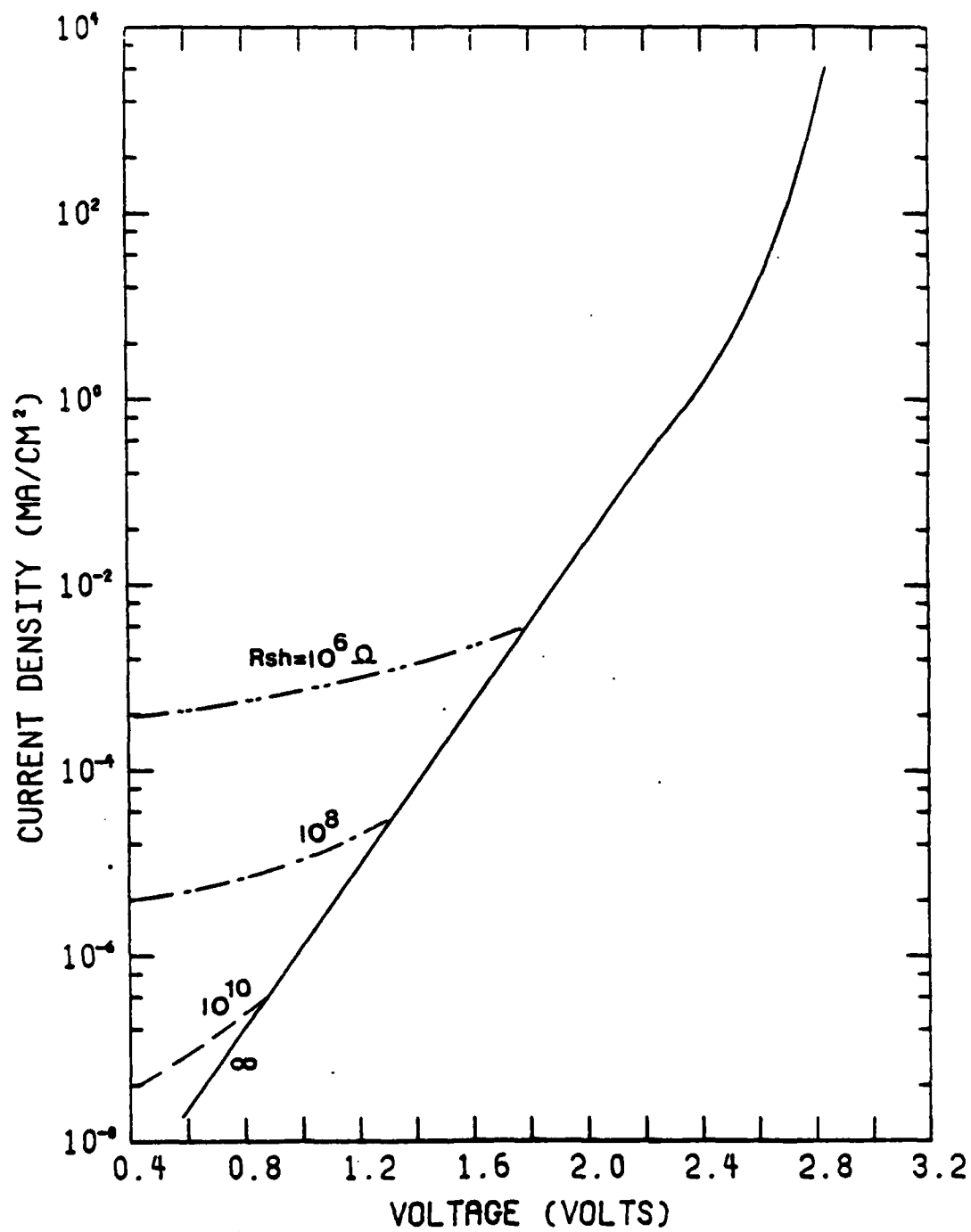


Figure 3.55(c) Shunt resistance effect on dark I-V characteristics of the cascade cell.

The fact that the shunt resistance takes on increased importance at low bias voltage indicates more attention must be paid to this effect for solar cells operated at low illumination levels. As can be seen in Figures 3.56a and 3.56b, the experimental results agree very well with the theoretical calculation when short carrier lifetimes are assumed for the bottom cell.

3.2.6.3 Contact Resistance

(See Section 2.3.3.1.)

3.2.7 Summary of Best Results

The preceding sections have explored in some detail the correlation between experimentally observed cascade characteristics and the results predicted by computer simulation. It is seen that a number of factors acting on I_{sc} , V_{oc} , and FF can have a pronounced effect on overall efficiency. Several of these factors are intimately related to the crystalline quality of the various epitaxial layers (see especially Section 2.3.2.3). The lateral distribution of these imperfections over the grown area is somewhat random. Thus it is to be expected that, with the small area ($\sim 1 \times 10^{-2} \text{ cm}^2$) devices fabricated in this program, some of these devices will be relatively free from the effects of these imperfections. These devices will have characteristics dependent on the design of the cell rather than on the dominant influence of material defects. The best of these devices had $V_{oc} = 2.13\text{V}$, $I_{sc} = 13 \text{ mA cm}^{-2}$, and FF = 0.74 for an active area efficiency of 15.1%.

These results support the belief that higher efficiencies can be achieved if the material problems stemming from the tunnel junction can be solved. Another illustration of this belief is shown in Table 3.3

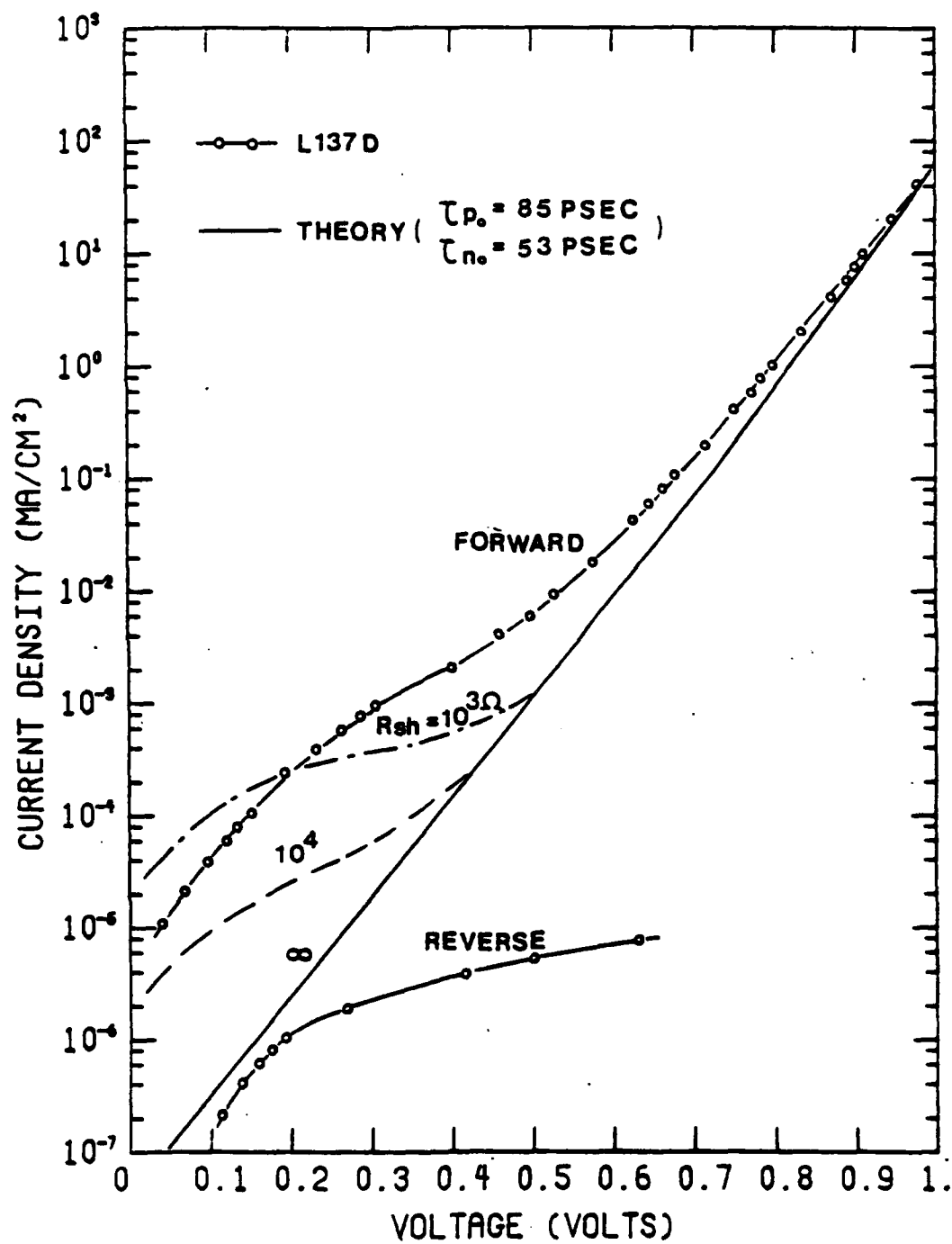


Figure 3.56(a) Comparison of the calculated dark I-V characteristics and experimental measurements of a bottom cell.

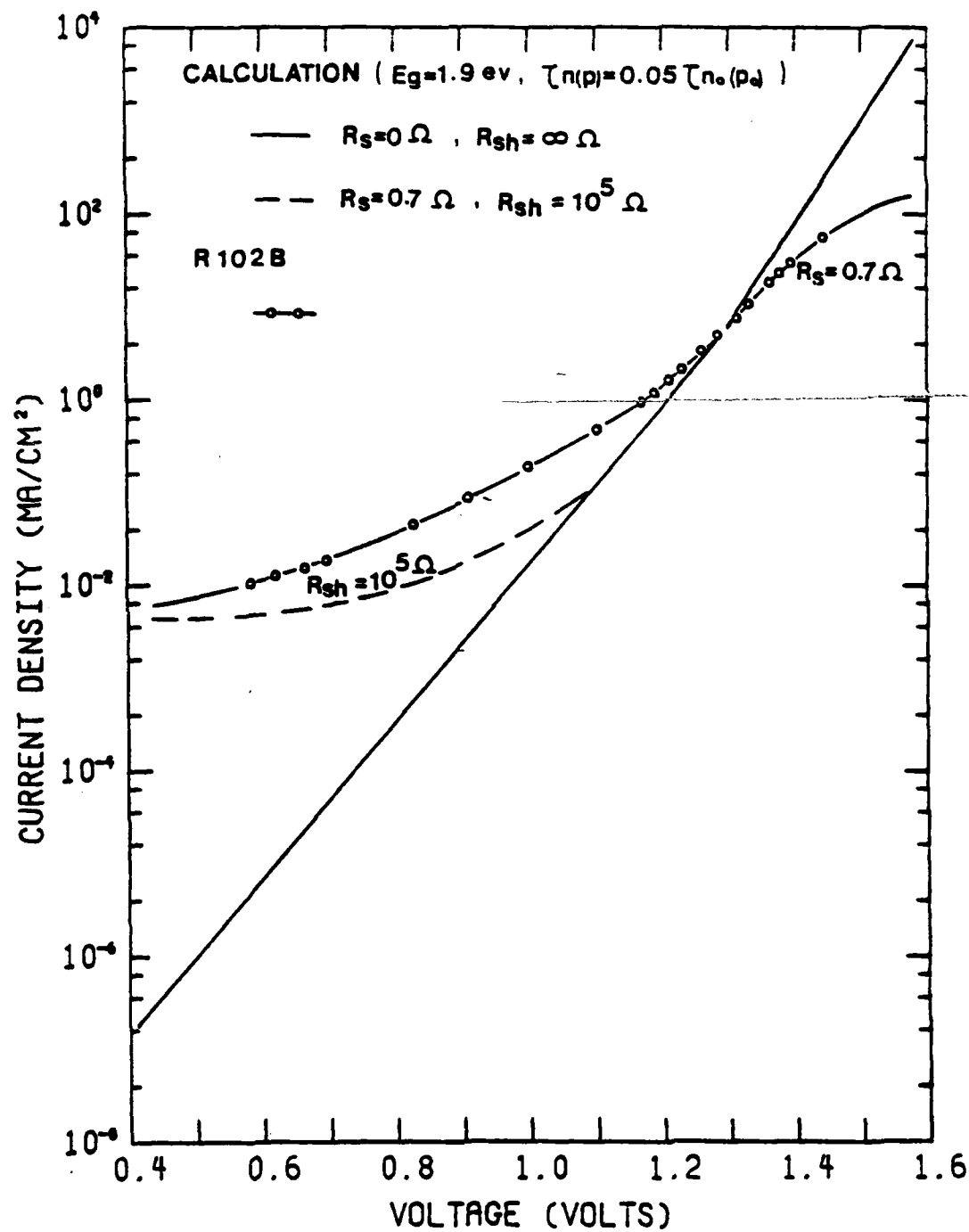


Figure 3.56(b) Comparison of calculated dark I-V characteristics and experimental measurements for a top cell.

in which the best measured parameters from three different cells lead to a projected AMO, 1 sun efficiency of 25%. While the illustration is not without its obvious shortcomings, it does provide an existence proof that the required parameters have been individually achieved. The challenge, of course, is to develop a compatible cascade cell fabrication technology that simultaneously yields acceptable values for all three parameters.

Table 3.3. Projected Cascade Efficiency Based on Best Measured Parameters

<u>Measured Values</u>			<u>Projected Efficiencies</u>	
V_{oc}	I_{sc}	FF	Efficiency (No AR coating)	Efficiency (Corrected for AR coating 1.28)
2.3	13.6	0.84	19.5	25%

A novel approach to these material problems will be discussed in the following section, along with some initial results.

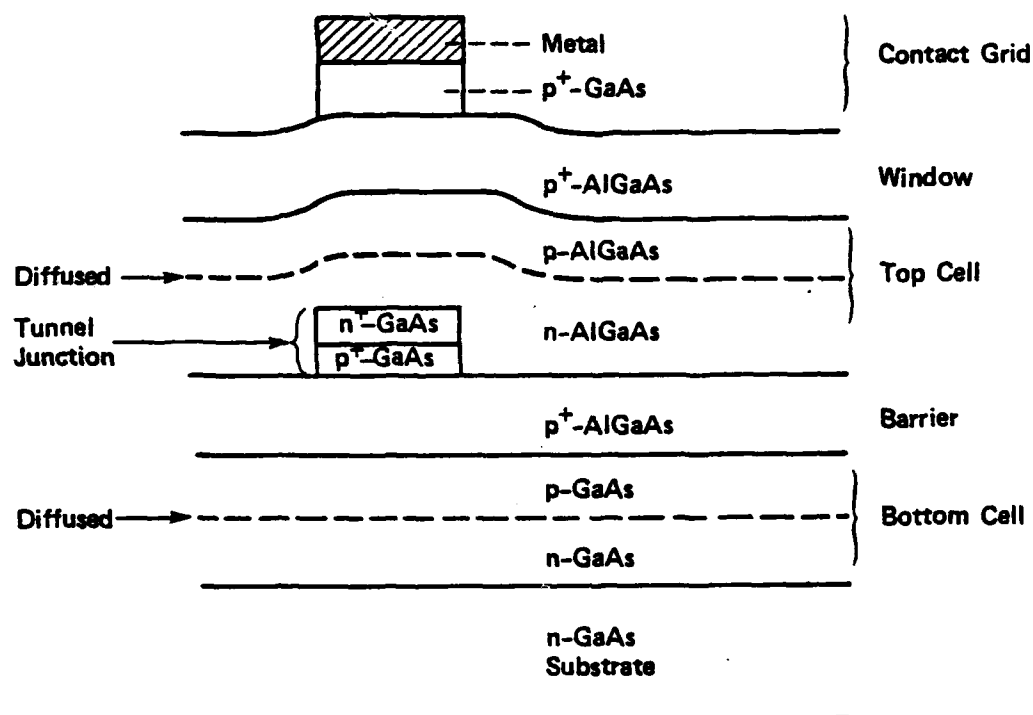
4.0 AlGaAs-GaAs PATTERNED TUNNEL JUNCTION CELL

4.1 Introduction

As an alternative to the planar tunnel junction device described above, RTI began development of a patterned tunnel junction cascade cell. This cell, shown in Figure 4.1, avoids the need to rely on a high bandgap tunnel junction. This is achieved by reducing the area of the tunnel junction relative to the total area of the cell, and by confining the tunneling areas to those areas of the cell shaded by the metallization. This results in no additional loss of active area of the cell and allows the use of a low bandgap GaAs tunnel junction.

This structure offers many advantages over the planar tunnel junction cell described previously, yet it does not represent a radical departure from the successful technologies developed for the planar structure device. As will be shown in Section 4.3, there are few changes necessary in the growth procedure; and those that are necessary, though they are important, do not require unproven technologies. The patterned tunnel junction structure has the following advantages:

1. The use of a GaAs tunnel junction takes advantage of the higher percentage of electrically active dopant incorporation in GaAs relative to that observed in the higher bandgap AlGaAs alloys. This reduces the total amount of dopant incorporated in the matrix.
2. The use of a GaAs tunnel junction takes advantage of the higher distribution coefficients observed for n^+ dopant incorporation in GaAs relative to AlGaAs. [$k_{GaAs}/k_{Al_{.36}Ga_{.64}As} \approx 26$ for Te, $n > 6 \times 10^{18} \text{ cm}^{-3}$ material growth by LPE at 772°C.] This reduces the total amount of



Note: See Table 4.2 for layer specifications.

Figure 4.1. AlGaAs-GaAs Cascade Cell with Patterned Tunnel Junction.
Homotunnel Junction Cell.

dopant in the melt. [Note that both 1 and 2 reduce second phase precipitation by reducing overall dopant concentrations.]

3. The problems resulting from telluride precipitation in GaAs are less severe than those encountered in AlGaAs. This is based on the fact that the Ga tellurides (Ga_xTe_y) have lower enthalpies of formation and lower melting points than the corresponding Al tellurides (Al_xTe_y). This both reduces precipitate formation and allows growth at temperatures above the melting point of the precipitates. In AlGaAs, the key precipitate, Al_2Te_3 , melts at 886.8°C ; growths at temperatures this high begin to compromise the abruptness of the tunnel junction dopant profiles. In GaAs, the key precipitate, GaTe, melts at 824°C ; growths at this temperature preserve the quality to the tunneling I-V characteristics. The doping profile's sensitivity to temperature can be appreciated by realizing the exponential temperature dependencies of the diffusion process. Thus, the 70 degree difference in melting points for Al_2Te_3 and GaTe is very significant (see Table 4.1).
4. GaAs is able to carry a larger current density than the higher bandgap AlGaAs alloys. This allows for successful reductions in tunnel junction area.
5. The patterned tunnel junction structure aligns the potentially absorbing GaAs tunnel layer in areas effectively shadowed by the metallization, thus active areas of the device are not sacrificed. Other work has been reported on n^+ -GaAs tunnel layers, using either GaAs or AlGaAs for the p^+

Table 4.1. Thermodynamic Data

Compound	ΔH_f° (kcal/mole)	T_m (°C)
Al_2Te_3	-78	886.8
GaTe	-28.6	824
Ga_2Te_3	-65	669.8
$GeAs_2$		732
GeAs		737
Al_2Se_3	-135	
GaSe	-35	960
Ga_2Se_3	-105	>1020

NOTE: ΔH_f° = enthalpy of formation

T_m = melting point

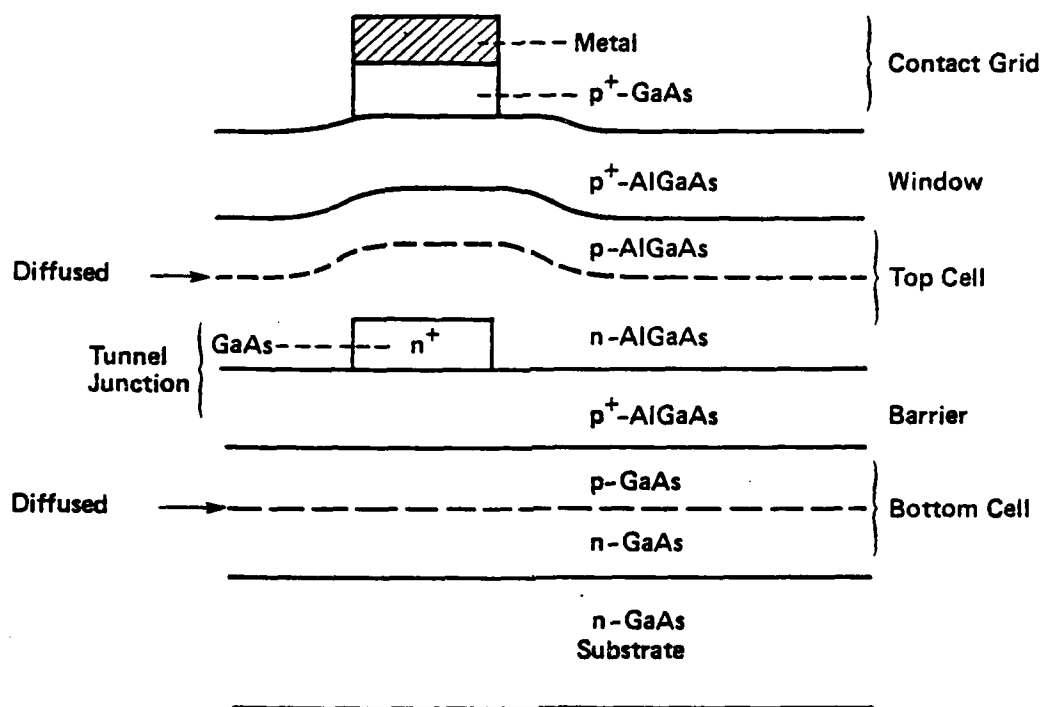
tunnel layer [4.1]. However, the work reported was in the context of a planar junction device (i.e., the tunnel junction covers the entire area of the cell). In such a scheme the high absorption coefficient of GaAs ($\sim 10^4 \text{ cm}^{-1}$) restricts the tunnel junction layer thicknesses to ~ 100 - 200 \AA (a 1000 \AA layer of GaAs produces a simple absorptive loss of 10 percent; the effective loss is somewhat greater due to interactive effects in the cascade structure). Tunnel structures as thin as 100 \AA have not demonstrated the required electrical performance necessary for efficient device operation, nor do we feel that this thickness is a practical dimension in a device 4 cm^2 or larger. The patterned tunnel junction device utilizes areas shadowed by the metallization, which allows a more practical tunnel junction layer thickness ($\sim 2.0 \text{ \mu m}$).

6. Points 1, 2, and 3 of this section advance arguments underlying expected improvements in the metallurgical quality of an n^+ -GaAs layer versus an n^+ -AlGaAs layer. However, in any degenerate or nearly degenerate material we expect some material defects. The proposed structure localizes the tunneling regions and reduces the total volume of the n^+ -layer by at least 90 percent. It is reasonable to expect that the residual defects in these isolated regions will have less of an impact on device performance than the same defect density in a layer covering the entire surface. In this structure, 90 percent of the nucleating surface for subsequent LPE growth is nondegenerate material.

7. The patterned tunnel junction structure is inherently a two-stage growth (growth \rightarrow etching \rightarrow overgrowth). Both growths have been successfully carried out with proven LPE techniques. However, a point for consideration is that the two-stage growth sequence for this structure is well suited to a mixed technology approach with proven LPE technology to fabricate the bottom cell and tunnel junction, combined with an alternate growth technology (e.g., MO-CVD) for the top cell overgrowth.

4.2 Device Structure

As shown in Figures 4.1 and 4.2, the patterned tunnel junction concept is applicable to either a homo-tunnel junction or a hetero-tunnel junction. Much of the discussion in Section 2.3 regarding defects in the n^+ (Te) AlGaAs layer also applies to a lesser degree to the p^+ (Ge) AlGaAs layer. Therefore, RTI emphasized the homojunction device, although the heterojunction device is an alternate and somewhat simpler structure. Since Figures 4.1 and 4.2 are not to scale, it should be emphasized that the cross-sectional aspect ratio formed by the metallization width and the n^+ -layer depth is currently 10:1, thus the GaAs layer is effectively shaded. The devices shown do not include an explicit barrier to prevent collection of top cell minority carriers (holes) by the tunnel junction. In the present device, collection is prevented by the thickness of the top cell n-layer being both several absorption lengths and several diffusion lengths long, which prevents photogenerated holes from reaching the reverse polarity center junction. Device refinement for



Note: See Table 4.3 for layer specifications.

Figure 4.2. AlGaAs-GaAs Cascade Cell with Patterned Tunnel Junction.
Heterotunnel Junction Cell.

for maximum efficiency and radiation resistance could result in a substantially thinner top cell, which would required an explicit barrier layer. Present device paramenters are given in Table 4.2 for the homo-tunnel junction device and Table 4.3 for the hetero-tunnel junction device.

Experimental results and the results of preliminary cell development will be presented in Section 4.3.1.4. The remaining discussion of the fabrication of the patterned tunnel junction cascade cell will be given in Section 4.3, Cell Development.

4.3 Cell Development

4.3.1 Material Growth

The growth of the patterned tunnel junction structure is very similar to the growth of the planar structure device, discussed in Section 2.3. The points where the two technologies differ will be discussed here. Information concerning the elements of the growth technique common to both structures may be found in Section 2.3.

4.3.1.1 Tunnel Junction and Bottom Cell

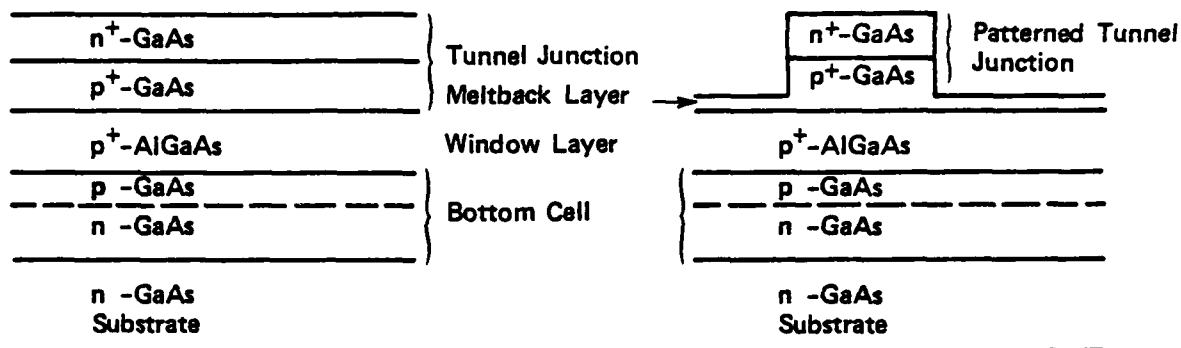
The tunnel junction and bottom cell are grown during the same epitaxial sequence resulting in the structure shown in Figure 4.3a or Figure 4.4a, depending on the tunnel junction configuration desired. This growth is carried out at a temperature above 824°C to avoid the formation of solid GaTe at the growth temperature. The tellurium concentration for the n^+ -melt is reduced ($\sim 20\times$) from the levels used for the n^+ -AlGaAs tunnel layer.

Table 4.2. Layer Specifications for the Patterned Tunnel-Junction Cascade Structure - Homotunnel Junction

Layer	$n(\text{cm}^{-3})$	$p(\text{cm}^{-3})$	Thickness (μm)	AlAs(%)
$\text{p}^+ \text{-GaAs}$		$2 \times 10^{18}(\text{Ge})$	0.5	0
$\text{p}^+ \text{-AlGaAs}$		$2 \times 10^{18}(\text{Be})$	0.2	90
n-AlGaAs	$2 \times 10^{17}(\text{Sn})$		5.0	35
$\text{n}^+ \text{-GaAs}$	$1 \times 10^{19}(\text{Te})$		2.0	0
$\text{p}^+ \text{-GaAs}$		$2 \times 10^{18}(\text{Ge})$	1.0	0
$\text{p}^+ \text{-AlGaAs}$		$1 \times 10^{18}(\text{Be})$	1.0	70
n-GaAs	$2 \times 10^{17}(\text{Sn})$		4.0	0

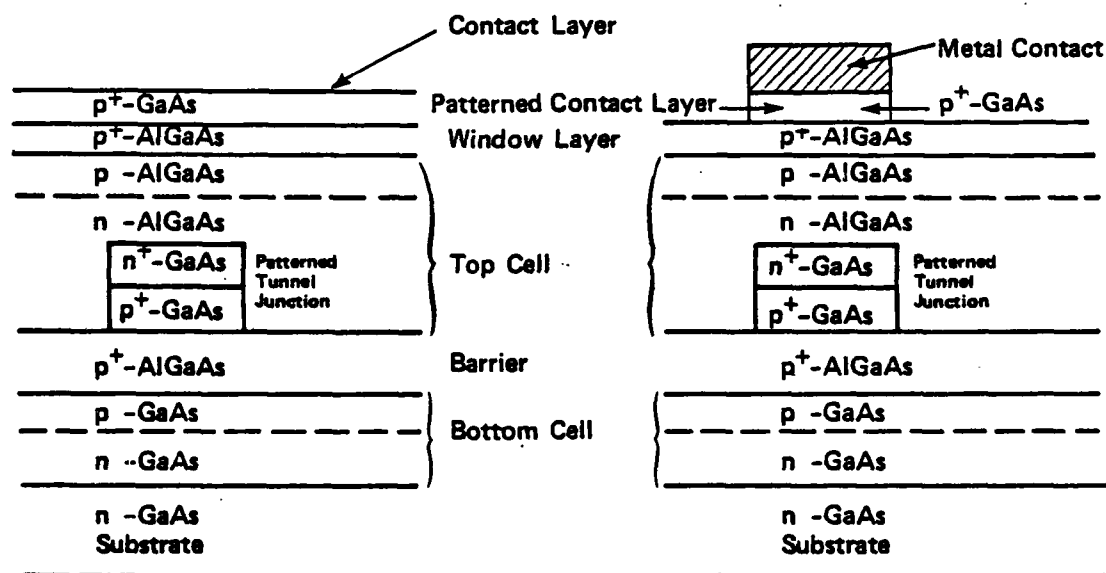
Table 4.3. Layer Specifications for the Patterned Tunnel-Junction Cascade Structure - Heterotunnel Junction

Layer	$n(\text{cm}^{-3})$	$p(\text{cm}^{-3})$	Thickness (μm)	AlAs(%)
$\text{p}^+ \text{-GaAs}$		$2 \times 10^{18}(\text{Ge})$	0.5	0
$\text{p}^+ \text{-AlGaAs}$		$2 \times 10^{18}(\text{Be})$	0.2	90
n-AlGaAs	$2 \times 10^{17}(\text{Sn})$		5.0	35
$\text{n}^+ \text{-GaAs}$	$1 \times 10^{19}(\text{Te})$		2.0	0
$\text{p}^+ \text{-AlGaAs}$		$2 \times 10^{18}(\text{Ge})$	1.0	35
$\text{p}^+ \text{-AlGaAs}$		$1 \times 10^{18}(\text{Be})$	0.5	70
n-GaAs	$2 \times 10^{17}(\text{Sn})$		4.0	0



a. Initial growth of the bottom cell and tunnel homojunction

b. Chemically patterned tunnel junction ready for meltback and top cell growth



c. Structure after meltback of the residual GaAs, and overgrowth of the top cell and contact layer

d. Structure after patterned metalization and removal of the excess contact layer

Figure 4.3. Homojunction Sequence.

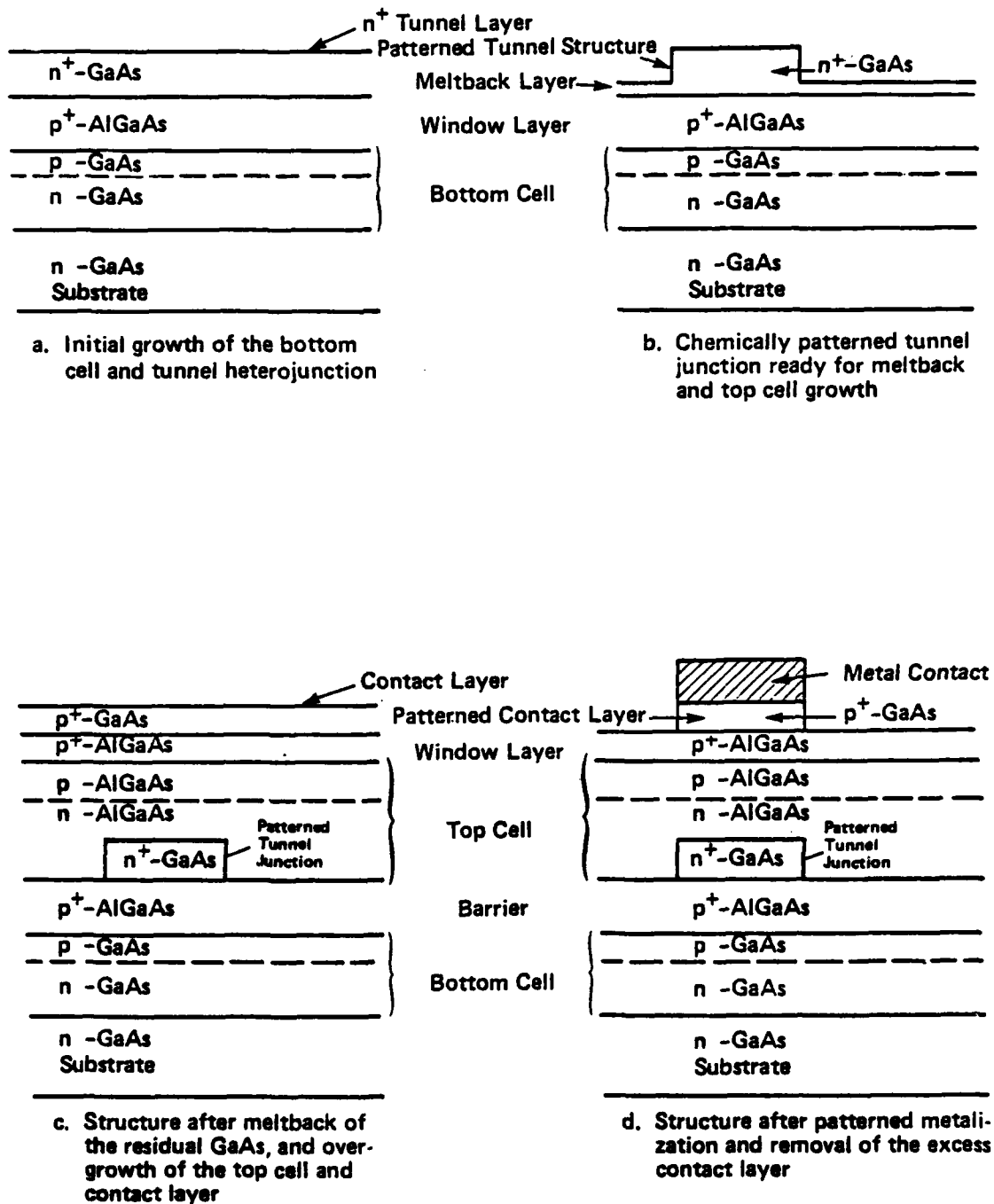


Figure 4.4. Heterojunction Sequence.

4.3.1.2 Tunnel Junction Etching

As discussed above, the p^+ -AlGaAs layer of the bottom cell serves two purposes: (1) it acts as a reproducible diffusion source for the p-GaAs bottom cell layer (Section 2.3), and (2) it serves as a barrier to minority carrier collection by the tunnel junction. Formation of the patterned tunnel junction structure requires exposure of this p^+ -AlGaAs layer and growth of the n-AlGaAs layer of the top cell, as shown in Figure 4.3c. However, if chemical etching is used to delineate the tunneling regions and to expose the intervening p^+ -AlGaAs, the surface of the p^+ -AlGaAs will be oxidized. An oxidized surface prevents high quality LPE growth. The procedure we have developed to avoid this problem is as follows. The chemical etchant used must be isotropic, relatively stable, and reproducible. It must also etch fairly slowly to allow accurate depth control. An etchant that meets all the criteria is $H_2SO_4:H_2O_2:H_2O$ [1:8:50 Vol @ 5°C]. The etch rate on (111B) GaAs is $0.35 \mu\text{m}/\text{min.} \pm 0.05 \mu\text{m}/\text{min.}$ Reproducibility depends on accurate mixing and accurate temperature control. The H_2SO_4 should be added to the $H_2O-H_2O_2$ mixture drop by drop to prevent overheating. The tunnel junction area is masked either with photoresist (Shipley AZ1350J) or with patterned SiO_2 (e-beam deposited). Our epitaxial layer thicknesses are known from SEM calibrations, and the etch interval is simply calculated based on the known etch rate. The etch interval is calculated to remove all but a thin layer of GaAs ($< 0.5 \mu\text{m}$). The accuracy of this technique has been repeatedly verified. The removal of the etch mask is a critical procedure since photoresist residue or other contaminants will interfere with overgrowth. The residual GaAs (Figure 4.3b) prevents the oxidation of the AlGaAs surface. At the beginning of the top cell

growth sequence, a slight meltback is performed to remove this GaAs. This meltback also serves to reduce the effects of any thermal degradation that may occur during equilibration and melt saturation. The GaAs layer remaining after chemical etching should be as thin as possible consistent with reproducibility. Using as an upper limit, 0.5 μm , we have experienced no problems due to layer uniformity on 2×2 cm substrates. The remainder of the growth is identical to the growth of the corresponding layers for the planar structure.

4.3.1.3 Tunnel Junction Stability

The split growth sequence used to fabricate the patterned tunnel junction structure exposes the tunnel junction to additional heat treatment. This is due to the need for a period of thermal equilibration and melt saturation before the actual overgrowth sequence begins. It is important to minimize both the time and the temperature used in the overgrowth sequence in order to maintain the abruptness of the dopant profiles. Recent top cell growths performed in the range 750° to 850°C show no sign of tunnel junction degradation. Isolated GaAs tunnel junction growths, with heat treatments to simulate overgrowth conditions, were not performed. We do know that heat treatment of the AlGaAs tunnel junction at 900°C severely degrades its electrical characteristics. Further experiments would clarify this behavior, but it should be emphasized that the results of our initial overgrowth experiments indicate excellent tunnel junction performance (Figure 4.5).

4.3.1.4 Initial Results on the Patterned Tunnel Junction Cell

In order to demonstrate that the patterned tunnel junction structure was a viable approach to the problems facing the planar device,

some initial experiments were carried out. AlGaAs top cells ($E_g \approx 1.85$ eV) were grown on patterned GaAs tunnel junctions, and small area devices were fabricated. Figure 4.5 shows the characteristics of this top cell both at 1 sun and at 6 suns. The corresponding open-circuit voltages are 1.1 and 1.26 V with fill-factors of 0.82 and 0.77 respectively. These results indicate that the top cell grown on the patterned n^+ -GaAs structure behaves better than an identical cell grown on a planar n^+ -AlGaAs layer. In the above device, the tunnel junction covered 10 percent of the substrate area.

Another test of cell quality is provided by the intensity and uniformity of LED action. When the structure is driven in the forward direction with relatively high-current densities, $0.5 - 1 \text{ A cm}^{-2}$, the top cell emits at $0.65 \text{ }\mu\text{m}$. The uniformity and intensity of the light emitted from the top cell have been found to be a good indication of the quality of the top cell. Low values of open-circuit voltage usually correspond to very low, nonuniform LED intensity. This nonuniformity correlates with defects originating in the n^+ -AlGaAs layer. The initial top cell growths on the patterned n^+ -GaAs have shown intense uniform emission from $1 \times 10^{-2} \text{ cm}^2$ area mesas taken at random from all areas of the $1 \text{ cm} \times 1 \text{ cm}$ substrates. This would indicate that this structure results in dramatically reduced dislocation density. A number of bottom cell/window layer/tunnel junction growths were performed to compare the difference in dislocation density between structures with GaAs tunnel junctions and structures with $\text{Al}_{0.35}\text{Ga}_{0.65}\text{As}$ tunnel junctions. The growth temperatures were chosen to be above (850°C) and below (800°C) the melting point of the principal Ga--tellurides (825°C) (see Table 4.1). In all cases, the dopants used were $\text{Te}(n^+)$ and $\text{Ge}(p^+)$. The substrates used were (111)B oriented Si-doped

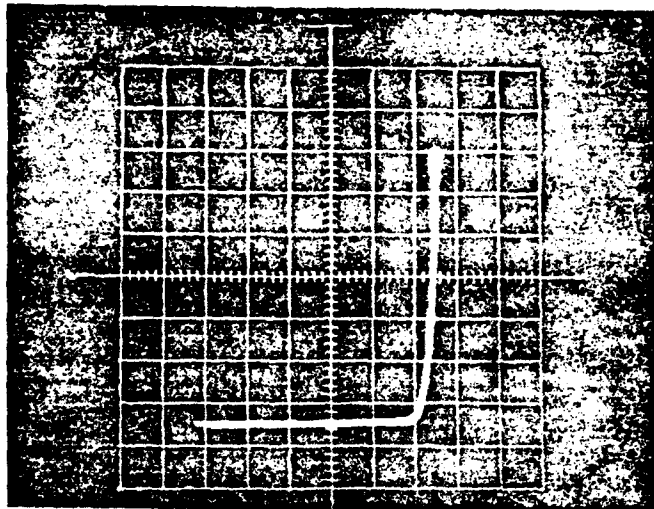


Figure 4.5(a) 0.5 V/div. Hor., 0.2 mA/div. Vert.

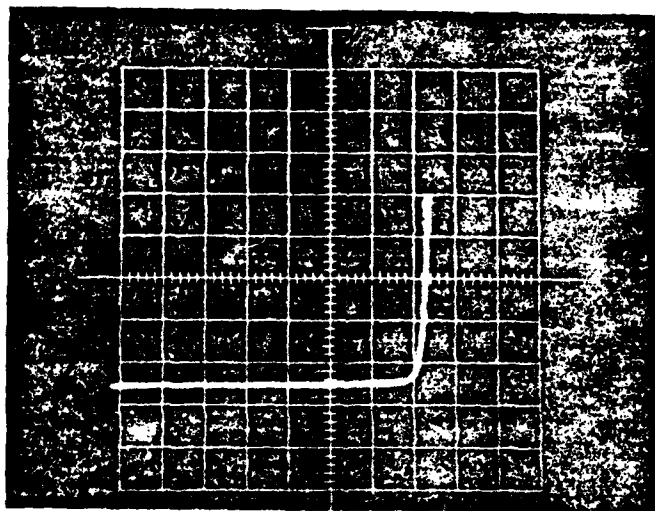


Figure 4.5(b) 0.5V/div. Hor., 0.05 mA/div. Vert.

Current-voltage characteristics of an AlGaAs top cell ($E_g = 1.85$ eV) grown on a patterned GaAs homotunnel junction: (a) 6 suns, FF 0.77, V_{oc} 1.26 V; (b) 1 sun, FF 0.82, V_{oc} 1.10V.

LEC material. The 1 cm \times 1 cm substrates were selected from four consecutive slices from the same boule. Care was taken to select substrates from areas of each slice at approximately the same radial distance from the boule axis. The as-cut wafers were 590 μ m thick. They were polished to 360 μ m with Br in methanol (1 ν /o) and three wafers were selected for etch pit evaluation. These wafers were etched 5 min in AB etch. Three sites on each wafer were used for etch pit counts. The area of each site was $3.3 \times 10^{-3} \text{ cm}^{-2}$. The results from these substrates are listed below (Table 4.4).

Table 4.4. Control Wafer EPD at 360 μ m.

Site	Wafer 1	Wafer 2	Wafer 3
1	$2.7 \times 10^3 / \text{cm}^2$	$1.8 \times 10^3 / \text{cm}^2$	$2.4 \times 10^3 / \text{cm}^2$
2	$0.9 \times 10^3 / \text{cm}^2$	$1.2 \times 10^3 / \text{cm}^2$	$1.8 \times 10^3 / \text{cm}^2$
3	$2.4 \times 10^3 / \text{cm}^2$	$0.9 \times 10^3 / \text{cm}^2$	$2.4 \times 10^3 / \text{cm}^2$

Based on this limited sample, we take the substrate EPD to be $1.8 \times 10^3 / \text{cm}^2$ with Standard Deviation, $\sigma = 0.65 \times 10^3 / \text{cm}^2$.

The samples were then polished again with Br in methanol until they were 250 μ m thick. A repeat of the etch pit determination was then conducted on the same three substrates with nearly identical results EPD = $2.0 \times 10^3 / \text{cm}^2$ with $\sigma = 0.66 \times 10^3 / \text{cm}^2$. The remainder of the wafers were used as growth substrates. Etch pit determinations on the As-grown wafers were made in the same way as for the control substrates. The results are shown in Table 4.5 for the four types of growths.

Table 4.5. EPD (Etch Pit Density) Results Comparing $n^+(Te)GaAs/p^+(Ge)GaAs$ Tunnel Junctions with $n^+(Te)Al_{.35}Ga_{.65}As/p^+(Ge)Al_{.35}Ga_{.65}As$ Tunnel Junctions.

TYPE 1			TYPE 2			TYPE 3			TYPE 4		
Al _{.35} Ga _{.65} As			Al _{.35} Ga _{.65} As			GaAs			GaAs		
Growth Temp. 800°C			Growth Temp. 850°C			Growth Temp. 800°C			Growth Temp. 850°C		
Sample	EPD(cm ⁻²)	No.	Sample	EPD(CM ⁻²)	No.	Sample	EPD(cm ⁻²)	No.	Sample	EPD(cm ⁻²)	No.
G411	1.2×10^4		G403	4×10^4		G402	2×10^4		G410	4×10^3	
G417	1.0×10^4		G404	4×10^3		G406	5×10^3		G405	9×10^3	
			G407	5×10^3		G409	3.5×10^3		G408	2.7×10^3	
			G410	3.6×10^3		G413	7×10^3		G412	3.8×10^3	
			G414	1.6×10^4		G416	1.6×10^4		G415	4×10^4	
mean	1.1×10^4		mean	1.4×10^4		mean	1×10^4		mean	4.7×10^3	
std.dev.	1×10^3		std.dev.	1.4×10^4		std.dev.	6.5×10^3		std.dev.	2.2×10^3	

Although this is a small sample, and would have benefited from lower dislocation starting material, a trend is evident in Table 4.5. The GaAs tunnel junction/window layer/bottom cell structure (Type 4) grown at 850°C is the only structure grown above the melting point of the relevant telluride (GaTe). In these samples, the measured EPD is nearly that of the substrate. As can be expected because of dislocation generation due to telluride precipitates, the other three growth types do show dislocation enhancement, with EPD's roughly an order of magnitude greater than that of the substrate material.

In addition to the higher dislocation density, the form of the etch pits observed on the TYPE 1, TYPE 2, and TYPE 3 samples suggests a cluster of dislocation loops isotropically distributed about a central core (see Figure 4.6). For the purposes of the EPD determination (Table 4.5) each of the clusters is counted as one dislocation. This seemed to be the safest course since TEM or another means of direct identification was not used to establish the relation of these etch features to the local dislocation structure. If these features are indeed dislocation clusters, then the dislocation densities for the TYPE 1, 2, and 3 samples as given in Table 4.5 are roughly a factor of 10 too small. We would then find a factor of 10^2 enhancement of dislocation density in the three sample types representing tunnel junction growth below the melting point of the principle telluride, and virtually no (2x) enhancement for the samples (TYPE 4) grown above the melting point of the relevant tellurides. A further point that has not been explored concerns the effect of such a cluster on a cell's performance relative to the effect of an equal number of uniformly distributed dislocations.



Magnification = 145x

Figure 4.6. Sample G409-GaAs tunnel junction grown at 800° C (Type 3) after a 10 min. etch in AB etchant at 25° C. (Magnification = 145x).

These results support the arguments previously advanced in favor of the patterned tunnel junction structure. These results are especially significant in that they represent progress in the fundamental area impeding the development of the cascade structure--the material quality of the top cell and tunnel junction. By eliminating the requirement for a transparent tunnel junction, this structure eliminates the need for a 1.94 eV low-resistance tunnel junction. This last point is essential in that no such tunnel junction has been fabricated. Thus a Patterned Tunnel Junction structure can effectively utilize a 1.94 eV top cell. This allows a gain in predicted performance of from 5 - 6% over a 1.8/1.43 eV cell.

A number of complete patterned tunnel junction structures have been grown using the wafers from the etch calibration experiments. These structures were similar to Figures 4.3b and 4.4b. The meltback process was not yet characterized, and no meltback of the residual GaAs was attempted. However, these growths could be expected to show voltage addition, with absolute performance limited by optical absorption in the tunnel junction. The resulting structures were, of course, current-limited by the bottom cell, and showed the effect of the tunnel junction bucking voltage. Nevertheless, these growths produced cells with V_{oc} values between 1.55 and 1.74 V. Spectral response yields a quantum efficiency of 0.63 (e/p) for the top cell without AR coating. These structures were entirely nucleated on degenerate GaAs, rather than the more favorable surface after meltback. In spite of this, we observe the improvements in top cell performance expected in switching to a GaAs tunnel junction, and initial growths on these patterned surfaces have yielded increases in top cell quantum efficiency and voltage.

5.0 SUMMARY AND CONCLUSIONS

In the course of this program RTI achieved the following significant advances in solar cell technology:

- The use of Be as an LPE dopant for p-type AlGaAs. Be was shown to be suitable for diffused junction formation with junction displacement of from 0.5 to 2.0 μm depending on the detailed growth conditions,
- Fabrication of AlGaAs tunnel junctions in the bandgap range from 1.6 eV to 1.8 eV. In particular 1.6 eV tunnel junctions with a series resistance of 0.7 Ω ,
- A monolithic AlGaAs/GaAs cascade solar cell with a tunnel junction interconnect and an active area efficiency of 15.1% at AMO, 1 sun, without AR coating,
- Demonstration that the individual cell parameters (V_{oc} , I_{sc} , FF) necessary for a 20% cell were experimentally achievable,
- By extensive analysis of a large number of cascade structures with varying parameters this program has isolated the technological issues limiting the performance of these structures.

The conclusions reached in this program constitute a brief review of the two principal issues that prevent the achievement of the theoretical performance criteria.

- (1) In the AlGaAs/GaAs system the minimum bandgap occurs at $x = 0$ for GaAs ($E_g(\text{GaAs}) = 1.424 \text{ eV}$ at 300°K). Thus this system cannot be used to fabricate the 0.95 eV bottom cell that would be ideal for a two-junction cascade cell operating under AMO, 1 sun conditions. To compensate for the higher bandgap bottom

cell in this system, the top cell bandgap should be increased to 1.94 eV, whereas in the ideal case the top cell bandgap is 1.6 eV. As a result the AlGaAs/GaAs cell requires a 1.94 eV low resistance tunnel junction that will carry an active area current density of 15 mA cm^{-2} under AMO, 1 sun conditions. Tunnel junctions with bandgaps greater than 1.85 eV have not been successfully demonstrated, in fact, tunnel junctions with bandgaps greater than 1.8 eV exhibit high resistance and poor current handling capability (Figure 2.15). Thus it seems unlikely that a planar cascade cell can be fabricated according to the optimum design parameters. If, as a compromise, a bandgap of 1.8 eV is used for the top cell and tunnel junction the predicted achievable efficiency is reduced from $\sim 27.5\%$ to $\sim 21\%$.

- (2) The Te-doped tunnel junction layer is the site of substantial dislocation generation. These dislocations act as shunting paths seriously degrading top cell performance. These dislocations have been correlated with the presence of telluride precipitates in the n^+ -AlGaAs tunnel junction layer. These precipitates also interfere with uniform nucleation of the top cell epilayers. Since the dislocations are randomly distributed, there will be some areas of the grown wafer with local dislocation densities exceeding the average density. Devices including one or more of these areas have shorted top cells. This has prevented the fabrication of large area devices. We have shown (Section 4.3.1.4) that these effects can be largely eliminated by growth at temperatures above the melting point of GaTe (824°C)

in GaAs epilayers. A comparable approach in AlGaAs would require growth at temperatures in excess of the melting point of Al_2Te_3 (887°C). At these temperatures the Te and Ge dopant profiles broaden during the remainder of the growth sequence (top cell/top cell window layer/contact layer). This broadening results in "backward diode-like" behavior of the tunnel junction. Small area ($\sim 1 \times 10^{-2} \text{ cm}^{-2}$) devices occasionally avoid the areas effectively shunted by these dislocation networks. Of course, the reproducibility of these devices depends to some extent on chance. Even in these devices the influence of the material quality of the top cell layers is dominant. The reverse saturation current of most cells is 1 \sim 2 orders of magnitude larger than theoretical values calculated using state-of-the-art lifetimes. This is largely responsible for the low open-circuit voltages. Similarly, the reduced diffusion length results in reduced short-circuit current.

Although several techniques have been developed to reduce these problems, this has not resulted in a reproducible technology for the production of 15% cells, nor is the technology suited to the fabrication of large area cells.

The patterned tunnel junction (PTJ) cell has been conceived in response to these fundamental problems. The patterned tunnel junction cell does not require a transparent tunnel junction; this allows the use of a GaAs tunnel junction. As was shown in Section 4.3.1.4 the problem of dislocation generation in GaAs tunnel junctions can be dealt with by properly choosing the growth parameters. The Patterned Tunnel Junction

structure simultaneously addresses the three major technological issues:

(1) reproducible high quality tunnel junctions; (2) optimal top cell epilayer parameters (lifetime, diffusion length), and (3) large area uniformity.

APPENDIX

During the initial stages of the cascade solar cell research program at RTI, computer modeling was developed to provide guidelines for the selection of appropriate materials consistent with obtaining optimum efficiency under a variety of operating conditions (1 sun, multi-sun, high temperature, low temperature, and for different spectral [air mass] conditions). These modeling results provided a range of bandgap combinations which, when combined with the fundamental constraint of close lattice-matching in monolithic structures, form the basic criteria for selecting appropriate material combinations.

Figure (A0) displays energy bandgap versus lattice constant for the various III-V semiconductors. Also shown are values for silicon and germanium as well as various solid lines representing selected ternary III-V alloys. The cross-hatched areas represent the desired bandgap ranges for the bottom cell and top cell of a two-junction cascade structure. The optimum bandgaps vary from the low range combinations (0.96 eV and 1.64 eV) to the high range combinations (1.2 eV and 1.8 eV). The selected semiconductors should ideally fall on a vertical (iso-lattice constant) line in Figure (A0).

Based on these simple criteria, six cascade combinations were investigated. Of these six, two were found to be promising--AlGaAs/AlGaAs/GaAs and AlGaAsSb/AlGaAsSb/GaAsSb [the convention is-window/top cell and tunnel junction/bottom cell unless specifically noted]. Of these two, the AlGaAsSb/AlGaAsSb/GaAsSb system continues to be the focus of a major program funded by SERI (subcontract No. XM-9-81361 under contract EG-77-C-01-4042). The SERI program was originally funded under contract

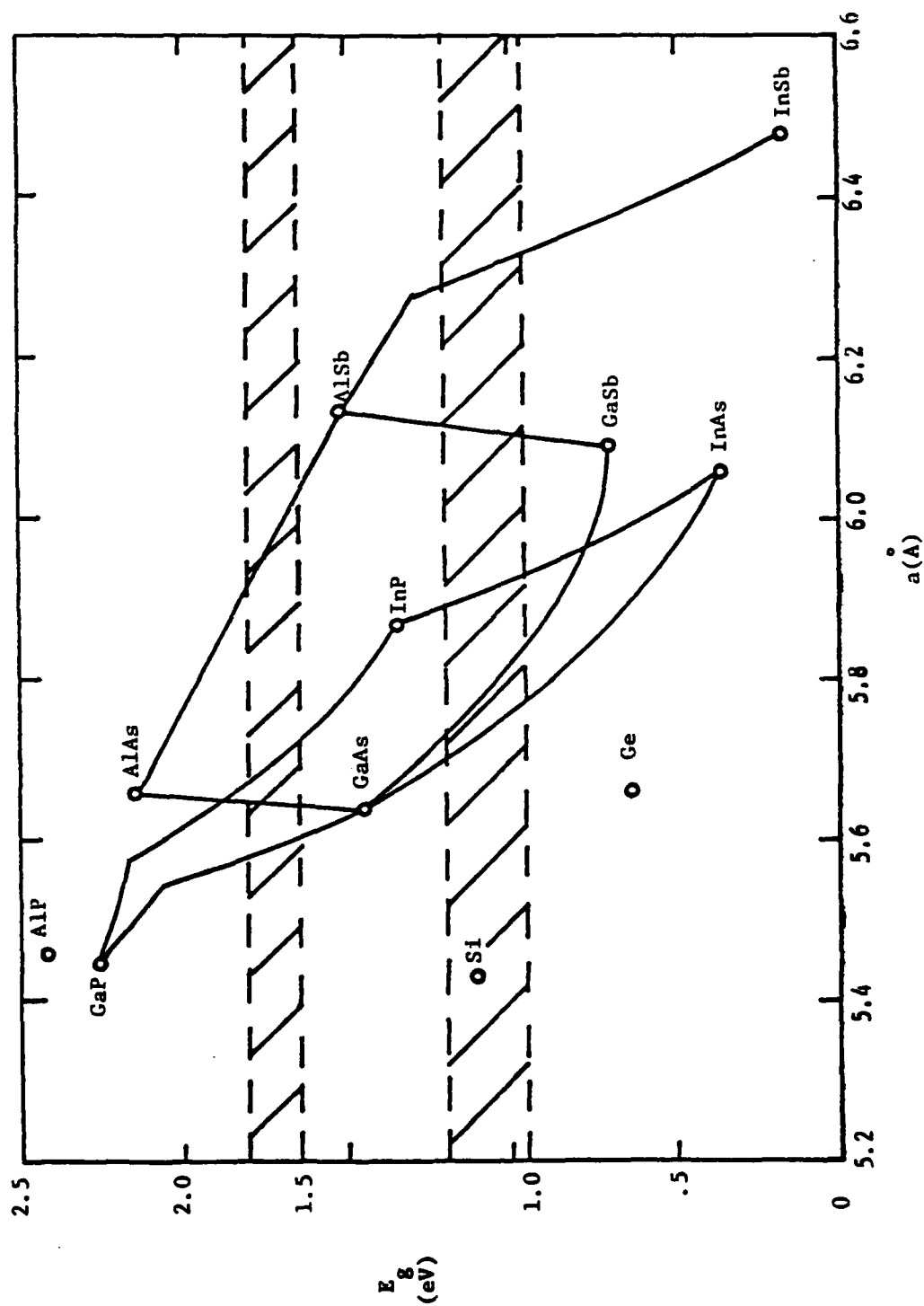


Figure A.0 Bandgap and lattice constant values for the III-V semiconductors.

from Sandia Laboratories contract No. 07-7149. The other successful combination--AlGaAs/AlGaAs/GaAs--was the prime focus of this contract. The other combinations considered were: (1) AlGaAs/AlGaAs/InGaAs, (2) AlAsSb/InGaP/InGaAs, (3) AlGaAsSb/AlGaAsSb/InGaAs, and an inverted structure grown as (4) InGaAs/AlGaAs/AlGaAs with the substrate later etched away.

This appendix presents the results of work done in these four alternative systems during the first stages of this project.

1. AlGaAs/AlGaAs/InGaAs Material System

This system is shown in Figure A1. The AlGaAs/AlGaAs/InGaAs system has two major difficulties: lattice parameter mismatch and melt-back effects during synthesis via LPE.

In $\text{Ga}_{1-x}\text{In}_x\text{As}$ crystals the lattice mismatch increases rapidly with x , being 7.15% for $x = 1.0$. For $\text{AlGa}_{1-y}\text{As}$, the change in lattice parameter is relatively small (approximately 0.14% for $y = 1$). Thus, the AlGaAs connecting junction and top cell layers have lattice parameters substantially smaller than that of the underlying GaInAs bottom cell layers. Since optimum design requires $x \approx 0.20$, the AlGaAs layers clearly should have a smaller lattice parameter--i.e., a negative mismatch--which is approximately 1.07% for an optimized structure. Monolithic semiconductor structures are much more sensitive to tension than to compression, and although dislocation generation and lattice distortion is common to either type of misfit, layers in tension often develop macroscopic faults (i.e., cracking).

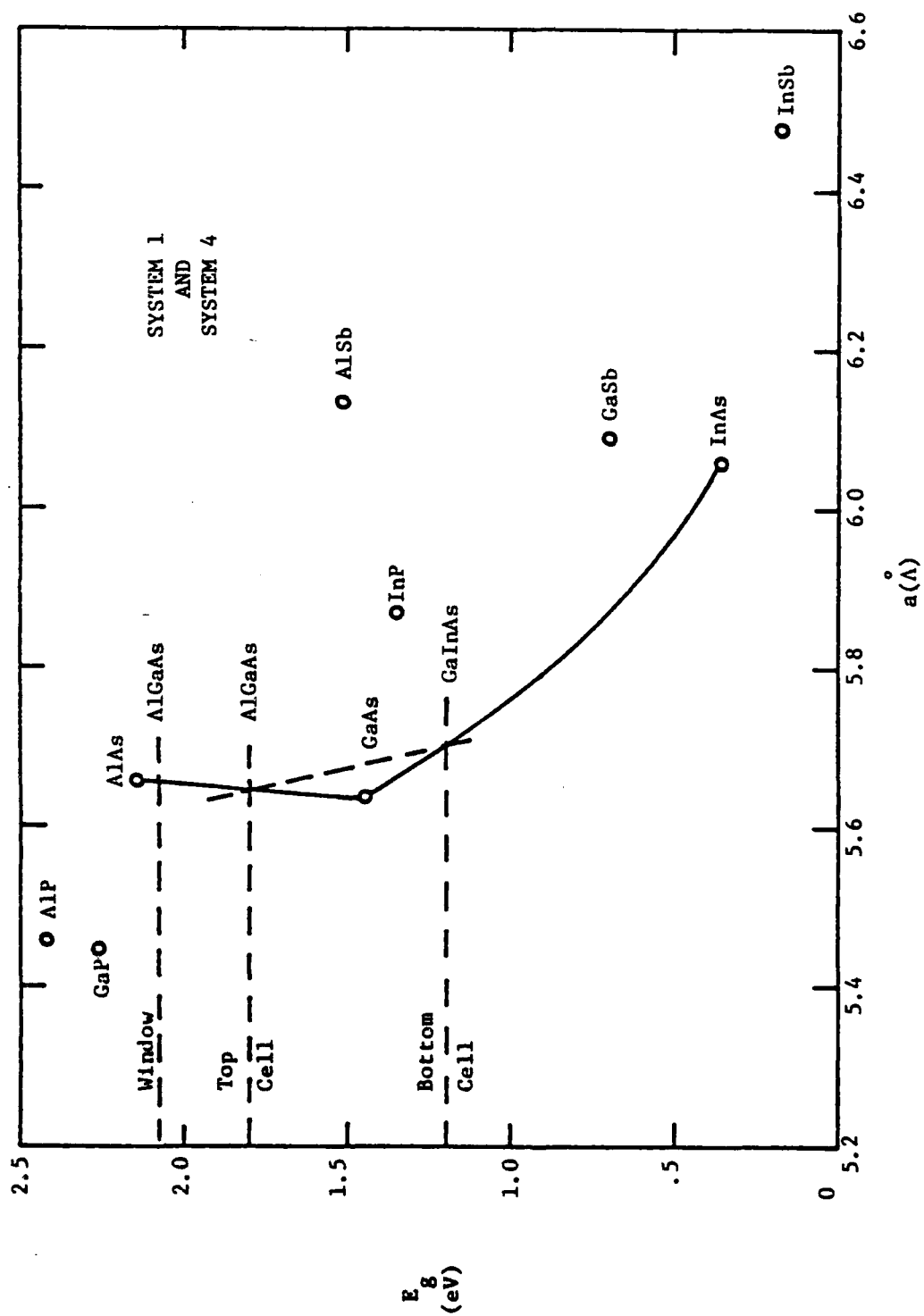


Figure A.1 AlGaAs/AlGaAs/InGaAs material system.

The second major consideration for this system is melt-back (or etch-back) during LPE growth. This stems from the fact that an AlGaAs melt can not be in equilibrium with solid phase InGaAs. The effect of this is that even a supersaturated AlGaAs melt will melt back an InGaAs epilayer. The typical situation is as follows: there is no In in the melt thus there exists a huge concentration gradient driving the transport of In into the melt. This results in dissolution of the InGaAs layer. The In containing boundary layer that is established enhances the diffusion of As from the sample surface. Finally, the gradients driving dissolution are reduced below the overall deposition gradients due to the initial supersaturation. However, deposition occurs from the AlInGaAs boundary layer resulting in the formation of a quaternary solid phase. This initially nucleated solid will show substantial grading due to the spatially nonuniform In distribution and due to the fact that the distribution coefficient of Al from a melt containing both In and Ga is huge. This dissolution/perturbed-growth process does not occur uniformly over the sample surface but is influenced by existing growth morphology and results in a non-planar interface. This process leads to reduced lower cell efficiency through increased interfacial recombination velocity.

Therefore, conventional LPE methods lead to reduced overall cell efficiency by degrading both the top and bottom cells. Realizing this, several approaches have been tried to overcome these problems. To reduce melt-back, high cooling rates of up to 100°C/hr have been used. This leads to a higher growth rate for the AlGaAs layers and the time of contact between the Al-Ga-As melt and the GaInAs epilayers is reduced. This approach has been used to deposit AlGaAs on $\text{Ga}_{1-x}\text{In}_x\text{As}$ with $x = 0.15$.

It should be noted that as expected melt-back increases with increasing x , and this fast-growth method becomes increasingly ineffective. In order to assess the quality of GaInAs bottom cells, some connecting junction/bottom cell structures have been grown. For $x \approx 0.15$, values of $V_{oc} \approx 0.7$ V and $J_{sc} \approx 16$ to 20 mA/cm² were obtained in small area mesa-etched devices (≈ 1 sun illumination). For $x \approx 0.15$, however, $V_{oc} \approx 0.4$ V and $J_{sc} \approx 5 - 10$ mA/cm² were obtained, indicating degradation due to melt-back.

The quality of the connecting junctions was ascertained by their optical inactivity. The impedance measured across bottom cells with and without connecting junctions showed no measurable change. This may be due to a shunt impedance across the tunnel diode connecting junction, thereby improving its performance (reducing series impedance). On the other hand, the top cell has to be grown on top of this highly strained connecting junction layer, and here the same effects (shunt impedance and poor quality) are extremely detrimental. In our experiments, a top cell made with 1.6 eV bandgap material had $V_{oc} \approx 0.2$ V when grown on connecting junctions, as opposed to $V_{oc} \approx 1$ V when grown on GaAs substrate material with minimal mismatch problems.

In order to achieve better crystalline quality and hence better top cells, attempts were made to isolate the top cell from the strained connecting junction by growing a buffer layer. Such buffer layers are used extensively in other device structures to improve crystalline quality. The major requirements for this purpose are that the buffer layers have a high bandgap for optical transparency and a low series resistance. Up to three AlGaAs buffer layers have been grown over the

connecting junction before growing the top cell. In these cells, evidence of cascade solar cell action has been observed. At the same time there is evidence that the top cell performance is still being degraded. From composite cell I-V curves, top cell degradation can be inferred from low J_{sc} and low V_{oc} , i.e., $V_{oc} = 1.1$ V instead of the ≈ 1.8 V expected from bandgap considerations. Similarly, reverse characteristics exhibit "double breakdown" like curves.

In view of the problems associated with the AlGaAs/GaInAs, it is useful to review all the factors involved. The optimum cell design calls for bottom and top cell bandgaps of ≈ 1.0 and ≈ 1.7 eV, respectively. A 1.0 eV bottom cell can be fabricated by growing GaInAs p-n junctions with $\approx 30\%$ InAs and a corresponding lattice parameter of ≈ 5.77 Å. In order to achieve device quality material, it is imperative to grow several (3 to 5) intermediate "step grading" GaInAs buffer layers, with each successive layer having a higher InAs mole fraction. Then, to grow an AlGaAs connecting junction (2 layers) on top of this, a carefully controlled fast growth technique has to be employed. Further, before any device-quality AlGaAs top cell material can be grown on the connecting junction, several buffer layers need to be used again. In spite of this tedious and complicated process, it seems doubtful that strain-free, device-quality layers can be synthesized via LPE. Thus, the improvement in overall cell efficiency resulting from reducing the bottom cell bandgap (increasing InAs mole fraction) must be weighed against the degradation in overall cell efficiency resulting from the reduced quality of individual cells.

In summary, improvements in the quality of AlGaAs/InGaAs structures have been made under the present contract. This has been achieved by using fast growth rates to minimize melt-back of the InGaAs layers and

by using several wide bandgap buffer layers between the tunnel junction and the active top cell. Cascade solar cell action has been observed for the first time in such AlGaAs/InGaAs cells. However, the performance of the top cell in such structures has been poor, and so far no improvement in cascade solar cell performance has been observed by replacing the GaAs of the bottom cell with an InGaAs layer.

2. AlAsSb/InGaP/InGaAs Material System

This system is shown in Figure A2. GaInAs is used for the lower cell, in common with the previous system, but InGaP is used for the upper cell and a lattice-matched AlAsSb alloy is used for the wide bandgap window layer. The advantage of using InGaP for the wide bandgap cell is a smaller lattice mismatch between the cells, especially for cells designed for low temperature operation. For the room temperature optimized design (0.95 eV and 1.6 eV), this system has a lattice mismatch of 0.83%, which is much less than that of the first system for the same bandgaps. However, the lattice mismatch (and the fact that the upper cell is still under tension) is a problem with this material system.

Other considerations are the relatively unknown properties of the GaInP layers and the difficulty in growing the desired GaInP layers. The GaInP layers are much more difficult to grow using liquid phase epitaxy (LPE) techniques than AlGaAs layers because of the high distribution coefficient of Ga in In and because of a lattice-pulling effect [A0]. During this work efforts have been directed toward the growth of GaInP using vapor phase epitaxy (VPE) techniques. Although a p-n junction has now been achieved in GaInP, the ability to heavily dope this material with both n- and p-type dopants needed for the connecting junction was not demonstrated.

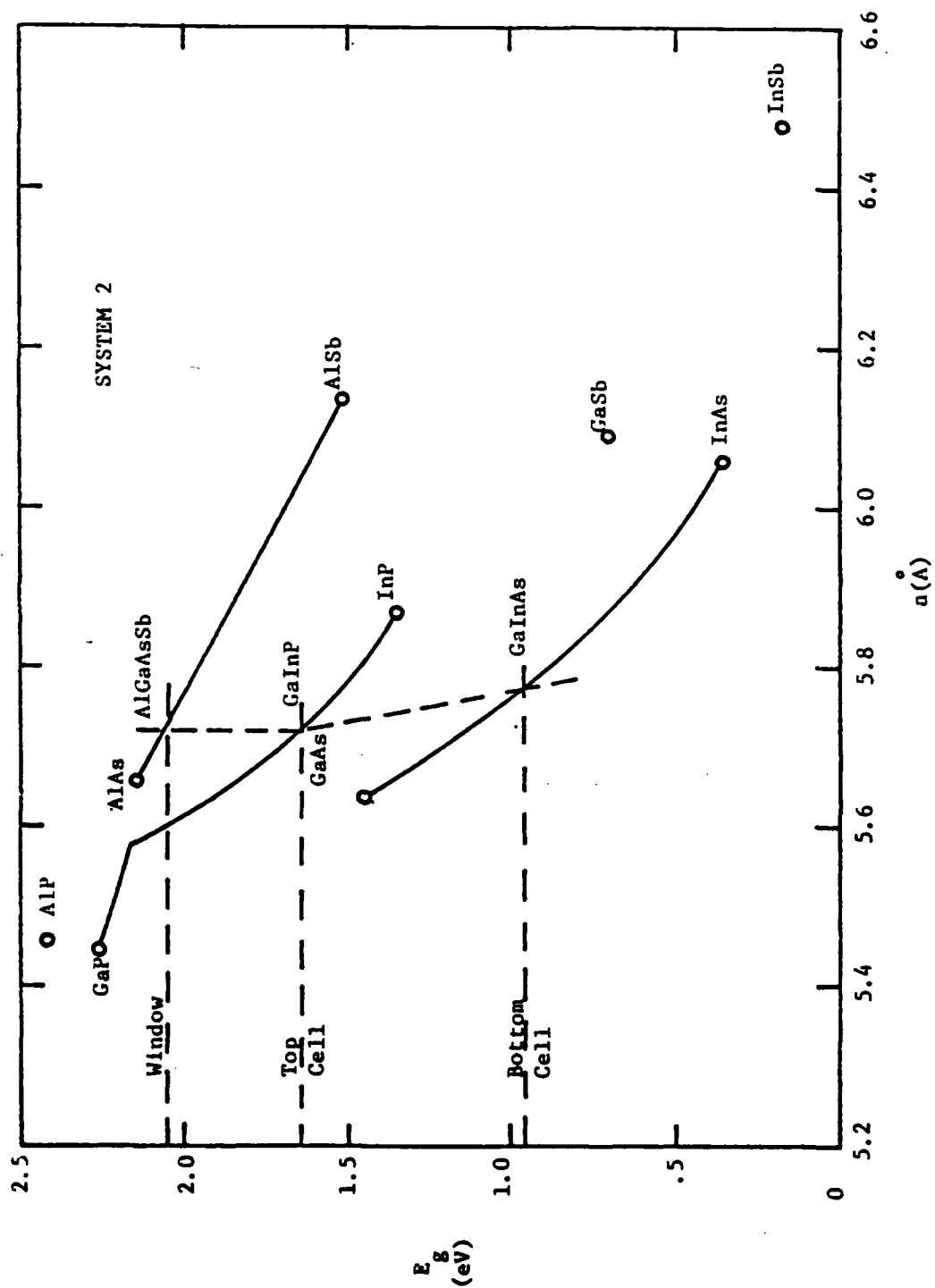


Figure A.2. AlGaAsSb/InGaP/InGaAs material system.

3. AlGaAsSb/AlGaAsSb/InGaAs Material System

This system uses the quaternary AlGaAsSb for the upper cell and window layer (see Figure A3). While this is a more complex material system, it is only by considering quaternary material systems that a lattice-matched cascade design can be obtained in the III-V materials. Figure A3 shows a lattice-matched combination for a 25°C optimum design. By moving along the GaInAs curve toward GaAs, bandgap combinations can be found for cells optimized at higher temperatures. The attractive feature of this system, as well as other quaternary systems, is that along a vertical line of constant lattice constant, all the desired bandgaps can be obtained within the quaternary plane.

Dissolution problems resulted from the growth of AlGaAsSb directly on InGaAs, but initial results with p-n junction in 1.4 to 1.5 eV quaternary material was encouraging. This system was abandoned in favor of the similar system AlGaAsSb/AlGaAsSb/GaAsSb which is being funded by SERI. This system, using GaAsSb as the bottom cell, avoids the dissolution problems associated with the growth of AlGaAsSb on InGaAs.

4. Inverted GaInAs/AlGaAs/AlGaAs Studies

The use of AlGaAs for the top cell and tunnel junction and of GaInAs for the bottom cell is very attractive because of the good electrical properties of individual diodes of AlGaAs and GaInAs. The fabrication of complete cells in this material system is very difficult, however, as noted in Section 1 of this Appendix.

Because of the problems discussed above, the fabrication of an inverted GaInAs/AlGaAs cell was attempted. The structure is shown in Figure A4. The cell fabrication sequence consists of growing in sequence on a substrate the window layer, top cell, tunnel junction, and bottom

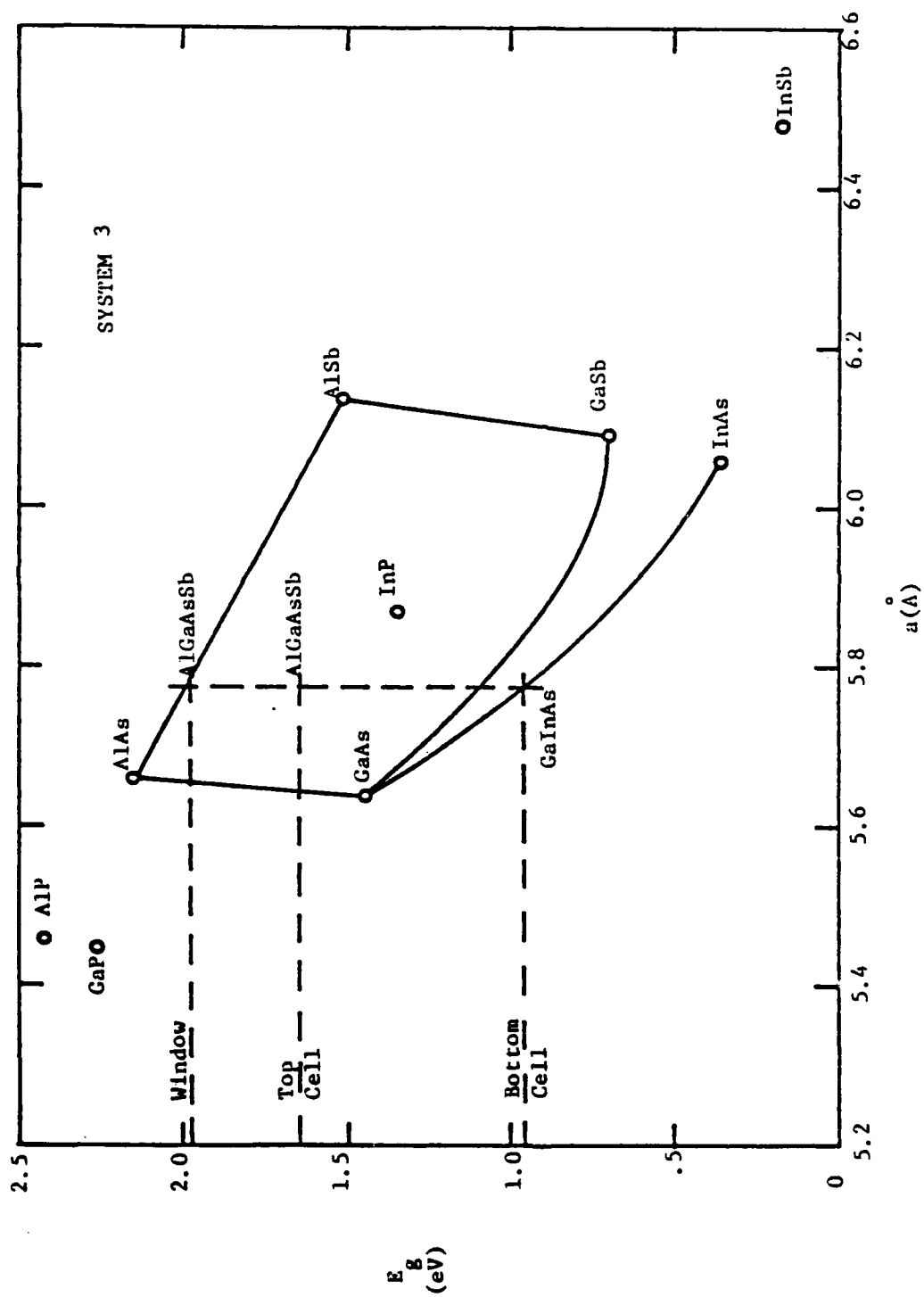


Figure A.3. AlGaAsSb/AlGaAsSb/InGaAs material system.

cell. This sequence of growing the layers has several advantages. First, the graded layers between a substrate and the bottom cell are eliminated and only one lattice mismatched interface occurs. Second, the top GaInAs layers can be grown under compressive stress, eliminating the problem of microcracks occurring in the normal structure. With this structure the cascade cell is completed by selectively etching away the GaAs substrate and inverting the cell so that light is incident on the window layer.

As a first step toward realizing this inverted structure, p-n junctions of GaInAs grown on AlGaAs were investigated. The quality of the GaInAs layers grown on AlGaAs was not as good as layers grown directly on GaAs. A possible explanation is that the In-rich melt attacks the AlGaAs layer and an intermediate layer of AlInGaAs rich in In is grown first. However, this quaternary shows a miscibility gap for high mole fractions of In; thus this intermediate layer may not grow or may grow with inferior quality. It was found that a slight degree of supersaturation (a few degrees) is helpful in improving the quality of the epitaxial InGaAs on AlGaAs layer.

An InGaAs p-n junction was epitaxially grown on an $\text{Al}_{0.2}\text{Ga}_{0.8}\text{As}$ layer with approximately 10% InAs and with $E_g = 1.27$ eV. The layers as grown are n-type and Mn was used as a p-type dopant. The I-V characteristics give an open circuit voltage of about 0.4 to 0.5 volt. This relatively low V_{oc} may be due to the presence of a low shunt impedance across the InGaAs p-n junction, resulting from the relatively high dislocation density from the 0.8% lattice mismatch between InGaAs and AlGaAs. Diffusion length (collection depth) measurements by the X-ray technique gave a collection depth of 0.44 μm . This relatively low value also

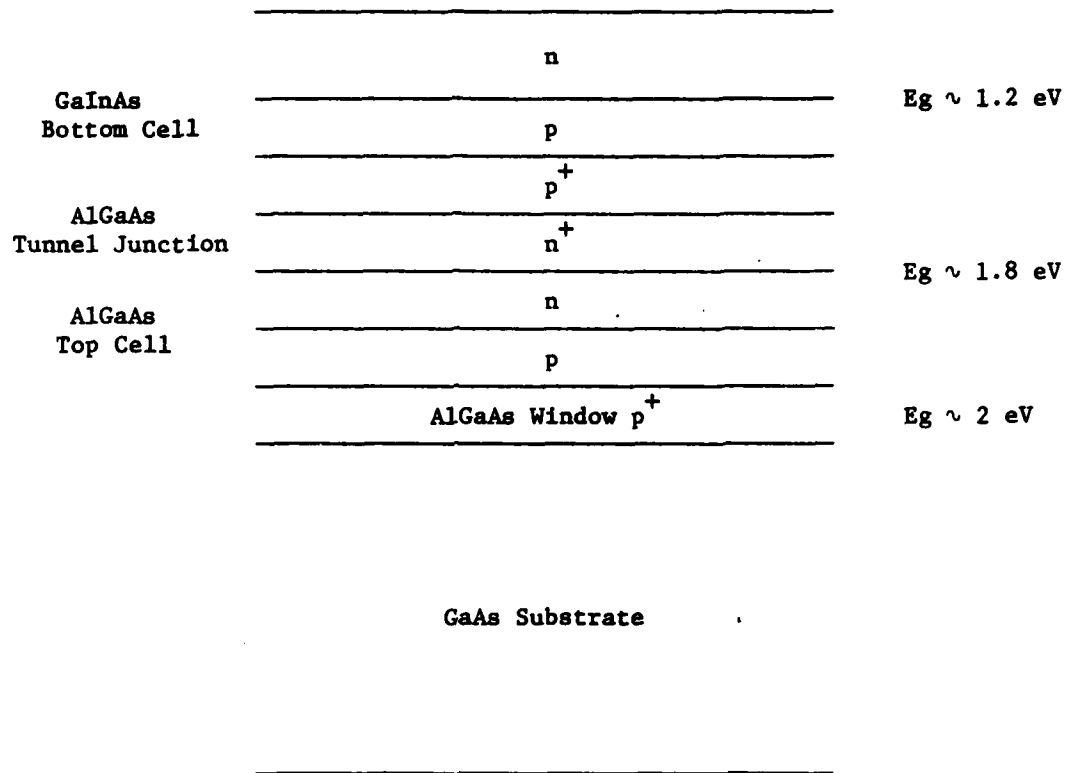


Figure A4. Inverted GaInAs/AlGaAs Cell Structure.

indicates a poor quality layer due to the high degree of mismatch and the relatively poor interface between InGaAs and AlGaAs.

In this study and in the work on the ion-inverted AlGaAs/AlGaAs/InGaAs cell (Section 1) we have used Mn as the InGaAs p-type dopant. Zn and Cd were unacceptable because of their high diffusivity and equally important because of their high vapor pressures which result in intermelt contamination. Ge is routinely used for doping GaAs and AlGaAs, however, for InGaAs with $x \geq 0.1$ Germanium's amphoteric nature results in its behavior as a net doner. Mn has been used in the past for LPE (liquid phase epitaxy) of GaAs [A1, A2], MBE (molecular beam epitaxy) of GaAs [A3], and for ion implantation in GaAs [A4]. It is characterized by a low diffusion coefficient [A4] and low vapor pressure. To our knowledge, ours was the first use of Mn as an acceptor for LPE InGaAs [A5]. The following will summarize the results of our characterization of Mn in LPE InGaAs. These results were previously published in more extensive form [A5].

5. Use of Mn as an Acceptor in LPE InGaAs

a. Distribution Coefficient

For LPE growth the concentration of the Mn in the melt (x_{Mn}^1) was varied between 0.1 and 1.0 atomic %. For higher Mn concentrations the solubility of As in Ga+In melts was found to increase substantially, accompanied by an increase in InAs mole fraction in the epitaxial layer, and a rough surface morphology of the epilayer. In earlier work [A1] on GaAs LPE, a similar observation was made regarding the increase of As solubility with the addition of Mn in a Ga melt. We have found that by keeping $x_{Mn}^1 < 1\%$ any detrimental effects of an epitaxial layer composition shift can be reduced.

The dependence of room-temperature hole concentration on Mn atom fraction in the melt is shown in Figure A5 for a growth temperature of 800°C, and for different epitaxial layer composition. It is seen that layers grown on different faces of (111) substrates show significant differences indicating that K_{Mn} is higher for layers grown on the Ga-face than on the As-face, reflecting the anisotropy of the zinc-blende structure. Secondly, no significant variation was found in the distribution coefficient of Mn when x was changed from 0.00 to 0.20. To determine the temperature dependence of K_{Mn} , some growth experiments were performed at reduced temperatures for $0 \leq x \leq 0.15$. The results plotted in Figure A6 show that K_{Mn} increases as growth temperature is lowered, consistent with observations on other dopants.

Mn has also been used to grow p-type GaInAs with $x = 0.53$ on InP substrates at 650°C to further demonstrate the viability of Mn as a p-type dopant over a wide range of $Ga_{1-x}In_xAs$ composition.

b. Electrical Properties

Measured values of room temperature Hall mobility are plotted as a function of hole concentration in Figure A7. In this figure, published data points for GaAs are also included for comparison. It is seen that the mobility in Mn doped samples does not show a systematic dependence on composition factor x , at least in the range used here ($0 < x < 0.2$). A similar effect has been observed for Zn doped GaInAs [A6].

From the work done on GaAs, it is known that Mn is not a shallow acceptor. In order to determine the activation energy of Mn in $Ga_{1-x}In_xAs$, Hall measurements were made for a sample with $x = 0.21$ in the temperature range 150-300 K. In Figure A8, the Hall mobility is plotted against

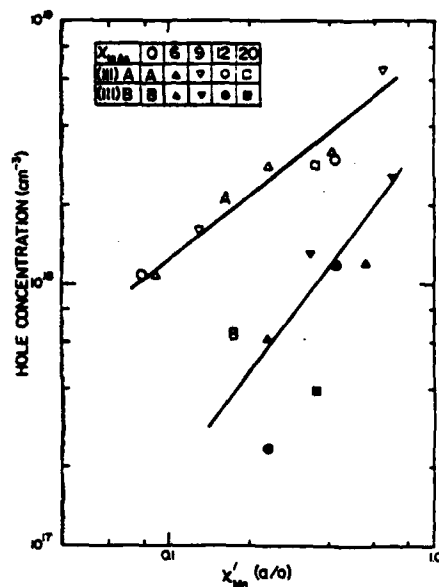


Fig. A.5. Hole concentration vs atomic fraction of Mn in melt.

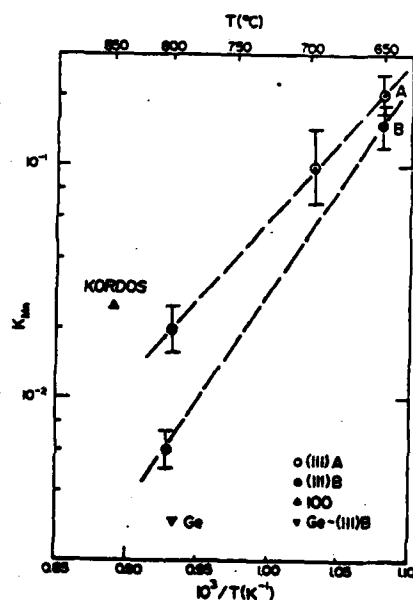


Fig. A.6. Temperature dependence of Mn distribution coefficient: Open and closed circles represent our data points. Also, included are data on Mn doped (100) GaAs from Ref. [A1] (Δ), and on Ge doped (111) B $\text{Ga}_{0.95}\text{In}_{0.05}\text{As}$ from Ref. [A11] (∇).

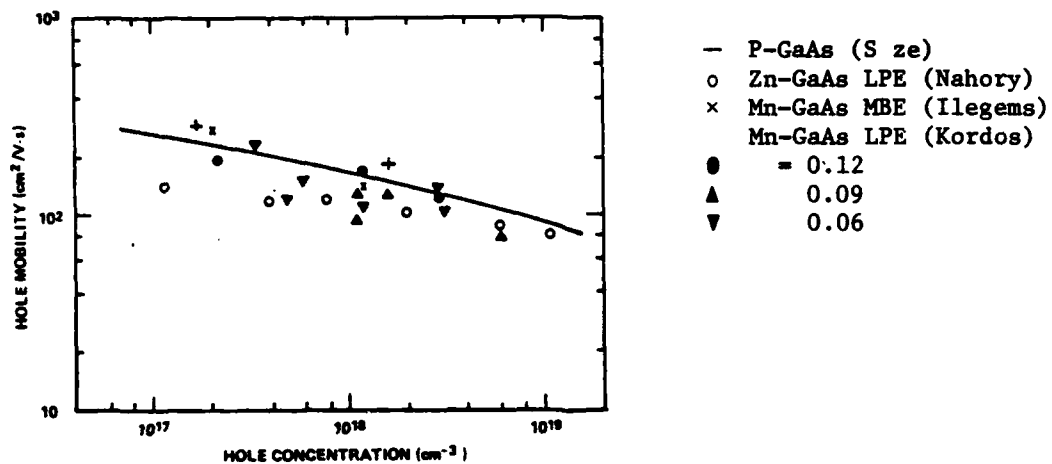


Figure. A.7. Dependence of Hall mobility on hole concentration. Solid data points (●, ▲, ▼) are from this work.

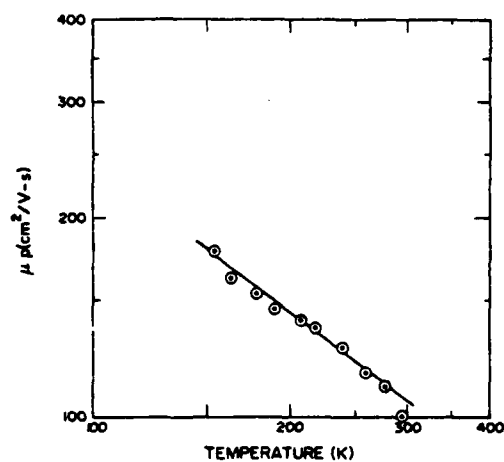


Figure A.8. Hall mobility vs. temperature for Mn doped
p-Ga_{0.79}In_{0.21}As.

temperature and in Figure A9 the variation in hole concentration with temperature is shown. Following the analysis given in Ref. [A2], an activation energy of $E_A \approx 77$ meV is derived for a bandgap of 1.20 eV. For GaAs the thermal activation energy E_A of the acceptor level associated with Mn has been determined to be between 72 and 114 meV. Considerable scatter in E_A values can be found in the published literature, e.g. 72-80 meV (LPE at 800°C, Ref. [A2]), 84-92 meV (LPE at 850°C, Ref. [A1]), 95 ± 15 meV (Mn-implanted GaAs, Ref. [A4]), and 97-114 meV (MBE GaAs, Ref. [A6]). Unfortunately, due to the uncertainty of E_A in GaAs, no definite conclusions can be drawn of how E_A varies when the bandgap decreases from 1.43 eV (GaAs) to 1.2 eV in the $\text{Ga}_{1-x}\text{In}_x\text{As}$ alloys. However, from the present results it can be concluded that E_A in these alloys tends to be lower than that in GaAs. Such a trend is in good agreement with the increase of E_A of several impurities with the increase of E_g reported for the AlGaAs system [A7,A8].

Diffusion length measurements on InGaAs p-n junctions with a γ -cell technique [A9] yielded $6 \mu\text{m} < (L_n + L_p + W_D) < 8 \mu\text{m}$ indicating the high quality of this Mn doped material, which L_n , L_p and W_D are the electron diffusion length, the hole diffusion length and the widths of the depletion region, respectively. Since, for this range of bandgap and carrier density, W_D is less than a micron and $L_n > L_p$, the major contribution to the collection depth is due to L_n . Thus, the present step grading process coupled with the use of Mn as a p-dopant has resulted in a diffusion length higher than previously reported values for GaInAs in the same composition range. For example, $\text{Ga}_{1-x}\text{In}_x\text{As}$ p-n junctions utilizing Zn doping have exhibited much lower electron diffusion lengths

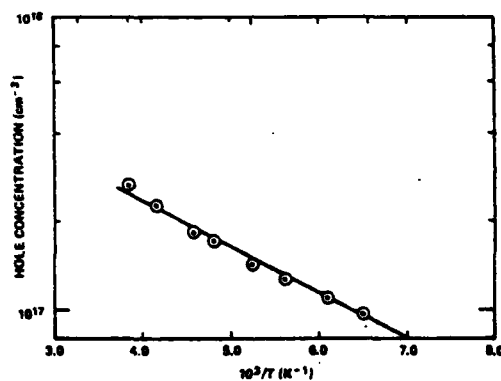


Figure A.9. Hole concentration vs. inverse temperature for Mn-doped $\text{p-Ga}_{0.79}\text{In}_{0.21}\text{As}$. (Same as in Figure A.8.)

in p-type material as reported by Ettenberg et al. [A10] for both LPE and VPE devices. They have reported that $L_N = 2.7 \mu\text{m}$ for $x = 0.205$ in VPE material grown with 5 intermediate grading layers, and $L_n = 0.5 \mu\text{m}$ for $x = 0.238$ in LPE material with 2 grading layers.

REFERENCES

- 2.1 M. R. Lorentz, R. Chicotka, G. D. Pettit, and P. J. Dean, Solid State Comm., 8, 1970, p. 693.
- 2.2 A. Onton, Extended Abstracts, International Conference of Semiconductors, 10th, Cambridge, August 1970.
- 2.3 A. Onton, M. R. Lorentz, and J. M. Woodal, Bulletin of the American Physics Society, 16, 1971, p. 371.
- 2.4 D. L. Rode, J. Appl. Phys., 45, 1974, p. 3887.
- 2.5 M. Neuberger, Handbook of Electronic Materials, Vol. 2, III-V Semiconducting Compounds, IFI/Plenum Press, New York, NY, 1971.
- 2.6 J. W. Harrison and J. R. Hauser, J. Appl. Phys., 47, 1976, p. 292.
- 2.7 R. Tsu, L. L. Chiang, G. A. Sai-Halasz, and L. Esaki, Phys. Rev. Lett., 34, 1975, p. 1509.
- 2.8 A. G. Milnes and D. L. Feucht, Heterojunctions and Metal-Semiconductor Junctions, Academic Press, New York, NY, 1972.
- 2.9 E. M. Conwell, High Field Transport in Semiconductors, Academic Press, New York, NY, 1967.
- 2.10 Obtained from a Monte Carlo Calculation by J. R. Hauser.
- 2.11 M. Konagai and K. Takahashi, J. Appl. Phys., 46, 1976, p. 3542.
- 2.12 M. Ettenberg and C. J. Neuse, J. Appl. Phys., 46, 1975, p. 3500.
- 2.13 G. A. Acket, W. Nijman, and H. 't Lam, J. Appl. Phys., 45, 1974, p. 3033.
- 2.14 D. B. Holt, J. Phys. Chem. Solids, 27, 1966, p. 1053.
- 2.15 M. Ettenberg and H. Kressel, J. Appl. Phys., 47, 1976, p. 1538.
- 2.16 S. M. Sze, Physics of Semiconductor Devices, New York: Wiley, 1969.
- 2.17 R. B. Emmons and G. Lucovsky, IEEE Trans. Electron Devices, ED-13, 1966, pp. 197-305.
- 2.18 R. VanOverstraeten and W. Nuyts, IEEE Trans. Electron Devices, ED-16, 1969, pp. 632-641.
- 2.19 E. S. Rittner, J. Energy, 1, 1977, pp. 9-17.
- 2.20 B. Ellis and T. S. Moss, Solid State Electron., 13, 1970, pp. 1-24.

- 2.21 J. Lindmayer, Comsat Tech. Rev., 2, 1972, pp. 105-121.
- 2.22 M. B. Prince, J. Appl. Phys., 26, 1955, pp. 534-540.
- 2.23 M. F. Lamorte and D. Abbott, "Analysis of a two-junction monolithic solar cell in a structure using $\text{Al Ga}_{1-u}\text{As}$ and $\text{Ga In}_{1-v}\text{As}$," presented at the 12th IEEE Photovoltaic Specialists Conf., Baton Rouge, La., Nov. 15-18, 1976.
- 2.24 M. F. Lamorte and D. Abbott, "General analysis to obtain solar cell V-I curve," presented at the 12th IEEE Photovoltaic Specialists Conf., Baton Rouge, La., Nov. 15-18, 1976.
- 2.25 "Solar cell design study," Research Triangle Institute, Research Triangle Park, N. C., Final Rep., Contract F33615-76-c-1283, Feb., 1977.
- 2.26 M. F. Lamorte and D. Abbott, "Analysis of a two-junction monolithic solar cell in a structure using $\text{Al Ga}_{1-u}\text{As}$ and $\text{Ga In}_{1-v}\text{As}$," presented at the DOE Photovoltaic Concentrator Systems Workshop, Scottsdale, Arizona, May 24-26, 1977.
- 2.27 _____, presented at the 13th IEEE Photovoltaic Specialists Conf., Washington, D.C., June 5-8, 1978.
- 2.28 M. F. Lamorte, Advanced Energy Conversion, 3, 1963, pp. 551-563.
- 2.29 H. A. VanderPlas, L. W. James, R. L. Moon, and N. J. Nelson, presented at the 13th IEEE Photovoltaic Specialists Conf., Washington, D. C., June 5-8, 1978.
- 2.30 J. Ewan, R. C. Knechtli, R. Loo, and G. S. Kamath, presented at the 13th IEEE Photovoltaic Specialists Conf., Washington, D. C., June 5-8, 1978.
- 2.31 R. Sahai, D. D. Edwall, and J. S. Harris, presented at the 13th IEEE Photovoltaic Specialists Conf., Washington, D. C., June 5-8, 1978.
- 2.32 J. C. C. Fan and C. Boyler, presented at the 13th IEEE Photovoltaic Specialists Conf., Washington, D. C., June 5-8, 1978.
- 2.33 S. Fujita, S. M. Bedair, M. A. Littlejohn, and J. R. Hauser, J. Appl. Phys., 51 (10), 1980, pp. 5438-5444.
- 2.34 S. M. Bedair, J. Appl. Phys., 51 (7), 1980, pp. 3935-3937.
- 2.35 B. Tuck and A. J. N. Houghton, Phys. Stat. Sol. (a), 65, 1981, p. 643.
- 2.36 K. K. Shih, J. W. Allen, and G. L. Pearson, J. Phys. Chem. Solids, 29, 1968, pp. 367-377.

- 2.37 C. P. Lee, S. Margalit, and A. Yariv, Solid-State Electron., 21, 1978, pp. 905-907.
- 2.38 A. J. Springthorpe, F. D. King, and A. Becke, J. Electron. Mater., 4, 1975, p. 101.
- 2.39 S. Zukotynski, S. Sumski, M. B. Panish, and H. C. Casey, Jr., J. Appl. Phys., 50, 1979, p. 5795.
- 2.40 L. Gousskov, S. Bilac, J. Pimentel, and A. Gousskov, Solid-State Electron., 20, 1977, pp. 653-656.
- 2.41 P. Kordos, L. Jansak, and V. Benc, Solid-State Electron., 18, 1975, pp. 223-226.
- 2.42 S. Muka, Y. Makita, S. Bonda, J. Appl. Phys., 50(3), 1979, pp. 1304-1307.
- 2.43 P. W. Yu and Y. S. Park, J. Appl. Phys., 48 (6), 1977, pp. 2434-2441.
- 2.44 D. J. Ashen, P. J. Dean, D. T. J. Hurde, J. B. Mullin, A. M. White, and P. D. Greene, J. Phys. Chem. Solids, 36, 1975, p. 1041.
- 2.45 M. Ilegems, J. Appl. Phys., 48, 1978, p. 1278.
- 2.46 M. B. Panish and I. Hayashi, Appl. Solid State Sci., 4, 1974, p. 235.
- 2.47 S. Zukotynski, S. Sumski, M. B. Panish, and H. C. Casey, Jr., J. Appl. Phys., 50, 1979, p. 5795.
- 2.48 P. Lawaetz, Phys. Rev. B, 4, 1971, p. 3460.
- 2.49 A. J. Springthorpe, F. D. King, and A. Becke, J. Electron. Mater., 4, 1975, p. 101.
- 2.50 B. I. Boltaks, T. D. Dzhaferov, Yu. P. Demakov, and I. E. Maronchuk, Sov. Phys. Semicond., 9, 1975, p. 545.
- 2.51 K. Masu, M. Konagai, and K. Takahashi, J. Appl. Phys., 51, 1980, p. 1060.
- 2.52 S. Mukai, Y. Makita, and S. Gonda, J. Appl. Phys., 50, 1979, p. 1304.
- 2.53 C. Flores and D. Passoni (private communication).
- 2.54 A. S. Jordan, J. Electrochem. Soc., 118, 1971, p. 781.
- 2.55 H. C. Casey, Jr. and M. B. Panish, Heterostructure Lasers, Academic Press, New York, NY, 1978, Part B, p. 96.
- 2.56 M. Ilegems and W. C. O'Mara, J. Appl. Phys., 43, 1972, p. 1190.
- 2.57 L. J. Vieland and I. Kudman, J. Phys. Chem. Solids, 24, 1963, p. 437.

- 2.58 H. Kressel, M. S. Abrahams, F. Z. Hawrylo, and C. J. Buicocchi, J. Appl. Phys., 39, 1968, p. 5139.
- 2.59 P. P. Debye and E. M. Conwell, Phys. Rev., 93, 1954, p. 693.
- 2.60 G. M. Stillman and C. M. Wolfe, Thin Solid Films, 31, 1976, p. 69.
- 2.61 J. W. Harrison and J. R. Hauser, Phys. Rev. B, 13, 1976, p. 5347.
- 2.62 J. W. Harrison and J. R. Hauser, J. Appl. Phys., 47, 1976, p. 292.
- 2.63 M. A. Littlejohn, J. R. Hauser, T. H. Glisson, D. K. Ferry, and J. W. Harrison, Solid State Electron., 21, 1978, p. 107.
- 2.64 J. Comas and S. M. Bedair, Appl. Phys. Lett., 39 (12), 1981, pp. 989-991.
- 2.65 W. V. McLevige, K. V. Vaidynathan, B. G. Streetman, M. Ilegems, L. Comas, and L. Flew, Appl. Phys. Lett., 33, 1978, p. 129.
- 2.66 L. Esaki, Phys. Rev., 109, 1958, p. 602.
- 2.67 F. E. Rosetoczy, F. Ermanis, I. Hayashi, and B. Schwartz, J. Appl. Phys., 41, (1), 1970, pp. 264-270.
- 2.68 S. Asai, S. Okasaki, and H. Kodera, Proc. 4th International Symp. on GaAs and Rel. Compds., Inst. Phys. Conf. Ser. No. 17, 1973.
- 2.69 M. B. Panish, J. Appl. Phys., 44, 1973, p. 2659.
- 2.70 N. Holonyak, Jr., J. Appl. Phys., 31, 1960, p. 130.
- 2.71 R. S. Classen, J. Appl. Phys., 32, 1961, p. 2372.
- 2.72 K. K. Shin and G. D. Pettit, J. Electron. Mater., 3, 1974, p. 391.
- 2.73 H. C. Casey, Jr. and F. Stern, J. Appl. Phys., 47 (2), 1976, pp. 631-643.
- 2.74 W. R. Wagner, Inst. Phys. Conf. Ser. No. 336, 1977, pp. 65-73.
- 2.75 W. R. Wagner, J. Electrochem. Soc., 128 (12), 1981, pp. 2641-2644.
- 2.76 W. R. Wagner, J. Appl. Phys., 49, 1978, pp. 173-180.
- 2.77 M. G. Mil'vidski, V. B. Osvenskii, A. G. Novikov, G. V. Fomin, and S. P. Grishina, Sov. Phys. Cryst., 18, 1974, p. 519.
- 2.78 M. Hansen, Constitution of Binary Alloys, McGraw-Hill, New York, NY, 1958, p. 165.
- 2.79 J. C. Phillips, Bonds and Bands in Semiconductors, Ch. 1, Academic Press, London, 1973.

- 2.80 L. Pauling, The Nature of the Chemical Bond, Ch. 4, Cornell Univ. Press, NY, 1960.
- 2.81 M. E. Weiner, J. Electro. Chem. Soc., 119 (4), 1972, pp. 496-503.
- 2.82 S. M. Pintus, E. A. Krivorotov, and A. A. Litvin, Sint. Rost. Soversh. Krist. Plenok Poluprovada, (Publ 1981), pp. 178-181.
- 3.1 J. H. Renolds and A. Meulenber, Jr., J. Appl. Phys., 45, 1974, p. 2582.
- 3.2 V. G. Weizer, IEEE Photo. Spec. Conf., 11th, 1976, p. 67.
- 3.3 A. M. Sekela, D. L. Feucht, and A. G. Milnes, "GaAs and Related Compounds," 1974, The Inst. of Physics, London, 1975, p. 245.
- 3.4 R. H. Cox and H. Strack, Solid-State Electron., 10, 1967, p. 1213.
- 3.5 C. H. Henry, R. A. Logan, and F. R. Merritt, Appl. Phys. Lett., 31, 1977, p. 454.
- 3.6 S. M. Sze, Physics of Semiconductor Devices, John Wiley and Sons, New York, NY, 1969.
- 3.7 J. Lindmayer, Comsat. Tech. Rev., 2, 1972, p. 105.
- 3.8 M. A. Green, Solid-State Electron, 20, 1977, p. 265.
- 3.9 D. L. Pulfrey, Solid-State Electron., 21, 1978, p. 519.
- 3.10 L. Y. L. Shen, J. Appl. Phys., 48, 1977, p. 3628.
- 3.11 J. P. Chiang and J. R. Hauser, Final Report on NASA Grant No. NSG-1116, March, 1979.
- 3.12 S. M. Bedair, J. Appl. Phys., 50, 1979, p. 7267.
- 3.13 J. W. Harrison and J. R. Hauser, Phys. Rev. B, 13, 1976, p. 5347.
- 3.14 A. Chandra and L. F. Eastman, J. Appl. Phys., 51, 1980, p. 2669.
- 3.15 E. O. Kane, J. Appl. Phys., 32, 1961, p. 83.
- 3.16 L. M. Frass and R. C. Knechtli, IEEE Photo. Spec. Conf., 13th, 1978, p. 886.
- 3.17 S. M. Bedair, J. Appl. Phys., 50, 1979, p. 7267.
- 4.1 L. Miller, S. W. Zehr, and J. S. Harris, Jr., J. Appl. Phys., 53 (1), 1982, pp. 744-748.
- A.1 P. Kordos, L. Jansak, and V. Benc, Solid-State Electron., 18, 1975, p. 223.

- A.2 L. Gouskov, S. Bilac, J. Pimentel, and A. Gouskov, Solid-State Electron., 20, 1977, p. 653.
- A.3 M. Ilegems, R. Dingle, and L. W. Rupp, Jr., J. Appl. Phys., 46, 1975, p. 3059.
- A.4 P. W. Yu and Y. S. Park, J. Appl. Phys., 50, 1979, p. 1097.
- A.5 S. B. Phatak, S. M. Bedair, and S. Fujita, Solid-State Electron., 23, 1980, pp. 839-844.
- A.6 R. E. Nahory, M. A. Pollack, and J. C. DeWinter, J. Appl. Phys., 46 (2), 1975, p. 775.
- A.7 S. Mukai, Y. Makita, S. Gonda, J. Appl. Phys., 50, 1979, p. 1304.
- A.8 A. J. Springthorpe, F. D. King, and A. Becke, J. Electron. Mater., 4, 1975, p. 101.
- A.9 S. H. Woltz, "Diffusion Length Measurements in Compound Semiconductors by a γ -Ray Technique," M.S. Thesis (unpublished), North Carolina State University, 1978.
- A.10 M. Ettenberg, C. J. Nuese, J. R. Appert, J. J. Gannon, and R. E. Enstrom, J. Electron. Mater., 4, 1975, p. 37.
- A.11 M. Kurihara, T. Morizumi, and K. Takahashi, Solid-State Electron., 16, 1973, p. 763.

END

DATE
FILMED

583

DT 11